eman ta zabal zazu

Universidad del País Vasco
Euskal Herriko Unibertsitatea

Bridging Nanotechnology and Neurobiology: Voltage-Sensing and Photothermal Control of Neural Activity Using Semiconductor and Metallic Nanocrystals

Thesis by

Zuzanna Lawera

for the degree of

Doctor of Philosophy in Physics

Universidad del País Vasco

Euskal Herriko Unibertsitatea

Supervised by

Marek Grzelczak and Rafael Yuste

Donostia, November 2025

Abstract

Driven by the need for minimally invasive, high-resolution neural interfaces, this dissertation bridges nanotechnology and neurobiology by developing nanoscale tools for optical detection and modulation of neural activity. With a focus on semiconductor quantum dots and plasmonic gold nanocrystals, this dissertation presents efforts to develop complementary platforms to "Read" and "Write" neural signals. Designed to either report changes in membrane potential or deliver light-driven stimuli, these nanomaterials offer functional advantages at dimensions inaccessible to conventional bioelectronic approaches.

Chapter 1 provides an interdisciplinary literature review, introducing the NanoNeuro, outlining how quantum dots and plasmonic nanoparticles can interact with neural systems and highlighting key challenges such as targeted delivery, biocompatibility, and integration with living cells. It provides an overview of the current state of the art and situates the objective of the presented research within this framework.

Chapter 2 describes an experimental platform of genetically engineered “self-spiking” HEK293 cells that fire spontaneous, synchronized action potentials. This in vitro workhorse model, validated via calcium imaging, provided a simplified yet consistent testbed for evaluating nanoscale voltage-sensitive probes.

At the heart of the dissertation, Chapter 3 details the development of a quantum dot-based voltage sensor. Spherical quantum well nanocrystals were synthesized and characterized using spectroscopic and electron microscopy techniques to confirm their physicochemical properties. To adapt the nanocrystals for biological environments, their surfaces were engineered for aqueous stability and incorporated into cell membranes using fusogenic liposomes. Their ability to uniformly label the plasma membrane was assessed by fluorescence microscopy in self-spiking HEK293 monolayers. Although the quantum dots remained photostable, fluorescence changes during action potentials remained below the threshold required for reliable detection. The absence of clear spike-correlated signals underscored limitations in sensitivity and temporal resolution of camera, pointing to the need for brighter probes, faster imaging, and improved signal-to-noise performance.

In parallel, Chapter 4 investigates photothermal modulation of neurons with plasmonic nanocrystals. Gold nanoparticles of controlled size and morphology (spheres and bipyramids) were synthesized and characterized by spectroscopy and transmission electron microscopy to

determine their optical properties and structural uniformity. Following surface functionalization to ensure biological compatibility, nanocrystals were introduced into cell cultures (SH-SY5Y and cortex primary neurons). Their association with cells and internalization was assessed using confocal fluorescence microscopy and electron microscopy. Upon optical stimulation, the nanoparticles converted incident light into localized heating. In a proof-of-concept experiment performed in brain slices, this effect was sufficient to elicit neuronal firing: single action potentials were induced at moderate excitation power, and bursts of activity at higher intensities. These findings support the feasibility of plasmonic nanocrystals as optically addressable actuators for controlled neuromodulation.

Chapter 5 summarizes the main findings and reflects on technological limitations and future directions of the work. The experimental research presented in this dissertation was carried out by the author at the Centro de Física de Materiales in Donostia, Spain (Marek Grzelczak's group), and complemented by research stays at the Neurotechnology Center at Columbia University in New York (Rafael Yuste's group), the Department of Chemistry at Columbia University (Jonathan Owen's group), and the FluoroNanoTools Laboratory at the Biofisika Institute in Bilbao, Spain (Monica Carril's group). These research stays formed the foundation of the experimental work described in this thesis. The broader collaborative framework extended beyond these four laboratories and included members of the IKUR Basque NanoNeuro Network (B3N), reinforcing the interdisciplinary nature of the project. Although some outcomes, particularly in voltage sensing, did not fully meet initial expectations, the work contributed to a deeper understanding of nanomaterial-cell interactions and clarified key design parameters for future tool development. The insights gained provide a foundation for more targeted and informed advancement of neural interfaces based on nanocrystals and nanoparticles.

Table of Contents

Chapter 1

Nano Neuro

Objective

The human brain, the most complex organ known, remains one of the greatest scientific challenges. To unravel the processes that govern behavior and cognition, it is essential to deepen our understanding of their primary driver: the central nervous system. Neurobiology, which investigates the structure and function of neural systems, has yielded foundational insights into perception, memory, and disease, catalyzing breakthroughs in the diagnosis and treatment of neurological disorders. The impact of these discoveries extends far beyond medicine, shaping fields as diverse as artificial intelligence and public policy. Yet, as our scientific questions grow increasingly precise, so too must the tools we employ.[1]

The computational capabilities of brain is driven by nanoscale machinery: ion channels just a few nanometres wide that gate millisecond electrical spikes, and synapses that compress thousands of molecular components into volumes smaller than a femtolitre.[2,3] Conventional tools such as electrodes and fluorescent dyes lack the temporal resolution and specificity to fully access or modulate these microscopic dynamics, leaving key biological processes obscured. This gap marks the emergence of Nano Neuro, a field at the intersection of nanoscience and neurobiology, which offers unprecedented opportunities for precision neural interfacing. Leveraging the distinctive electronic, optical, and biochemical properties of nanomaterials, researchers can now sense, manipulate, and study neural circuits at scales previously inaccessible.[1]

The promise of Nano Neuro is profound: to reveal hidden patterns of neural activity, enable localized neuromodulation, and drive innovation in both therapeutic intervention and neural enhancement. Nonetheless, the field faces formidable challenges, including the need for precise targeting, long-term biocompatibility, and minimally invasive integration with living tissue.

Chapter 1 establishes the conceptual and technical foundation for introducing Nano Neuro. It begins with a review of essential neurobiological principles, followed by an introduction to nanotechnology and the materials most relevant to neural applications. With this groundwork in place, we examine the convergence of these disciplines, highlighting current technologies, landmark studies, and emerging directions. The goal is to situate the work presented in this dissertation within its broader scientific context and highlight the foundational questions it seeks to address: reading and writing neural activity.

1. Neurobiology

1.1. Neural Networks and Brain Function

The central nervous system (CNS), composed of the brain and spinal cord, serves as the primary center for processing, integrating, and coordinating information throughout the body. Within the brain, extensive networks of interconnected neurons enable perception, thought, movement, and behavior. The spinal cord acts as a critical communication pathway, transmitting signals between the brain and peripheral organs, and regulating reflexive motor responses. Together, the brain and spinal cord form the core structure responsible for receiving sensory input, generating motor output, and maintaining essential bodily functions.[4]

The CNS is built from two main types of cells: neurons, and glia cells (astrocytes, oligodendrocytes, and microglia).[5] Although glial cells contribute significantly to neural function, the following discussion will focus on neurons, as they are the most relevant to the topics explored in this dissertation.

Neurons are highly specialized for the transmission of information through electrical impulses and chemical signaling. Despite variation in morphology and function, most neurons share a common structural organization: dendrites, which receive synaptic inputs; the cell body (soma), where these inputs are integrated; and a single axon, which conducts the output signal, known as an action potential, toward target cells via specialized connections called synapses (Figure 1.1).[6] Many axons are wrapped in segments of myelin, a lipid-rich insulating layer produced by glial cells, which significantly increases the speed and efficiency of signal conduction.[7] Collectively, neurons form a distributed input-output network whose coordinated activity underlies the full range of neural functions, from basic reflexes to higher cognitive processes.[4,8]

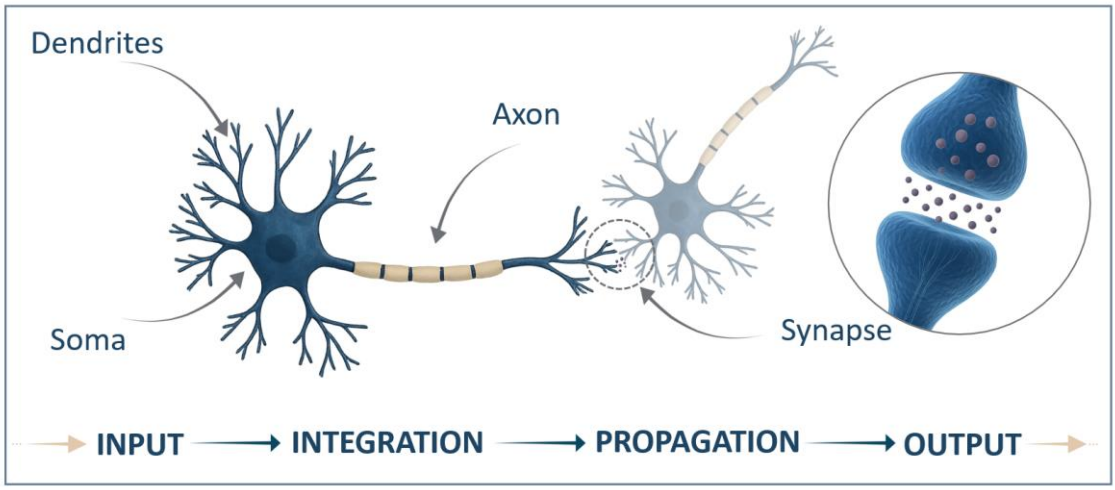

Figure 1.1 Schematic of neuronal morphology and signal flow. Dendrites receive synaptic inputs, which are integrated in the soma. If threshold is reached, an action potential is generated at the axon hillock and propagates along the axon – often myelinated – to presynaptic terminals. At the synapse (inset), neurotransmitter release enables communication with downstream cells. This input → integration → propagation → output sequence supports neural circuit function from reflexes to cognition.

Neuronal input processing begins on the dendrites or soma, when synapses receive a signal that cause small voltage changes in the postsynaptic membrane.[9] A synaptic input that makes the inside of the neuron more positive than the resting state results in a depolarizing postsynaptic potential, which is excitatory because it brings the neuron closer to firing (EPSP – excitatory postsynaptic potential, Figure 1.2 D). In contrast, an input that makes the inside more negative leads to hyperpolarization, which is inhibitory as it moves the membrane potential further from the firing threshold (IPSP – inhibitory postsynaptic potential, Figure 1.2 E). These small, graded voltage changes spread passively across the membrane, diminishing with distance.[10] The neuron continuously integrates these excitatory and inhibitory signals over time and space, a process known as synaptic summation. This integration occurs at the axon hillock, a specialized region near the base of the axon, characterized by a high density of voltage-gated ion channels. If the combined input reaches a critical threshold potential, an action potential is triggered (Figure 1.2 C). If not, the membrane potential returns to rest and no output signal is generated.[8,11]

To better understand what an action potential is, and what drives the voltage changes that lead to its initiation, it is essential to first introduce two key components underlying all neuronal electrical activity: the cell membrane and ion channels.[2,12] The neuronal cell membrane, like that of other eukaryotic cells, is composed of phospholipid molecules arranged in a bilayer. This structure separates the intracellular environment from the extracellular space. The hydrophilic heads of phospholipids face the aqueous environments on either side of the membrane, while the hydrophobic tails orient inward, forming a nonpolar core that is impermeable to ions. This impermeability is critical, as it allows the neuron to maintain different ion concentrations on

either side of the membrane.[12] As ions carry electrical charge, this separation leads to an unequal distribution of charge, which generates a voltage difference across the membrane. In a neuron at rest (not actively firing), this voltage difference is referred to as the resting membrane potential, with the inside of the cell typically measuring about -70 millivolts (mV) more negative than the outside.[13] To regulate the movement of ions across the membrane, neurons rely on ion channels. These are proteins integrated into the cell membrane that act as selective gates, allowing specific types of ions to enter or exit the cell. Ion channels play a key role in many physiological processes, including nerve impulse transmission, muscle contraction, and cellular signaling. In the context of this dissertation, the focus will be on their role in generating and propagating the action potential, the electrical signal that enables communication between neurons.[14]

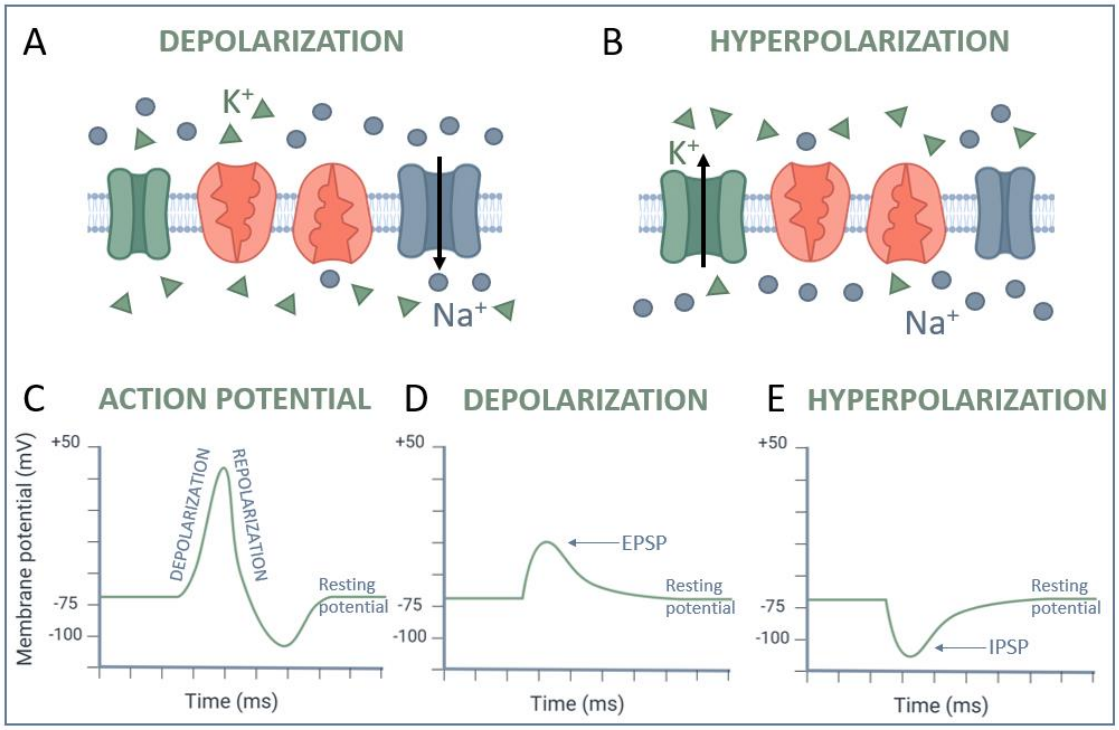

Figure 1.2 Membrane potential changes during neuronal signaling. (A) Depolarization: Voltage-gated Na^+ channels (blue) open in response to a threshold stimulus, allowing Na^+ influx and driving the membrane potential toward more positive values. Voltage-gated K^+ channels (green) remain mostly closed at this stage. Na^+/K^+ ATPase pumps (orange) maintain resting ion gradients. (B) Hyperpolarization: Following action potential peak, voltage-gated K^+ channels (green) open, promoting K^+ efflux and a membrane potential more negative than resting. Na^+ channels (blue) are inactivated. Ion pumps (orange) continue sustaining electrochemical gradients. (C) An action potential is a rapid, all-or-none depolarization triggered when integrated synaptic inputs raise the membrane potential above threshold, followed by repolarization and a brief afterhyperpolarization. (D) An excitatory postsynaptic potential (EPSP) is a small, graded depolarization that brings the membrane closer to threshold, increasing the likelihood of firing. (E) An inhibitory postsynaptic potential (IPSP) is a transient hyperpolarization that drives the membrane potential further from threshold, reducing excitability.

If the total depolarizing input at the axon hillock reaches a critical threshold (typically around -55 mV), voltage-gated Na^+ channels open rapidly (Figure 1.2 A). Na^+ ions rush into the cell, reversing the membrane polarity and causing a rapid spike in voltage: this is the action potential. Almost immediately, Na^+ channels inactivate and voltage-gated K^+ channels open, allowing K^+ to exit the cell (Figure 1.2 B). This outflow restores the negative membrane potential in a process called repolarization, which is often followed by a brief hyperpolarization, as K^+ channels remain open slightly longer. The disturbance of the membrane's electric field activates following channels and allow the action potential to propagate along the axon.[9,15] In essence, an action potential is a self-propagating wave of depolarization followed by repolarization. Because it is actively renewed as it moves, it does not lose strength over distance. This enables neurons to transmit signals rapidly and reliably, even over long distances – for example, from the spinal cord to the tips of the toes.[4]

This voltage change across the membrane also alters the electric field within the lipid bilayer. For a typical 5 nm thick membrane, a resting potential of -70 mV generates an electric field of approximately 1.4×10^7 V/m, directed inward. As the action potential peaks near +30 mV, the field reverses and reaches about -6×10^6 V/m.[16] This results in a total change in electric field of roughly 2×10^7 V/m (200 kV/cm) across the spike. Outside the membrane, the field decays rapidly with radial distance, following an approximate 1/r dependence due to geometric dispersion, and is further attenuated by ionic screening in the extracellular medium. As a result, while extracellular recordings are feasible, high-sensitivity detection of membrane electric activity likely requires probes positioned in close proximity to – or embedded within – the lipid bilayer.[11]

However, a single active neuron is not sufficient on its own. The power of the nervous system arises from the ability of neurons to communicate with one another, forming complex and dynamic networks. This communication occurs at specialized junctions called synapses, which form the interface between the axon terminal of one neuron (the presynaptic neuron) and the dendrite or soma of another (the postsynaptic neuron). Synaptic communication can occur through two primary mechanisms: chemical synapses and electrical synapses.[17]

The vast majority of synapses in the nervous system are chemical. In these, the electrical signal arriving at the axon terminal triggers the release of neurotransmitters – chemical messengers stored in membrane-bound vesicles. These neurotransmitters diffuse across a narrow extracellular gap known as the synaptic cleft, where they bind to ligand-gated ion channels (or receptors) on the postsynaptic membrane. The binding of neurotransmitters opens these channels, allowing ions to enter the postsynaptic cell and influence its membrane potential.[18]

In contrast, electrical synapses involve a direct physical connection between neurons through gap junctions – protein channels that allow ions to pass directly from one cell to another. This form of communication is extremely fast and allows for synchronized activity but offers less flexibility and modulation compared to chemical synapses.[19]

While most neuronal excitability is governed by voltage-gated and ligand-gated ion channels, other classes of ion channels have also been identified, including mechanically-gated and thermally-gated channels. Mechanosensitive channels respond to physical forces such as stretch or pressure, while thermally-gated channels are activated by changes in temperature. The discovery of these sensory transducers earned David Julius and Ardem Patapoutian the 2021 Nobel Prize in Physiology or Medicine, highlighting their importance in sensory biology.[20–22]

Of particular interest to this dissertation are the thermosensitive ion channels, which allow certain neurons to detect heat or cold. These channels play a key role in thermoreception, the neural mechanism that underlies temperature sensation, and they are also increasingly studied for their potential use in neural stimulation techniques that rely on thermal activation. The best-known group of these channels belongs to the transient receptor potential (TRP) family. Some TRP channels are activated by elevated temperatures (e.g., TRPV1–4, TRPM2–5), while others respond to cooling (e.g., TRPM8, TRPA1, TRPC5).[23–25]

Among them, TRPV1 is perhaps the most widely studied. It remains inactive at normal physiological temperatures but becomes permeable to cations when the local temperature exceeds approximately 42 °C. Activation of TRPV1 leads to inward ion flow, membrane depolarization, and ultimately, the generation of an action potential. This property makes TRPV1 a valuable molecular target in both sensory neuroscience and emerging thermally driven neuromodulation strategies.

Importantly, temperature-sensitive ion channels often function as polymodal receptors – they can respond not only to temperature changes but also to other stimuli such as voltage, pH, mechanical stress, and chemical ligands. Rather than acting as simple thermal switches, these channels serve as integrators of multiple environmental cues, making them critical for dynamic physiological responses such as pain perception, inflammation, and thermoregulation.

While a detailed exploration of their signaling networks is beyond the scope of this section, the ability of these channels to transduce thermal stimuli into electrical signals provides the foundation for photo-thermal stimulation of neurons with nanomaterial as light-to-heat transducers. This concept will be further developed in the following subchapters.

The ability to modulate neuronal activity-known as neuromodulation-has transformed both basic neuroscience research and clinical neurotechnology. By deliberately altering the excitability or firing patterns of neurons, researchers and clinicians can influence how the brain processes information, adapts to stimuli, or recovers from injury. Neuromodulation can be achieved through a variety of physical and biochemical methods, including electrical stimulation, optical or thermal activation, pharmacological agents, and genetically targeted approaches. These techniques range from millisecond-scale, highly localized interventions to broad, long-lasting network effects. Beyond therapeutic applications, such as treating Parkinson's disease or depression, neuromodulation also opens the door to neuroaugmentation – the enhancement or extension of neural function using engineered interfaces. This emerging field aims not only to restore lost capabilities but also to expand human sensory, motor, or cognitive capacity. Together, neuromodulation and neuroaugmentation represent powerful strategies for interacting with the nervous system, with applications spanning clinical therapies, brain-machine interfaces, and adaptive neurotechnologies.[26]

With this, we conclude the introduction to the fundamental concepts required to understand how neural activity can be externally modulated – or "written" – through physical, chemical, or genetic means. The focus now shifts to the complementary aspect of this interaction: detecting, or "reading," neural activity. The following section explores how electrical signals generated by the brain can be captured and interpreted, forming the basis for responsive and bidirectional neural interfaces.

1.2. Current Methods of Bioimaging

Curiosity about the brain dates back millennia, with one of the earliest recorded medical texts – the Egyptian *Papyrus Ebers* from the 16th century BCE – describing symptoms and treatments related to cranial trauma and brain function.[27,28] Yet it was not until the late 19th century that scientists gained the means to systematically explore the structure of the brain. A pivotal moment came with Camillo Golgi's development of the silver chromate staining technique in 1873, which, for the first time, allowed for the visualization of individual neurons. This breakthrough enabled Santiago Ramón y Cajal to produce detailed anatomical drawings that laid the foundation for modern neuroscience by revealing the architecture of neurons. In recognition of their contributions to understanding the structure of the nervous system, Golgi and Cajal were jointly awarded the Nobel Prize in Physiology or Medicine in 1906.[29] From this foundational moment, the field has progressed rapidly, driven by the development of increasingly advanced

bioimaging and electrophysiological methods that continue to expand our ability to observe and interpret neural activity. As understanding the brain requires not only identifying its components but also recording and visualizing their dynamic interactions, the development of imaging technologies has become central to neuroscience – transforming it from a descriptive discipline into one capable of real-time, multiscale interrogation of neural activity.[30]

Current methods for recording brain activity fall into two main categories: electrical and optical techniques, each with distinct advantages in temporal and spatial resolution (Figure 1.3).[31] Electrical approaches directly measure neuronal voltage changes. At the single-cell level, patch-clamp recording offers high temporal precision and is used to study ion channel activity.[32] For population-level recordings, multielectrode arrays (MEAs) capture signals from dozens to hundreds of neurons simultaneously,[33,34] while high-density probes such as Neuropixels allow recordings from thousands of sites across brain regions in behaving animals.[35,36] Optical methods rely on translating neural signals into light, using either chemical dyes or genetically encoded indicators. Calcium imaging, one of the most widely used techniques, detects intracellular calcium transients associated with neuronal firing.[37] Genetically encoded calcium indicators (e.g., GCaMP variants) enable long-term imaging in specific cell types with cellular resolution.[37] Voltage imaging, though technically more challenging, uses indicators such as ASAP (Accelerated Sensor of Action Potential) or Archon to directly track changes in membrane potential with improved temporal fidelity.[38–40] Additionally, fluorescent biosensors have been developed to visualize neurotransmitter release (e.g., iGluSnFR for glutamate) and intracellular signaling pathways.[41–44] These techniques can be integrated with advanced microscopy methods, to achieve deep tissue access and high-resolution recordings. On the systems level, functional magnetic resonance imaging (fMRI), electroencephalography (EEG) and magnetoencephalography (MEG) provide non-invasive measurements of brain activity with whole-brain coverage, offering important context for linking cellular activity to behavior.[45,46]

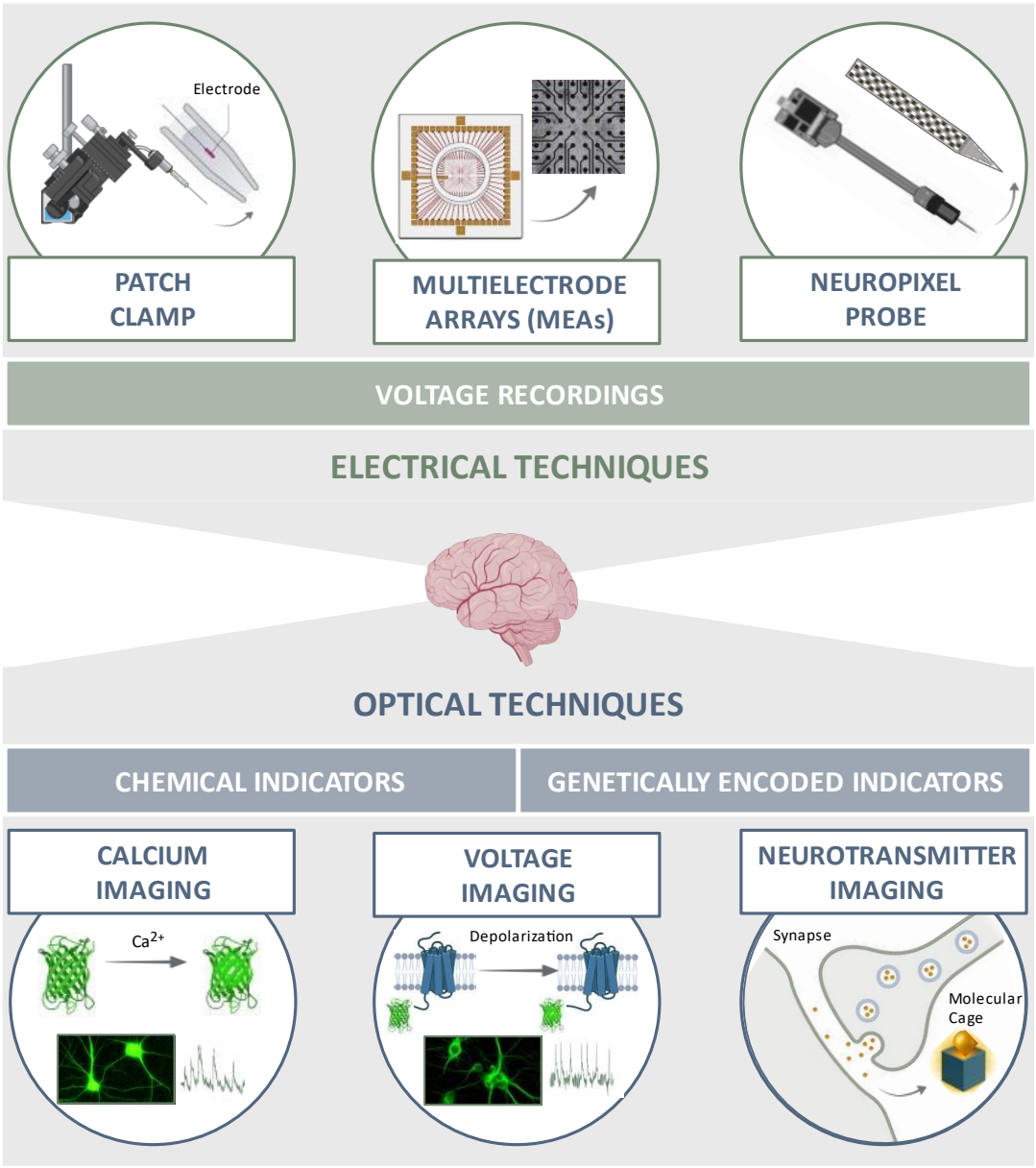

Figure 1.3 Overview of electrical and optical neuronal recording techniques. Electrical methods (top): Patch-clamp – high-precision, single-cell measurements of ion channel and membrane dynamics; Multielectrode arrays (MEAs) – simultaneous recordings from tens to hundreds of neurons in vitro or ex vivo; Neuropixels probes – high-density, thousands-site in vivo recordings across brain regions. Optical methods (bottom): Chemical indicators (e.g., Ca^{2+} dyes) – report intracellular calcium transients linked to spiking; Genetically encoded indicators – cell type-specific fluorescence reporters for calcium (GCaMP), membrane voltage (ASAP/Archon), and neurotransmitter release (e.g., iGluSnFR).

Calcium Imaging

Calcium imaging is a central technique in modern neuroscience, providing means to monitor neuronal activity by visualizing intracellular calcium dynamics that are tightly coupled to action potential firing and a vast array of cellular processes.[47] Cells at rest maintain a very low intracellular calcium concentration of around 50-100 nM, but this level can transiently increase

to approximately 1 µM upon activation, with localized "hot-spots" near active channels potentially reaching tens of micromolar.[48] The diversity of cellular processes regulated by calcium arises from the versatility of its signaling dynamics, ranging in speed, amplitude, and spatial or temporal distribution. As a result, the choice of calcium imaging tools must be carefully matched to the specific characteristics of the process under study, as different indicators vary in their kinetics, sensitivity, and spatial resolution.[48] The underlying principle of the technique involves detecting free intracellular calcium ions through their binding to sensor molecules that undergo a measurable change in fluorescence upon calcium binding.[49]

Calcium indicators are broadly classified into two types: synthetic small-molecule dyes (chemical indicators) and genetically encoded calcium indicators (GECIs).[50] GECIs, such as the commonly used GCaMP family, are protein-based sensors that can be introduced via viral vectors or expressed in transgenic animals. The basic design often involves a fluorescent protein fused to the calcium-binding protein calmodulin and a calmodulin-binding peptide (M13).[31] They enable long-term imaging in specific cell types, offering excellent spatial resolution and compatibility with in vivo microscopy.[31,51] Their main limitations include slower kinetics compared to chemical dyes and potential buffering effects on intracellular calcium, which can affect the fidelity of spike detection – particularly during high-frequency activity.[49] Additionally, delivery via viral transduction or in utero electroporation is invasive and can lead to heterogeneous cellular labeling or tissue damage.[49]

Chemical calcium indicators offer a valuable alternative to genetically encoded sensors, particularly in experiments that demand rapid kinetics and high temporal resolution.[52] These synthetic fluorescent dyes are typically derived from calcium chelators such as EGTA or BAPTA, chemically modified to include fluorescent reporter groups.[47] Their fast-binding kinetics and strong fluorescence responses provide higher signal-to-noise ratios, making them well-suited for detecting brief calcium transients, such as those associated with high-frequency neuronal firing or localized events in dendritic spines. Unlike GECIs, chemical indicators do not require genetic manipulation; instead, they are introduced into cells as membrane-permeable acetoxymethyl (AM) esters, which are activated by intracellular esterases to release the active dye.[50] Early examples such as Fura-2 allowed for ratiometric calcium measurements, while single-wavelength indicators like Fluo-4 and Calcium Green-1 became widely used due to their strong fluorescence changes upon calcium binding and compatibility with standard excitation wavelengths.[47] Although this method allows for rapid and widespread labeling, it lacks cell-type specificity and can lead to variability in loading, dye extrusion, or compartmentalization. Despite these limitations, chemical calcium indicators remain essential for acute preparations where

high-speed, high-resolution imaging is required, including studies in brain slices and at subcellular compartments such as synaptic terminals.[51]

These indicators comprise a large toolkit offering a broad range of calcium affinities and excitation/emission spectra, enabling researchers to tailor imaging protocols to specific experimental needs, from low- to high-calcium environments and across various optical setups. While such advances continue to expand the capabilities of calcium imaging, the focus of this dissertation is on chemical calcium imaging using Calcium Green-1, chosen for its sensitivity, fast kinetics, and suitability for high-resolution imaging in vitro.

1.3. Experimental Models of the Human Nervous System

The human nervous system is complex, with billions of neurons interconnected by trillions of synapses.[53] Direct study of this system in humans is constrained by significant ethical and technical challenges, limiting the extent to which we can experimentally manipulate or observe neural processes in vivo.[54] To address these constraints, researchers employ model systems that capture essential features of the nervous system while offering greater accessibility and experimental control.

Many features of neurons and networks are conserved across species. Fundamental properties of neurons and networks observed in humans are often mirrored in model organisms such as non-human primates,[55–57] rodents (mice, rats and squirrels),[58–60] zebrafish,[61] fruit fly[62,63] and even hydrozoans like Hydra.[64,65] Relying on animal stand-ins to explore human physiology is a tradition rooted in ancient Greek medicine and carried into modern research.[66] Each occupies a distinct investigative niche: primates enable analyses of higher-order cognition and fine motor control; rodents provide exceptional genetic tractability for cortical and behavioral studies; zebrafish allow whole-brain optical access throughout development; and the simple diffuse nerve net of Hydra offers a minimalist framework for exploring the evolutionary origins of coordinated neural activity.[54,67–69]

Beyond evolutionary inquiry, model systems serve as essential platforms for translational research.[70] Many neurological disorders – ranging from neurodegenerative diseases like Alzheimer's and Parkinson's to conditions involving aberrant excitability such as epilepsy – cannot be fully understood through human clinical data alone. An extensive repertoire of experimental models, from cultured neuronal cells to genetically modified animals, provides the foundational tools for exploring the structure and function of the human nervous system. These models not only offer insight into basic biological questions but also facilitate the development

of diagnostic and therapeutic strategies, forming a critical bridge between experimental neuroscience and clinical application (Figure 1.4).[57,64]

One way to study the nervous system is to isolate its building blocks – the cells – and examine them in controlled laboratory conditions (in vitro). This ranges from immortal cell lines to actual neurons kept alive outside the body. These models let researchers observe molecular and cellular processes up close, free from the complexity of a whole organism.[70,71]

Immortalized cell lines are cells that can grow indefinitely in the lab. Though they are not neurons, cell lines like HEK293 (human embryonic kidney cells) or HeLa (human cell line derived from cancer cells) are invaluable for neurobiological research.[72] Scientists often use these cells as host systems to study specific neural proteins. For example, HEK293 cells are widely used to produce and analyze neuronal ion channels or receptors by inserting the relevant genes.[73]

While these cell lines do not fire impulses or form networks like real neurons, they offer a high-throughput, easy-to-maintain platform to dissect molecular details. By contrast, primary neurons are nerve cells taken directly from an animal's brain or spinal cord and grown in a dish. A common example is rodent hippocampal neurons cultured from newborn rats or mice. These primary neuron cultures do form synapses and electrical activity, essentially creating a miniature neural network in the dish. Researchers use them to study synaptic communication, development of neural connections, and the effects of drugs or genetic changes on neuron behavior. Because they are real neurons, primary cultures more closely mimic brain function than cell lines. The downside is that primary neurons are delicate and have a finite lifespan in vitro. Nonetheless, they have been a workhorse for studying mechanisms of neurodevelopment and neuroplasticity at the cellular level (for example, uncovering how synapses strengthen or weaken during learning-like processes).[70]

Extending the elemental power of primary cultures to the network scale, brain-slice preparations maintain authentic synaptic architecture in a fully manipulable ex-vivo setting. Introduced by Henry McIlwain in the 1950s,[74] this preparation – maintained in precisely defined artificial cerebrospinal fluid – proved its worth early on by demonstrating normal resting potentials, intact synaptic transmission, and stimulation-evoked metabolic shifts. Today, hippocampal slices remain the benchmark for dissecting long-term potentiation and other forms of synaptic plasticity, whereas cortical slices support real-time imaging of network oscillations and high-throughput pharmacological screening.[75] Their relative "quietude," combined with unobstructed optical and electrode access to dendrites and axons, enables mechanistic analyses – from ion-channel kinetics to circuit-level disease models – that are impractical in vivo. Brain-

slice work thus occupies a pivotal middle ground between cell cultures and whole-animal studies, offering a cost-effective, ethically favorable platform that continues to drive modern neurobiology.

A revolutionary advance in the last decade has been the use of stem cells to model the human brain. Stem cells (especially induced pluripotent stem cells, iPSCs, made from adult human cells) can be guided to develop into neural cells. From these, scientists can grow 3D brain organoids – tiny, pea-sized blobs of tissue that self-organize into layers and cell types reminiscent of a developing brain. These organoids are not full brains, but they can mimic specific aspects of the human nervous system, such as forming cortical-like structures or even primitive eye cups in a dish. This approach allows us to study human neural development and disease in vitro. For instance, researchers have created patient-specific brain organoids to investigate microcephaly (a developmental brain disorder) and found that certain genetic mutations or viruses (like Zika virus) can stunt organoid growth, reflecting the patient's condition. Organoids thus serve as experimental avatars of a human brain, enabling tests of drug treatments or genetic corrections on patient-derived tissue. There are also structures called assembloids**,** where multiple organoids (e.g., cortical and spinal cord, or brain and muscle) are fused to study interactions between regions, and even experiments transplanting human organoid tissue into animal brains (to observe how human neurons integrate in vivo). While still a developing area, these stem cell–derived models are a major step toward bridging the gap between animal models and the human brain itself, especially for understanding human-specific neurodevelopmental disorders and evolution.[76,77]

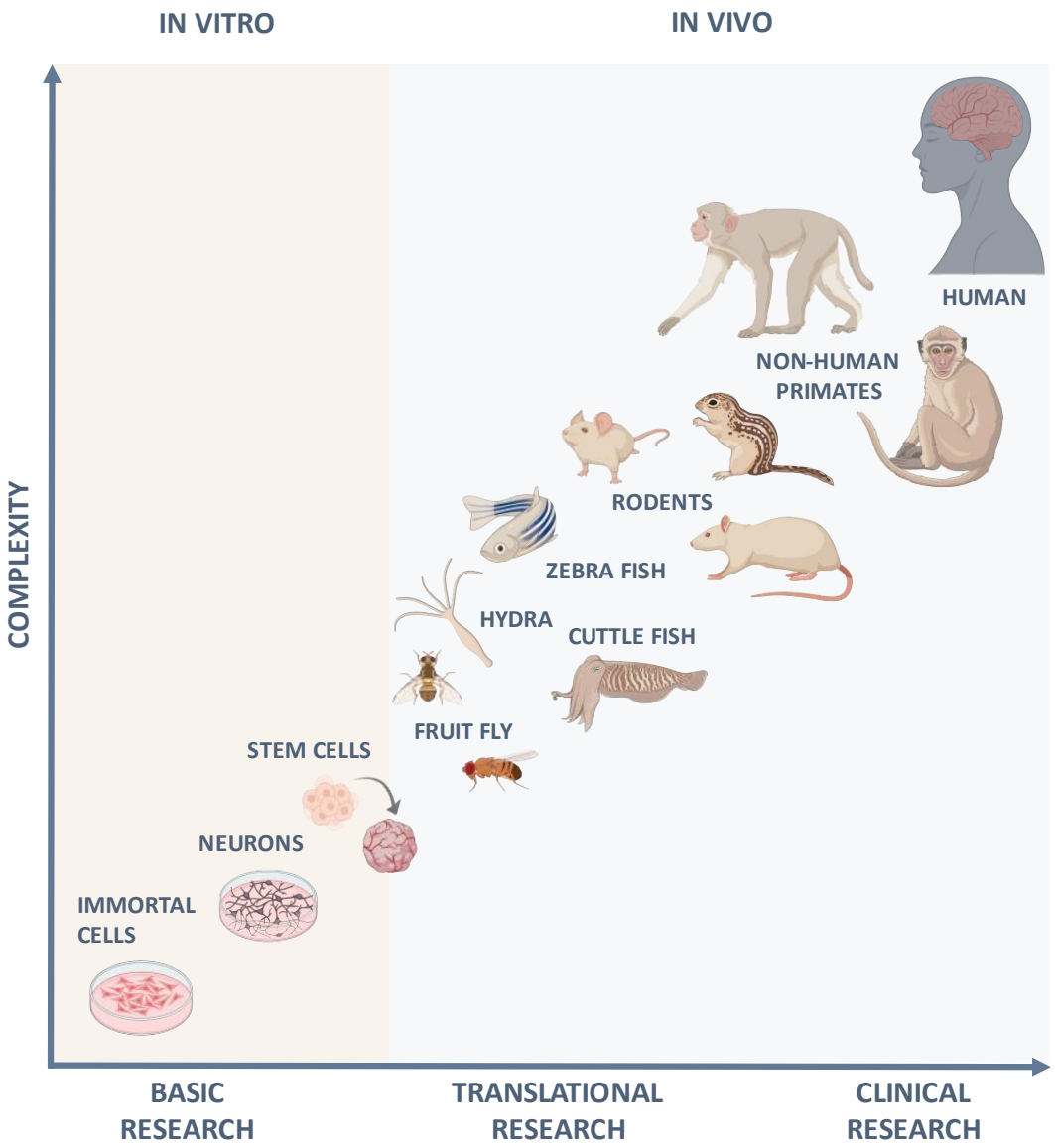

Figure 1.4 Spectrum of experimental models used in neuroscience. This chart organizes model systems by biological complexity (vertical axis) and research focus, ranging from basic research to clinical applications (horizontal axis). Models are categorized as in vitro or in vivo. In vitro systems include immortalized cell lines, primary neurons, stem-cell–derived preparations, and brain slices obtained from animals. In vivo models span from simple invertebrates (e.g., Hydra, fruit fly, cuttlefish) to aquatic vertebrates (e.g., zebrafish), rodents, non-human primates, and humans. These are selected examples from a broader array of experimental models used in neuroscience.

2. Nanotechnology

Since the devil is said to dwell in the details, modern materials science looks downward – toward atoms, molecules, and nanoscale structures. Nanotechnology is the interdisciplinary field that focuses on the design, synthesis, and characterization of structures typically ranging from 1 to 100 nanometers. At this scale, materials often display properties that differ significantly from their bulk counterparts. These differences arise primarily from two factors:

(1) Surface effects, due to a high surface area-to-volume ratio, where a large proportion of atoms reside on the surface with fewer neighboring atoms. This can reduce cohesive energy, lower melting points (e.g., 2.5 nm gold particles melt at much lower temperatures than bulk gold), and enhance chemical reactivity. Catalytic activity, for instance, often increases at the nanoscale due to the abundance of active surface sites.[78,79]

(2) Quantum effects, which become relevant when particle dimensions approach the characteristic length scales of electrons (e.g., the exciton Bohr radius). In such cases, energy levels become quantized, leading to new optical, electronic, and magnetic behaviors. For example, while bulk platinum is non-magnetic, 2 nm clusters can exhibit magnetism. Similarly, semiconductor nanoparticles show size-dependent bandgaps, resulting in a blue shift in optical absorption.[78,79]

Together, these surface and quantum effects give rise to the unique mechanical, thermal, electronic, optical, and catalytic properties.[80] Nanomaterials are commonly classified by their dimensionality, according to the number of degrees of freedom in the particle momentum. While nanoparticles – structures with all three dimensions in the 1–100 nm range – are considered zero-dimensional (0D) due to their roughly isotropic shape, several other forms of nanomaterials exist.[78,81]

One-dimensional (1D) category of nanomaterials includes nanotubes (e.g., carbon nanotubes), nanorods, nanowires, nanofibers, and nanohorns. Electrons in these structures are typically confined in two dimensions, allowing free movement along the length. Two-dimensional (2D) nanomaterials have nanoscale thickness but extended lateral dimensions. Examples include nanosheets, nanofilms, nanolayers, and graphene-derived materials.[23] These structures confine electrons in one dimension. Three-dimensional (3D) nanomaterials refer to bulk assemblies or structures that are not confined to the nanoscale in any single dimension but are composed of nanoscale building blocks (e.g., arrays of nanoparticles, nanowires, or nanotubes).[78,82]

Nanomaterials can be synthesized using two general strategies: top-down and bottom-up approaches.[79,80] Top-down methods start with bulk materials that are physically or mechanically reduced to the nanoscale, using techniques such as high-energy ball milling, lithography, laser ablation, or arc discharge.[82,83] These methods are well-suited for large-scale production but often result in broader size distributions and potential structural defects. In contrast, bottom-up approaches assemble nanostructures atom-by-atom or molecule-by-molecule through chemical or biological processes.[79] Examples include chemical vapor deposition (CVD), sol-gel synthesis, co-precipitation, and colloidal chemical reduction. Bottom-up techniques generally offer better control over particle size, shape, and crystallinity. In many cases, a combination of both approaches is employed to optimize structure and functionality, depending on the material system and application.[84,85]

As this thesis centers on colloidal nanoparticles, the subsequent sections will explore this class of nanomaterials in more detail. Nanoparticles can be classified in various ways; one useful approach is to group them based on their chemical composition and the dominant physical phenomena that govern their behavior at the nanoscale:

Semiconductor quantum dots (QDs) are semiconductor nanocrystals, typically below 10 nm in diameter, often composed from CdSe, CdTe, or InP. QDs are used in biological imaging, light-emitting devices, solar cells, and quantum electronics.[79,86,87]

Plasmonic metal nanoparticles, commonly made of gold (Au) or silver (Ag), but also non-noble metals such as copper (Cu), aluminum (Al) or nickel (Ni), exhibit localized surface plasmon resonance (LSPR) – the collective oscillation of conduction electrons induced by incident light. This leads to strong, size- and shape-dependent optical absorption and scattering. Common applications are biosensing, diagnostics, catalysis, and surface-enhanced spectroscopy.[84,88,89]

Magnetic nanoparticles, such as iron oxides (Fe_3O_4, Fe_2O_3) or FePt alloys, can exhibit superparamagnetism at sizes below the single-domain limit. These particles respond strongly to external magnetic fields but exhibit no remanent magnetization, making them ideal for use in MRI contrast agents, magnetic hyperthermia, drug delivery, and magnetic separation technologies.[90,91]

Carbon-based nanomaterials include several structurally distinct systems. Fullerenes (e.g., C_{60}) are spherical carbon cages with high electron affinity. Carbon nanotubes (CNTs) are rolled graphene sheets with exceptional mechanical strength and electrical conductivity, available in single- or multi-walled forms. Carbon quantum dots (CQDs) and carbon dots (CDs) are quasi-spherical particles below 10 nm, with size- or defect-dependent photoluminescence. These

materials are applied in bioimaging, sensing, energy storage, and environmental technologies.[78,82,92]

Ceramic nanoparticles, such as titanium dioxide (TiO_2) and zinc oxide (ZnO), are inorganic, non-metallic materials with high thermal stability and chemical resistance. Depending on synthesis conditions, they may be amorphous or crystalline, dense or porous. They are widely used in catalysis, biomedical coatings, photonics, and energy conversion devices.[93,94]

Lipid-based nanoparticles – including liposomes and solid lipid nanoparticles (SLNs) – are typically spherical and range from 10 to 1000 nm. Their amphiphilic composition enables encapsulation and controlled release of therapeutic agents, making them central to drug delivery, imaging, and diagnostic systems.[90,95,96]

Polymeric nanoparticles are formed from synthetic or natural polymers and range from 1 to 1000 nm. They can carry active substances either on their surface or within a polymer matrix. A notable subclass, conjugated polymer nanoparticles (CPNs) or polymer dots (Pdots), displays high brightness and tunable photophysical properties, making them suitable for imaging and biosensing.[90,97]

Nanoparticles exhibit a broad diversity in shape, size, and internal structure – ranging from spherical, rod-like, cylindrical, tubular, and hollow-core geometries to chiral forms; they may be crystalline (single- or multi-domain), amorphous, uniform, or composed of multiple layers – reflecting a rapidly expanding library of materials that continues to grow as synthesis methods advance.[78,98]

2.1. Semiconductor Nanocrystals

Over the past decade, quantum dot (QD) research has evolved from fundamental studies in nanochemistry into a broad technology platform supporting advances in displays, lighting, photovoltaics, quantum information systems, and bioanalytics. The field began in the early 1980s, when Ekimov and Brus independently observed that semiconductor nanocrystals exhibit size-dependent optical properties due to quantum confinement. In 1993, Bawendi and co-workers introduced a reliable synthetic route producing highly uniform colloidal QDs with tunable emission, which catalyzed rapid progress in the field. Continued innovations in composition, shape, and surface chemistry have since enabled QDs with high brightness, stability, and spectral control. In recognition of these contributions, Ekimov, Brus, and Bawendi

were awarded the 2023 Nobel Prize in Chemistry “for the discovery and development of quantum dots”.[99,100]

Building on these early breakthroughs, the field advanced rapidly with the introduction of core-shell structures like CdSe/ZnS, which significantly improved luminescence efficiency by passivating surface defects.[101,102] Progress in shape-controlled synthesis led to anisotropic quantum dots – such as rods, platelets, and tetrapods[103–105] – enabling precise control over exciton behavior and charge separation.[106,107] In recent years, research has increasingly focused on environmentally benign alternatives, including InP-based and lead-free perovskite quantum dots, to meet performance demands while addressing regulatory and sustainability concerns.[108,109]

QDs exhibit unique optical and electronic properties as a result of quantum confinement, which becomes significant when the size of a semiconductor nanocrystal approaches or falls below the exciton Bohr radius – the average distance between an excited electron and its corresponding hole in the bulk material. Under these conditions, electrons and holes are confined in all three spatial dimensions, and the continuous energy bands typical of bulk semiconductors are replaced by a set of discrete, quantized energy levels. From a quantum mechanical perspective, these charge carriers behave as standing waves within a finite potential well, where only specific wavelengths, corresponding to allowed energy states, are permitted. As the size of the quantum dot decreases, the confinement becomes stronger, leading to a larger energy separation between levels and an increase in the effective band gap.[79,101]

The emission color, one of the most distinctive features of QDs, is governed by their size-dependent electronic structure. When a photon with energy equal to or greater than the band gap is absorbed, an electron is excited from the valence band (ground state) to a quantized conduction band level, leaving behind a positively charged hole. The resulting electron-hole pair, bound by Coulomb interaction, forms a confined exciton. As with any excited state, the system eventually returns to its ground state. After rapid non-radiative relaxation to the band-edge levels, the electron recombines with the hole, emitting a photon whose energy closely corresponds to the band gap. Since the band gap increases as QD size decreases, the emission shifts toward shorter wavelengths – a phenomenon known as a blue shift. This precisely tunable absorption and photoluminescence is a defining property of QDs and underlies their wide-ranging applications in optoelectronics, bioimaging, lighting, and display technologies.[79,106]

Following this quantum confinement effect of quantized energy levels, there is several related phenomena that makes quantum dots special. They show narrow, symmetric, and bright

photoluminescence (PL) with higher photostability compared to conventional fluorophores. However, many QDs exhibit blinking (intermittent PL), caused by non-radiative recombination processes often linked to photoinduced ionization and surface trap states. To mitigate these effects and improve quantum yield, QDs are frequently synthesized with core/shell architectures – where a high-bandgap shell material (e.g., ZnS) encapsulates the core (e.g., CdSe). This structure passivates surface defects and spatially confines charge carriers. Depending on the band alignment, core/shell QDs can be classified as Type I (both carriers confined to the core), Type II (electron and hole spatially separated across core and shell), or Quasi-Type II (one carrier partially delocalized). These configurations influence both emission energy and PL lifetime. Additionally, under high excitation conditions, QDs may undergo non-radiative Auger recombination, a process in which the recombination energy of an electron–hole pair is transferred to a third charge carrier instead of being emitted as light. This results in the suppression of photoluminescence and reduced quantum yield. To mitigate this effect, core/shell engineering strategies – such as incorporating thicker or compositionally graded shells – are employed to decrease wavefunction overlap between carriers and thereby suppress Auger processes.[79]

Sensitivity to Electrical Field

In a neutral QD, an exciton – a bound state of an electron and a hole – is formed through their mutual Coulomb attraction. In the absence of an external electric field, both charge carriers are confined within nanostructure and their wavefunctions strongly overlap, enabling efficient radiative recombination and bright photoluminescence. When an electric field is applied, it acts on the oppositely charged electron and hole, pulling them in opposite directions (Figure 1.5). This spatial alters nanocrystal's optical and electronic properties, through the phenomena called Quantum-Confined Stark Effect (QCSE) and its influence on Auger Recombination.[110]

Polarization of the exciton reduces the overlap between electron and hole wavefunctions, lowering the transition dipole moment.[111] This, in turn, decreases the rate of radiative recombination and increases the exciton lifetime.[110] Simultaneously, the emission energy shifts to lower values (redshift) due to the field-induced reduction in confinement, analogous to the effect of increasing the physical size of quantum dots.[112] The same spatial separation decreases the oscillator strength of the transition, leading to diminished absorption efficiency and photoluminescence intensity.[113] In ensemble measurements, variations in quantum dot size, shape, and local dielectric environment cause differences in how individual dots respond to the

field, resulting in inhomogeneous broadening of the emission spectrum.[110,111] This effect is further amplified by fluctuating internal electric fields originating from trapped charges or Auger-related events, which lead to dynamic spectral diffusion. In addition, strong fields can enhance non-radiative decay pathways – such as Auger recombination or exciton dissociation – contributing further to the overall suppression of.[112–114]

The strength of this effect depends on the material composition, geometry, and band alignment of the nanocrystal.[112] Larger dots or elongated nanorods develop stronger field-induced dipoles and therefore exhibit more pronounced spectral shifts, whereas symmetric type-I spherical structures typically display only modest, quadratic redshifts.

In the quadratic Stark regime, envelope-function calculations using the effective-mass approximation and an infinite-well model show that the energy shift and radiative lifetime elongation scale as $\Delta E \propto F^2 r^4 m_{e,h}^*$ and $\Delta\tau \propto F^2 r^6 (m_e^* + m_h^*)^2$, respectively. Here, F is the strength of applied electric field, r represents nanocrystal radius, and $m_{e,h}^*$ is an effective mass of electron and hole. The emission (and absorption) intensity follows the electron-hole wavefunction overlap in the same manner as the radiative rate, exhibiting equivalent dependence on the electric field strength, nanocrystal size, and carrier effective masses. [115,116]

In type-II or quasi-type-II heterostructures, particularly in asymmetric seed-in-rod architectures, pre-existing carrier separation enhances the field response. This often leads to large, nearly linear energy shifts, which may reverse direction depending on the field orientation.[112] Thicker shells help to smooth the confinement potential and screen random local electric fields, thereby suppressing Auger recombination and enabling clear observation of ensemble Stark shifts at room temperature.[117,118] In contrast, thin or strained shells, dielectric mismatch, and trap-induced internal fields can introduce spectral broadening and obscure the intrinsic QCSE.[112] Overall, nanostructures with low exciton binding energy and high polarizability – such as type-II systems, asymmetric heterostructures, or large-volume cores – exhibit the strongest and most tunable Stark response.[102,112,113,117,119]

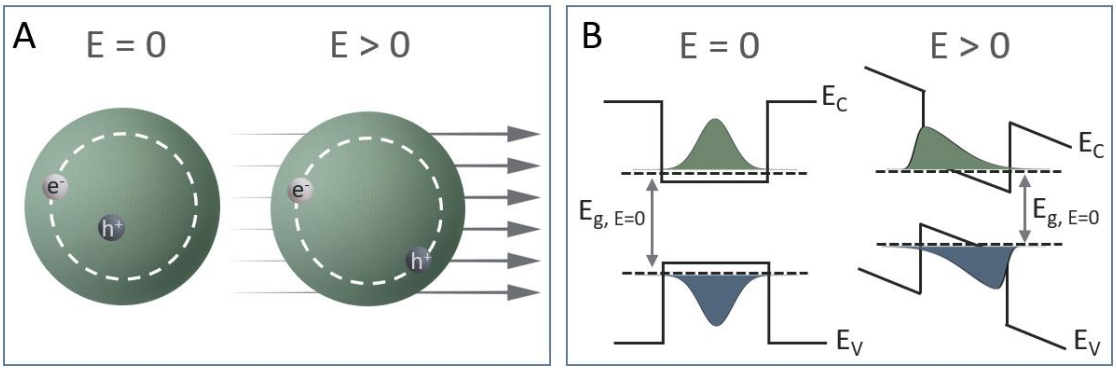

Figure 1.5 Quantum-Confined Stark Effect (QCSE) in semiconductor nanocrystals. (A) Schematic of an exciton in a quantum dot. Without an electric field (E = 0), the electron (e^-) and hole (h^+) are spatially overlapping, enabling efficient radiative recombination. Under an applied electric field (E > 0), the carriers are pulled apart, reducing wavefunction overlap. (B) Corresponding energy band diagrams. The field-induced separation lowers the exciton transition energy (redshift) and oscillator strength, diminishing absorption and emission efficiency.

2.2. Plasmonic Nanoparticles

Plasmonic nanomaterials possess unique optoelectronic properties that position them at the forefront of catalysis, bioimaging, chemical and biological sensing, photothermal therapy, and photonics.[120] These properties arise from localized surface plasmon resonances (LSPR) – the collective oscillation of conduction electrons in response to incident light.[121] This phenomenon occurs in metallic nanoparticles when nanocrystal is much smaller than the wavelength of incident light, allowing the electric field to be treated as nearly uniform across the particle – a condition known as the quasi-static regime. Under these conditions, the external field displaces the conduction electron cloud relative to the positively charged lattice. A restoring force arises from the Coulomb attraction between the electrons and the lattice, causing the electrons to oscillate collectively at a resonant frequency. Once excited, the nanoparticle behaves as an oscillating dipole, generating an enhanced and localized electromagnetic field near its surface. This leads to efficient, wavelength-selective absorption and conversion of incident light into heat or energetic carriers.[122]

The resonance characteristics are highly tunable and depend on particle composition, size, shape, and the surrounding dielectric environment. This allows spectral control, from the ultraviolet to the mid-infrared, by engineering nanoparticle geometry or surface chemistry. As a result, plasmonic nanoparticles can be tailored for specific spectral windows suitable for desired applications.[123]

Noble metals, particularly gold and silver, are the most widely used materials for plasmonic nanoparticles due to their high free-electron density and strong interaction with electromagnetic fields.[122,124] A characteristic feature of plasmonic nanostructures is the magnitude of their optical extinction cross-section, which can exceed the physical cross-section by an order of magnitude. The extinction cross-section is determined by the complex dielectric function of the metal and the dielectric constant of the surrounding medium. For spherical nanoparticles in the quasistatic limit, this relationship is described by

$$\sigma_{\text{ext}} \sim \frac{\varepsilon_2}{(\varepsilon_1+2\varepsilon_m)^2+\varepsilon_2^2} \tag{1.1}$$

indicating that maximum absorption occurs when the real part of the dielectric function of the metal ε_1 approaches minus twice the permittivity of the environment ε_m, while the imaginary part ε_2 remains low. The real component of the dielectric function, defines the polarizability of the material and governs the response of the conduction electron cloud to an external electromagnetic field. The imaginary component, is associated with energy dissipation and reflects the probability of photon absorption within the material. Due to their electronic structure, specifically the presence of a filled d-band below the Fermi level, noble metals have relatively low ε_2 values in the visible range, whereas most non-nobel metals exhibit larger ε_2 values.[125,126]

Gold is especially valued in biomedical applications for its chemical stability, biocompatibility, and ease of surface functionalization.[127] Silver, although chemically less stable (susceptible to oxidation), offers more sensitive plasmonic responses.[128] Beyond these, other metals such as copper (Cu), palladium (Pd), and platinum (Pt) also exhibit plasmonic properties.[123] Copper is more prone to oxidation, which limits its practical use, but at the same time has a broad absorbance window and is cost-efficient.[129] Copper is often used for photoacoustic imaging, computed tomography, or photothermal therapy, since it exhibits LSPR in the NIR region, which is beneficial for deep tissue penetration purposes.[122,123] Palladium and platinum are commonly integrated with gold or silver nanostructures to enhance functionality beyond conventional plasmonic behavior. Platinum nanoparticles can capture hot electrons generated during plasmon decay, while palladium is recognized for its high photothermal conversion efficiency and thermal stability. Such modifications improve properties including catalytic activity and enable broader use in light-driven processes.[123,129] A brief summary of this overview is provided in Table 1.1.

Table 1.1 Overview of plasmonic material families, their key properties, typical LSPR ranges, and representative applications, grouped by electronic structure and composition.

Material family	Hallmarks	Typical LSPR	Key opportunities
Noble metals (Au, Ag, Cu)	High free-electron density; robust wet-chemistry syntheses; rich shape library	Visible - NIR (Au, Cu); UV-vis (Ag)	Biophotonics, catalysis, metasurfaces
Post-transition metals (Al, Ga, In)	Abundant, CMOS-compatible, support UV plasmons	Deep-UV–vis	UV lithography, sterilisation, UV photodetectors
Refractory & noble-alloyed metals (TiN, W, Pt, Pd)	High melting point, chemical resilience	Vis–NIR	High-flux solar harvesting, harsh-environment sensing
Doped semiconductors & oxides (ITO, AZO, MoO_{3-x})	Tunable carrier density via doping or gating	NIR–mid-IR	Dynamic plasmonics, modulators, IR photovoltaics

Among the various plasmonic materials, gold nanoparticles have been the primary focus in this work due to their reliable and versatile synthesis, precise morphological control, and favorable physicochemical characteristics that support their integration into biologically relevant environments[130] – a key requirement for the goals of the NanoNeuro project.[1]

Spherical gold nanoparticles (AuNPs) with diameters in the range of 10–30 nm typically exhibit a single, well-defined LSPR band centered around 520 nm.[131] As particle size increases, this peak red-shifts and broadens due to increased radiative damping and multipolar contributions.[123] In contrast, anisotropic nanostructures – such as rods,[129,132] bipyramids,[133–135] cubes,[121,127] stars,[136] shells,[137] cages,[131] and plates[138] – support multiple plasmon modes and exhibit significantly enhanced local electromagnetic fields at sharp edges or tips. Gold nanorods, for example, display two distinct LSPR modes: a transverse mode near 520 nm and a longitudinal mode tunable from the visible to the near-infrared (700-900 nm) by adjusting the aspect ratio, defined as the length-to-width ratio of the nanocrystal.[132]

The synthesis of gold nanocrystals is dominated by colloidal methods, which offer precise control over morphology, size distribution, and surface chemistry. The Turkevich method – based on citrate reduction of gold salts – is widely used to produce monodisperse nanospheres.[139] For anisotropic shapes, seed-mediated growth strategies have become the standard.[140] These involve the initial formation of small spherical seeds followed by their controlled overgrowth in the presence of mild reducing agents (e.g., ascorbic acid), surfactants such as CTAB (Cetyltrimethylammonium bromide), and trace silver ions. This approach enables

the synthesis of diverse anisotropic morphologies, including high-aspect-ratio rods, bipyramids, and nanostars with sharp protrusions, whose structural features give rise to narrow spectral linewidths and tunable optical properties.[124] More complex architectures, including nanoshells and nanocages, are typically synthesized via templating approaches, such as gold deposition on dielectric cores (e.g., silica) or galvanic replacement reactions using silver templates.[127,128]

A key advantage of gold nanocrystals lies in their amenability to surface modification.[121,141] Their strong affinity for thiol groups allows straightforward functionalization with polymers, biomolecules, or other targeting ligands.[127,129,142,143] For biological applications, polyethylene glycol (PEG) is commonly grafted to enhance colloidal stability and reduce non-specific interactions with biological components.[127,131] Specificity can be further introduced through conjugation with antibodies, peptides, or nucleic acids[138,144]. In many cases, the removal or exchange of toxic surfactants (such as CTAB) is necessary prior to in vivo use.[145,146] Ligand exchange protocols, combined with surface characterization techniques like ζ-potential measurements, FTIR (Fourier-Transform Infrared Spectroscopy), or XPS (X-ray Photoelectron Spectroscopy), are essential to confirm the chemical composition and stability of the final nanostructure.

These features make gold nanocrystals highly versatile for biomedical and sensing applications.[130,131,138] In photothermal therapy, NIR-resonant particles – such as nanorods, shells, or branched structures – efficiently convert light into localized heat to ablate targeted tissue with minimal invasiveness.[146,147] In photoacoustic imaging, pulsed laser excitation of AuNPs generates strong ultrasonic signals for deep-tissue imaging.[121,122] Surface-enhanced Raman scattering (SERS) exploits local field enhancements for ultra-sensitive molecular detection, while simple aggregation-based assays enable rapid, colorimetric biosensing.[124,128,138] Furthermore, their integration into lab-on-chip platforms allows real-time, label-free detection of analytes through LSPR shifts induced by biomolecular interactions at the nanoparticle surface.[129,138]

Looking ahead, continued progress in shape-controlled synthesis, hybrid design (e.g., multilayer core-shell structures or Janus structures , with two chemically distinct surfaces), and tailored light-matter interactions is expanding the functional landscape of gold nanocrystals.[127,135,146] While challenges such as scalability, batch-to-batch reproducibility, and long-term biocompatibility persist, the synergistic development of synthetic strategies, surface engineering, and application-specific performance continues to drive innovation in areas spanning nanomedicine,[148] diagnostics,[128,149] catalysis,[130,143] and photonic devices[150,151].

Photothermal Effect

The photothermal effect is a direct nanoscale conversion of absorbed light into heat. When a plasmonic nanostructure is illuminated at LSPR, the incident electromagnetic energy is absorbed, causing the collective oscillation of free conduction electrons.[147] According to the principle of energy conservation, this absorbed optical energy must subsequently be converted to other forms.[152] The excited plasmon decays non-radiatively within femtoseconds (typically ~100 fs), generating energetic charge carriers called "hot electrons" and "hot holes" through a process known as Landau damping.[129,153,154] These hot electrons possess kinetic energies higher than their equilibrium thermal values and initially do not follow a thermalized Fermi-Dirac distribution. Within approximately 10 fs, hot electrons lose energy through electron-electron scattering, redistributing their energy across the broader electron gas and thereby thermalizing into a Fermi-Dirac distribution.[123,147] Subsequently, this hot electron gas relaxes by transferring its energy to the ionic lattice of the plasmonic nanoparticle through electron-phonon interactions. For gold, this electron-phonon relaxation occurs over a characteristic timescale of around 1.7 ps, resulting in an increased lattice temperature of the nanoparticle.[121] From another perspective, this heat generation can be viewed as analogous to Joule heating, involving energy dissipation within the metallic structure. Finally, heat diffuses outward from the nanoparticle into the surrounding medium (e.g., liquid or glass), leading to an elevated temperature in its immediate environment. This external heat diffusion occurs over relatively longer timescales, typically ranging from approximately 100 ps to a few nanoseconds, depending on factors such as nanoparticle size and the thermal conductivity of the surrounding medium.[155]

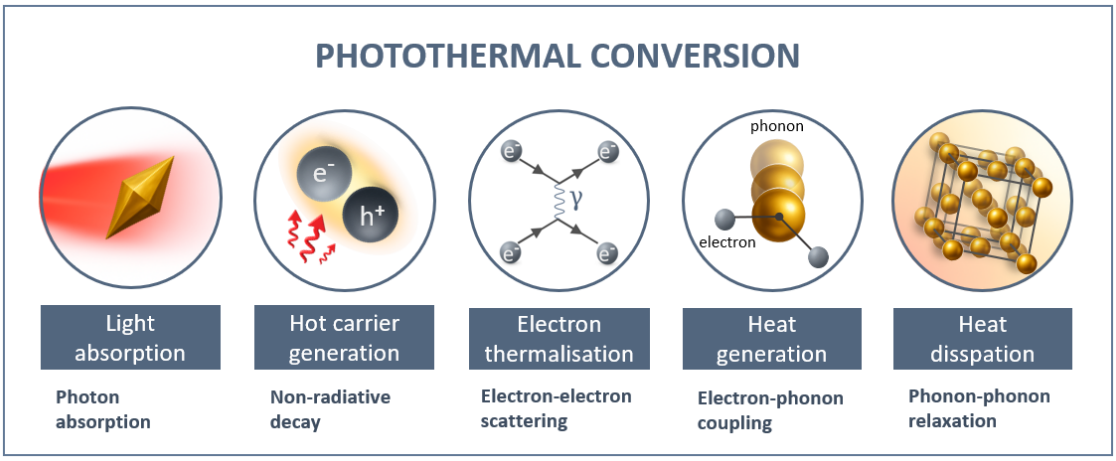

Figure 1.6 Photothermal conversion in plasmonic nanoparticles: (1) Light absorption at the localized surface plasmon resonance. (2) Non-radiative plasmon decay (~100 fs) generates hot electrons and holes. (3) Electron-electron scattering (~10 fs) thermalizes the carrier distribution. (4) Electron-phonon coupling (~1.7 ps for Au) transfers energy to the lattice, raising nanoparticle temperature. (5) Phonon-phonon heat dissipation into the surrounding medium occurs over ≈100 ps to a few ns.

The efficiency of the photothermal effect in plasmonic nanomaterials depends on nanoparticle size and morphology determining the balance between absorption and scattering.[121] Small nanocrystals absorb incident radiation, converting it efficiently into localized heat. Furthermore, the geometry of nanoparticles dictates the internal spatial distribution of generated heat: elongated shapes facilitate more uniform heating across their volume, whereas spheres primarily heat at the particle surface. [156] Additionally, the illumination conditions, particularly wavelength, irradiation intensity, and illumination mode, are decisive. Tailoring the excitation wavelength to coincide with the nanoparticle plasmon resonance maximizes absorption-driven heat generation and can be adjusted, for example, to match the biologically transparent NIR-I (650–950 nm) or NIR-II (1000–1350 nm) windows.[141,157,158] The nature of illumination, continuous-wave versus pulsed, also shapes thermal dynamics. Under CW illumination, the system reaches a steady-state temperature distribution, with the heat dissipating into the surrounding medium according to a radial profile that decays as $1/r$, where r is the distance from the heat source. In contrast, pulsed illumination, particularly with ultrashort (femtosecond) pulses, confines heat more tightly in space and time. The resulting temperature decays more steeply with distance, scaling as $1/r^3$, and can give rise to additional effects such as acoustic wave generation or structural modifications of the nanoparticle.[121,159] In addition, heat dissipation rates depend on the surrounding medium's thermal conductivity, influencing nanoparticle internal temperature uniformity and environmental heating dynamics.[129,147,160] Collective photothermal effects emerge from interparticle interactions, amplifying and homogenizing temperature increases across nanoparticle ensembles.[120,159] Finally, modifying the nanoparticle surface chemistry via coatings or functional groups not only enhances colloidal stability and biocompatibility but also can significantly boost optical absorption and overall photothermal conversion efficiency. This enhancement arises through several mechanisms: increasing the local refractive index, introducing broadband-absorbing layers, and forming junctions that intensify the local electromagnetic field. Surface coatings such as titanium oxide, melanin, polydopamine, and graphene oxide have been shown to increase laser absorption in plasmonic nanomaterials.[122]

In steady-state CW illumination, the temperature rise experienced by a plasmonic nanoparticle is ultimately set by the balance between the optical power it absorbs and the ability of the surrounding medium to conduct that heat. Expressing the absorbed power as $Q = \sigma_{abs} \cdot \mathrm{I}$ and solving the stationary heat-diffusion equation gives the canonical relation:

$$\delta T_{NP} = \frac{Q}{4\pi\kappa_s R_{eq}} \tag{1.2}$$

where R_{eq} is a thermal radius (Laplace radius) that characterizes how the particle geometry influences heat diffusion and κ_s the thermal conductivity of the host medium.[147] To simplify comparison across different materials and shapes, the optical term σ_{abs} can be factored out into the dimensionless Joule number:

$$J_o = \frac{\sigma_{abs}\,\lambda_{ref}}{2\pi V} \tag{1.3}$$

figure of merit that reports the light-to-heat conversion capability per unit volume at an arbitrary reference wavelength λ_{ref} (commonly 1240 nm). Because absorption cross-section σ_{abs} scales with the local plasmonic field enhancement, J_o is increasing as the anisotropy of a material increases (the bigger aspect ratio, the higher J_o). For example, in gold nanorods, increasing the aspect ratio from 1 to about 8 can increase J_o by nearly two orders of magnitude due to the stronger and red-shifted longitudinal surface plasmon resonance. By substituting J_o into the expression for δT_{NP} makes explicit how geometry (through aspect ratio), material permittivity and the ambient thermal conductance collectively dictate the temperature jump that drives the "nanoscale heat-engine" described above.

With the physical principles and technical capabilities of plasmonic heating established, we now explore how these can be adapted to the challenges of neural modulation, where precision, compatibility, and responsiveness are paramount.

3. Nano Neuro

Since the beginning of the 21st century, nanotechnology has steadily advanced from a speculative frontier into a practical and versatile toolkit for neuroscience.[161] In 2000, Mattson and colleagues demonstrated that functionalized multi-walled carbon nanotubes (MWCNTs) could support neuronal adhesion and neurite outgrowth, establishing the first clear evidence that engineered nanomaterials could interface directly with neural tissue.[162] Within a few years, researchers began modifying the surface chemistry of carbon nanotubes to selectively promote neural differentiation and synaptogenesis, while also improving conductivity and biocompatibility. By 2005, studies showed that purified MWCNTs enhanced the efficiency of electrical signal propagation in cultured networks, laying the groundwork for their integration into low-impedance neural probes.[163] In 2007, aligned carbon nanofiber arrays were successfully used for stable extracellular recordings and targeted synaptic stimulation, illustrating the potential of nanoscale electrodes for chronic neural interfacing.[164] Since then carbon nanotubes

are intensively studied as a tool that could boost the performance of microelectronic interfaces with brain tissue.[163]

Beyond carbon allotropes, two-dimensional graphene and its derivatives have become foundational materials for transparent, flexible neural interfaces.[163] Monolayer and nanoporous graphene sheets are capable of modulating ion-channel activity, delivering photothermal or photoelectrical stimulation, and – when patterned into micro-transistors – recording cortical dynamics across a broad frequency spectrum, from infraslow oscillations to high-gamma bursts. Their optical transparency preserves the imaging window, enabling multimodal investigations. Notably, large-area reduced graphene oxide (rGO) electrocorticography foils are now undergoing first-in-human trials for intraoperative brain mapping, underscoring their translational potential.[163]

To address the mechanical mismatch between rigid implants and the soft neural tissue, that may lead to immunological response and cell damage, recent research has turned to conductive polymer hydrogels. These are semi-interpenetrating networks composed of conjugated polymers (like PEDOT:PSS, polypyrrole, or polythiophene) combined with PEG or gelatin-methacryloyl (GelMA) matrices. Such composites exhibit brain-like elastic moduli (≤10 kPa) while maintaining high charge-injection capacities (>1 $mA \cdot cm^{-2}$) and excellent long-term electrochemical stability. These hydrogels are not only robust under cyclic stress and sonication but are also compatible with advanced fabrication techniques such as 3D printing and two-photon polymerization, enabling microscale patterning of bioactive cues for guided axon growth and reduced tissue inflammation.[163]

Metallic nanostructures also contribute significantly to the neurotechnology landscape. Even though we will explore plasmonic nanostructures – especially gold nanoparticles for neuromodulation – in more detail shortly, it is worth noting now that other metal-based nanomaterials have already played a significant role in advancing neurotechnology. For example, silver nanowire networks, either free-standing or embedded in ultrathin, flexible Parylene-C polymer films, have been developed as low-impedance electrocorticography arrays. These arrays are mechanically compliant, can be folded or injected, and conform closely to the brain's surface, allowing stable signal acquisition with minimal tissue disturbance. In parallel, superparamagnetic iron-oxide nanoparticles (SPIONs) have enabled wireless neural stimulation. When exposed to alternating magnetic fields, these particles can either generate localized heating (magnetothermal effect) or produce mechanical torque. Under magnetic stimulation, SPIONs oscillate or rotate and apply mechanical forces to the nearby cell membrane; this membrane strain opens Piezo-family mechanosensitive ion channels, allowing sub-millisecond

control of neuronal firing entirely wirelessly – without the need for implanted electrodes or optical fibers. Proof-of-concept studies have demonstrated that such magnetically controlled particles can modulate neuronal activity and behavior in freely moving animal models, highlighting their potential as minimally invasive, remotely controlled neuromodulation tools.[163]

Before diving into the core focus of this dissertation – plasmonic nanoparticles (with particular emphasis on gold) and semiconductor quantum dots – it is important to first consider several critical factors that must be addressed when integrating nanotechnology into biological research.

First aspect to consider is the blood-brain barrier (BBB) that severely restricts nanoparticle delivery to the central nervous system. BBB is a highly selective membrane barrier located in the central nervous system that plays a crucial role in maintaining brain balance and protecting it from harmful substances and pathogens.[165] Delivery of nanomaterials requires employing strategies as: passive diffusion with long-circulating or ultrasmall particles (around 2 nm diameter); temporary BBB disruption through focused ultrasound (often combined with microbubbles), osmotic agents such as mannitol, or nitric oxide-releasing nanoparticles; targeted delivery using surface-modified lipid carriers, receptor-targeted ligands, cationic vesicles, apolipoprotein adsorption, or receptor-mediated transcytosis; and magnetic guidance of iron-oxide or magnetoelectric nanoparticles using external magnetic fields to enhance brain uptake in a minimally invasive manner.[165]

Second, once in biological fluids, nanoparticles rapidly acquire a “protein corona”.[166] In this spontaneous process layer of biomolecules, primarily proteins, are adsorbed on the surface of nanomaterial driven by various physicochemical interactions between proteins and the nanomaterial surface. Protein corona alters aggregation and biodistribution, cellular uptake, or potential toxicity of nanoparticles.[163] Understanding and controlling corona composition is essential for predictable in vivo behavior. Strategies to minimize undesired corona formation include surface modification with polymers such as PEG or zwitterionic ligands, coating nanoparticles with natural cell membranes to mimic biological identity, and removing contaminants that promote non-specific interactions.[163] Alternatively, the protein corona can be deliberately engineered – for example, through ligand functionalization or controlled protein adsorption – to enhance selective uptake, facilitate receptor-mediated transport, and reduce off-target effects.[166]

Third, cellular endocytosis, the process by which cells immerse extracellular material into membrane-bound vesicles, is a double-edged sword for nanoparticle applications.[167–169] On one

hand, it enables intracellular delivery of cargos such as biosensors, drugs, or imaging agents, and underlies the design of nanomedicines that exploit receptor-mediated or adsorptive uptake pathways to reach specific organelles or cell types. Typical endocytic uptake begins within minutes – clathrin-mediated pit formation and vesicle scission occur within 15-60 seconds, and caveolae-mediated processes take about 5-10 minutes – while full internalization, sorting within endosomes, and transport to lysosomes can take up to one or two hours.[170] When optimizing nanoparticles for desired application it is crucial to take into consideration the uptake kinetics and properly tune the size, charge, and surface of nanomaterial.[171] For neuromodulation strategies that activate thermosensitive ion channels through photothermal heating, endocytic uptake must be suppressed so that nanoparticles remain at the membrane in close proximity to the channels.

Fourth, the unique reactivity of nanomaterials raises neurotoxic risks – oxidative stress, inflammation, barrier disruption, and direct membrane damage – that depend sensitively on composition, coating, and dose. This highlights the need for rigorous and physiologically relevant toxicity assessments, particularly when considering in vivo use and future clinical translation.[170]

Finally, slow clearance and long-term retention of non-degradable particles threaten chronic accumulation and inflammation. PEG-coated QDs have been shown to persist in bone marrow and lymph nodes for several months following intravenous injection in animal models.[172] While this prolonged visibility makes them valuable as long-term imaging probes, it also raises important questions about the potential long-term effects and safety of nanomaterial accumulation in vivo. On the other hand, magnetoelectric nanoparticles were detectable in cortical tissue for about 24 hours, with their stimulatory effects dissipating within three days – suggesting that they are likely cleared from the brain within that period. These findings suggest that nanoparticle retention is highly dependent on both the type of nanomaterial and the specific tissue to which it is delivered, underscoring the importance of thorough in vivo studies and the development of biodegradable materials to ensure long-term safety and clinical viability. The development of biodegradable cores and immunologically inert coatings is imperative, and addressing these challenges is key to harnessing nanotechnology safely and effectively in neuroscience.[170,173]

Semiconductor Nanoparticles in Neurobiology – State of the Art

Semiconductor nanocrystals quickly captured the interest of biologists, not only for their exceptional brightness and photostability as fluorescent labels, but also for their potential as tools for neuromodulation. While quantum dot-mediated neuronal stimulation has been explored experimentally,[174,175] this thesis will not address that direction. Instead, the focus here is on their optical detection properties. This section first considers their role in visualization, with a later discussion addressing their neuromodulatory potential. A key advantage that distinguishes QDs from conventional dyes is not only their higher quantum yield – often reaching 65-95% compared to 30-50% in standard fluorophores – but also their significantly larger one-, two-, and three-photon absorption cross-sections. These properties help overcome the long-standing trade-off between imaging depth and spatial resolution.[176]

When discussing the use of semiconductor nanocrystals in deep brain imaging, it is important to distinguish between two main modalities: structural imaging and functional imaging. Structural imaging aims to reveal anatomical features such as vasculature, fiber tracts, and cellular organization. In contrast, functional imaging captures dynamic physiological processes like neural activity, membrane potential fluctuations, or neurotransmitter release. The application of QDs in deep brain imaging began in the early 2000s, with pioneering studies that demonstrated their effectiveness in penetrating deep tissue and providing stable, high-resolution signals.

In 2002, Dubertret et al. achieved the first in vivo visualization of QDs by encapsulating them in phospholipid micelles.[177] Early breakthroughs began in 2003, when Dahan et al. demonstrated real-time tracking of glycine receptors in living neurons using single QDs, followed by Larson et al. that successfully used water-soluble quantum dots for in vivo multiphoton fluorescence imaging of labeled blood vescels.[178–180] The exploration of QDs for deep brain imaging gained significant momentum in the 2010s, with main focus on harnessing QDs as tools for voltage sensing.[176] The following discussion examines key developments that have established QDs as a prominent tool in both structural and functional neuroimaging.

In structural imaging applications, the high quantum yield and narrow, tunable emission spectra of QDs significantly enhance signal-to-background ratios, particularly at long excitation wavelengths (1.3-2.2 µm), where tissue scattering is minimized. Commercially available probes such as Qtracker655, when excited at 1700 nm, have enabled three-photon imaging to depths of up to 2100 µm in the mouse brain – outperforming conventional fluorophores like Texas Red dextran, which is typically limited to around 1340 µm. Custom-engineered heterostructures,

including CdSe/CdS/ZnS QDs, have demonstrated imaging depths of 850 µm through an intact skull and 1550 µm following craniotomy. QDs have been employed across multiphoton imaging modalities, supporting two-, three-, and even four-photon fluorescence detection.[181] Among these, three-photon excitation offers the greatest penetration depth with reduced risk of photodamage. Additionally, the broad spectral tunability of QDs facilitates multicolor visualization of vasculature, neurons, and microglia.[176] Most structural applications have focused on the mouse brain vasculature, with particularly detailed imaging of deep subcortical regions such as the hippocampus. Advances in ligand design are further expanding the potential of QDs, enabling more targeted labeling strategies and improved traversal of the blood-brain barrier.[176]

Functionally, QDs extend these optical advantages to real-time physiology. Their resistance to photobleaching allows sustained excitation, supporting hemodynamic measurements at significant depths. For example, commercially available Qtracker800 has been used to quantify blood-flow velocities up to 600 µm deep, while Qtracker655 enables detailed vascular imaging at depths reaching 1600 µm. More importantly, the quantum-confined Stark effect and engineered energy- or charge-transfer (FRET and ET) constructs equip QDs with millisecond-scale voltage sensitivity.[176,179]

In 2013, Marshall and Schnitzer proposed the use of QDs as fluorescent voltage indicators, leveraging the quantum-confined Stark effect (QCSE) to detect changes in membrane potential.[179] This foundational concept was subsequently advanced by the research groups of Shimon Weiss and James B. Delehanty through the development of membrane-inserting QD nanosensors.[163] Both simulations and in vivo experiments demonstrated that single action potentials could be resolved using significant larger optical response than with conventional voltage-sensitive dyes or genetically encoded voltage indicators (GEVIs). Notably, Delehanty's group further introduced bioconjugated QD-fullerene platforms that enabled the detection of electrically evoked cortical responses through charge transfer mechanism (Figure 1.7 A).[182]

In parallel, the groups of Rafael Yuste and Jonathan Owen[183] developed quartz nanopipettes with ultra-narrow tip diameters (15–30 nm), coated with QDs to facilitate two-photon visualization.[183] These nanopipettes functioned as minimally invasive nanoelectrodes for intracellular voltage recordings and were successfully targeted to dendritic spines of hippocampal neurons in both cultured cells and acute cortical slices. This approach was further refined in a follow-up study[184] where a flexible version of the nanopipette was introduced and deployed in vivo.[184] Using cranial microprisms, the authors were able to access and record from

visually identified pyramidal neurons and interneurons in both anesthetized and awake, head-fixed mice.

Complementing these advances, S. Weiss, K. Park, and colleagues (2018) demonstrated that rod-shaped QDs functionalized with specific peptides could spontaneously insert into lipid membranes and detect single-particle voltage responses in model systems (Figure 1.7 C).[185] These results provided experimental confirmation of prior theoretical work by the same group.[112,186] Building on this work, S. Weiss together with A. Ludwig and collaborators reported in 2020 that type-II ZnSe/CdS seeded nanorods (NRs), when functionalized with a lipid mixture derived from brain tissue, could spontaneously incorporate into neuronal plasma membranes.[187] This insertion was driven by the intrinsic compatibility of the nanorod coating with the native lipid composition of the membrane. Once embedded, the nanorods, operating through QCSE, were able to sense local changes in membrane potential. This functionality was demonstrated across multiple systems, including self-spiking and patched HEK293 cells, as well as primary cortical neurons – all without the need for genetic modification.[187,188] Another recent study by Qiangbin Wang's group[189] demonstrated that glutathione-capped CdSe/ZnS quantum dots can localize to neuronal membranes and function as voltage sensors (Figure 1.7 B). The sensing mechanism relies on Förster resonance energy transfer (FRET), with dipicrylamine (DPA) acting as an acceptor within the lipid bilayer. Changes in membrane potential alter the position of DPA relative to the QD surface: during depolarization or hyperpolarization, DPA migrates within the membrane, thereby modulating the donor–acceptor distance and, consequently, the fluorescence intensity of QDs.[189] Caglar et al. (2019) demonstrated that InP/ZnS QDs could detect subthreshold voltage fluctuations in live cells with greater sensitivity than calcium-based indicators, which is a significant progress to offer improved biocompatibility.[190]

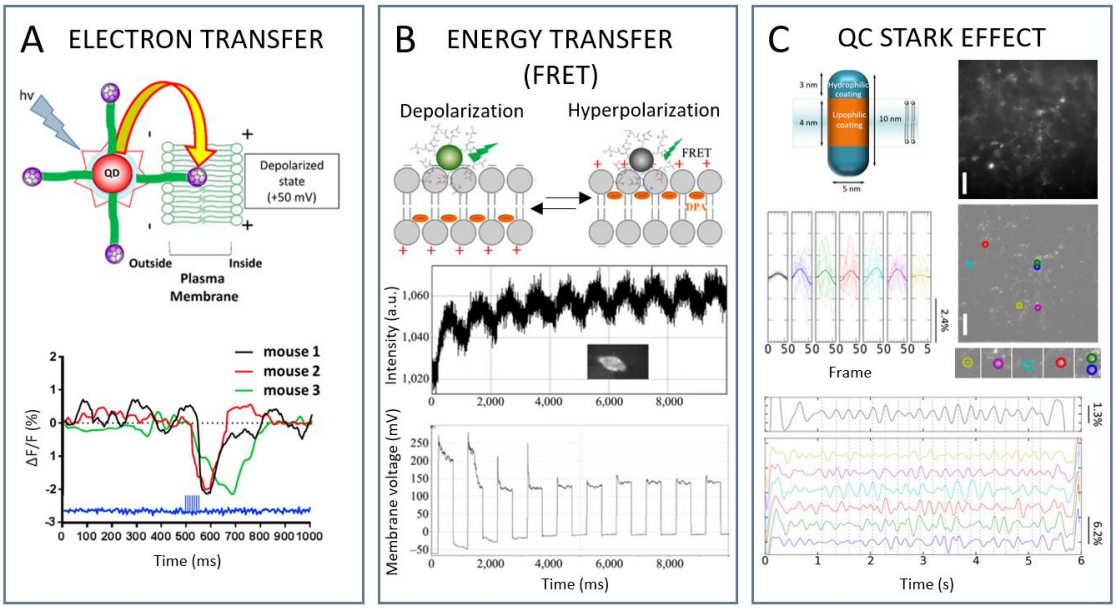

Figure 1.7 Photophysical mechanisms exploited by semiconductor nanocrystal voltage sensors. (A) Electron-transfer (ET) modality. A membrane-anchored quantum-dot/peptide/C_{60} construct undergoes voltage-dependent ET to the fullerene acceptor; depolarisation enhances ET and quenches QD photoluminescence, yielding optical ΔF/F signals up to ~20%. (B) Fluorescence-resonance-energy-transfer (FRET) modality. Glutathione-capped CdSe@ZnS QDs form a two-component sensor with dipicrylamine; field-driven redistribution of the anionic quencher modulates QD emission with millisecond fidelity to the membrane potential. (C) Quantum-confined Stark-effect (QCSE) modality. Peptide-coated, type-II CdSe/CdS nanorods spontaneously insert perpendicularly into lipid bilayers; the trans-membrane electric field shifts their excitonic energy, enabling single-particle voltage read-out. Reprinted with permission from Nag et al., ACS Nano 11, 5598-5613 (2017); Chen et al., Nano Research 12, 1321-1326 (2019); and Park et al., Science Advances 4, e1601453 (2018).

While much of the research on QDs has focused on their role as sensors, QDs and related semiconductor nanocrystals – such as upconversion nanoparticles (UCNPs) – are also being explored for their potential to modulate neuronal activity. Early work by J. Winter and B. Korgel (2001) attempted to achieve light-induced neurostimulation by conjugating semiconductor nanocrystals with antibodies or peptides to target specific neuronal receptors.[191] The proposed mechanism relied on neuron-bound QDs absorbing photons and converting them into electrons to initiate activation. Although the study demonstrated precise molecular targeting, it did not provide evidence of successful neuronal activation.

A more conclusive result was reported in 2007 by Nicholas Kotov's laboratory,[192] which demonstrated in vitro neuronal activation using mercury telluride (HgTe) QDs embedded in a thin film via layer-by-layer (LBL) assembly with poly(dimethyl diallyl ammonium chloride) (PDDA). Mouse neuroblastoma/rat glioma hybrid cells (NG108) were cultured on this QD-integrated substrate. Upon illumination, charge-transfer interactions between the QDs and the extracellular medium produced a photocurrent. Patch-clamp recordings revealed a temporal correlation between light exposure and the generation of inward currents and membrane

depolarization. The authors proposed that the photocurrent served as an external current source that flowed across the membrane, triggering action potentials independently of direct ion channel modulation.[164,191]

More recently, Karatum et al. (2022) developed a flexible, near-infrared (NIR) responsive QD-based biointerface capable of stimulating primary hippocampal neurons.[193] This system employed a thin film of PbS QDs that generated capacitive currents upon NIR illumination, leading to depolarization without direct electrical contact. Intracellular recordings confirmed that the stimulation was light intensity-dependent.[176]

Collectively, these studies reflect the progress in adapting QDs to the demands of neuroscience. Their continued refinement highlights the growing integration of nanotechnology into neurobiological research, opening new opportunities for precise mapping of neural systems. Although, as shown above, QDs have demonstrated potential for neuromodulation, much of the research in this area has focused instead on magnetic and plasmonic nanocrystals. Let us then shift focus to the next section, which examines plasmonic nanocrystals and their emerging role as tools in neuroscience.

Plasmonic Nanoparticles in Neurobiology – State of the Art

The spotlight now moves to plasmonic nanocrystals, whose photothermal properties allow us to interface with the nervous system from different angle. Unlike fluorescence-based approaches, these materials enable modulation and sensing via localized electromagnetic interactions. Beyond their well-characterized photothermal effects, where localized heating under light excitation enables modulation of neuronal activity, plasmonic nanostructures can serve as functional tools beyond those aspects. These include high-sensitivity chemical detection via SERS, enabling label-free monitoring of neurotransmitter dynamics;[194] or reversible mechanical modulation of ion channel through steric interactions, which can be selectively controlled using photothermal activation.[195] Such versatility illustrates the rich potential of plasmonic nanostructures to interface with the nervous system through diverse modalities. Nevertheless, it is the photothermal mechanism and its broad utility that currently drives the majority of experimental and translational efforts in this field. Importantly, the photothermal effect is not a singular mode of action but rather a foundation for several distinct strategies by which plasmonic nanostructures can interface with neural systems.

One of the most direct approaches involves the activation of thermosensitive ion channels, particularly TRPV1 (discussed previously in Section 1.1 Neural Networks and Brain Function).[191]

When illuminated with near-infrared (NIR) light, gold nanocrystals generate localized heat that can raise membrane temperature by a few degrees, enough to open these channels and initiate calcium influx or action potentials. This effect has been demonstrated both in cultured cells and in vivo, with gold nanorods triggering TRPV1 at around 43 °C[196] and AuNPs inducing neuronal firing with temperature increases as small as 5 °C near the membrane surface.[195,197] Another proposed mechanism relies on changes in membrane capacitance.[198] Since capacitance is inherently temperature-dependent, short heat pulses can modify the electrical properties of the lipid bilayer, generating so-called optocapacitive currents that depolarize the membrane and initiate neural activity – without requiring direct activation of thermosensitive channels.[199,200] Both mechanisms use plasmonic nanostructures to elicit action potentials in neurons through distinct yet complementary thermal pathways.[198,201]

In parallel, plasmonic heating of internalized nanoparticles can trigger intracellular calcium signaling. Heating even a single endolysosome may lead to widespread calcium release from internal stores, such as the endoplasmic reticulum, via calcium-induced calcium release.[163,202,203] This amplified signaling cascade is closely associated with neurotransmitter exocytosis and points to opportunities for controlling vesicle-mediated signaling or intracellular drug delivery with high precision.[198] Building on this principle, plasmonic nanoparticles could also serve as localized heat sources to trigger the release of bioactive compounds from thermally responsive carriers, such as polymer[204] or microscale hydrogel capsules[205] – an approach often referred to as photothermal uncaging.

Another approach is to use plasmonic nanoparticles as photoacoustic transducers. Upon excitation with nanosecond laser pulses, these particles undergo rapid thermal expansion, producing pressure waves through the thermoelastic effect.[165] While this phenomenon is widely used in deep-tissue photoacoustic imaging due to its high spatial resolution and compatibility with near-infrared light, the same pressure waves can also be repurposed for neuromodulation. Specifically, the resulting mechanical stimuli can activate mechanosensitive ion channels or influence nearby piezosensitive proteins, leading to neuronal excitation. Moreover, incorporating nanoporous gold, a three-dimensional dealloyed gold network characterized by high surface area and low electrochemical impedance, can further amplify thermoelastic pressure waves by improving acoustic coupling. At the same time, it modulates the local mechanical and electrical microenvironment to favor neuronal interfacing.[163]

As outlined above, the strategies that leverage plasmonic nanoparticles for neuroscience are both diverse and rapidly advancing. This evolution is marked by a series of experimental milestones that have defined the current state of the field. Since the early 2010s, research has

progressed from initial proof-of-concept studies to increasingly refined and sophisticated in vivo neuromodulation approaches. In 2014, Eom and colleagues demonstrated that gold nanorods (AuNRs) injected into the rat sciatic nerve could enhance infrared-induced neural stimulation six-fold.[195,206] The following year, Carvalho-de Souza et al. showed that AuNPs can be conjugated with high-avidity molecules for precise targeting.[207] They reported that Ts1-Conjugated AuNPs, tethered to dorsal root ganglion neurons, could evoke action potentials through a modest plasmonic membrane heating of just 1-2 °C without significant evidence of cellular demage. Concurrently, Nakatsuji's group used cationic protein/lipid-coated AuNRs to activate TRPV1 channels in HEK 293T cells under 780 nm illumination, confirming thermally induced channel opening at 43 °C (Figure 1.8 A).[196] In 2016, Lavoie-Cardinal et al. achieved genetically targeted stimulation by decorating HA-tagged AMPA receptors in rat hippocampal neurons with 100 nm AuNPs conjugated to anti-HA antibodies.[208] Subsequent 800 nm laser pulsing evoked robust Ca^{2+} transients and action potentials. A major technical advance came in 2018, when de Boer and colleagues in Rafael Yuste's lab employed 1040 nm femtosecond laser pulses to activate neurons via second-harmonic Mie scattering, enabling nonlinear photothermal stimulation in acute mouse brain slices, live mice, and Hydra (Figure 1.8 C).[197] In 2019, two notable refinements were introduced: Carvalho-de Souza's cholesterol-functionalized AuNPs allowed for effective stimulation at tenfold lower laser power (Figure 1.8 B),[169] while Muroski et al. demonstrated reversible modulation of membrane potential by using AuNPs linked to the potassium channel blocker Tertiapin-Q, which could be released through plasmonic heating.[209]

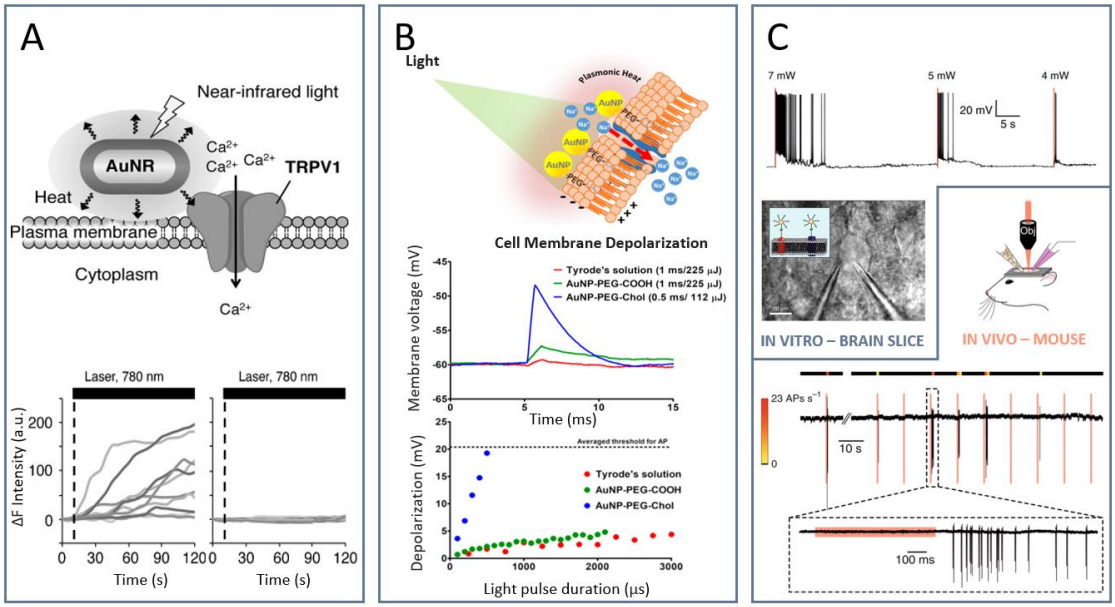

Figure 1.8 Plasmonic gold nanosystems for optical control of neuronal excitability. (A) TRPV1-mediated Ca^{2+} entry. Near-infrared heating of plasma-membrane-anchored gold nanorods (AuNRs) raises the local temperature above the TRPV1 threshold, triggering rapid Ca^{2+} influx without membrane damage.[196] (B) Optocapacitive depolarization by cholesterol-tethered AuNPs. AuNPs functionalized with PEG-cholesterol insert into the lipid bilayer; sub-millisecond laser pulses induce nanoscale heating that produces capacitive depolarizations and action potentials whose amplitude scales with pulse energy and surface chemistry.[169] (C) Second-harmonic near-IR stimulation in brain tissue. Membrane-bound AuNPs excited at 1040 nm via a non-linear (second-harmonic) process elicit reproducible spike bursts in cortical neurons ex vivo and in vivo, enabling single-cell-precision photostimulation through millimetres of tissue.[197] Reprinted with permission from: Nakatsuji H. et al., Angew. Chem. Int. Ed. 54, 11725–11729 (2015); Carvalho-de-Souza J. L. et al., ACS Chem. Neurosci. 10, 1478–1487 (2019); de Boer W. et al., Light: Sci. Appl. 7, 100 (2018).

In parallel to these developments, the Stoddart group was advancing a similar strategy using gold nanorods. In 2014, Yong and Stoddart demonstrated that gold nanorods could stimulate primary rat auditory neurons in vitro under 780 nm near-infrared illumination, establishing a non-genetic, contactless method for neural excitation. In 2023, Begeng and Stoddart applied this platform to ex vivo retinal explants from photoreceptor-degenerate rats. They showed that short light pulses (100–500 µs) effectively triggered action potentials in retinal ganglion cells, while longer exposures (200 ms) suppressed activity, indicating that pulse duration could be used to tune excitation and inhibition. In 2024, Cheng and Li introduced an alternative plasmonic architecture, reporting that highly branched gold nanostructures interfaced efficiently with primary mouse hippocampal neurons and achieved photothermal conversion efficiencies above 90%, significantly outperforming nanorods (<50%). This morphology-dependent enhancement suggested a new direction for optimizing neuromodulation platforms. Most recently, in 2025, Wu and Chen developed a multifunctional system for in vivo deep brain stimulation. Their design employed gold nanoshells conjugated with a TRPV1-targeting antibody and a β-synuclein peptide tethered via an infrared-responsive linker. Near-infrared irradiation produced localized

heating to activate TRPV1 channels and release β-synuclein, which disrupted α-synuclein aggregates. This dual mechanism recovered degenerated dopaminergic neurons and restored locomotor function in Parkinson's disease mouse model. While still early-stage, this proof-of-concept study provides a strong basis for cautious optimism regarding the translation of plasmonic neuromodulation technologies toward clinical applications.

Taken together, all these strategies illustrate how plasmonic heating can be precisely adapted for diverse forms of neural control, ranging from ion channel activation to intracellular signaling and mechanical actuation. While the functional capabilities of plasmonic nanostructures in neural systems have expanded rapidly, the precise cellular and molecular mechanisms underlying these effects remain largely unresolved. Questions persist regarding the exact biophysical triggers of neural responses, the variability across cell types, and the long-term consequences of repeated stimulation. Addressing these unknowns will be critical for translating current experimental successes into reliable, controllable neurotechnologies. Nonetheless, the unique ability of plasmonic nanoparticles to transduce light into localized, tunable stimuli at the nanoscale continues to position this approach as a highly promising avenue for non-genetic, minimally invasive neural interfacing.

4. References for Chapter 1

(1) Garcia-Etxarri, A.; Yuste, R. Time for NanoNeuro. *Nat. Methods* **2021**. https://doi.org/10.1038/s41592-021-01270-9.

(2) Langthaler, S.; Lozanović Šajić, J.; Rienmüller, T.; Weinberg, S. H.; et al. Ion Channel Modeling beyond State of the Art: A Comparison with a System Theory-Based Model of the Shaker-Related Voltage-Gated Potassium Channel Kv1.1. *Cells* **2022**, *11* (2), 239. https://doi.org/10.3390/cells11020239.

(3) Hübel, N.; Dahlem, M. A. Dynamics from Seconds to Hours in Hodgkin-Huxley Model with Time-Dependent Ion Concentrations and Buffer Reservoirs. *PLoS Comput. Biol.* **2014**, *10* (12), e1003941. https://doi.org/10.1371/journal.pcbi.1003941.

(4) Yuste, R. *Lectures in Neuroscience*; Columbia University Press, 2023.

(5) Lyons, D. A.; Nicola J. Allen. Glia as Architects of Central Nervous System Formation and Function. *Science* **2018**, *362* (6411), 181–185. https://doi.org/10.1126/science.aat0473.

(6) Stuart, G. J.; Spruston, N. Dendritic Integration: 60 Years of Progress. *Nat. Neurosci.* **2015**, *18* (12), 1713–1721. https://doi.org/10.1038/nn.4157.

(7) Fields, R. D. A New Mechanism of Nervous System Plasticity: Activity-Dependent Myelination. *Nat. Rev. Neurosci.* **2015**, *16* (12), 756–767. https://doi.org/10.1038/nrn4023.

(8) Eric Kandel, John D. Koester, Sarah H. Mack, Steven Siegelbaum. *Principles of Neural Science, Sixth Edition*; McGraw-Hill Education, 2021.

(9) Kole, M. H. P.; Stuart, G. J. Signal Processing in the Axon Initial Segment. *Neuron* **2012**, *73* (2), 235–247. https://doi.org/10.1016/j.neuron.2012.01.007.

(10) Hwang, S.; Chang, J.; Oh, M.-H.; Lee, J.-H.; et al. Impact of the Sub-Resting Membrane Potential on Accurate Inference in Spiking Neural Networks. *Sci. Rep.* **2020**, *10* (1), 3515. https://doi.org/10.1038/s41598-020-60572-8.

(11) Bean, B. P. The Action Potential in Mammalian Central Neurons. *Nat. Rev. Neurosci.* **2007**, *8* (6), 451–465. https://doi.org/10.1038/nrn2148.

(12) Geoffrey M Cooper. *The Cell*, 2nd ed.; Sinauer Associates, 2000.

(13) Yoo, M.; Yang, Y.-S.; Rah, J.-C.; Choi, J. H. Different Resting Membrane Potentials in Posterior Parietal Cortex and Prefrontal Cortex in the View of Recurrent Synaptic Strengths and Neural Network Dynamics. *Front. Cell. Neurosci.* **2023**, *17*. https://doi.org/10.3389/fncel.2023.1153970.

(14) Gerstner, W.; Kistler, W. M.; Naud, R.; Paninski, L. *Neuronal Dynamics: From Single Neurons to Networks and Models of Cognition*; Cambridge University Press, 2014.

(15) David Cardozo. *An intuitive approach to understanding the resting membrane potential*. https://doi.org/10.1152/advan.00049.2016.

(16) Melendy, R. F. A Single Differential Equation Description of Membrane Properties Underlying the Action Potential and the Axon Electric Field. *J. Electr. Bioimpedance* **2018**, *9* (1), 106–114. https://doi.org/10.2478/joeb-2018-0015.

(17) Kennedy, M. B. Synaptic Signaling in Learning and Memory. *Cold Spring Harb. Perspect. Biol.* **2016**, *8* (2), a016824. https://doi.org/10.1101/cshperspect.a016824.

(18) Citri, A.; Malenka, R. C. Synaptic Plasticity: Multiple Forms, Functions, and Mechanisms. *Neuropsychopharmacology* **2008**, *33* (1), 18–41. https://doi.org/10.1038/sj.npp.1301559.

(19) Goda, Y.; Davis, G. W. Mechanisms of Synapse Assembly and Disassembly. *Neuron* **2003**, *40* (2), 243–264. https://doi.org/10.1016/S0896-6273(03)00608-1.

(20) Caterina, M. J.; Schumacher, M. A.; Tominaga, M.; Rosen, T. A.; et al. The Capsaicin Receptor: A Heat-Activated Ion Channel in the Pain Pathway. *Nature* **1997**, *389* (6653), 816–824. https://doi.org/10.1038/39807.

(21) McKemy, D. D.; Neuhausser, W. M.; Julius, D. Identification of a Cold Receptor Reveals a General Role for TRP Channels in Thermosensation. *Nature* **2002**, *416* (6876), 52–58. https://doi.org/10.1038/nature719.

(22) Coste, B.; Mathur, J.; Schmidt, M.; Earley, T. J.; et al. Piezo1 and Piezo2 Are Essential Components of Distinct Mechanically Activated Cation Channels. *Science* **2010**, *330* (6000), 55–60. https://doi.org/10.1126/science.1193270.

(23) Baez, D.; Raddatz, N.; Ferreira, G.; Gonzalez, C.; et al. Chapter Three - Gating of Thermally Activated Channels. In *Current Topics in Membranes*; Islas, L. D., Qin, F., Eds.; Thermal Sensors; Academic Press, 2014; Vol. 74, pp 51–87. https://doi.org/10.1016/B978-0-12-800181-3.00003-8.

(24) Lamas, J. A.; Rueda-Ruzafa, L.; Herrera-Pérez, S. Ion Channels and Thermosensitivity: TRP, TREK, or Both? *Int. J. Mol. Sci.* **2019**, *20* (10), 2371. https://doi.org/10.3390/ijms20102371.

(25) Uchida, K. TRPM3, TRPM4, and TRPM5 as Thermo-Sensitive Channels. *J. Physiol. Sci.* **2024**, *74* (1), 43. https://doi.org/10.1186/s12576-024-00937-0.

(26) Luan, S.; Williams, I.; Nikolic, K.; Constandinou, T. G. Neuromodulation: Present and Emerging Methods. *Front. Neuroengineering* **2014**, *7*. https://doi.org/10.3389/fneng.2014.00027.

(27) York, G. K.; Steinberg, D. A. Chapter 3 Neurology in Ancient Egypt. In *Handbook of Clinical Neurology*; Aminoff, M. J., Boller, F., Swaab, D. F., Eds.; History of Neurology; Elsevier, 2009; Vol. 95, pp 29–36. https://doi.org/10.1016/S0072-9752(08)02103-9.

(28) Keshavan, M. S.; (Michael) Song, S. H.; Zhang, Y.; Lizano, P. Neuroscience in Pictures:1. History of Psychiatric Neuroscience. *Asian J. Psychiatry* **2024**, *92*, 103869. https://doi.org/10.1016/j.ajp.2023.103869.

(29) Glickstein, M. Golgi and Cajal: The Neuron Doctrine and the 100th Anniversary of the 1906 Nobel Prize. *Curr. Biol.* **2006**, *16* (5), R147–R151. https://doi.org/10.1016/j.cub.2006.02.053.

(30) *Advanced Imaging Methods in Neuroscience*; Malva, J. O., Valero, J., Castelo-Branco, M., Roebroeck, A., Eds.; Frontiers Research Topics; Frontiers Media SA, 2022. https://doi.org/10.3389/978-2-88971-725-5.

(31) Roth, R. H.; Ding, J. B. From Neurons to Cognition: Technologies for Precise Recording of Neural Activity Underlying Behavior. *BME Front.* **2020**, *2020*, 7190517. https://doi.org/10.34133/2020/7190517.

(32) Ghovanloo, M.-R.; Dib-Hajj, S. D.; Waxman, S. G. The Evolution of Patch-Clamp Electrophysiology: Robotic, Multiplex, and Dynamic. *Mol. Pharmacol.* **2025**, *107* (1), 100001. https://doi.org/10.1124/molpharm.124.000954.

(33) Ferrea, E.; Maccione, A.; Medrihan, L.; Nieus, T.; et al. Large-Scale, High-Resolution Electrophysiological Imaging of Field Potentials in Brain Slices with Microelectronic Multielectrode Arrays. *Front. Neural Circuits* **2012**, *6*, 80. https://doi.org/10.3389/fncir.2012.00080.

(34) Soscia, D. A.; Lam, D.; Tooker, A. C.; Enright, H. A.; et al. A Flexible 3-Dimensional Microelectrode Array for in Vitro Brain Models. *Lab. Chip* **2020**, *20* (5), 901–911. https://doi.org/10.1039/C9LC01148J.

(35) Jun, J. J.; Steinmetz, N. A.; Siegle, J. H.; Denman, D. J.; et al. Fully Integrated Silicon Probes for High-Density Recording of Neural Activity. *Nature* **2017**, *551* (7679), 232–236. https://doi.org/10.1038/nature24636.

(36) Durand, S.; Heller, G. R.; Ramirez, T. K.; Luviano, J. A.; et al. Acute Head-Fixed Recordings in Awake Mice with Multiple Neuropixels Probes. *Nat. Protoc.* **2023**, *18* (2), 424–457. https://doi.org/10.1038/s41596-022-00768-6.

(37) Two-Photon Calcium Imaging of Neuronal Activity. *Nat. Rev. Methods Primer* **2022**, *2* (1), 1–1. https://doi.org/10.1038/s43586-022-00160-4.

(38) Bando, Y.; Sakamoto, M.; Kim, S.; Ayzenshtat, I.; et al. Comparative Evaluation of Genetically Encoded Voltage Indicators. *Cell Rep.* **2019**, *26* (3), 802-813.e4. https://doi.org/10.1016/j.celrep.2018.12.088.

(39) Miller, E. W. Small Molecule Fluorescent Voltage Indicators for Studying Membrane Potential. *Curr. Opin. Chem. Biol.* **2016**, *33*, 74–80. https://doi.org/10.1016/j.cbpa.2016.06.003.

(40) Peng, L.; Xu, Y.; Zou, P. Genetically-Encoded Voltage Indicators. *Chin. Chem. Lett.* **2017**, *28* (10), 1925–1928. https://doi.org/10.1016/j.cclet.2017.09.037.

(41) Wright, E. C.; Scott, E.; Tian, L. Applications of Functional Neurotransmitter Release Imaging with Genetically Encoded Sensors in Psychiatric Research. *Neuropsychopharmacology* **2025**, *50* (1), 269–273. https://doi.org/10.1038/s41386-024-01903-5.

(42) Aggarwal, A.; Liu, R.; Chen, Y.; Ralowicz, A. J.; et al. Glutamate Indicators with Improved Activation Kinetics and Localization for Imaging Synaptic Transmission. *Nat. Methods* **2023**, *20* (6), 925–934. https://doi.org/10.1038/s41592-023-01863-6.

(43) Bade, A.; Yadav, P.; Zhang, L.; Naidu Bypaneni, R.; et al. Imaging Neurotransmitters with Small-Molecule Fluorescent Probes. *Angew. Chem. Int. Ed.* **2024**, *63* (34), e202406401. https://doi.org/10.1002/anie.202406401.

(44) Szyszka, Ł.; Górecki, M.; Cmoch, P.; Jarosz, S. Fluorescent Molecular Cages with Sucrose and Cyclotriveratrylene Units for the Selective Recognition of Choline and Acetylcholine. *J. Org. Chem.* **2021**, *86* (7), 5129–5141. https://doi.org/10.1021/acs.joc.1c00019.

(45) Babiloni, C.; Pizzella, V.; Gratta, C. D.; Ferretti, A.; et al. Chapter 5 Fundamentals of Electroencefalography, Magnetoencefalography, and Functional Magnetic Resonance Imaging. In *International Review of Neurobiology*; Academic Press, 2009; Vol. 86, pp 67–80. https://doi.org/10.1016/S0074-7742(09)86005-4.

(46) Babaeeghazvini, P.; Rueda-Delgado, L. M.; Gooijers, J.; Swinnen, S. P.; et al. Brain Structural and Functional Connectivity: A Review of Combined Works of Diffusion Magnetic Resonance Imaging and Electro-Encephalography. *Front. Hum. Neurosci.* **2021**, *15*. https://doi.org/10.3389/fnhum.2021.721206.

(47) Thomas, D.; Tovey, S. C.; Collins, T. J.; Bootman, M. D.; et al. A Comparison of Fluorescent Ca2+indicator Properties and Their Use in Measuring Elementary and Global Ca2+signals. *Cell Calcium* **2000**, *28* (4), 213–223. https://doi.org/10.1054/ceca.2000.0152.

(48) Berridge, M. J.; Lipp, P.; Bootman, M. D. The Versatility and Universality of Calcium Signalling. *Nat. Rev. Mol. Cell Biol.* **2000**, *1* (1), 11–21. https://doi.org/10.1038/35036035.

(49) Grienberger, C.; Konnerth, A. Imaging Calcium in Neurons. *Neuron* **2012**, *73* (5), 862–885. https://doi.org/10.1016/j.neuron.2012.02.011.

(50) Paredes, R. M.; Etzler, J. C.; Watts, L. T.; Zheng, W.; et al. Chemical Calcium Indicators. *Methods San Diego Calif* **2008**, *46* (3), 143–151. https://doi.org/10.1016/j.ymeth.2008.09.025.

(51) Mertes, N.; Busch, M.; Huppertz, M.-C.; Hacker, C. N.; et al. Fluorescent and Bioluminescent Calcium Indicators with Tuneable Colors and Affinities. *J. Am. Chem. Soc.* **2022**, *144* (15), 6928–6935. https://doi.org/10.1021/jacs.2c01465.

(52) Bootman, M. D. Calcium Signaling. *Cold Spring Harb. Perspect. Biol.* **2012**, *4* (7), a011171. https://doi.org/10.1101/cshperspect.a011171.

(53) Lent, R.; Azevedo, F. A. C.; Andrade-Moraes, C. H.; Pinto, A. V. O. How Many Neurons Do You Have? Some Dogmas of Quantitative Neuroscience under Revision. *Eur. J. Neurosci.* **2012**, *35* (1), 1–9. https://doi.org/10.1111/j.1460-9568.2011.07923.x.

(54) Neziri, S.; Köseoğlu, A. E.; Deniz Köseoğlu, G.; Özgültekin, B.; et al. Animal Models in Neuroscience with Alternative Approaches: Evolutionary, Biomedical, and Ethical Perspectives. *Anim. Models Exp. Med.* **2024**, *7* (6), 868–880. https://doi.org/10.1002/ame2.12487.

(55) Lear, A.; Baker, S. N.; Clarke, H. F.; Roberts, A. C.; et al. Understanding Them to Understand Ourselves: The Importance of NHP Research for Translational Neuroscience. *Curr. Res. Neurobiol.* **2022**, *3*, 100049. https://doi.org/10.1016/j.crneur.2022.100049.

(56) Capitanio, J. P.; Emborg, M. E. Contributions of Non-Human Primates to Neuroscience Research. *The Lancet* **2008**, *371* (9618), 1126–1135. https://doi.org/10.1016/S0140-6736(08)60489-4.

(57) Higo, N. Non-Human Primate Models to Explore the Adaptive Mechanisms After Stroke. *Front. Syst. Neurosci.* **2021**, *15*. https://doi.org/10.3389/fnsys.2021.760311.

(58) Dennis, E. J.; Hady, A. E.; Michaiel, A.; Clemens, A.; et al. Systems Neuroscience of Natural Behaviors in Rodents. *J. Neurosci.* **2021**, *41* (5), 911–919. https://doi.org/10.1523/JNEUROSCI.1877-20.2020.

(59) Feketa, V. V.; Bagriantsev, S. N.; Gracheva, E. O. Ground Squirrels – Experts in Thermoregulatory Adaptation. *Trends Neurosci.* **2023**, *46* (7), 505–507. https://doi.org/10.1016/j.tins.2023.04.008.

(60) Mohr, S. M.; Dai Pra, R.; Platt, M. P.; Feketa, V. V.; et al. Hypothalamic Hormone Deficiency Enables Physiological Anorexia in Ground Squirrels during Hibernation. *Nat. Commun.* **2024**, *15* (1), 5803. https://doi.org/10.1038/s41467-024-49996-2.

(61) Doszyn, O.; Dulski, T.; Zmorzynska, J. Diving into the Zebrafish Brain: Exploring Neuroscience Frontiers with Genetic Tools, Imaging Techniques, and Behavioral Insights. *Front. Mol. Neurosci.* **2024**, *17*, 1358844. https://doi.org/10.3389/fnmol.2024.1358844.

(62) Quadros-Mennella, P. S.; Lucin, K. M.; White, R. E. What Can the Common Fruit Fly Teach Us about Stroke?: Lessons Learned from the Hypoxic Tolerant Drosophila Melanogaster. *Front. Cell. Neurosci.* **2024**, *18*. https://doi.org/10.3389/fncel.2024.1347980.

(63) Moulin, T. C.; Covill, L. E.; Itskov, P. M.; Williams, M. J.; et al. Rodent and Fly Models in Behavioral Neuroscience: An Evaluation of Methodological Advances, Comparative Research, and Future Perspectives. *Neurosci. Biobehav. Rev.* **2021**, *120*, 1–12. https://doi.org/10.1016/j.neubiorev.2020.11.014.

(64) Lages, Y. V.; McNaughton, N. Non-Human Contributions to Personality Neuroscience – from Fish through Primates. An Introduction to the Special Issue. *Personal. Neurosci.* **2022**, *5*, e11. https://doi.org/10.1017/pen.2022.4.

(65) Hanson, A.; Reme, R.; Telerman, N.; Yamamoto, W.; et al. Automatic Monitoring of Neural Activity with Single-Cell Resolution in Behaving Hydra. *Sci. Rep.* **2024**, *14* (1), 5083. https://doi.org/10.1038/s41598-024-55608-2.

(66) Soto Veliz, D.; Lin, K.-L.; Sahlgren, C. Organ-on-a-Chip Technologies for Biomedical Research and Drug Development: A Focus on the Vasculature. *Smart Med.* **2023**, *2* (1), e20220030. https://doi.org/10.1002/SMMD.20220030.

(67) Hanson, A. On Being a Hydra with, and without, a Nervous System: What Do Neurons Add? *Anim. Cogn.* **2023**, *26* (6), 1799–1816. https://doi.org/10.1007/s10071-023-01816-8.

(68) Kanwisher, N. Animal Models of the Human Brain: Successes, Limitations, and Alternatives. *Curr. Opin. Neurobiol.* **2025**, *90*, 102969. https://doi.org/10.1016/j.conb.2024.102969.

(69) *Ethical Issues in Behavioral Neuroscience*; Lee, G., Illes, J., Ohl, F., Eds.; Current Topics in Behavioral Neurosciences; Springer Berlin Heidelberg: Berlin, Heidelberg, 2015; Vol. 19. https://doi.org/10.1007/978-3-662-44866-3.

(70) Ghiasvand, K.; Amirfazli, M.; Moghimi, P.; Safari, F.; et al. The Role of Neuron-like Cell Lines and Primary Neuron Cell Models in Unraveling the Complexity of Neurodegenerative Diseases: A Comprehensive Review. *Mol. Biol. Rep.* **2024**, *51* (1), 1024. https://doi.org/10.1007/s11033-024-09964-x.

(71) Zhang, J.; Yang, H.; Wu, J.; Zhang, D.; et al. Recent Progresses in Novel in Vitro Models of Primary Neurons: A Biomaterial Perspective. *Front. Bioeng. Biotechnol.* **2022**, *10*. https://doi.org/10.3389/fbioe.2022.953031.

(72) Obinata, M. The Immortalized Cell Lines with Differentiation Potentials: Their Establishment and Possible Application. *Cancer Sci.* **2007**, *98* (3), 275–283. https://doi.org/10.1111/j.1349-7006.2007.00399.x.

(73) He, B.; Soderlund, D. M. Human Embryonic Kidney (HEK293) Cells Express Endogenous Voltage-Gated Sodium Currents and Nav1.7 Sodium Channels. *Neurosci. Lett.* **2010**, *469* (2), 268–272. https://doi.org/10.1016/j.neulet.2009.12.012.

(74) Collingridge, G. L. The Brain Slice Preparation: A Tribute to the Pioneer Henry Mcllfwain.

(75) Khurana, S.; Li, W.-K. Baptisms of Fire or Death Knells for Acute-Slice Physiology in the Age of 'Omics' and Light? *Rev. Neurosci.* **2013**, *24* (5), 527–536. https://doi.org/10.1515/revneuro-2013-0028.

(76) Pașca, S. P.; Arlotta, P.; Bateup, H. S.; Camp, J. G.; et al. A Framework for Neural Organoids, Assembloids and Transplantation Studies. *Nature* **2025**, *639* (8054), 315–320. https://doi.org/10.1038/s41586-024-08487-6.

(77) Kim, Y.; Kim, I.; Shin, K. A New Era of Stem Cell and Developmental Biology: From Blastoids to Synthetic Embryos and Beyond. *Exp. Mol. Med.* **2023**, *55* (10), 2127–2137. https://doi.org/10.1038/s12276-023-01097-8.

(78) Joudeh, N.; Linke, D. Nanoparticle Classification, Physicochemical Properties, Characterization, and Applications: A Comprehensive Review for Biologists. *J. Nanobiotechnology* **2022**, *20* (1), 262. https://doi.org/10.1186/s12951-022-01477-8.

(79) Sumanth Kumar, D.; Jai Kumar, B.; Mahesh, H. M. In *Quantum Nanostructures (QDs): An Overview*; Elsevier Ltd., 2018. https://doi.org/10.1016/b978-0-08-101975-7.00003-8.

(80) Altammar, K. A. A Review on Nanoparticles: Characteristics, Synthesis, Applications, and Challenges. *Front. Microbiol.* **2023**, *14*. https://doi.org/10.3389/fmicb.2023.1155622.

(81) Kolahalam, L. A.; Kasi Viswanath, I. V.; Diwakar, B. S.; Govindh, B.; et al. Review on Nanomaterials: Synthesis and Applications. *Mater. Today Proc.* **2019**, *18*, 2182–2190. https://doi.org/10.1016/j.matpr.2019.07.371.

(82) Algar, W. R.; Massey, M.; Rees, K.; Higgins, R.; et al. Photoluminescent Nanoparticles for Chemical and Biological Analysis and Imaging. *Chem. Rev.* **2021**, *121* (15), 9243–9358. https://doi.org/10.1021/acs.chemrev.0c01176.

(83) Zhang, J.; Zhang, S.; Zhang, Y.; Al-Hartomy, O. A.; et al. Colloidal Quantum Dots: Synthesis, Composition, Structure, and Emerging Optoelectronic Applications. *Laser Photonics Rev.* **2023**, *17* (3), 2200551. https://doi.org/10.1002/lpor.202200551.

(84) Park, J.; Joo, J.; Soon, G. K.; Jang, Y.; et al. Synthesis of Monodisperse Spherical Nanocrystals. *Angew. Chem. - Int. Ed.* **2007**, *46* (25), 4630–4660. https://doi.org/10.1002/anie.200603148.

(85) Murray, C. B.; Norris, D. J.; Bawendi, M. G. Synthesis and Characterization of Nearly Monodisperse CdE (E = S, Se, Te) Semiconductor Nanocrystallites. *J. Am. Chem. Soc.* **1993**, *115* (19), 8706–8715. https://doi.org/10.1021/ja00072a025.

(86) Battaglia, D.; Li, J. J.; Wang, Y.; Peng, X. Colloidal Two-Dimensional Systems: CdSe Quantum Shells and Wells. *Angew. Chem. Int. Ed.* **2003**, *42* (41), 5035–5039. https://doi.org/10.1002/anie.200352120.

(87) Kagan, C. R.; Lifshitz, E.; Sargent, E. H.; Talapin, D. V. Building Devices from Colloidal Quantum Dots. https://doi.org/10.1126/science.aac5523.

(88) Rasch, M. R.; Rossinyol, E.; Hueso, J. L.; Goodfellow, B. W.; et al. Hydrophobic Gold Nanoparticle Self-Assembly with Phosphatidylcholine Lipid: Membrane-Loaded and Janus Vesicles. *Nano Lett.* **2010**, *10* (9), 3733–3739. https://doi.org/10.1021/nl102387n.

(89) Sayed, M.; Yu, J.; Liu, G.; Jaroniec, M. Non-Noble Plasmonic Metal-Based Photocatalysts. *Chem. Rev.* **2022**, *122* (11), 10484–10537. https://doi.org/10.1021/acs.chemrev.1c00473.

(90) Khan, I.; Saeed, K.; Khan, I. Nanoparticles: Properties, Applications and Toxicities. *Arab. J. Chem.* **2019**, *12* (7), 908–931. https://doi.org/10.1016/j.arabjc.2017.05.011.

(91) Mittal, A.; Roy, I.; Gandhi, S. Magnetic Nanoparticles: An Overview for Biomedical Applications. *Magnetochemistry* **2022**, *8* (9), 107. https://doi.org/10.3390/magnetochemistry8090107.

(92) Ayanda, O. S.; Mmuoegbulam, A. O.; Okezie, O.; Durumin Iya, N. I.; et al. Recent Progress in Carbon-Based Nanomaterials: Critical Review. *J. Nanoparticle Res.* **2024**, *26* (5), 106. https://doi.org/10.1007/s11051-024-06006-2.

(93) Marinho, T.; Costa, P.; Lizundia, E.; Costa, C. M.; et al. Ceramic Nanoparticles and Carbon Nanotubes Reinforced Thermoplastic Materials for Piezocapacitive Sensing Applications. *Compos. Sci. Technol.* **2019**, *183*, 107804. https://doi.org/10.1016/j.compscitech.2019.107804.

(94) Wang, N.; Thameem Dheen, S.; Fuh, J. Y. H.; Senthil Kumar, A. A Review of Multi-Functional Ceramic Nanoparticles in 3D Printed Bone Tissue Engineering. *Bioprinting* **2021**, *23*, e00146. https://doi.org/10.1016/j.bprint.2021.e00146.

(95) Xu, Y.; Fourniols, T.; Labrak, Y.; Préat, V.; et al. Surface Modification of Lipid-Based Nanoparticles. *ACS Nano* **2022**, *16* (5), 7168–7196. https://doi.org/10.1021/acsnano.2c02347.

(96) Puri, A.; Loomis, K.; Smith, B.; Lee, J.-H.; et al. Lipid-Based Nanoparticles as Pharmaceutical Drug Carriers: From Concepts to Clinic. *Crit. Rev. Ther. Drug Carr. Syst.* **2009**, *26* (6). https://doi.org/10.1615/CritRevTherDrugCarrierSyst.v26.i6.10.

(97) Zielińska, A.; Carreiró, F.; Oliveira, A. M.; Neves, A.; et al. Polymeric Nanoparticles: Production, Characterization, Toxicology and Ecotoxicology. *Molecules* **2020**, *25* (16), 3731. https://doi.org/10.3390/molecules25163731.

(98) Anu Mary Ealia, S.; Saravanakumar, M. P. A Review on the Classification, Characterisation, Synthesis of Nanoparticles and Their Application. *IOP Conf. Ser. Mater. Sci. Eng.* **2017**, *263* (3), 032019. https://doi.org/10.1088/1757-899X/263/3/032019.

(99) Ann Fernholm; Peter Brzezinski; Heiner Linke; Johan Åqvist. They Added Colour to Nanotechnology. **2023**.

(100) Quesada-González, D.; Merkoçi, A. Quantum Dots for Biosensing: Classification and Applications. *Biosens. Bioelectron.* **2025**, *273*, 117180. https://doi.org/10.1016/j.bios.2025.117180.

(101) Bera, D.; Qian, L.; Tseng, T.-K.; Holloway, P. H. Quantum Dots and Their Multimodal Applications: A Review. *Materials* **2010**, *3* (4), 2260–2345. https://doi.org/10.3390/ma3042260.

(102) Bae, W. K.; Padilha, L. A.; Park, Y.-S.; McDaniel, H.; et al. Controlled Alloying of the Core–Shell Interface in CdSe/CdS Quantum Dots for Suppression of Auger Recombination. *ACS Nano* **2013**, *7* (4), 3411–3419. https://doi.org/10.1021/nn4002825.

(103) Yong, K. T.; Sahoo, Y.; Swihart, M. T.; Prasad, P. N. Shape Control of CdS Nanocrystals in One-Pot Synthesis. *J. Phys. Chem. C* **2007**, *111* (6), 2447–2458. https://doi.org/10.1021/jp066392z.

(104) Lawera, Z.; Parzyszek, S.; Pociecha, D.; Lewandowski, W. Small CdS Nanorods via Sacrificial Synthesis on Perovskite Nanocrystals – Synthesis and Hierarchical Assembly. *J. Mater. Chem. C* **2024**, *12* (16), 5793–5800. https://doi.org/10.1039/D3TC03556E.

(105) Lim, S. J.; Smith, A.; Nie, S. The More Exotic Shapes of Semiconductor Nanocrystals: Emerging Applications in Bioimaging. *Curr. Opin. Chem. Eng.* **2014**, *4*, 137–143. https://doi.org/10.1016/j.coche.2014.01.013.

(106) García de Arquer, F. P.; Talapin, D. V.; Klimov, V. I.; Arakawa, Y.; et al. Semiconductor Quantum Dots: Technological Progress and Future Challenges. *Science* **2021**, *373* (6555), eaaz8541. https://doi.org/10.1126/science.aaz8541.

(107) Chae, W. S.; Shin, H. W.; Lee, E. S.; Shin, E. J.; et al. Excitation Dynamics in Anisotropic Nanostructures of Star-Shaped CdS. *J. Phys. Chem. B* **2005**, *109* (13), 6204–6209. https://doi.org/10.1021/jp044402v.

(108) Ghasemi, M.; Hao, M.; Xiao, M.; Chen, P.; et al. *Lead-Free Metal-Halide Double Perovskites: From Optoelectronic Properties to Applications*; 2021. https://doi.org/10.1515/nanoph-2020-0548.

(109) Almeida, G.; Ubbink, R. F.; Stam, M.; du Fossé, I.; et al. InP Colloidal Quantum Dots for Visible and Near-Infrared Photonics. *Nat. Rev. Mater.* **2023**, *8* (11), 742–758. https://doi.org/10.1038/s41578-023-00596-4.

(110) Wen, G. W.; Lin, J. Y.; Jiang, H. X.; Chen, Z. Quantum-Confined Stark Effects in Semiconductor Quantum Dots. *Phys. Rev. B* **1995**, *52* (8), 5913–5922. https://doi.org/10.1103/PhysRevB.52.5913.

(111) Empedocles, S. A.; Bawendi, M. G. Quantum-Confined Stark Effect in Single CdSe Nanocrystallite Quantum Dots. *Science* **1997**, *278* (5346), 2114–2117. https://doi.org/10.1126/science.278.5346.2114.

(112) Park, K.; Deutsch, Z.; Li, J. J.; Oron, D.; et al. Single Molecule Quantum-Confined Stark Effect Measurements of Semiconductor Nanoparticles at Room Temperature. *ACS Nano* **2012**, *6* (11), 10013–10023. https://doi.org/10.1021/nn303719m.

(113) Kuo, Y.; Li, J.; Michalet, X.; Chizhik, A.; et al. Characterizing the Quantum-Confined Stark Effect in Semiconductor Quantum Dots and Nanorods for Single-Molecule Electrophysiology. *ACS Photonics* **2018**, *5* (12), 4788–4800. https://doi.org/10.1021/acsphotonics.8b00617.

(114) Chen, C.; Yan, J.-Y.; Babin, H.-G.; Wang, J.; et al. Wavelength-Tunable High-Fidelity Entangled Photon Sources Enabled by Dual Stark Effects. *Nat. Commun.* **2024**, *15* (1), 5792. https://doi.org/10.1038/s41467-024-50062-0.

(115) Walters, G.; Wei, M.; Voznyy, O.; Quintero-Bermudez, R.; et al. The Quantum-Confined Stark Effect in Layered Hybrid Perovskites Mediated by Orientational Polarizability of Confined Dipoles. *Nat. Commun.* **2018**, *9* (1), 4214. https://doi.org/10.1038/s41467-018-06746-5.

(116) Miller, D. A. B.; Chemla, D. S.; Damen, T. C.; Gossard, A. C.; et al. Electric Field Dependence of Optical Absorption near the Band Gap of Quantum-Well Structures. *Phys. Rev. B* **1985**, *32* (2), 1043–1060. https://doi.org/10.1103/PhysRevB.32.1043.

(117) Efros, A. L.; Nesbitt, D. J. Origin and Control of Blinking in Quantum Dots. *Nat. Nanotechnol.* **2016**, *11* (8), 661–671. https://doi.org/10.1038/nnano.2016.140.

(118) Bae, W. K.; Park, Y.-S.; Lim, J.; Lee, D.; et al. Controlling the Influence of Auger Recombination on the Performance of Quantum-Dot Light-Emitting Diodes. *Nat. Commun.* **2013**, *4* (1), 2661. https://doi.org/10.1038/ncomms3661.

(119) Cragg, G. E.; Efros, A. L. Suppression of Auger Processes in Confined Structures. *Nano Lett.* **2010**, *10* (1), 313–317. https://doi.org/10.1021/nl903592h.

(120) Baffou, G.; Cichos, F.; Quidant, R. Applications and Challenges of Thermoplasmonics. *Nat. Mater.* **2020**, *19* (9), 946–958. https://doi.org/10.1038/s41563-020-0740-6.

(121) Baffou, G.; Quidant, R. Thermo-Plasmonics: Using Metallic Nanostructures as Nano-Sources of Heat. *Laser Photonics Rev.* **2013**, *7* (2), 171–187. https://doi.org/10.1002/lpor.201200003.

(122) Yan, T.; Su, M.; Wang, Z.; Zhang, J. Second Near-Infrared Plasmonic Nanomaterials for Photoacoustic Imaging and Photothermal Therapy. *Small* **2023**, *19* (30), 2300539. https://doi.org/10.1002/smll.202300539.

(123) Indhu, A. R.; Keerthana, L.; Dharmalingam, G. Plasmonic Nanotechnology for Photothermal Applications – an Evaluation. *Beilstein J. Nanotechnol.* **2023**, *14*, 380–419. https://doi.org/10.3762/bjnano.14.33.

(124) Kant, K.; Beeram, R.; Cao, Y.; Santos, P. S. S. dos; et al. Plasmonic Nanoparticle Sensors: Current Progress, Challenges, and Future Prospects. *Nanoscale Horiz.* **2024**, *9* (12), 2085–2166. https://doi.org/10.1039/D4NH00226A.

(125) Aslam, U.; Rao, V. G.; Chavez, S.; Linic, S. Catalytic Conversion of Solar to Chemical Energy on Plasmonic Metal Nanostructures. *Nat. Catal.* **2018**, *1* (9), 656–665. https://doi.org/10.1038/s41929-018-0138-x.

(126) Zhan, C.; Chen, X.-J.; Yi, J.; Li, J.-F.; et al. From Plasmon-Enhanced Molecular Spectroscopy to Plasmon-Mediated Chemical Reactions. *Nat. Rev. Chem.* **2018**, *2* (9), 216–230. https://doi.org/10.1038/s41570-018-0031-9.

(127) Zare, I.; Yaraki, M. T.; Speranza, G.; Najafabadi, A. H.; et al. Gold Nanostructures: Synthesis, Properties, and Neurological Applications. *Chem. Soc. Rev.* **2022**, *51* (7), 2601–2680. https://doi.org/10.1039/D1CS01111A.

(128) Loiseau, A.; Asila, V.; Boitel-Aullen, G.; Lam, M.; et al. Silver-Based Plasmonic Nanoparticles for and Their Use in Biosensing. *Biosensors* **2019**, *9* (2), 78. https://doi.org/10.3390/bios9020078.

(129) Zheng, J.; Cheng, X.; Zhang, H.; Bai, X.; et al. Gold Nanorods: The Most Versatile Plasmonic Nanoparticles. *Chem. Rev.* **2021**, *121* (21), 13342–13453. https://doi.org/10.1021/acs.chemrev.1c00422.

(130) Hammami, I.; Alabdallah, N. M.; Jomaa, A. A.; Kamoun, M. Gold Nanoparticles: Synthesis Properties and Applications. *J. King Saud Univ. - Sci.* **2021**, *33* (7), 101560. https://doi.org/10.1016/j.jksus.2021.101560.

(131) Amina, S. J.; Guo, B. A Review on the Synthesis and Functionalization of Gold Nanoparticles as a Drug Delivery Vehicle. *Int. J. Nanomedicine* **2020**, *Volume 15*, 9823–9857. https://doi.org/10.2147/IJN.S279094.

(132) Goldmann, C.; Li, X.; Kociak, M.; Constantin, D.; et al. Longitudinal and Transversal Directed Overgrowth of Pentatwinned Silver Nanorods with Tunable Optical Properties. *J. Phys. Chem. C* **2022**, *126* (28), 11667–11673. https://doi.org/10.1021/acs.jpcc.2c02846.

(133) Lee, J.-H.; Gibson, K. J.; Chen, G.; Weizmann, Y. Bipyramid-Templated Synthesis of Monodisperse Anisotropic Gold Nanocrystals. *Nat. Commun.* **2015**, *6* (1), 7571. https://doi.org/10.1038/ncomms8571.

(134) Liu, M.; Guyot-Sionnest, P. Mechanism of Silver(I)-Assisted Growth of Gold Nanorods and Bipyramids. *J. Phys. Chem. B* **2005**, *109* (47), 22192–22200. https://doi.org/10.1021/jp054808n.

(135) Sánchez-Iglesias, A.; Grzelczak, M. Expanding Chemical Space in the Synthesis of Gold Bipyramids. *Small* **2025**, *21* (2), 2407735. https://doi.org/10.1002/smll.202407735.

(136) Becerril-Castro, I. B.; Calderon, I.; Pazos-Perez, N.; Guerrini, L.; et al. Gold Nanostars: Synthesis, Optical and SERS Analytical Properties. *Anal. Sens.* **2022**, *2* (3), e202200005. https://doi.org/10.1002/anse.202200005.

(137) Topete, A.; Varela, A.; Navarro-Real, M.; Rial, R.; et al. Revisiting Gold Nanoshells as Multifunctional Biomedical Nanotools. *Coord. Chem. Rev.* **2025**, *523*, 216250. https://doi.org/10.1016/j.ccr.2024.216250.

(138) Anik, M. I.; Mahmud, N.; Al Masud, A.; Hasan, M. Gold Nanoparticles (GNPs) in Biomedical and Clinical Applications: A Review. *Nano Sel.* **2022**, *3* (4), 792–828. https://doi.org/10.1002/nano.202100255.

(139) Herizchi, R.; Abbasi ,Elham; Milani ,Morteza; and Akbarzadeh, A. Current Methods for Synthesis of Gold Nanoparticles. *Artif. Cells Nanomedicine Biotechnol.* **2016**, *44* (2), 596–602. https://doi.org/10.3109/21691401.2014.971807.

(140) Sánchez-Iglesias, A.; Winckelmans, N.; Altantzis, T.; Bals, S.; et al. High-Yield Seeded Growth of Monodisperse Pentatwinned Gold Nanoparticles through Thermally Induced Seed Twinning. *J. Am. Chem. Soc.* **2017**, *139* (1), 107–110. https://doi.org/10.1021/jacs.6b12143.

(141) Liu, X.; Atwater, M.; Wang, J.; Huo, Q. Extinction Coefficient of Gold Nanoparticles with Different Sizes and Different Capping Ligands. *Colloids Surf. B Biointerfaces* **2007**, *58* (1), 3–7. https://doi.org/10.1016/j.colsurfb.2006.08.005.

(142) Jumbo-Nogales, A.; Rao, A.; Olejniczak, A.; Grzelczak, M.; et al. Unveiling the Synergy of Coupled Gold Nanoparticles and J-Aggregates in Plexcitonic Systems for Enhanced Photochemical Applications. *Nanomaterials* **2024**, *14* (1), 35. https://doi.org/10.3390/nano14010035.

(143) Rogolino, A.; Claes, N.; Cizaurre, J.; Marauri, A.; et al. Metal–Polymer Heterojunction in Colloidal-Phase Plasmonic Catalysis. *J. Phys. Chem. Lett.* **2022**, *13* (10), 2264–2272. https://doi.org/10.1021/acs.jpclett.1c04242.

(144) Rao, A.; Iglesias, A. S.; Grzelczak, M. Choreographing Oscillatory Hydrodynamics with DNA-Coated Gold Nanoparticles. *J. Am. Chem. Soc.* **2024**, *146* (27), 18236–18240. https://doi.org/10.1021/jacs.4c06868.

(145) Mehtala, J. G.; Zemlyanov, D. Y.; Max, J. P.; Kadasala, N.; et al. Citrate-Stabilized Gold Nanorods. *Langmuir* **2014**, *30* (46), 13727–13730. https://doi.org/10.1021/la5029542.

(146) Zhang, Y.; Li ,Yawen; Liao ,Wei; Peng ,Wenzao; et al. Citrate-Stabilized Gold Nanorods-Directed Osteogenic Differentiation of Multiple Cells. *Int. J. Nanomedicine* **2021**, *16*, 2789–2801. https://doi.org/10.2147/IJN.S299515.

(147) Baffou, G.; Quidant, R. Nanoplasmonics for Chemistry. *Chem. Soc. Rev.* **2014**, *43* (11), 3898. https://doi.org/10.1039/c3cs60364d.

(148) Bayda, S.; Adeel, M.; Tuccinardi, T.; Cordani, M.; et al. The History of Nanoscience and Nanotechnology: From Chemical-Physical Applications to Nanomedicine. *Molecules* **2020**, *25* (1), 1–15. https://doi.org/10.3390/molecules25010112.

(149) Oliveira, B. B.; Ferreira, D.; Fernandes, A. R.; Baptista, P. V. Engineering Gold Nanoparticles for Molecular Diagnostics and Biosensing. *WIREs Nanomedicine Nanobiotechnology* **2023**, *15* (1), e1836. https://doi.org/10.1002/wnan.1836.

(150) Olejniczak, A.; Lawera, Z.; Zapata-Herrera, M.; Chuvilin, A.; et al. On-Demand Reversible Switching of the Emission Mode of Individual Semiconductor Quantum Emitters Using Plasmonic Metasurfaces. *APL Photonics* **2024**, *9* (1), 016107. https://doi.org/10.1063/5.0170535.

(151) Ullah, I.; Guo, J.; Wang, C.; Liu, Z.; et al. Design and Analysis of High-Efficiency Perovskite Solar Cell Using the Controllable Photonic Structure and Plasmonic Nanoparticles. *J. Alloys Compd.* **2023**, *960*, 170994. https://doi.org/10.1016/j.jallcom.2023.170994.

(152) Cui, X.; Ruan, Q.; Zhuo, X.; Xia, X.; et al. Photothermal Nanomaterials: A Powerful Light-to-Heat Converter. *Chem. Rev.* **2023**, *123* (11), 6891–6952. https://doi.org/10.1021/acs.chemrev.3c00159.

(153) Peruch, S.; Neira, A.; Wurtz, G. A.; Wells, B.; et al. Geometry Defines Ultrafast Hot-Carrier Dynamics and Kerr Nonlinearity in Plasmonic Metamaterial Waveguides and Cavities. *Adv. Opt. Mater.* **2017**, *5* (15), 1700299. https://doi.org/10.1002/adom.201700299.

(154) Prakash, G.; Kundu, S.; Roy, A.; Singh, A. K.; et al. Carrier Dynamics in Ultrathin Gold Nanowires: Role of Auger Processes. *Plasmonics* **2020**, *15* (4), 1151–1158. https://doi.org/10.1007/s11468-020-01125-7.

(155) Baffou, G. Nanoplasmonics. In *Thermoplasmonics Heating Metal Nanoparticles Using Ligh*; Cambridge University Press, 2017; pp 1–35. https://doi.org/10.1017/9781108289801.003.

(156) Baffou, G.; Quidant, R.; Girard, C. Heat Generation in Plasmonic Nanostructures: Influence of Morphology. *Appl. Phys. Lett.* **2009**, *94* (15), 153109. https://doi.org/10.1063/1.3116645.

(157) Dijk, M. A. van; Tchebotareva, A. L.; Orrit, M.; Lippitz, M.; et al. Absorption and Scattering Microscopy of Single Metal Nanoparticles. *Phys. Chem. Chem. Phys.* **2006**, *8* (30), 3486–3495. https://doi.org/10.1039/B606090K.

(158) Huang, X.; El-Sayed, I. H.; Qian, W.; El-Sayed, M. A. Cancer Cell Imaging and Photothermal Therapy in the Near-Infrared Region by Using Gold Nanorods. *J. Am. Chem. Soc.* **2006**, *128* (6), 2115–2120. https://doi.org/10.1021/ja057254a.

(159) Baffou, G. *Thermoplasmonics: Heating Metal Nanoparticles Using Light*, 1st ed.; Cambridge University Press, 2017. https://doi.org/10.1017/9781108289801.

(160) Montaño-Priede, J. L.; Rao, A.; Sánchez-Iglesias, A.; Grzelczak, M. Accelerated Design of Gold Nanoparticles with Enhanced Plasmonic Performance. Chemistry February 28, 2025. https://doi.org/10.26434/chemrxiv-2025-fckd0.

(161) Kumar, A.; Tan, A.; Wong, J.; Spagnoli, J. C.; et al. Nanotechnology for Neuroscience: Promising Approaches for Diagnostics, Therapeutics and Brain Activity Mapping. *Adv. Funct. Mater.* **2017**, *27* (39), 1700489. https://doi.org/10.1002/adfm.201700489.

(162) Mattson, M. P.; Haddon, R. C.; Rao, A. M. Molecular Functionalization of Carbon Nanotubes and Use as Substrates for Neuronal Growth. *J. Mol. Neurosci.* **2000**, *14* (3), 175–182. https://doi.org/10.1385/JMN:14:3:175.

(163) Ahmed, A. A. A.; Alegret, N.; Almeida, B.; Alvarez-Puebla, R.; et al. Interfacing with the Brain: How Nanotechnology Can Contribute. *ACS Nano* **2025**, *19* (11), 10630–10717. https://doi.org/10.1021/acsnano.4c10525.

(164) Pampaloni, N. P.; Giugliano, M.; Scaini, D.; Ballerini, L.; et al. Advances in Nano Neuroscience: From Nanomaterials to Nanotools. *Front. Neurosci.* **2019**, *12*. https://doi.org/10.3389/fnins.2018.00953.

(165) Sisubalan, N.; Shalini, R.; Ramya, S.; Sivamaruthi, B. S.; et al. Recent Advances in Nanomaterials for Neural Applications: Opportunities and Challenges. *Nanomed.* **2023**, *18* (26), 1979–1994. https://doi.org/10.2217/nnm-2023-0261.

(166) Wheeler, K. E.; Chetwynd, A. J.; Fahy, K. M.; Hong, B. S.; et al. Environmental Dimensions of the Protein Corona. *Nat. Nanotechnol.* **2021**, *16* (6), 617–629. https://doi.org/10.1038/s41565-021-00924-1.

(167) Liang, E.; Shi, J.; Tian, B. Freestanding Nanomaterials for Subcellular Neuronal Interfaces. *iScience* **2022**, *25* (1), 103534. https://doi.org/10.1016/j.isci.2021.103534.

(168) Cavalcanti, R. R. M.; Lira, R. B.; Riske, K. A. Membrane Fusion Biophysical Analysis of Fusogenic Liposomes. *Langmuir* **2022**, *38* (34), 10430–10441. https://doi.org/10.1021/acs.langmuir.2c01169.

(169) Carvalho-De-Souza, J. L.; Nag, O. K.; Oh, E.; Huston, A. L.; et al. Cholesterol Functionalization of Gold Nanoparticles Enhances Photoactivation of Neural Activity. *ACS Chem. Neurosci.* **2019**, *10* (3), 1478–1487. https://doi.org/10.1021/acschemneuro.8b00486.

(170) Boyes, W. K.; van Thriel, C. Neurotoxicology of Nanomaterials. *Chem. Res. Toxicol.* **2020**, *33* (5), 1121–1144. https://doi.org/10.1021/acs.chemrestox.0c00050.

(171) Shabani, L.; Abbasi, M.; Azarnew, Z.; Amani, A. M.; et al. Neuro-Nanotechnology: Diagnostic and Therapeutic Nano-Based Strategies in Applied Neuroscience. *Biomed. Eng. OnLine* **2023**, *22* (1), 1. https://doi.org/10.1186/s12938-022-01062-y.

(172) Michalet, X.; Pinaud, F. F.; Bentolila, L. A.; Tsay, J. M.; et al. Quantum Dots for Live Cells, in Vivo Imaging, and Diagnostics. *Science* **2005**, *307* (5709), 538–544. https://doi.org/10.1126/science.1104274.

(173) Yang, X.; McGlynn, E.; Das, R.; Paşca, S. P.; et al. Nanotechnology Enables Novel Modalities for Neuromodulation. *Adv. Mater.* **2021**, *33* (52), 2103208. https://doi.org/10.1002/adma.202103208.

(174) Han, M.; Karatum, O.; Nizamoglu, S. Optoelectronic Neural Interfaces Based on Quantum Dots. *ACS Appl. Mater. Interfaces* **2022**, *14* (18), 20468–20490. https://doi.org/10.1021/acsami.1c25009.

(175) Karatum, O.; Kaleli, H. N.; Eren, G. O.; Sahin, A.; et al. Electrical Stimulation of Neurons with Quantum Dots via Near-Infrared Light. *ACS Nano* **2022**, *16* (5), 8233–8243. https://doi.org/10.1021/acsnano.2c01989.

(176) Connor, T.; Weerasinghe, H.; Lathia, J.; Burda, C.; et al. Advances in Deep Brain Imaging with Quantum Dots: Structural, Functional, and Disease-Specific Roles. *Photonics* **2025**, *12* (1), 3. https://doi.org/10.3390/photonics12010003.

(177) Dubertret, B.; Skourides, P.; Norris, D. J.; Noireaux, V.; et al. In Vivo Imaging of Quantum Dots Encapsulated in Phospholipid Micelles. *Science* **2002**, *298* (5599), 1759–1762. https://doi.org/10.1126/science.1077194.

(178) Dahan, M.; Lévi, S.; Luccardini, C.; Rostaing, P.; et al. Diffusion Dynamics of Glycine Receptors Revealed by Single-Quantum Dot Tracking. *Science* **2003**, *302* (5644), 442–445. https://doi.org/10.1126/science.1088525.

(179) Marshall, J. D.; Schnitzer, M. J. Optical Strategies for Sensing Neuronal Voltage Using Quantum Dots and Other Semiconductor Nanocrystals. *ACS Nano* **2013**, *7* (5), 4601–4609. https://doi.org/10.1021/nn401410k.

(180) Larson, D. R.; Zipfel, W. R.; Williams, R. M.; Clark, S. W.; et al. Water-Soluble Quantum Dots for Multiphoton Fluorescence Imaging in Vivo. *Science* **2003**, *300* (5624), 1434–1436. https://doi.org/10.1126/science.1083780.

(181) Tong, S.; Zhong, J.; Chen, X.; Deng, X.; et al. In Vivo Deep-Brain 3- and 4-Photon Fluorescence Imaging of Subcortical Structures Labeled by Quantum Dots Excited at the 2200 Nm Window. *ACS Nano* **2023**, *17* (4), 3686–3695. https://doi.org/10.1021/acsnano.2c10724.

(182) Nag, O. K.; Stewart, M. H.; Deschamps, J. R.; Susumu, K.; et al. Quantum Dot–Peptide–Fullerene Bioconjugates for Visualization of in Vitro and in Vivo Cellular Membrane Potential. *ACS Nano* **2017**, *11* (6), 5598–5613.https://doi.org/10.1021/acsnano.7b00954.

(183) Jayant, K.; Hirtz, J. J.; Plante, I. J.-L.; Tsai, D. M.; et al. Targeted Intracellular Voltage Recordings from Dendritic Spines Using Quantum-Dot-Coated Nanopipettes. *Nat. Nanotechnol.* **2017**, *12* (4), 335–342. https://doi.org/10.1038/nnano.2016.268.

(184) Jayant, K.; Wenzel, M.; Bando, Y.; Hamm, J. P.; et al. Flexible Nanopipettes for Minimally Invasive Intracellular Electrophysiology In Vivo. *Cell Rep.* **2019**, *26* (1), 266-278.e5. https://doi.org/10.1016/j.celrep.2018.12.019.

(185) Park, K.; Kuo, Y.; Shvadchak, V.; Ingargiola, A.; et al. Membrane Insertion of—and Membrane Potential Sensing by—Semiconductor Voltage Nanosensors: Feasibility Demonstration. *Sci. Adv.* **2018**.

(186) Park, K.; Weiss, S. Design Rules for Membrane-Embedded Voltage-Sensing Nanoparticles. *Biophys. J.* **2017**, *112* (4), 703–713. https://doi.org/10.1016/j.bpj.2016.12.047.

(187) Ludwig, A.; Serna, P.; Morgenstein, L.; Yang, G.; et al. Development of Lipid-Coated Semiconductor Nanosensors for Recording of Membrane Potential in Neurons. *ACS Photonics* **2020**, *7* (5), 1141–1152. https://doi.org/10.1021/acsphotonics.9b01558.

(188) Roy, D.; Shapira, Z.; Weiss, S. Membrane Potential Sensing: Material Design and Method Development for Single Particle Optical Electrophysiology. *J. Chem. Phys.* **2022**, *156* (8), 084201. https://doi.org/10.1063/5.0076522.

(189) Chen, G.; Zhang, Y.; Peng, Z.; Huang, D.; et al. Glutathione-Capped Quantum Dots for Plasma Membrane Labeling and Membrane Potential Imaging. *Nano Res.* **2019**, *12* (6), 1321–1326. https://doi.org/10.1007/s12274-019-2283-1.

(190) Caglar, M.; Pandya, R.; Xiao, J.; Foster, S. K.; et al. All-Optical Detection of Neuronal Membrane Depolarization in Live Cells Using Colloidal Quantum Dots. *Nano Lett.* **2019**, *19* (12), 8539–8549. https://doi.org/10.1021/acs.nanolett.9b03026.

(191) Xu, Z.; Xu, J.; Yang, W.; Lin, H.; et al. Remote Neurostimulation with Physical Fields at Cellular Level Enabled by Nanomaterials: Toward Medical Applications. *APL Bioeng.* **2020**, *4* (4), 040901. https://doi.org/10.1063/5.0022206.

(192) Pappas, T. C.; Wickramanyake, W. M. S.; Jan, E.; Motamedi, M.; et al. Nanoscale Engineering of a Cellular Interface with Semiconductor Nanoparticle Films for Photoelectric Stimulation of Neurons. *Nano Lett.* **2007**, *7* (2), 513–519. https://doi.org/10.1021/nl062513v.

(193) Karatum, O.; Kaleli, H. N.; Eren, G. O.; Sahin, A.; et al. Electrical Stimulation of Neurons with Quantum Dots via Near-Infrared Light. *ACS Nano* **2022**, *16* (5), 8233–8243. https://doi.org/10.1021/acsnano.2c01989.

(194) Zheng, D.; Pisano, F.; Collard, L.; Balena, A.; et al. Toward Plasmonic Neural Probes: SERS Detection of Neurotransmitters through Gold-Nanoislands-Decorated Tapered Optical Fibers with Sub-10 Nm Gaps. *Adv. Mater.* **2023**, *35* (11), 2200902. https://doi.org/10.1002/adma.202200902.

(195) Nag, O. K.; Muroski, M. E.; Hastman, D. A.; Almeida, B.; et al. Nanoparticle-Mediated Visualization and Control of Cellular Membrane Potential: Strategies, Progress, and Remaining Issues. *ACS Nano* **2020**, *14* (3), 2659–2677. https://doi.org/10.1021/acsnano.9b10163.

(196) Nakatsuji, H.; Numata, T.; Morone, N.; Kaneko, S.; et al. Thermosensitive Ion Channel Activation in Single Neuronal Cells by Using Surface-Engineered Plasmonic Nanoparticles. *Angew. Chem. Int. Ed.* **2015**, *54* (40), 11725–11729. https://doi.org/10.1002/anie.201505534.

(197) Wieteke D. A. M. de Boer; Jan J. Hirtz; Antonio Capretti; Tom Gregorkiewicz; et al. Neuronal Photoactivation through Second-Harmonic near-Infrared Absorption by Gold Nanoparticles _ Enhanced Reader.

(198) Mousavi, N. S. S.; Ramadi, K. B.; Song, Y.-A.; Kumar, S. Plasmonics for Neuroengineering. *Commun. Mater.* **2023**, *4* (1), 101. https://doi.org/10.1038/s43246-023-00429-5.

(199) Fribance, S.; Wang, J.; Roppolo, J. R.; de Groat, W. C.; et al. Axonal Model for Temperature Stimulation. *J. Comput. Neurosci.* **2016**, *41* (2), 185–192. https://doi.org/10.1007/s10827-016-0612-x.

(200) Shapiro, M. G.; Homma, K.; Villarreal, S.; Richter, C.-P.; et al. Infrared Light Excites Cells by Changing Their Electrical Capacitance. *Nat. Commun.* **2012**, *3* (1), 736. https://doi.org/10.1038/ncomms1742.

(201) Carvalho-de-Souza, J. L.; Pinto, B. I.; Pepperberg, D. R.; Bezanilla, F. Optocapacitive Generation of Action Potentials by Microsecond Laser Pulses of Nanojoule Energy. *Biophys. J.* **2018**, *114* (2), 283–288. https://doi.org/10.1016/j.bpj.2017.11.018.

(202) Skirtach, A. G.; Dejugnat, C.; Braun, D.; Susha, A. S.; et al. The Role of Metal Nanoparticles in Remote Release of Encapsulated Materials. *Nano Lett.* **2005**, *5* (7), 1371–1377. https://doi.org/10.1021/nl050693n.

(203) Li, P.; Gu, M.; Xu, H. Lysosomal Ion Channels as Decoders of Cellular Signals. *Trends Biochem. Sci.* **2019**, *44* (2), 110–124. https://doi.org/10.1016/j.tibs.2018.10.006.

(204) Yavuz, M. S.; Cheng, Y.; Chen, J.; Cobley, C. M.; et al. Gold Nanocages Covered by Smart Polymers for Controlled Release with Near-Infrared Light. *Nat. Mater.* **2009**, *8* (12), 935–939. https://doi.org/10.1038/nmat2564.

(205) Li, W.; Luo, R.; Lin, X.; Jadhav, A. D.; et al. Remote Modulation of Neural Activities via Near-Infrared Triggered Release of Biomolecules. *Biomaterials* **2015**, *65*, 76–85. https://doi.org/10.1016/j.biomaterials.2015.06.041.

(206) Eom, K.; Kim, J.; Choi, J. M.; Kang, T.; et al. Enhanced Infrared Neural Stimulation Using Localized Surface Plasmon Resonance of Gold Nanorods. *Small* **2014**, *10* (19), 3853–3857. https://doi.org/10.1002/smll.201400599.

(207) Carvalho-de-Souza, J. L.; Treger, J. S.; Dang, B.; Kent, S. B. H.; et al. Photosensitivity of Neurons Enabled by Cell-Targeted Gold Nanoparticles. *Neuron* **2015**, *86* (1), 207–217. https://doi.org/10.1016/j.neuron.2015.02.033.

(208) Lavoie-Cardinal, F.; Salesse, C.; Bergeron, É.; Meunier, M.; et al. Gold Nanoparticle-Assisted All Optical Localized Stimulation and Monitoring of Ca2+ Signaling in Neurons. *Sci. Rep.* **2016**, *6* (1), 20619. https://doi.org/10.1038/srep20619.

(209) Muroski, M. E.; Oh, E.; Nag, O. K.; Medintz, I. L.; et al. Gold-Nanoparticle-Mediated Depolarization of Membrane Potential Is Dependent on Concentration and Tethering Distance from the Plasma Membrane. *Bioconjug. Chem.* **2020**, *31* (3), 567–576. https://doi.org/10.1021/acs.bioconjchem.9b00656.

Chapter 2

Self-spiking HEK Cells

Cell lines, defined as continuously dividing populations of cells derived from original tissue samples, have become fundamental tools in biology, physiology, and medicine. Their importance lies in offering a stable and reproducible system for investigating cellular processes, screening drug candidates, and producing therapeutic proteins or viral vectors. The ability to culture cells outside the organism was first demonstrated in 1907 by Ross Granville Harrison, who maintained frog nerve cells in a clot of lymph, observing their survival and the extension of nerve fibers.[1] Although these early cultures were not capable of indefinite growth, they established the principle that living animal cells could function in vitro. During the mid-twentieth century, the development of antibiotics such as penicillin (A. Flaming, 1928) and streptomycin (A. Schatz, 1943), along with improved sterile techniques, enabled the routine maintenance of primary cell cultures in laboratories.[2] However, these cells still had a limited lifespan. A turning point came in 1951 with the creation of the HeLa cell line, derived from a cervical tumor. HeLa cells were the first human cells shown to proliferate indefinitely under laboratory conditions, providing a platform for biomedical research. Two decades later, in 1973, the HEK293 cell line was established by introducing adenoviral DNA into human embryonic kidney cells. This intervention led to stable integration of viral genes that support continuous growth and survival, effectively immortalizing the cell line. HEK293 cells soon gained widespread use due to their human origin, ease of transfection, and adaptability to diverse experimental applications. Since then, numerous other immortalized lines have been established-each optimized for specific research or industrial purposes-marking a significant evolution in the experimental toolbox of life sciences.

1. Creation and Maintenance of the Cell Line

Cell culture is the process of growing cells in a controlled laboratory environment outside their natural context.[3] This involves placing cells in a nutrient-rich medium and maintaining appropriate temperature, humidity, and gas composition to support their survival and proliferation. HEK293 cells can be cultured in two main formats: adherent, where cells attach to the surface of a vessel and spread into a flattened monolayer, and suspension, where cells grow freely in liquid medium. Suspension-adapted derivatives such as 293F and 293H are optimized for high-density growth in serum-free, chemically defined media.[3]

Adherent HEK293 cells, when cultured adherently in media supplemented with 10% fetal bovine serum (FBS), exhibit a doubling time of approximately 24 to 36 hours, with individual cells measuring approximately 10- 18 µm in diameter.[4,5] In adherent culture, HEK293 cells are typically passaged when they reach approximately 80% confluency. Confluency refers to the

proportion of the culture surface covered by cells. Transferring cells to a new vessel at this stage prevents overgrowth and maintains favorable conditions for continued replication. Between passages, the culture medium may be partially or fully replaced to restore nutrients and remove waste products.[6] These standard practices help ensure stable cell physiology and reproducible experimental outcomes. As an immortalized line, HEK293 cells can be propagated indefinitely, though to minimize genomic drift-such as chromosomal rearrangements and gene copy number changes-cultures are commonly maintained for no more than twenty passages.[3,5]

Several genetically modified derivatives of the original HEK293 cell line have been developed over the years to meet specific experimental and industrial demands. A particularly innovative adaptation of the HEK293 cell line was developed by Adam E. Cohen's group at Harvard University to create a reliable and accessible model of electrical excitability through the stable expression of defined ion channels, known as spiking HEK cells (Table 2.2). This engineered system enables high-throughput screening and detailed characterization of fluorescent voltage indicators, while also supporting a broad range of applications including ion channel research, all-optical electrophysiology, compound screening, toxicity evaluation, and studies of electroporation dynamics. In our research, it provides a central platform for evaluating voltage-sensitive nanomaterials within a simplified, scalable, and well-controlled experimental context.[7,8]

Spiking HEK cells are genetically modified to stably express one of two key ion channels: $Na_V1.3$ or $Na_V1.5$ - voltage-gated sodium channels that initiate action potentials, and $K_{ir}2.1$, an inward rectifier potassium channel that stabilizes the resting membrane potential near physiological values. The inclusion of $K_{ir}2.1$ reduces the resting potential to approximately -66 mV, allowing the cells to exhibit repetitive action potential firing upon depolarization. In some versions of the system, $K_{ir}2.1$ expression is placed under the control of a doxycycline-inducible promoter, enabling the generation of both spiking and non-spiking variants from the same line for comparative studies. $K_{ir}2.1$ channel might be additionally tagged with cyan fluorescent protein (CFP) as a fluorescent tag, which enables optical assessment which cells express the channel.[9]

When cultured as a monolayer at high confluency (90-95%), spiking HEK cells form a functionally integrated network through intercellular coupling mediated by endogenous gap junctions, so called connexin-45. This electrical connectivity supports spontaneous, rhythmic action potentials that propagate uniformly across the culture in a coordinated, metronome-like pattern.[7] In addition to their intrinsic activity, action potentials can be externally triggered using electrical stimulation. In certain variants of the cell line, the optogenetic protein CheRiff is additionally expressed, enabling precise, light-induced activation of action potentials through

blue light stimulation. These electrophysiological properties make spiking HEK cells particularly well suited for optical electrophysiology, including the evaluation of genetically encoded voltage indicators (GEVIs) and voltage-sensitive dyes (VSDs). The system also enables high-throughput screening of pharmacological agents targeting ion channels, as well as phenotypic assays relevant to neurological and cardiac disorders. It is especially valuable for identifying modulators of excitability, assessing potential neurotoxicity or cardiotoxicity, and investigating disease mechanisms through all-optical control and monitoring of membrane voltage. While spiking HEK cells do not fully replicate the biophysical properties of neurons-due to longer action potentials and variable repolarization kinetics-they offer a robust, scalable, and experimentally accessible model for studying excitable cell behavior in a controlled setting.[7–9]

Table 2.2 Spiking HEK293 cell line variants with their ion channel payloads, inducible systems, sources, and key practical notes. Commercially available lines were developed in the Adam E. Cohen laboratory and are distributed by ATCC (https://www.atcc.org/).

Cell line	Payload	Inducible system	Source	Practical notes
Spiking HEK (Original, Not catalogued)	Constitutive: •$Na_V1.3$ •$K_{ir}2.1$ *No fluoro tags*	None (constitutive expression)	A. Cohen lab; not commercially available	Less stable; $K_{ir}2.1$ expression lost after a few passages.
tet-on Spiking HEK (ATCC CRL-3479)	Constitutive: •$Na_V1.5$ Inducible: • $K_{ir}2.1$-CFP	rtTA-Tet-On; induce with 1-2 µg mL^{-1} doxycycline for 24-36 h	Commercial (ATCC)	HEK cells do not tolerate sustained $K_{ir}2.1$-maintain a master plate *without* doxycycline and induce only plates destined for assays.
CheRiff-eGFP tet-on Spiking HEK (ATCC CRL-3480)	Constitutive: •$Na_V1.5$ •CheRiff-eGFP Inducible: •$K_{ir}2.1$-CFP	rtTA-Tet-On; induce with 1-2 µg mL^{-1} doxycycline for 24-36 h	Commercial (ATCC)	Adds optical stimulation capability via CheRiff.

1.1.Cell Culture

Standard culture conditions for adherent HEK293 cells involve maintaining the cells at 37 °C in a humidified atmosphere with 5% carbon dioxide (CO_2).[6] Cells are typically grown in Dulbecco's Modified Eagle Medium (DMEM), usually combined with nutrient mixture, and supplemented with FBS, L-glutamine, and antibiotics.[6] Antibiotics in cell culture serve two main purposes: they prevent bacterial contamination, commonly through the use of agents such as penicillin and streptomycin, and they function as selective agents to isolate or maintain genetically modified cells that carry antibiotic resistance genes. For example, compounds such as tetracycline, geneticin, puromycin, and blasticidin are routinely used to select cells that have been successfully transfected with genes of interest.[4,7]

Cultures are usually passaged two to three times per week. As cells grow and metabolize, they gradually acidify the surrounding medium. This shift is easily monitored by the color change of DMEM containing phenol red, which transitions from red to orange or yellow as the pH drops-often serving as a visual cue that the culture is due for passaging or medium replacement (workflow illustrated on Figure 2.9).

Passaging begins by removing the old culture medium from the flask. If the cell monolayer is well attached and stable, the cells can be gently rinsed with phosphate-buffered saline (PBS) to wash away dead cells and waste. To detach cells from the surface, a mild enzymatic treatment with trypsin is used.[5] After a short incubation (typically 1-3 minutes at 37 °C), the cells begin to round up and lift from the surface. At this point, the enzyme is neutralized by adding fresh DMEM10. The suspension is pipetted gently to break up any clumps, then transferred to a sterile centrifuge tube. The cell suspension is centrifuged to pellet the cells, forming a visible puck at the bottom of the tube. The supernatant is carefully discarded, and the cells are resuspended in fresh medium, again pipetting up and down to ensure a uniform, single-cell suspension.

Controlling the seeding density is important for experiments like spiking monolayer cultures for imaging, and this requires a precise cell count using a hemocytometer. Optionally, trypan blue dye can be added to discriminate between viable and non-viable cells, as the dye penetrates only the membranes of dead cells. Based on the calculated cell concentration, the appropriate number of cells is seeded into new culture flasks and experimental sample plates, using fresh DMEM10 supplemented with antibiotics to maintain selectiveness and ensure consistent gene expression where relevant. In some cases, culture vessels or sample dishes may be coated with poly-D-lysine-a synthetic, positively charged polypeptide that enhances cell adhesion and supports growth on the culture surface.[3,7] Once seeded, all vessels are clearly labeled and placed

back into the incubator to allow the cells to reattach and continue growing under standard conditions. A detailed protocol, including the complete media recipe, exact reagent volumes, and the step-by-step cell counting procedure, is provided in the Appendix (Section 2.2.1 *Cell Culture Protocols*).

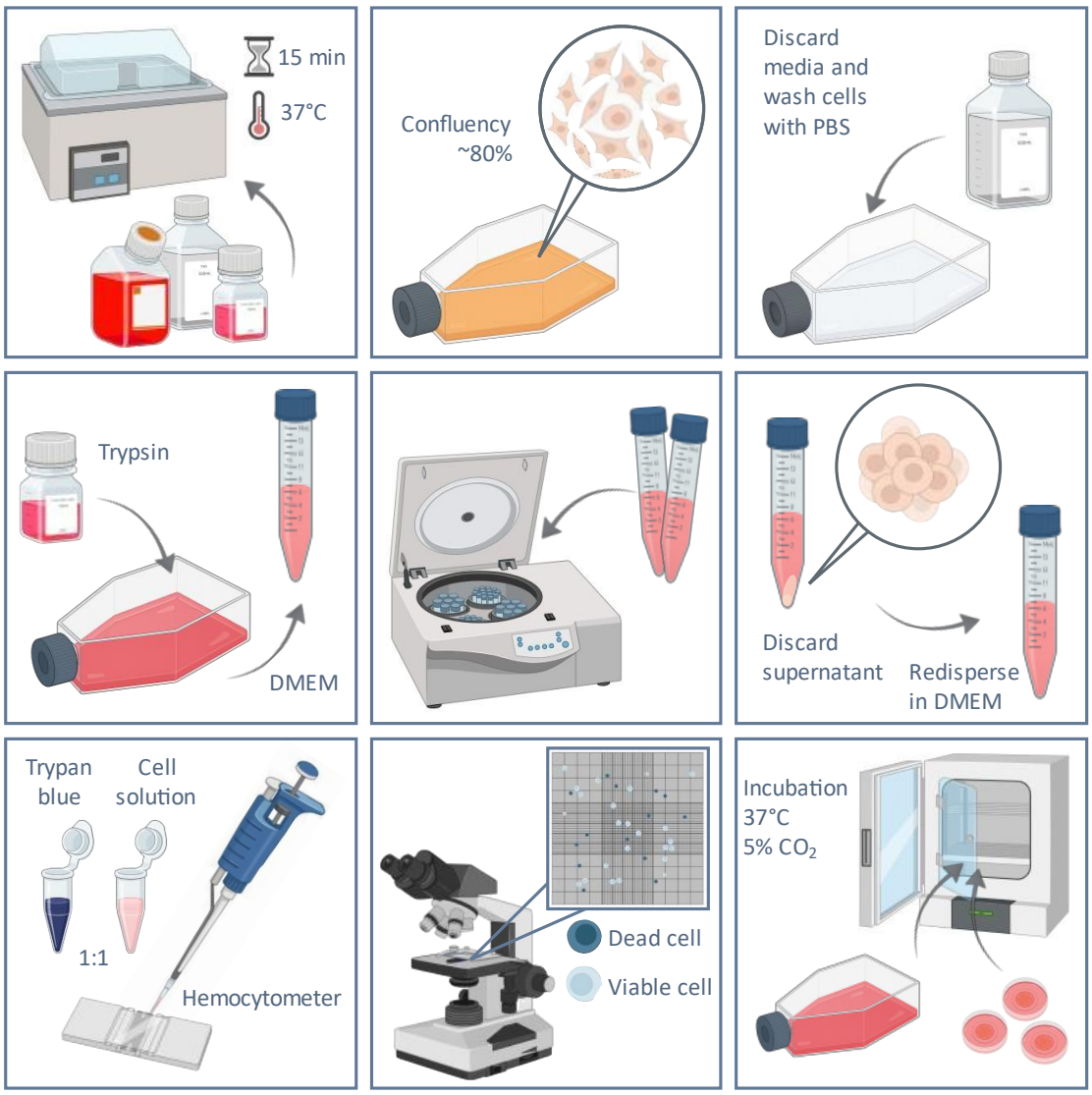

Figure 2.9 Schematic overview of the HEK293 cell passaging workflow. Steps include reagent preparation, cell detachment with trypsin, centrifugation and resuspension in fresh medium, cell counting with trypan blue exclusion, and reseeding into new culture vessels for continued incubation.

2. Calcium Imaging of Spiking HEK Cells

Fluorescence serves as a fundamental indicator of neural structure and dynamics, forming the basis for numerous imaging techniques employed by neurobiologists (see Chapter 1.1.2). By leveraging fluorescent signals, it is possible to achieve high-resolution imaging of neurons and their functional activities, thereby enabling exploration of cellular mechanisms underlying neural activity.[10] The choice of fluorescence microscope plays a pivotal role in determining the spatial and temporal resolution achievable, and neurobiological studies frequently employ wide-field, confocal, two-photon, or multiphoton microscopes, each suited to particular experimental requirements and imaging depths. While confocal microscopy offers excellent optical sectioning for moderate-depth samples, two-photon microscopy has become a mainstay in imaging neural activity deep within scattering tissues, such as intact brain preparations.[11,12] With these considerations in mind, this chapter describes the use of fluorescence microscopy to study calcium dynamics in self-spiking HEK cells. The imaging setup employs standard epi-fluorescence illumination and camera-based detection, which allows monitoring of intracellular calcium changes in response to electrical activity. This straightforward configuration was selected to support the development of an approach that can be easily adopted in typical biological laboratory environments without requiring specialized instrumentation.

2.1. Fluorescence Microscope Setup

Fluorescence microscopy visualizes biological samples by detecting emitted fluorescence light from molecules called fluorophores. Fluorophores absorb excitation light at a shorter wavelength and emit fluorescence at a longer wavelength; this shift, known as the Stokes shift, allows clear separation of emitted fluorescence from excitation illumination.[13] A typical fluorescence microscope employs an epi-fluorescence setup, where the same objective lens serves both to deliver excitation light and to collect emitted fluorescence (Figure 2.10 A).[14] Objectives with a high numerical aperture (NA) are preferred, as they increase light-gathering efficiency and improve spatial resolution. Immersion objectives-used with a medium such as water, oil, or glycerol between the lens and the specimen-can further enhance image quality by minimizing refractive index mismatches and reducing optical distortions.[13]

Central element of such a fluorescent setup is the filtering cube, containing three essential components: an excitation filter that transmits only specific wavelengths required to excite the fluorophores, a dichroic mirror placed at a 45-degree angle that reflects excitation wavelengths onto the sample and transmits emitted fluorescence towards the detector, and an emission (barrier) filter that selectively allows only the longer-wavelength fluorescence signal to reach

the detector, blocking residual excitation light.[11,13] These filters must be carefully matched to the spectral properties of the fluorophore used. Illumination is typically provided by a mercury lamp, which emits intense, broad-spectrum light with strong peaks strong peaks in the UV and visible spectrum. To regulate illumination intensity and minimize photobleaching or phototoxicity, neutral density (ND) filters can be introduced into the optical path to reduce the amount of excitation light reaching the sample.[11]

Fluorescence signals are typically recorded using sensitive digital devices such as CCDs (Charge-Coupled Device), EMCCDs (Electron-Multiplying CCD), or sCMOS (Scientific Complementary Metal-Oxide-Semiconductor) cameras.[10,11,13,14] Camera selection should be guided by experimental needs, weighing factors such as signal sensitivity, temporal and spatial resolution, as well as cost and accessibility. Prior to data collection, key recording parameters such as camera exposure time, frame rate (frames per second, fps), pixel binning, and the size of the recorded area must be carefully considered. Shorter exposures enable higher frame rates and improved temporal resolution but may require increased excitation intensity or higher detector sensitivity to preserve signal quality. Binning, which combines adjacent pixels into larger units, enhances the signal-to-noise ratio at the cost of spatial resolution, and can support faster acquisition by reducing data volume. Similarly, reducing the recorded field of view (FOV) allows faster readout and higher frame rates. These parameters must be tuned to achieve the appropriate balance between temporal and spatial resolution, signal quality, data size, and sample viability, based on the specific goals and constraints of the experiment.[13,14]

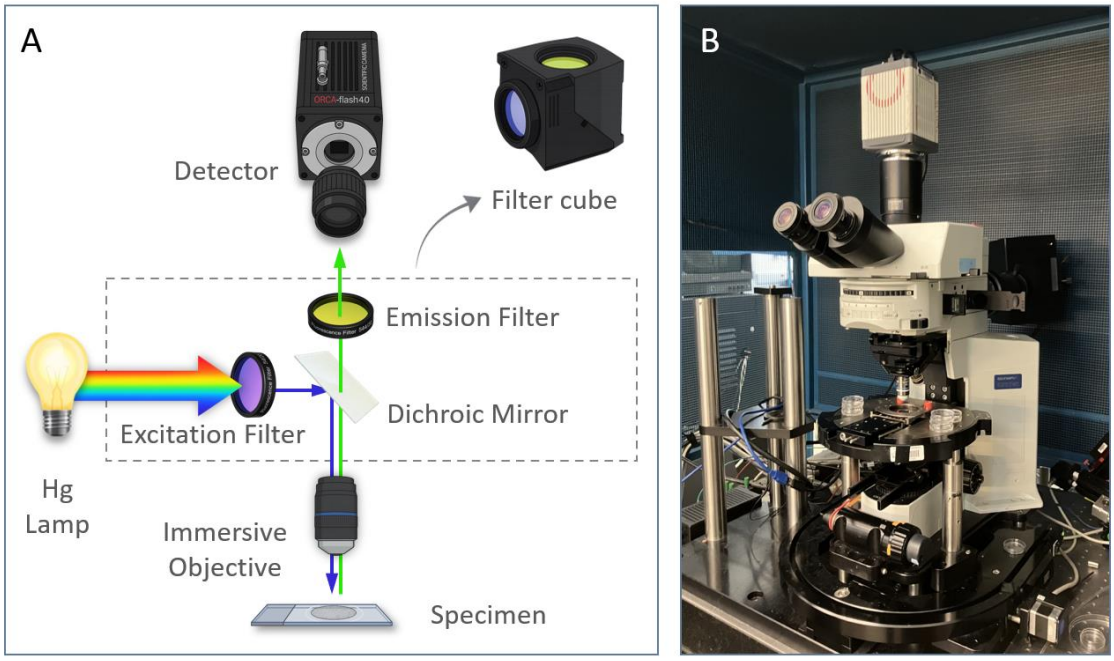

Figure 2.10 Epi-fluorescence microscopy setup used for calcium imaging experiments. (A) Optical diagram of the fluorescence light path, showing key components including the mercury arc lamp, excitation and emission filters, dichroic mirror, immersive objective, and detector. The system is equipped with a motorized filter cube turret, allowing rapid switching between multiple filter cubes during experiments. (B) Photograph of the fluorescence microscope system located at the Neurotechnology Center, Columbia University.

The microscope used for the majority of measurements presented in this dissertation was an upright fixed stage microscope system located in the Yuste Laboratory at the Neurotechnology Center, Columbia University. This setup, internally referred to as the "North Rig", was configured for single-channel calcium imaging using Calcium Green-1, with FITC filter cube matched to the dye's excitation and emission characteristics (Figure 2.10 B). Excitation light from a mercury lamp was spectrally filtered through a 475/85 nm band-pass excitation filter and directed onto the specimen via a 500 nm long-pass dichroic mirror and a water-immersion objective. The same objective lens collected the emitted fluorescence, which then passed through a 535/50 (passing approximately 510-560 nm wavelengths) emission filter before being detected by a sCMOS Hamamatsu camera mounted on the microscope's trinocular port.[11,13] An immersion objective was used to minimize refractive index mismatch between the objective lens, the coverslip, and the aqueous medium covering the sample, thereby improving light collection efficiency and preserving spatial resolution. Acquisition parameters-including exposure time, pixel binning, and frame rate-were optimized under continuous illumination to capture rapid calcium transients with minimal signal loss. Recordings were performed at 50, 100, and 200 ms exposure times; an exposure of 100 ms (corresponding to 10 frames per second) provided a suitable

balance between temporal resolution and fluorescence signal brightness for detecting spiking events.

In addition to fluorescence illumination, a secondary white light source was positioned beneath the specimen, enabling the acquisition of bright-field images aligned with the corresponding fluorescence fields of view. The microscope is equipped with a filter cube turret, allowing rapid switching between filter sets during experiments to support imaging of different fluorophores.

2.2. Results and Discussion

The genetically modified HEK cells, described by Park and Cohen (2013), spontaneously generate electrical spikes when cultured as a monolayer at high confluence (80-95%). This activity emerges as coordinated depolarization events, with reported spike frequencies around 3 Hz and propagation velocities of approximately 2 cm/s. These spikes are characterized by a resting membrane potential near -66 mV, peak depolarizations reaching +34 mV, and rise times of approximately 3 ms, reflecting stable and repeatable action potential dynamics across the culture.[7]

For imaging, monolayers were stained with the chemical calcium indicator Calcium Green-1 and recorded in Tyrode's solution, a physiological extracellular buffer with defined ionic composition; detailed protocols for both are provided in the Appendix (Section 2, *Supplementary Material for Chapter #2*).

To determine the optimal time window for reliable recordings, we monitored cultures at days 3, 4, and 5 post-seeding (Figure 2.11). Examples shown for each day illustrate representative recordings from qualitative analysis of three culture plates per time point, with several regions examined in each dish. On day 3, the monolayer was often incomplete, and spontaneous spiking was not detected. Even in more confluent regions, cells appeared insufficiently mature to support the ion channel expression necessary for robust spiking. In these areas, we observed slow calcium transients, but not the fast, periodic signals characteristic of electrical spikes. By day 4, the cultures consistently formed dense and uniform monolayers, and spiking activity became clear, rhythmic, and reproducible across samples. Estimating dominant frequency of the calcium signals in presented sample yielded peak value of 0.26 Hz, as determined using the Welch method. On day 5, signs of overgrowth were evident, with cells growing in multiple layers. Under these conditions, spiking activity was reduced or absent, and when present, it was often unreliable and not synchronized. The corresponding Welch spectrum of the day 5 trace identify a dominant frequency at 0.26 Hz, but the power spectral density of the peak was approximately

threefold lower compared to day 4. These observations define a narrow experimental window, with day 4 representing the most favorable conditions for capturing spontaneous, synchronized spiking events in this system.

We next examined whether the observed activity reflected coordinated behavior across the monolayer rather than independent cellular responses (Figure 2.12). Fluorescence was recorded from a 166.4 × 166.4 µm field of view at 10 frames per second, using 100 ms exposures. With a reported wave propagation speed of approximately 2 cm/s, a spike would traverse the field in about 10 ms, well below the temporal resolution of our acquisition. Under these conditions, propagating spikes are expected to appear as simultaneous events across the field, enabling synchronized activity to be captured as a uniform signal. The averaged fluorescence trace of whole FOV (Figure 2.12 B) shows regular calcium transients with consistent shape and timing. A heatmap of 500 individual cell traces (Figure 2.12C) reveals a uniform pattern: nearly all cells within the field exhibit aligned spiking, no significant variation in timing. This synchrony is further illustrated in selected single-cell traces (Figure 2.12 D), which follow the same rhythm and phase. These results confirm that the culture behaves as a synchronized system, with cells spiking collectively at regular intervals.

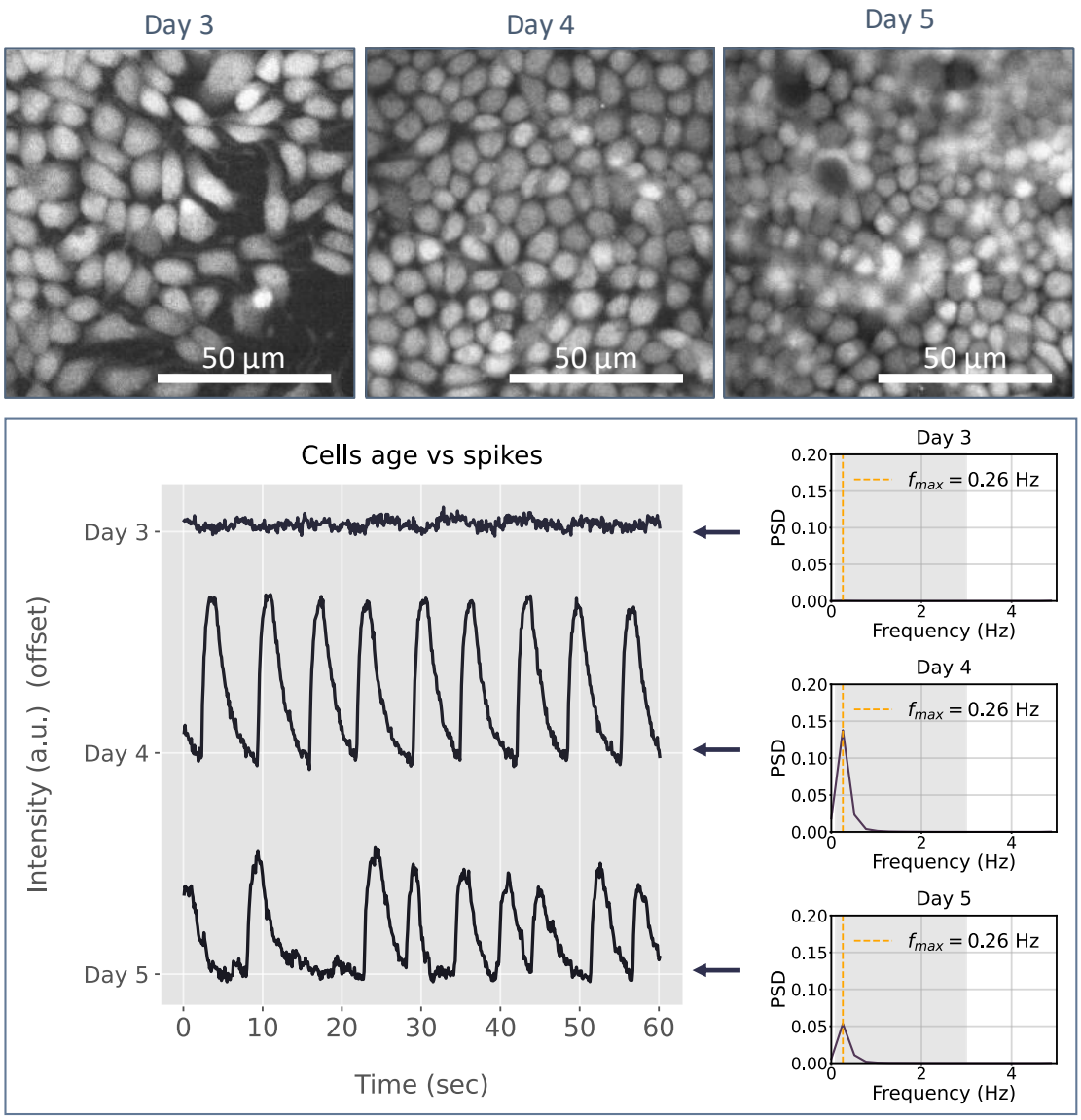

Figure 2.11 Spontaneous spiking activity in Calcium Green-1-labeled cells monolayers at different days post-seeding. Top: Fluorescence images from days 3, 4, and 5. Bottom: Average fluorescence traces over 60 seconds for whole field of view (full frame average). Day 3 monolayers are incomplete and show no spiking. On day 4, uniform monolayers start to exhibit periodic spiking. By day 5, cultures are overgrown and activity is diminished or absent. On the right, power spectral density plots from Welch analysis illustrate the frequency components corresponding to each trace.

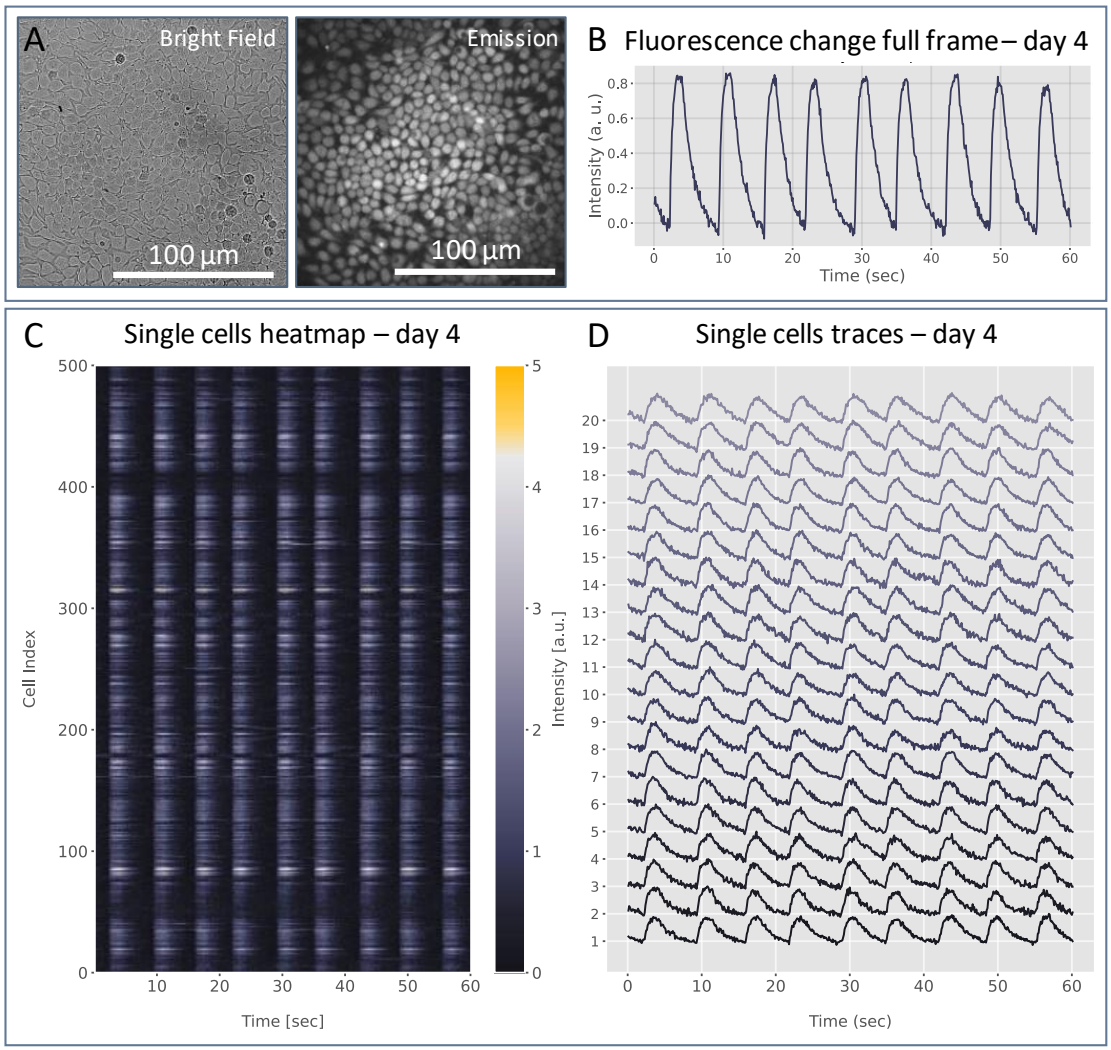

Figure 2.12 Synchronized spiking activity in HEK cell monolayer on day 4. (A) Bright field and green channel fluorescence images showing a confluent monolayer within a 166.4 × 166.4 µm field of view. (B) Average fluorescence trace from the entire field shows regular calcium transients with consistent shape and timing. (C) Heatmap of 500 individual cell traces reveals highly synchronized spiking across the population. (D) Selected single-cell traces further confirm that cells spike with similar rhythm and phase, indicating coordinated activity across the monolayer.

The frequency of spontaneous spikes in these genetically engineered HEK cells can vary based on multiple factors, including cell confluency, maturity, and passage number (genetic age). In our experiments, spike frequencies ranged from ~0.3 Hz to 3.0 Hz. Figure 2.13 illustrates representative examples starting at 0.6 Hz, while slower activity (0.26 Hz) is shown in Figure 2.12. This variability in spike frequency reflects the sensitivity of the system to experimental conditions and underscores the importance of consistent protocols when using these cells for electrophysiological applications. Corresponding figure with Welch power density spectra can be found in the Appendix (Figure A.1, Section 2, *Supplementary Material for Chapter #2*).

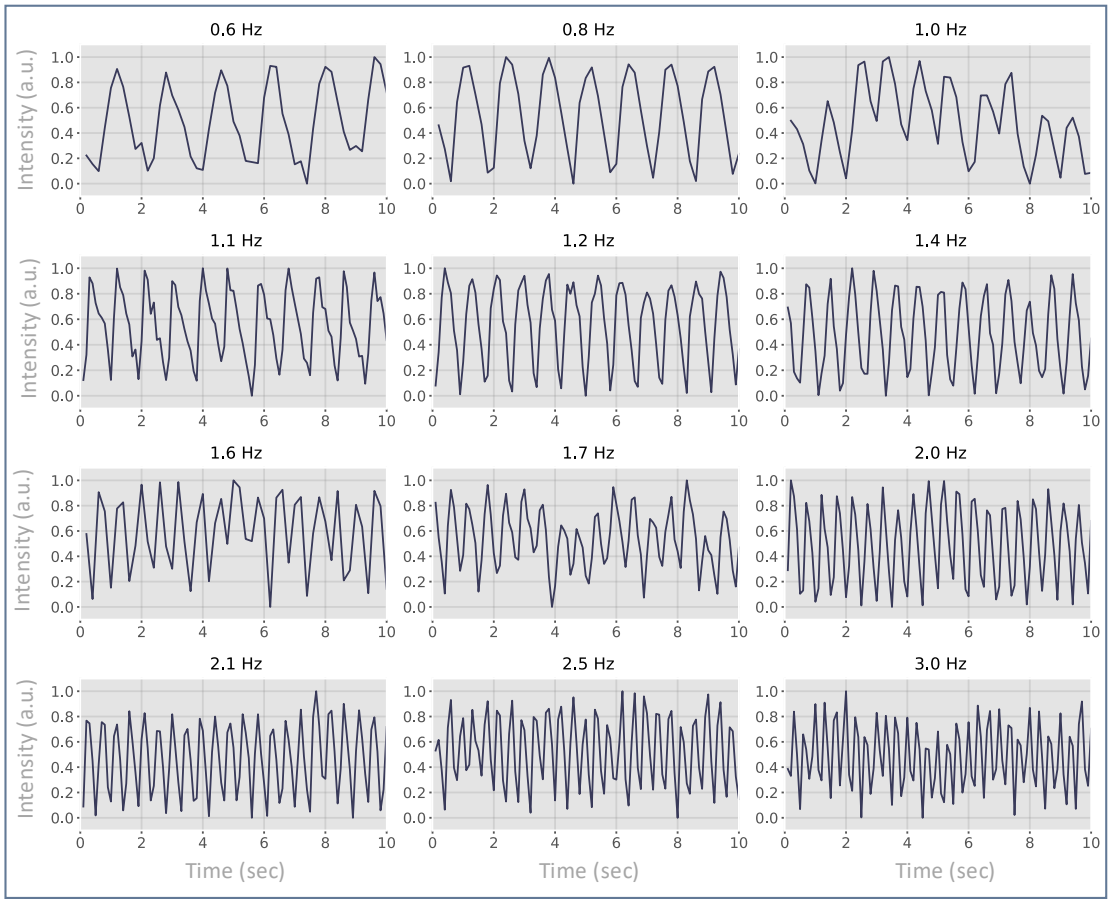

Figure 2.13 Representative examples of spontaneous spiking activity in HEK cell monolayers across a range of frequencies. Fluorescence traces (10 s duration) from different recordings, showing spike frequencies between 0.6 Hz and 3.0 Hz. Each trace represents the normalized calcium signal averaged over the entire recorded field of view. Dominant frequencies were estimated using Welch's method.

To confirm that the observed calcium signals were driven by electrical spiking, we performed pharmacological validation using tetrodotoxin (TTX), a selective blocker of voltage-gated sodium channels (Figure 2.14). Although TTX can suppress spiking at concentrations as low as 10 nM, we applied it at 10 µM to ensure complete block. Prior to its addition (Figure 2.14 A), spontaneous spiking was consistently present throughout the recording at a frequency of 0.7 Hz.

After TTX injection (Figure 2.14 B), spikes became irregular and less predictable, and were completely absent after 60 s. Following TTX washout (Figure 2.14 C), spiking reappeared at a stable frequency 0.9 Hz, accompanied by a marked increase in peak power in the corresponding Welch-derived power spectra, indicating the recovery of strong, periodic activity. These results demonstrate that the spontaneous calcium transients depend on sodium-channel activity and reflect genuine action potential-driven electrical events within the culture.

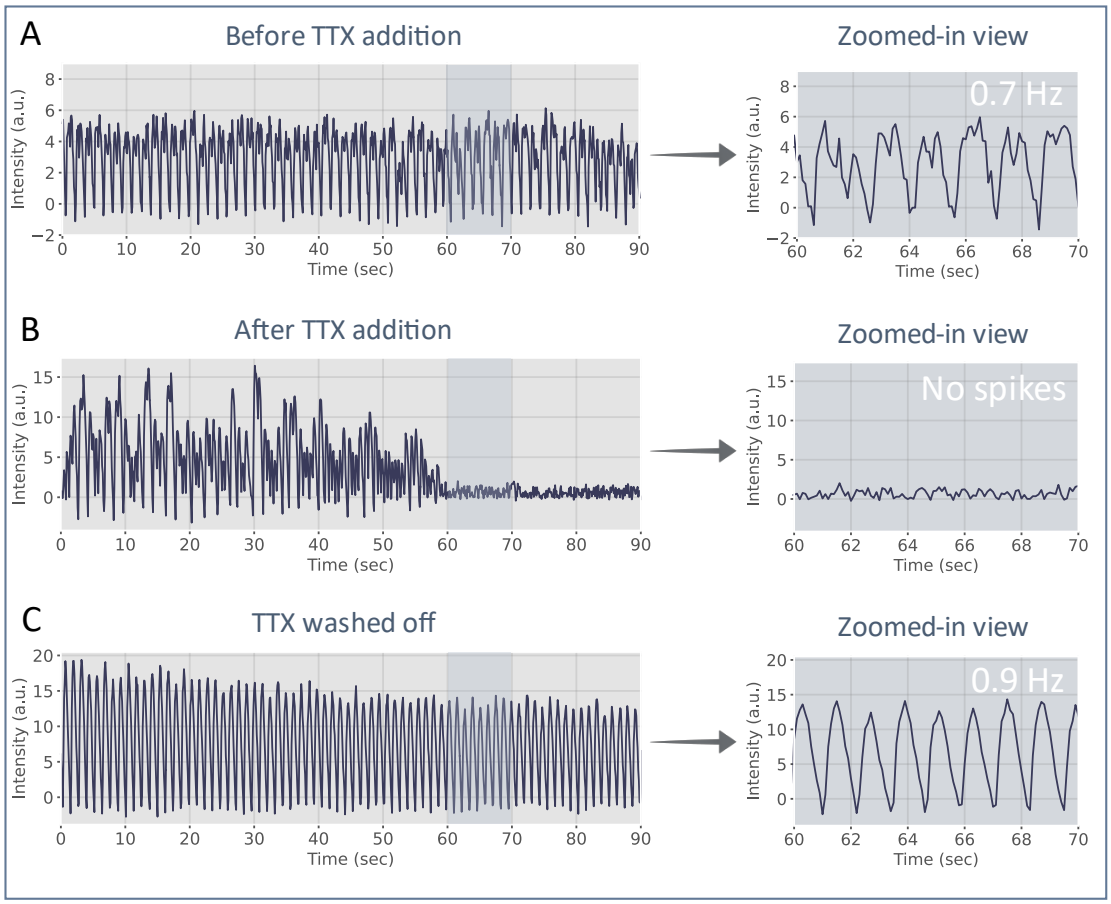

Figure 2.14 Pharmacological validation of sodium channel-mediated spiking using tetrodotoxin (TTX). (A) Before TTX addition, consistent spiking is observed at 0.7 Hz. (B) After addition of 10 µM TTX at t = 0 s, spiking becomes irregular and less predictable, and is completely arrested after 60 s. (C) Following TTX washout, spiking resumes uniformly at 0.9 Hz with increased peak amplitude. Experiment confirms the sodium channel dependence of the calcium transients.

In the absence of external intervention-such as media exchange, pharmacological treatment, or mechanical disturbance-the spiking activity remained stable over time. We continuously recorded calcium signals from the same field of view for three hours under unaltered conditions (Figure 2.15). Spontaneous spikes persisted throughout the recording, with a progressive decrease in spike frequency over time. The dominant frequency remained stable at 2.5 Hz during the first hour of recording (15-60 min) and then gradually decreased to 1.4 Hz by the final time window (165-180 min), as determined using Welch's method. This gradual reduction in spiking

frequency is likely driven by physiological changes that accumulate under static, non-perfused conditions. One key factor may be the buildup of extracellular potassium, which depolarizes the resting membrane potential and leaves a portion of NaV1.3 channels inactivated.[15] As a result, the system requires more time for channels to recover between spikes, extending the inter-spike interval. Additionally, reduced activity of the Na^+/K^+-ATPase pump-which relies on cellular ATP (adenosine triphosphate, the cell's main energy source)-can lead to a gradual loss of ionic balance and reduced membrane excitability. As ATP levels decline, electrical communication between cells (via gap junctions) may weaken, and the function of Kir2.1 potassium channels may decrease, making it harder for cells to reset between spikes and maintain synchronized activity.[16] Although the ambient temperature is not actively lowered during the experiment, prolonged exposure to room temperature may gradually affect cell viability and further contribute to these effects. Taken together, these mechanisms likely account for the observed slowing of spike frequency over time, while underscoring the resilience of the system under passive conditions. For this reason, spike frequency should be verified using a well-established method when assessing system performance with a new tool.

While the decline in frequency over time is clear and quantitatively significant, the persistence of coordinated spiking for at least three hours (despite the absence of media exchange and suboptimal conditions such as room temperature) highlights the stability of the monolayer. Even at reduced frequencies, the cells continued to spike rhythmically and in synchrony, maintaining the characteristic metronome-like behavior of this system. All of the above makes those cells a tool of interest for our research.

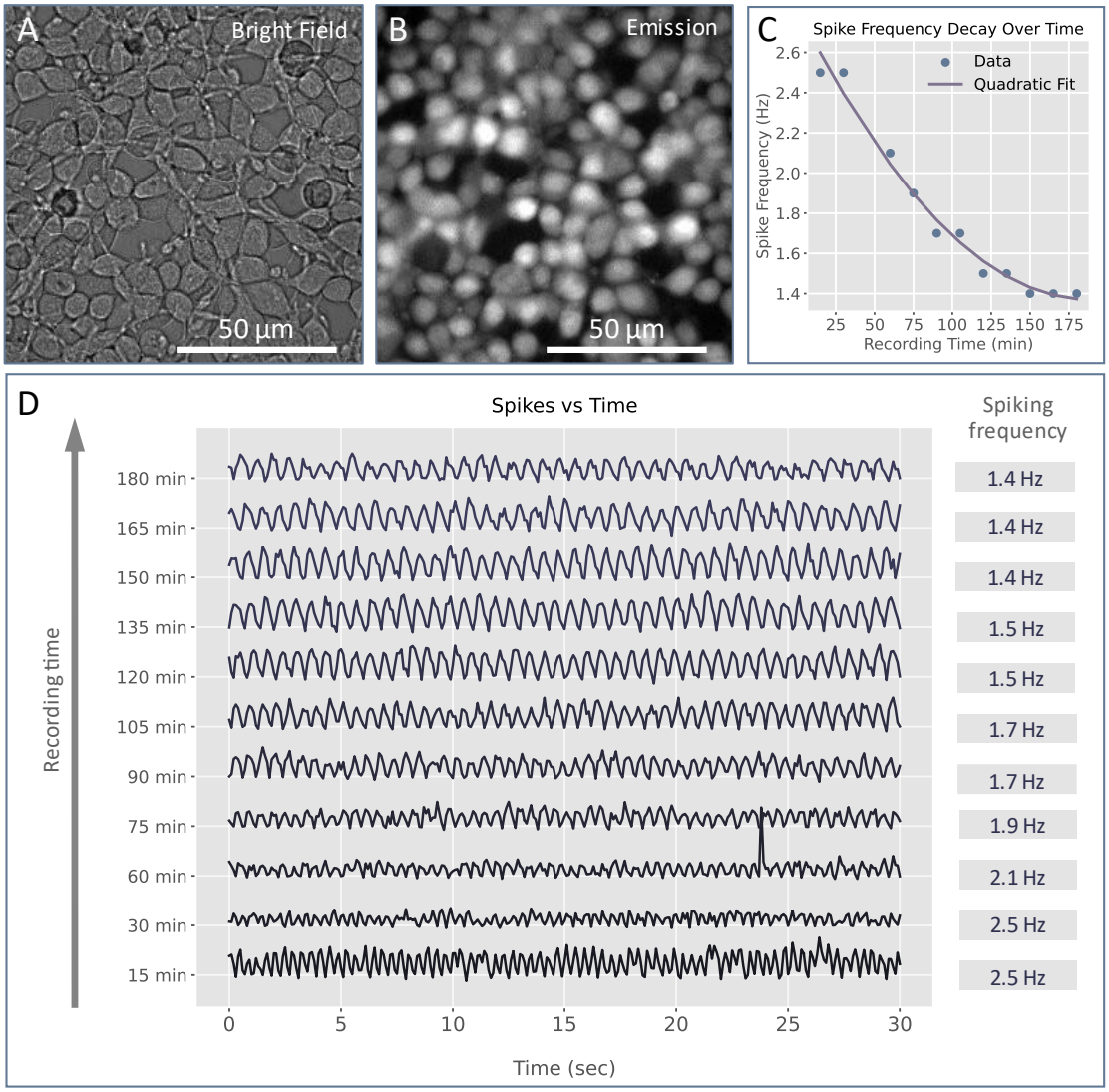

Figure 2.15 Stability of spontaneous spiking activity in static recording conditions. (A) Bright-field and (B) fluorescence image of the recorded field of view, showing a confluent monolayer labeled with Calcium Green-1. (C) Spike frequency as a function of time, showing a gradual decrease over 3 hours. Each point represents the dominant frequency; the decline followed a quadratic trend, consistent with second-order kinetics. (D) Fluorescence traces from the same field of view, acquired at 15-minute intervals. Spiking activity remained robust throughout the session, with a frequency of 2.5 Hz maintained during the first hour, followed by a gradual decline to 1.4 Hz by 180 minutes. No media change or external perturbation was introduced. These results highlight the capacity of the system to sustain rhythmic, synchronized electrical activity over extended imaging sessions, even at room temperature.

3. References for Chapter 2

(1) Pacitti, D.; Privolizzi, R.; Bax, B. E. Organs to Cells and Cells to Organoids: The Evolution of in Vitro Central Nervous System Modelling. *Front. Cell. Neurosci.* **2019**, *13*. https://doi.org/10.3389/fncel.2019.00129.

(2) Estee Torok; Ed Moran; Fiona Cooke. *Oxford Handbook of Infectious Diseases and Microbiology*; 2009.

(3) Geisse, S. Reflections on More than 10 Years of TGE Approaches. *Protein Expr. Purif.* **2009**, *64* (2), 99–107. https://doi.org/10.1016/j.pep.2008.10.017.

(4) Batista Napotnik, T.; Kos, B.; Jarm, T.; Miklavčič, D.; et al. Genetically Engineered HEK Cells as a Valuable Tool for Studying Electroporation in Excitable Cells. *Sci. Rep.* **2024**, *14* (1), 720. https://doi.org/10.1038/s41598-023-51073-5.

(5) Malm, M.; Saghaleyni, R.; Lundqvist, M.; Giudici, M.; et al. Evolution from Adherent to Suspension: Systems Biology of HEK293 Cell Line Development. *Sci. Rep.* **2020**, *10* (1), 18996. https://doi.org/10.1038/s41598-020-76137-8.

(6) Lin, Y.-C.; Boone, M.; Meuris, L.; Lemmens, I.; et al. Genome Dynamics of the Human Embryonic Kidney 293 Lineage in Response to Cell Biology Manipulations. *Nat. Commun.* **2014**, *5* (1), 4767. https://doi.org/10.1038/ncomms5767.

(7) Park, J.; Werley, C. A.; Venkatachalam, V.; Kralj, J. M.; et al. Screening Fluorescent Voltage Indicators with Spontaneously Spiking HEK Cells. *PLOS ONE* **2013**, *8* (12), e85221. https://doi.org/10.1371/journal.pone.0085221.

(8) Tian, H.; Davis, H. C.; Wong-Campos, J. D.; Park, P.; et al. Video-Based Pooled Screening Yields Improved Far-Red Genetically Encoded Voltage Indicators. *Nat. Methods* **2023**, *20* (7), 1082–1094. https://doi.org/10.1038/s41592-022-01743-5.

(9) Zhang, H.; Cohen, A. E. Optogenetic Approaches to Drug Discovery in Neuroscience and Beyond. *Trends Biotechnol.* **2017**, *35* (7), 625–639. https://doi.org/10.1016/j.tibtech.2017.04.002.

(10) Combs, C. A.; Shroff, H. Fluorescence Microscopy: A Concise Guide to Current Imaging Methods. *Curr. Protoc. Neurosci.* **2017**, *79* (1), 2.1.1-2.1.25. https://doi.org/10.1002/cpns.29.

(11) Sanderson, M. J.; Smith, I.; Parker, I.; Bootman, M. D. Fluorescence Microscopy. *Cold Spring Harb. Protoc.* **2014**, *2014* (10), pdb.top071795. https://doi.org/10.1101/pdb.top071795.

(12) Two-Photon Calcium Imaging of Neuronal Activity. *Nat. Rev. Methods Primer* **2022**, *2* (1), 1–1. https://doi.org/10.1038/s43586-022-00160-4.

(13) Lichtman, J. W.; Conchello, J.-A. Fluorescence Microscopy. *Nat. Methods* **2005**, *2* (12), 910–919. https://doi.org/10.1038/nmeth817.

(14) Ettinger, A.; Wittmann, T. Chapter 5 - Fluorescence Live Cell Imaging. In *Methods in Cell Biology*; Waters, J. C., Wittman, T., Eds.; Quantitative Imaging in Cell Biology; Academic Press, 2014; Vol. 123, pp 77–94. https://doi.org/10.1016/B978-0-12-420138-5.00005-7.

(15) Chen, R.; Chung, S.-H. Mechanism of Tetrodotoxin Block and Resistance in Sodium Channels. *Biochem. Biophys. Res. Commun.* **2014**, *446* (1), 370–374. https://doi.org/10.1016/j.bbrc.2014.02.115.

(16) Même, W.; Ezan, P.; Venance, L.; Glowinski, J.; et al. ATP-Induced Inhibition of Gap Junctional Communication Is Enhanced by Interleukin-1 β Treatment in Cultured Astrocytes. *Neuroscience* **2004**, *126* (1), 95–104. https://doi.org/10.1016/j.neuroscience.2004.03.031.

Chapter 3

Quantum Dots for Detecting Neuronal Activity

1. Spherical Quantum Wells

Spherical quantum wells (SQWs) represent an advanced category of colloidal semiconductor nanocrystals that feature a multilayered architecture, commonly referred to as core/well/shell heterostructures. These structures consist of a central semiconductor core surrounded by two distinct shell layers, each contributing to the overall quantum confinement and optical behavior of the material.[1,2] One of the most extensively investigated configurations is the CdS/CdSe/CdS structure, composed of a CdS core (2.7 eV bulk bandgap), a middle CdSe layer functioning as the quantum well (1.75 eV bulk bandgap), and an outer CdS shell.[3,4] In this architecture, the intermediate CdSe layer acts as a three-dimensionally confined region for hole wavefunctions, while electron wavefunctions are delocalized over the entire volume of the nanocrystal, which leads to a quasi-type-II band alignment. This unique spatial distribution of charge carriers is central to the distinctive optical and electronic properties of SQWs, distinguishing them from both 2D planar quantum wells and 0D systems such as traditional quantum dots (QDs) or conventional core/shell quantum dots (CSQDs).

Strong confinement within the spherical CdSe layer contributes to high photochemical stability and quantum yields approaching unity.[1] Moreover, the strong confinement leads to well-separated electronic states and altered recombination dynamics, including suppressed Auger recombination and extended carrier lifetimes.[5–7] In particular, thick-shell CdS/CdSe/CdS SQWs have achieved near-unity photoluminescence quantum yield (PLQY) at room temperature (Figure 3.16 A). This high efficiency results from reduced lattice mismatch between the CdSe well and CdS layers, where coherent strain suppresses misfit defect formation. These structures also exhibit strongly reduced blinking, spending up to 90% of the time in the emissive “on” state.[1,3,8] Another noteworthy property of SQWs is their enhanced multiexciton emission, especially in large-core structures. SQWs with larger core diameters have shown high biexciton quantum yields, sometimes approaching 100%. This efficiency arises from reduced Auger recombination rates and increased effective exciton volumes (Figure 3.16 B). Furthermore, the well-defined spherical quantum confinement allows higher biexciton binding energies compared to purely spherical core nanocrystals.[4,7] Although the CdS/CdSe/CdS system is extensively studied – benefiting from the well-established understanding of CdSe and CdS quantum dots and core/shell structures – other material combinations, including ZnS/CdS/ZnS,[9] InP/ZnSe/ZnS (cadmium free alternative)[10], and CdSe/CdS/ZnS[11] have also been investigated. These alternative architectures aim to tailor exciton dynamics, carrier confinement, and band alignments to meet the demands of specific technological applications.

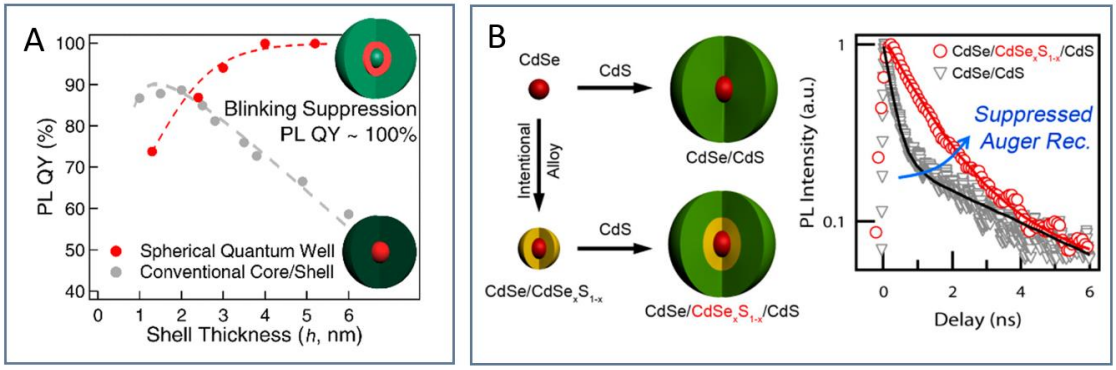

Figure 3.16 Optical performance enhancement in semiconductor nanocrystal heterostructures through spherical-well geometry and interfacial alloying. (A) Comparison of photoluminescence quantum yield (PLQY) as a function of CdS shell thickness for CdS/CdSe/CdS spherical quantum well (SQW) nanocrystals and conventional CdSe/CdS core/shell structures. SQW nanocrystals achieve near-unity PLQY and suppressed blinking at shell thicknesses greater than 5 nm, attributed to coherent strain in the CdSe layer, defect-free outer shell growth, and reduced hole trapping at the surface. (B) Photoluminescence decay dynamics for conventional CdSe/CdS core/shell quantum dots with an abrupt interface and core/alloy/shell structures incorporating a $CdSe_xS_{1-x}$ alloy interlayer. The presence of the alloyed interface slows multiexciton decay, indicating suppressed Auger recombination due to a smoother hole confinement potential.

Panel A reprinted with permission from B. G. Jeong, Y.-S. Park, J. H. Chang, et al., ACS Nano, 2016, 10, 10, 9297–9305. Copyright © 2016 American Chemical Society. Panel B reprinted with permission from W. K. Bae, L. A. Padilha, Y.-S. Park, et al., ACS Nano, 2013, 7, 4, 3411–3419. Copyright © 2013 American Chemical Society.

Due to these superior photophysical properties, SQWs have been identified as highly promising candidates for a wide range of advanced optoelectronic applications. In quantum light sources, their suppressed blinking and near-unity photoluminescence quantum yield (PLQY) make them excellent single-photon emitters for quantum cryptography, with antibunching sustained even at telecom wavelengths when integrated into photonic cavities.[3,8,12] In light-emitting devices, SQWs have improved microcavity laser performance and enabled flexible displays with broad color gamut coverage and extended lifetimes.[4,7] They also show promise in radiation detection, with fast X-ray response times that outperform traditional scintillators, opening the possibility for new generation of radiation detection.[8,13]

Among these diverse applications, bioimaging stands out as a particularly promising area. Quantum dots, including SQWs, are actively researched as fluorescent probes for biosensing applications. Due to their brightness, photostability, and the ability to be functionalized for targeting specific cellular structures they are widely used for bio-labeling and cellular imaging.[14] Their bright and tunable emission can be tailored as preferred for particular application. If needed, it can be engineered into the near-infrared region, facilitating deep-tissue imaging with minimal photodamage and reduced background autofluorescence. Additionally, their enhanced two-photon absorption cross-sections enable high-resolution imaging using near-infrared excitation, which is advantageous for in vivo applications.[4,7,15]

In summary, SQWs constitute a major advancement in colloidal nanocrystal technology, effectively combining beneficial aspects from planar quantum wells and classical nanocrystals. By strategically managing exciton dynamics and band alignment through material and structural optimization, SQWs significantly outperform conventional semiconductor nanostructures (Table 3.3), providing new opportunities across multiple scientific and industrial domains.

Table 3.3 Comparison of conventional quantum dots and spherical quantum well (SQW) nanocrystals across structural, optical, and functional properties.

Aspect	Quantum Dots (single-component or thin core/shell)	Spherical Quantum Wells (core/well/shell)	Reference
Dimensional confinement	Confinement in all three dimensions; band-gap rises and the DOS becomes discrete as the diameter decreases	Confined radially, with free carrier motion around the well; results in quasi-2D shell states governed mainly by well thickness, not particle diameter	[6] Battaglia *et al.* Angew. Chem. 2003
Energy-level structure, exciton wave-functions	1S-1P energy spacing set by core radius; electron & hole wave-functions overlap strongly (type-I) unless thick graded shells are added	Quasi-type-II: hole in CdSe, electron in CdS, weak overlap; gap set by CdSe thickness – each added monolayer red-shifts, size largely irrelevant	[5] Peng *et al.* APL 2005 [6] Battaglia & Peng Angew. Chem. 2003
Optical properties (absorption& PL)	PL FWHM 30-40 nm (broader due to size distribution and phonon interactions)	PL FWHM narrower, often ~20 nm, color tunning by altering well thickness	[1] Jeong *et al.* ACS Nano 2016
	Absorption onset is broader, gradual rise, caused mainly by size dispersion and variations in electron structure	Absorption onset is steep and well-defined, from consistent well thickness and quantized 2D-like energy levels	
	Stokes shift moderate (~20 meV), varies by structure. PLQY 50-70 % after passivation	Stokes shift larger (30-60 meV) due to quasi-type-II alignment, PLQY ~ 100%	
Carrier dynamics (radiative & non-radiative lifetimes)	Radiative lifetimes 5-20 ns; Auger recombination of multiexcitons is fast (0.1 ns); blinking and gain loss	Exciton lifetime similar to QDs, but multiexciton lifetime extended to >1 ns ("giant" suppression); biexciton PLQY 80-100%	[4] Nagamine *et al.* ACS Photonics 2020 ; [7] Marder *et al.* ACS Mater. Lett. 2023
Response to external electric fields	Nearly co-located carriers, the Stark response is largely quadratic and red-shifts stay modest (0-2 meV/10 kV cm^{-1})	Build in radial dipole makes thin-well SQWs respond linearly (3-6 meV/10 kV cm^{-1} for 1-2 ML wells), but thick CdS barrier screens modest external fields.	[1] Jeong et al. ACS Nano 2016
High-order nonlinear optics	TPA cross-section σ_2 ~10^3-10^4 GM; enhanced in anisotropic structures	SQWs show σ_2 up to 1.8 × 10^2 GM/nm^3 and low ASE thresholds (~10 μJ/cm^2); biexciton binding tunable (-130 to -50 meV)	[8] Xiang *et al.* Nanomaterials 2024
Applications demonstrated	QD-LEDs, photodetectors, LSCs, single-photon sources.	Low-threshold solution-processed lasers, optical amplifiers, single-photon emitters, down-converters for SSL; quantum-light sources	[16] García-de-Arquer *et al.* Science 2021; [3] Allemand *et al.* Nanotechnology 2022
Key challenges	Auger losses & blinking, Surface-trap passivation	Precise control of well thickness at ML level, Scale-up	[17] Cragg et al. Nano Lett. 2010; [18] Giansante et al. JPCL 2017

The study introduced in this PhD dissertation focuses on the CdS/CdSe/CdS configuration as the primary structural model, based on both theoretical predictions and experimental findings that highlight its high optical efficiency and strong sensitivity to external electric fields.[5,8,19] These attributes position SQWs as promising candidates for sensing neuronal activity, where changes in membrane voltage could modulate their optical emission.[20] Such voltage sensitivity offers a potential pathway for non-invasive neural imaging with high spatial and temporal resolution.[21] While experimental validation is still underway, emerging studies suggest that SQWs could play a pivotal role in the development of advanced neuroimaging tools and brain-computer interface technologies.

1.1. Overview of Quantum-dot-based Platforms

Before diving into the experimental protocols and performance analysis, it is important to provide a clear overview of the quantum dot (QD) systems explored in this study. These nanocrystal architectures form the basis for all subsequent investigations presented in this chapter. Although the rationale behind the selection and development of each system will be discussed in detail in later sections, introducing the full set of materials here will help orient the reader and provide a consistent reference point throughout the text.

Figure 3.17 summarizes the six QDs-based systems, identified as Systems I-VI, that were included in the course of study presented in this dissertation. These systems span a range of core-shell geometries and surface chemistries, allowing for a systematic examination of how structural variations influence both optical performance and biological interactions. System I is a commercially available CdSe/ZnS core-shell nanocrystal capped with tri-n-octylphosphine oxide (TOPO), serving as a widely used reference standard. Systems II, III, and IV share a CdS/CdSe/CdS spherical quantum well (SQW) configuration but differ in their surface coordination strategies: cadmium oleate (system II), zinc oleate (system III), and a combination of cadmium fluoride and octylamine (system IV). System V builds on the structure of III by incorporating an additional ZnS outer shell, enabling evaluation of the effects of extended passivation. System VI, on the other hand, modifies the ligand environment by replacing linear oleate with a branched 2-hexyldecanoate, providing insights into how ligand geometry impacts colloidal behavior and biological interactions.

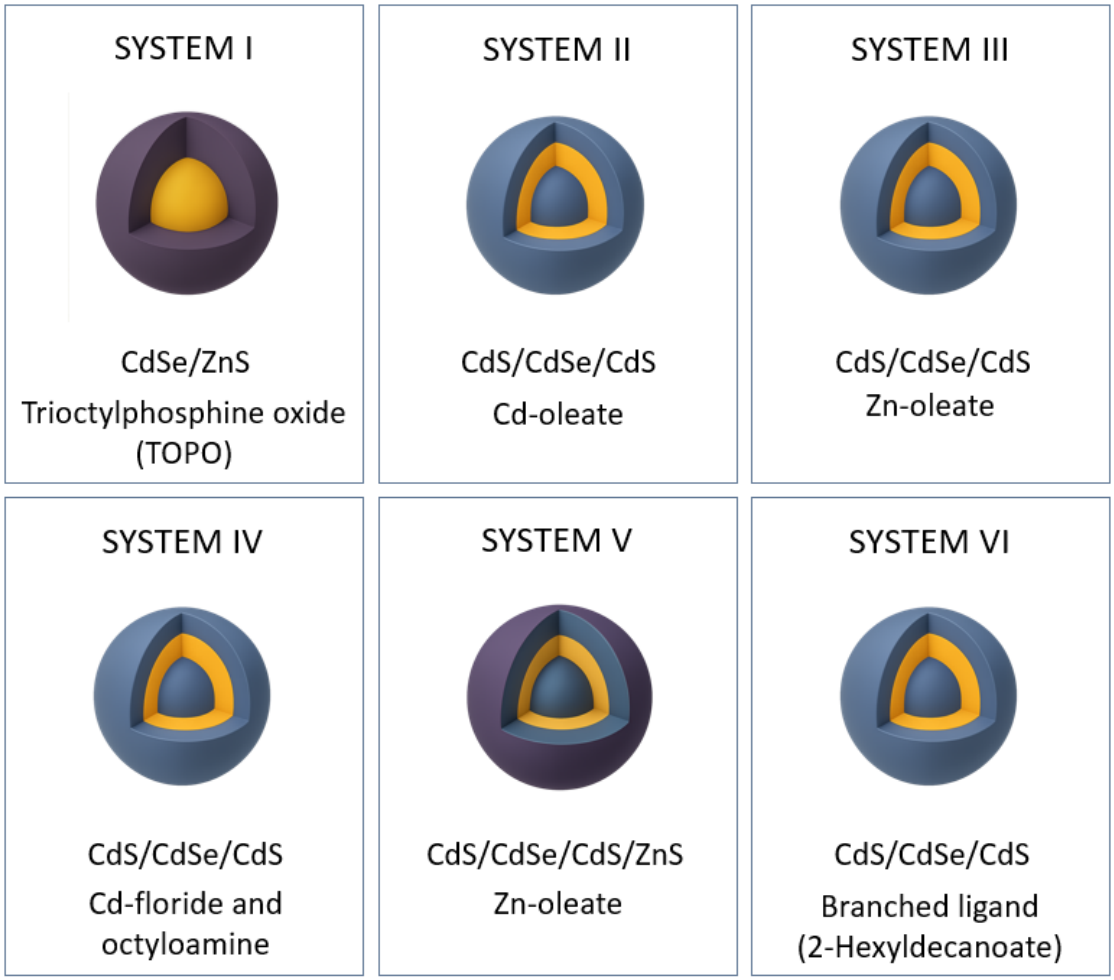

Figure 3.17 Overview of quantum dot systems investigated throughout this study. Six distinct nanocrystal architectures were evaluated, differing in core-shell structure and surface ligand composition. System I represents a commercially available CdSe/ZnS core-shell quantum dot capped with tri-n-octylphosphine oxide (TOPO), serving as a reference material. Systems II-VI are custom-synthesized CdS/CdSe/CdS or CdS/CdSe/CdS/ZnS spherical quantum wells (SQWs), each modified with a distinct surface coordination environment: cadmium oleate (II), zinc oleate (III and V), cadmium fluoride and octylamine (IV), and a branched 2-hexyldecanoate ligand (VI). This materials library enables a systematic investigation into how nanocrystal architecture and surface chemistry influence optical behavior, colloidal stability, and membrane fusion efficiency.

All systems were designed and prepared with reproducible protocols, ensuring consistent core size and quantum well thickness. This uniformity enables the evaluation of the influence of surface chemistry and shell composition on the physical of quantum dots. The sections that follow will first detail the synthetic strategies used for each custom-made nanocrystal system (3.1.3 *Surface Chemistry on CdS/CdSe/CdS Nanocrystals*), followed by investigations of water transfer (3.2 *Strategies for Water Transfer*), and their interaction with biological material (3.3 *Cell Membrane* Insertion). From this point forward, each system will be referred to by its assigned Roman numeral, with Figure 3.17 serving as a visual reference throughout the chapter.

1.2. Synthetic Approaches

Synthesis of layered CdS/CdSe/CdS nanocrystals

CdS/CdSe/CdS nanocrystals with layered radial composition were synthesized under an inert argon atmosphere using a combination of single and sequential injection strategies at 240 °C. The method relied on the simultaneous injection of sulfide and selenide precursors into a cadmium oleate and oleic acid solution to initiate the growth of the CdS/CdSe core/shell structure, followed by the sequential growth of an outer CdS shell. The chalcogen precursor mixture consisted of thiourea[22] and selenourea[23] derivatives, which served as sulfur and selenium sources and enabled precise control of nucleation and growth. As reported by the group of Jonathan Owen, these precursors release metal-chalcogen monomers, which serve as building blocks for nanocrystals, at tunable rates, allowing control over the number of nuclei formed and thus the final size of the nanocrystals. Unlike traditional methods that stop the reaction early to control size, often at the expense of yield, this approach allows the reaction to proceed to full completion, producing nanocrystals with uniform size, well-defined composition, and high efficiency. Furthermore, by adjusting the reactivity of the precursors, the method can be tailored to work with different metal sources, enabling the synthesis of a wide range of metal sulfide and selenide nanocrystals.

Large-scale synthesis of air-stable N,N'-disubstituted and N,N,N'-trisubstituted thioureas can be efficiently achieved in a single-step reaction, in most cases performed in a room temperature. This process involves the direct coupling of readily available substituted isothiocyanates with primary or secondary amines, resulting in high reaction efficiency.[22] Detailed protocols can be found in the Appendix (Section 3.1.1).

Small CdS/CdSe/CdS quantum wells were synthesized using a sequential injection strategy under an inert argon atmosphere, inside a glovebox. For the initial CdS/CdSe formation, a solution of cadmium oleate (0.244 g, 0.36 mmol), oleic acid (0.204 g, 0.72 mmol), and hexadecane (28.46 mL, 22 g) was loaded into a 100 mL three-neck round-bottom flask equipped with a magnetic stir bar, connected to the Schlenk line under Argon and heated to 240 °C (Figure 3.18, panel A). In parallel, a chalcogen precursor mixture was prepared by dissolving N-hexyl-N'-dodecyl thiourea (0.0496 g, 0.15 mmol) and 1,3-diethy imidazolidine selone (0.0308 g, 0.15 mmol) in tetraglyme (0.8 g, 0.848 mL). The chalcogen precursor solution was swiftly injected into the hot cadmium mixture, and the reaction was maintained at 240 °C for 60 minutes (Figure 3.18, panel B). The reaction of this fast-converting thiourea (conversion rate constant k_{conv} = 0.03 s^{-1})[22] and slower-converting selenourea (k_{conv} = 0.001 s^{-1})[23] with cadmium

oleate at 240 °C leads to the formation of CdS/CdSe core/shell nanocrystal products. If the selenourea conversion rate were higher than that of thiourea under these conditions, the reaction sequence would be reversed, resulting in the formation of CdSe/CdS core/shell nanocrystals.

To grow the outer CdS shell, a second precursor mixture was prepared by combining cadmium oleate (0.3579 g, 0.53 mmol), N,N,N'N'-tetramethyl thiourea (k_{conv} = 0.0004 s^{-1})[22] (0.0701 g, 0.53 mmol), octadecene (0.5 g, 0.634 mL), and tetraglyme (1 g, 1.06 mL), which was gently heated to yield a homogeneous solution. This mixture was injected dropwise into the reaction over 2h using a syringe pump (at rate 8 mL per hour). Thirty minutes after the final addition of CdS shell precursors, heating was discontinued, and the reaction mixture was allowed to cool to the room temperature (Figure 3.18, panel C). Once cooled down, the nanocrystals were precipitated by the addition of acetone and isolated by centrifugation (8000 rpm, 10 min). The resulting pellet was redispersed in hexane. Further purification was necessary to reduce the concentration of free, unreacted cadmium oleate in the solution. The reaction mixture was first precipitated by the addition of methyl acetate and collected by centrifugation (wash #1). The resulting solid was redissolved in a minimal volume of hexane, followed by the addition of five volumes of methyl acetate to induce precipitation. This redissolution-precipitation cycle was repeated twice more (wash #2 and #3), with centrifugation and decanting after each step.

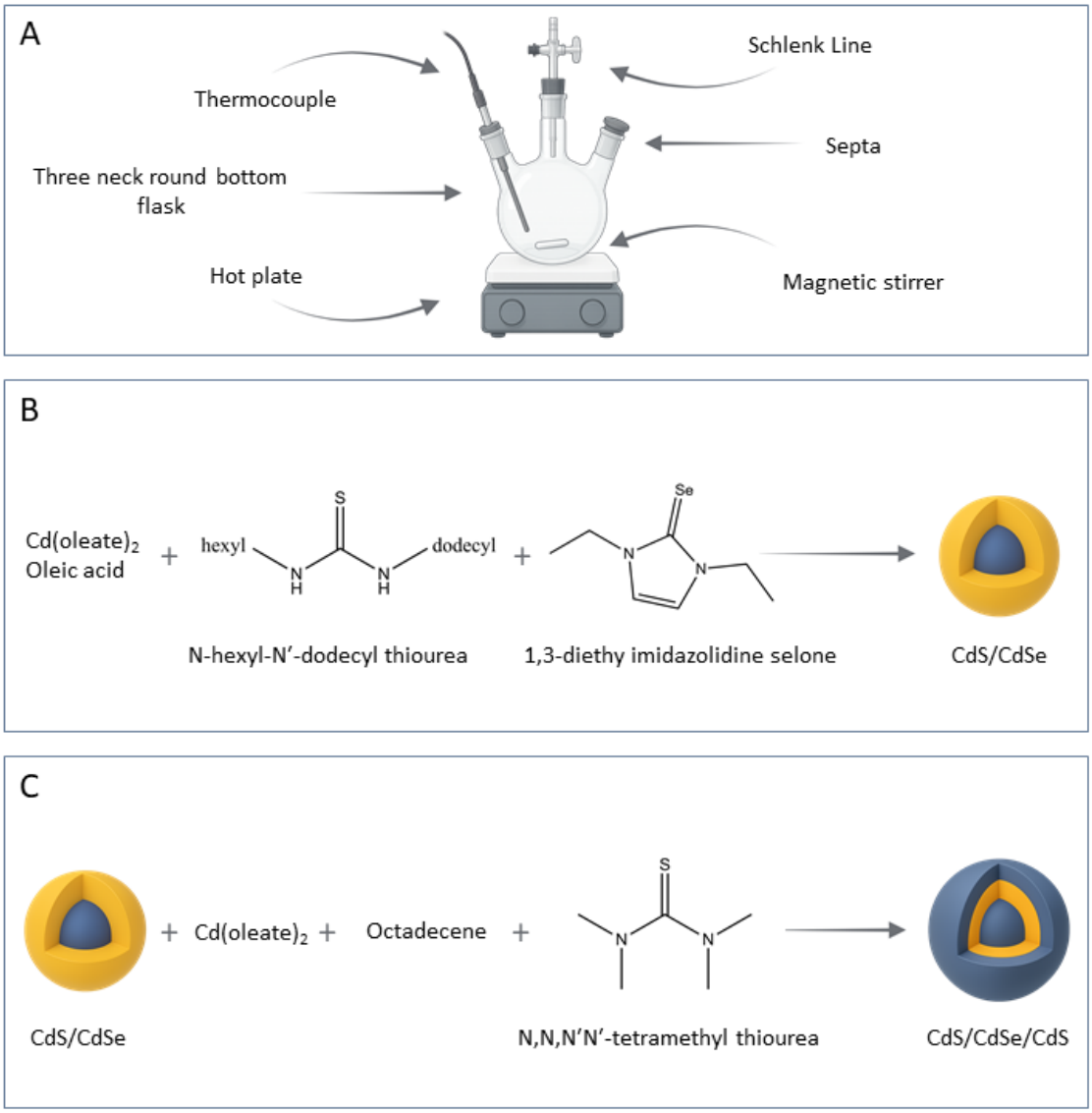

Figure 3.18 (A) Diagram of the experimental setup used for CdS/CdSe/CdS quantum well synthesis. The reaction was conducted in a 100 mL three-neck round-bottom flask equipped with a magnetic stir bar and connected to a Schlenk line under an argon atmosphere. The flask was heated using a heating mantle, and the internal temperature was monitored with a thermocouple submerged in the reaction mixture. (B) Schematic of the CdS/CdSe core/shell synthesis. A hot solution of cadmium oleate, oleic acid, and hexadecane was swiftly injected with a tetraglyme-based precursor containing N-hexyl-N'-dodecyl thiourea and 1,3-diethy imidazolidine selone. The differing conversion rates of sulfur and selenium sources drive the sequential formation of the CdS core and CdSe shell. (C) Final growth of the outer CdS shell. A cadmium oleate, N,N,N',N'-tetramethyl thiourea, octadecene, and tetraglyme mixture was slowly added over 2 hours using a syringe pump, completing the formation of the CdS/CdSe/CdS core/well/shell nanocrystal structure.

We carried out structural and optical characterizations on the synthesized nanomaterials. Transmission electron microscopy (TEM) imaging confirmed the formation of monodisperse, spherical nanoparticles with uniform size (Figure 3.19 B). Statistical analysis of approximately 300 particles diameters from TEM images revealed a narrow size distribution centered at 3.2 ± 0.4 nm (Figure 3.19 E), indicating uniformity, crucial for reproducible optical performance

in biological contexts. Under UV illumination, the SQWs displayed intense green fluorescence (Figure 3.19 C), indicative of efficient radiative recombination, thus underscoring their potential as bright, stable bioimaging probes. Time-resolved photoluminescence (PL) data, analyzed using a biexponential decay model, yielded two distinct lifetimes: a longer-lived state with $\tau_1 = 44.0 \pm 2.10$ ns and a shorter-lived state with $\tau_2 = 13.0 \pm 0.79$ ns (Figure 3.19 D). These lifetimes suggest recombination dynamics involving both excitonic states and surface/interface traps. Optical absorption and PL emission spectra (Figure 3.19 F) further confirmed the high optical quality of the SQWs, with the first excitonic absorption peak observed at 490 nm and a PL emission maximum at 520 nm, yielding a favorable Stokes shift (~30 nm) which minimizes reabsorption, thereby enhancing fluorescence detection sensitivity for neuronal imaging applications. Collectively, these results confirm that the synthesized CdS/CdSe/CdS SQWs possess the structural integrity, size uniformity, and optical properties required for their deployment as voltage-sensitive optical probes.

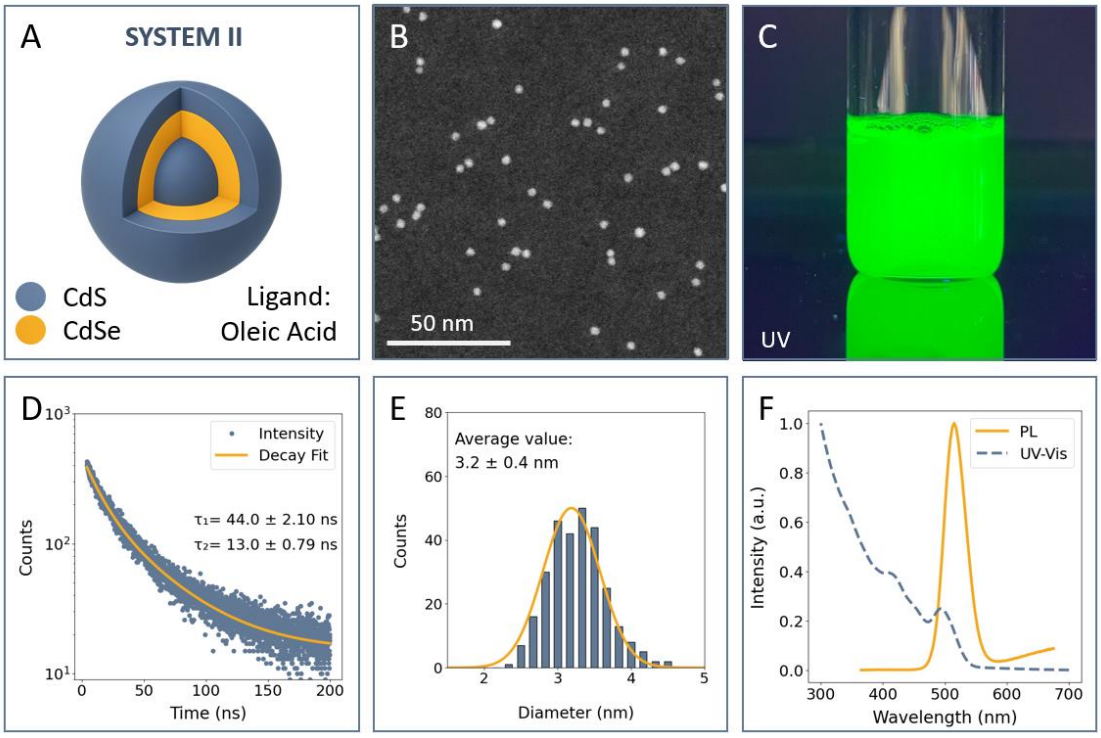

Figure 3.19 Structural and optical characterization of CdS/CdSe/CdS spherical quantum wells (SQWs). (A) Schematic representation of the multilayer core/well/shell architecture comprising a CdSe well (yellow) surrounded by inner and outer CdS layers (blue). (B) TEM image showing monodisperse SQWs. (C) Fluorescence of SQWs under UV illumination, indicating strong visible light emission (bright green color). (D) Time-resolved photoluminescence (PL) decay of Cd-oleate-functionalized SQWs fitted with a biexponential model, yielding lifetimes of $\tau_1 = 44.0 \pm 2.10$ ns and $\tau_2 = 13.0 \pm 0.79$ ns. (E) Size distribution histogram derived from TEM image analysis, showing an average particle diameter of 3.2 ± 0.4 nm. (F) UV-Vis absorption and PL emission spectra of SQWs, with the first excitonic absorption peak at 490 nm and an emission maximum at 520 nm.

To assess the potential of spherical quantum wells (SQWs) as voltage-sensitive probes for neuronal applications, their excitonic behavior under externally applied electric fields was systematically investigated. Photoluminescence (PL) spectra measured across a range of electric fields (0-1800 kV/cm) revealed pronounced spectral redshifts, peak broadening, and fluorescence quenching in SQWs – indicative of increased sensitivity to the applied electric field. In contrast, core/shell nanocrystals exhibited more modest changes. Quantitative analysis of the Stark shift and relative fluorescence change (ΔF/F), attributed in part to field-enhanced Auger recombination, further confirmed that SQWs display significantly stronger spectral modulation than core/shell counterparts (Figure 3.20 A and B).

To elucidate the origin of this enhanced sensitivity, tight-binding simulations were conducted to model the excitonic responses of both nanostructure types under electric field perturbation (Figure 3.20). Spatial maps of the calculated excited-state wavefunctions revealed a substantial field-induced separation of electron and hole densities in SQWs, consistent with a strong quantum-confined Stark effect (QCSE). In contrast, the wavefunctions in core/shell structures remained largely co-localized under identical conditions, explaining their weaker experimental response. Together, these experimental and theoretical results support the superior suitability of SQWs for detecting membrane potential changes with high sensitivity.

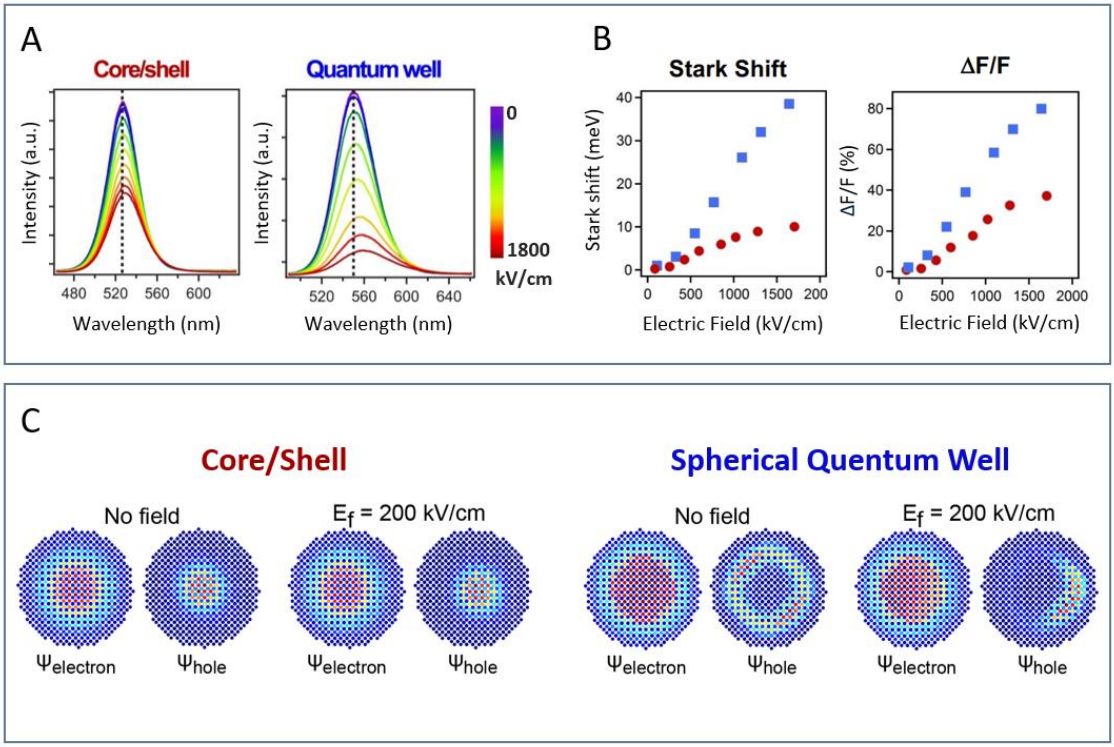

Figure 3.20 Comparison of electric field responses in CdSe/CdS core/shell and CdS/CdSe/CdS spherical quantum well nanocrystals. (A) Experimentally measured photoluminescence (PL) spectra of core/shell (left) and spherical quantum well (right) nanocrystals under increasing applied electric field strengths (0-1800 kV/cm). Both systems exhibit spectral shifts, broadening, and PL quenching with increasing field, with more pronounced effects in the quantum well structures. (B) Experimental quantification of the quantum-confined Stark effect (QCSE), showing Stark shift (left) and relative fluorescence change (ΔF/F, right) as functions of electric field. The spherical quantum well (blue squares) exhibits significantly greater sensitivity to the applied field compared to the core/shell structure (red dots). (C) Tight-binding calculations of the excited-state wavefunctions (electron and hole probability densities) in core/shell (left) and spherical quantum well (right) nanocrystals, shown under zero field and an applied field of 200 kV/cm. Under bias, the spherical quantum well structure displays stronger electron-hole separation, consistent with its enhanced QCSE response observed experimentally. These results support the selection of spherical quantum wells as optimal architectures for membrane potential sensing. Data provided by Prof. Jonathan Owen and Ilan Jen La Plante (unpublished, used with permission).

Complementing these results, another experimental study explored how variations in the outer CdS shell thickness influenced electric-field-dependent PL modulation in SQWs (Figure 3.21). SQWs featuring thinner CdS shells showed distinct PL redshifts and progressively increasing ΔF/F values under applied voltages of 0-8 V (Figure 3.21). Conversely, SQWs with thicker CdS shells demonstrated even more pronounced fluorescence modulation and energy shifts at higher fields (up to ~800 kV/cm), when exposed to external biases ranging from 0-10 V (Figure 3.21). These observations emphasize a clear relationship between shell thickness and electric-field-induced PL modulation magnitude, likely resulting from increased spatial separation of charge carriers and improved dielectric confinement provided by thicker shells. The results presented

in the figures (Figure 3.20 and Figure 3.21) were provided by Prof. Jonathan Owen and Ilan Jen La Plante and are included in this dissertation with their permission.

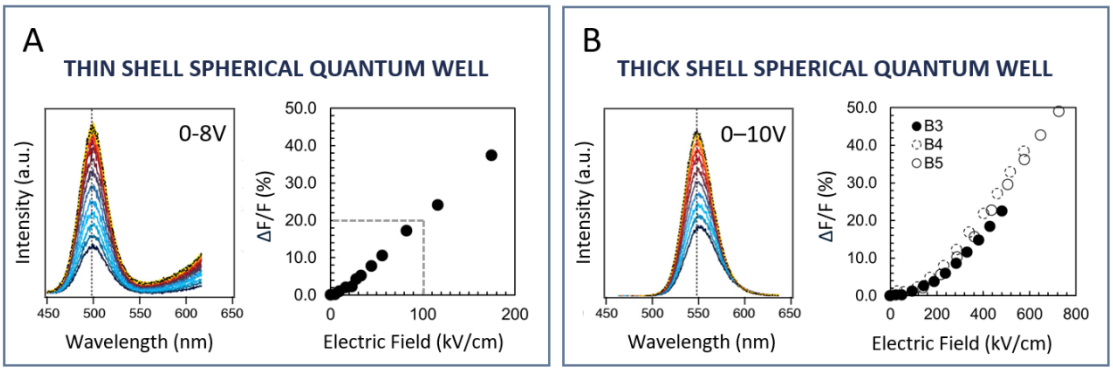

Figure 3.21 Electric field-dependent photoluminescence in CdS/CdSe/CdS spherical quantum well nanocrystals with varying shell thickness. (A) Photoluminescence spectra (left) and corresponding field-dependent fluorescence modulation (ΔF/F, right) for nanocrystals with a thin CdS shell under external bias of 0-8 V. ΔF/F values are plotted as a function of electric field strength across the quantum dot film. (B) Equivalent measurements for nanocrystals with a thick CdS shell under an external bias of 0-10 V. The ΔF/F data also reflect emission energy shifts under increasing field strength. Dashed lines in the spectra guide the eye to the zero-field peak position, illustrating field-induced spectral modulation and intensity changes. Data provided by Prof. Jonathan Owen and Ilan Jen La Plante (unpublished, used with permission).

It is worth noting that effective integration of CdS/CdSe/CdS SQWs into neuronal lipid bilayers necessitates nanocrystal dimensions smaller than the membrane thickness, requiring the synthesis of SQWs with thinner shells. Although reducing shell thickness typically decreases quantum yield and photostability, it is particularly advantageous that these thinner-shell nanocrystals exhibit enhanced sensitivity to externally applied electric fields, thus representing a significant advantage for neuronal voltage-sensing applications.

1.3. Surface Chemistry on CdS/CdSe/CdS Nanocrystals

Ligand exchange to $Zn(oleate)_2$

Cd-oleate-stabilized SQWs (0.100 µmol) were dried under vacuum and redispersed in octadecene (10 mL) in a 50 mL three-neck round-bottom flask equipped with a magnetic stir bar and connected to a Schlenk line under an argon atmosphere. Zinc oleate (0.3141 g, 0.5 mmol) was added to the flask, and the reaction mixture was heated to 240 °C with continuous stirring. After maintaining the temperature for 60 minutes, the flask was removed from heat and allowed to cool to room temperature. The resulting nanocrystals were purified by sequential precipitation using a 5:1 v/v methyl acetate to toluene mixture.

Ligand exchange for Zn(2-hexyldecanoate)$_2$

Ligand exchange using Zn(2-hexyldecanoate)$_2$ was performed following the same procedure as described for Zn(oleate)$_2$, with the only modification being the substitution of zinc oleate with an equimolar amount of Zn(2-hexyldecanoate)$_2$. All other reaction conditions and purification steps remained unchanged.

Ligand exchange – fluorination

Cd-oleate-stabilized SQWs (0.100 µmol) were dried under vacuum and redispersed in octadecene (15 mL). Octylamine (0.0259 g, 0.0331 mL, 0.2 mmol) and benzoyl fluoride (0.0248 g, 0.0205 mL, 0.2 mmol) were added to the dispersion, and the reaction mixture was stirred at room temperature for 1 hour. The resulting nanocrystals were purified by precipitation with acetone and centrifugation.

Shelling with additional ZnS layer

To obtain CdS/CdSe/CdS/ZnS multilayer structure, Cd-oleate-stabilized CdS/CdSe/CdS SQWs were prepared as previously described, with the CdS shelling step modified to use half the reagent quantities and half the reaction time. Following CdS shell growth, a ZnS shelling solution was prepared by dissolving zinc oleate (0.3393 g, 0.357 mL, 0.54 mmol), 2-hexyldecanoic acid (0.1385 g, 0.1556 mL, 0.54 mmol), and N-hexyl-N',N'-dibutyl thiourea (0.1472 g, 0.54 mmol) in octadecene (14.2 g, 18.0 mL). This mixture was injected into the reaction via syringe pump over 2 hours at a rate of 9 mL/h. The resulting nanocrystals were purified by four sequential precipitations using a 5:1 v/v methyl acetate to toluene mixture.

2. Strategies for Water Transfer

In order for spherical quantum wells to be applicable in biological systems, their transition from organic solvents to water or water-based buffers is critical. After the synthesis, nanocrystals are typically stabilized with organic molecules (e.g., trioctylphosphine oxide, oleic acid), which makes them soluble in non-polar organic solvents such as hexane, toluene or chloroform and ensure colloidal stability. This hydrophobic surface chemistry also drives the initial association with the cell membrane: by the classic hydrophobic effect, alkyl chains on the QD surface minimize unfavorable water contacts by partitioning into the lipid bilayer's hydrophobic core.[24]

Bar et al. demonstrate on simplified supported lipid bilayers that negatively charged QDs first dock onto the membrane via electrostatic attraction and then penetrate at high-curvature or defect sites – where hydrophobic ligand chains insert into the lipid tails – supporting a two-step, defect-mediated mechanism for membrane embedding.[24]

Lipophilic-coated quantum dots inherently partition into the hydrophobic core of the membrane rather than staying in the surrounding aqueous phase. Yet, to enable efficient cellular delivery – and, ultimately, reliable voltage sensing – these nanoparticles must first feature colloidal stability in physiological media.

To transfer QDs into aqueous solution, several strategies have been reported in the literature. Ligand exchange replaces native hydrophobic ligands with hydrophilic ones (such as thiols or multidentate ligands).[25,26] This method is relatively straightforward but can disturb the QD surface and often results in significant loss of photoluminescence quantum yield (QY) and reduced colloidal stability. In contrast, encapsulation techniques preserve the original ligand shell by wrapping the hydrophobic QD with an amphiphilic coating. These include polymer or surfactant micelle encapsulation and coating with biomolecules like lipids or proteins. Encapsulation is generally more complex but tends to better retain the QDs' optical properties. For example, amphiphilic polymer coatings maintain the native hydrocarbon ligand environment, yielding water-dispersible QDs with minimal changes in absorption or emission spectra.[27,28] Similarly, protein-based coatings (e.g., embedding QDs in bovine serum albumin or polymer-protein hybrid shell) can confer water solubility while keeping the original ligand in place, preserving fluorescence and providing biological interfaces.[29–31] Each approach differs in complexity and effectiveness. Ligand exchange produces smaller hydrodynamic diameters but risks diminished photostability, whereas polymer or lipid encapsulation yields larger bioconjugates with excellent photophysical retention.

Among methods that maintain the native hydrophobic coating on QDs, two prominent strategies are encapsulation in octyl glucoside (OCG) micelles and lipid vesicles (liposomes). These approaches avoid direct chemical modification of the QD surface, thereby aiming to preserve the original ligand passivation and the QD's photophysical properties.

2.1. OCG Micelles

n-Octyl-β-D-glucoside (OCG) is a small non-ionic detergent with a hydrophobic octyl tail and a hydrophilic glucose head (Figure 3.7 A). It is widely used in membrane biochemistry due to its ability to gently solubilize lipid bilayers while maintaining the structural and functional integrity of membrane-associated proteins. OCG is particularly effective for isolating functional membrane proteins, as it disrupts the membrane environment without denaturation and can be readily removed through dialysis or dilution.[32] Additionally, OCG is employed to induce controlled transitions between lipid vesicles and micelles by modulating its concentration near the critical micelle concentration.[33,34] This property is valuable for studying membrane curvature, lipid packing, and the energetics of bilayer assembly.[32] In supported lipid bilayer systems, OCG facilitates the precise solubilization and reformation of membranes on solid substrates, which is essential for techniques such as atomic force microscopy and other surface-based analyses.

Although the encapsulation of quantum dots within OG micelles has not been previously reported, a related study by Rasch et al. demonstrated the successful aqueous phase transfer of small gold nanoparticles using OCG molecules, resulting in the formation of nanoparticle-vesicle hybrid structures.[35] Since previous studies have shown that TOPO-capped CdSe quantum dots can be effectively transferred to aqueous media through encapsulation with surfactants forming micellar structures,[36] and given the widespread use of OCG in membrane biochemistry, we aimed to investigate its potential for membrane staining. OCG's ability to solubilize hydrophobic environments while preserving molecular integrity, along with its established role in modulating vesicle-micelle transitions, makes it a strong candidate for encapsulating hydrophobic quantum dots without altering their native surface chemistry. In this study, we evaluate the use of OCG micelles for aqueous phase transfer of QDs and assess their utility for trans-membrane delivery in biological systems.

Encapsulation protocol

Data shown in this subchapter, for SQWs encapsulated within OCG micelles, are based on the sample described in a previous section (Figure 3.19).

Prior to conducting any experiments, it was essential to determine the concentration of spherical quantum dots in solution. This was accomplished using the Beer-Lambert law, expressed as $A = \varepsilon c l$, where A is the absorbance, ε is the molar extinction coefficient, c is the concentration, and l is the optical path length. In our calculations, we utilized the absorbance value at a wavelength of 350 nm and assumed an extinction coefficient of 1.7, which aligns with reported values for CdSe quantum dots of comparable size and optical properties.[37]

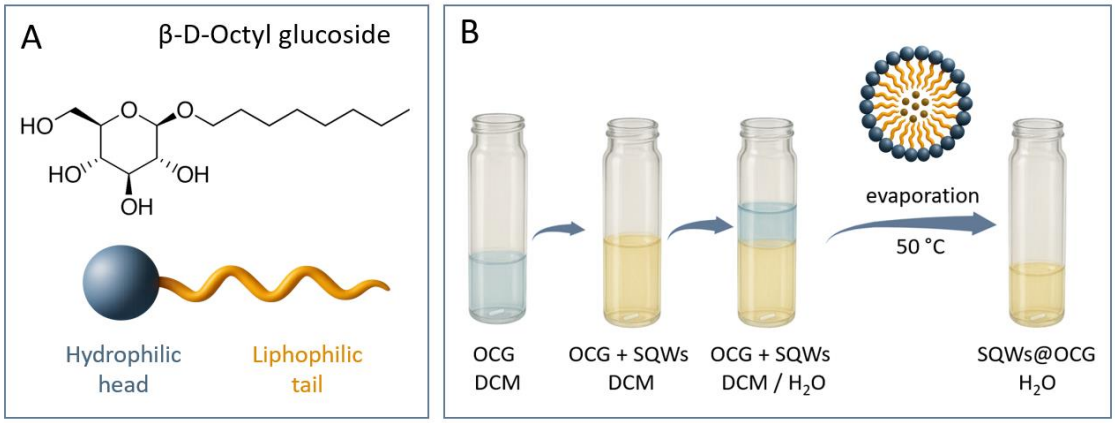

Figure 3.22 Encapsulation of CdS/CdSe/CdS spherical quantum wells (SQWs) using the amphiphilic surfactant β-D-octyl glucoside (OCG). (A) Chemical structure and schematic representation of OCG, highlighting its amphiphilic nature with a hydrophilic glucose head (blue) and a lipophilic alkyl tail (yellow). (B) Schematic illustration of the SQW encapsulation process. Hydrophobic SQWs are phase-transferred from dichloromethane (DCM) to water via OCG-assisted encapsulation, forming stable SQWs@OCG micelles upon DCM evaporation at 50 °C.

To optimize the protocol, several key parameters were systematically investigated and adjusted. These included the choice of organic solvent, the water-to-solvent ratio, the OCG-to-SQW ratio, stirring speed and temperature. Multiple phase transfer strategies were evaluated, with the scheme presented above in Figure 3.22 representing the most reproducible method identified during the study. The following section focuses on the influence of OCG concentration on the quality of the micelles obtained.

In a 4 mL glass vial equipped with a magnetic stirrer, 500 µL of OCG solution in dichloromethane (DCM) at the desired concentration was mixed with 100 µL of SQWs redispersed in DCM (0.06 µM). The mixture was stirred at room temperature for at least 5 minutes. Subsequently, 250 µL of water was added under vigorous stirring, and the system was stirred for an additional 5 minutes at room temperature. The solution was then heated to 50 °C until the DCM had fully

evaporated. Finally, an additional 250 µL of water was introduced, and the resulting dispersion was subjected to further optical characterization.

Characterization

The concentration of β-D-octyl glucoside (OCG) used during encapsulation had a pronounced effect on the physical and optical quality of the resulting SQW formulations. Above its critical micelle concentration (CMC, ~20-25 mM), OCG molecules spontaneously assemble into micelles in aqueous media. When hydrophobic SQWs are introduced into an aqueous OCG solution, the alkyl chains of OCG interact with the hydrophobic ligand shell of the SQWs via the hydrophobic effect, while the sugar headgroups orient toward the surrounding water, resulting in the formation of a micellar colloid. The encapsulation process can be carried out under mild conditions, involving moderate stirring and gentle heating, which makes it straightforward to implement while minimizing the risk of altering the nanocrystal surface chemistry. As shown in Figure 3.23, samples prepared with 25 mM (sample 1), 50 mM (sample 2), and 100 mM (sample 3) OCG display progressively greater turbidity and light scattering, particularly at the highest concentration. Dynamic light scattering (DLS) measurements support this observation: sample 1 exhibits small micelles with a hydrodynamic diameter of 35.2 ± 7.5 nm and a low polydispersity index, indicating uniform size. In contrast, higher OCG concentrations yield much larger and more polydisperse aggregates, with hydrodynamic diameters of 260.8 ± 126.0 nm and 347.2 ± 146.4 nm for the samples 2 and 3, respectively (Figure 3.23 B).

Photophysical characterization confirmed that micellization preserves the optical properties of the SQWs. The corresponding UV-Vis spectra of sample 1 shows pronounced scattering, while lower-concentration samples show minimal deviation from baseline, suggesting the presence of well-dispersed micelles or particles smaller than 100 nm (Figure 3.23 C). Emission spectra reveal a concentration-dependent blue shift in photoluminescence maximum from 529 nm (sample 1, 25 mM) to 526 nm (sample 2, 50 mM) and 523 nm (sample 3, 100 mM) (Figure 3.23 D). All micellar samples are therefore slightly red shifted relative to the same SQWs dispersed in toluene (520 nm, Figure 3.19).

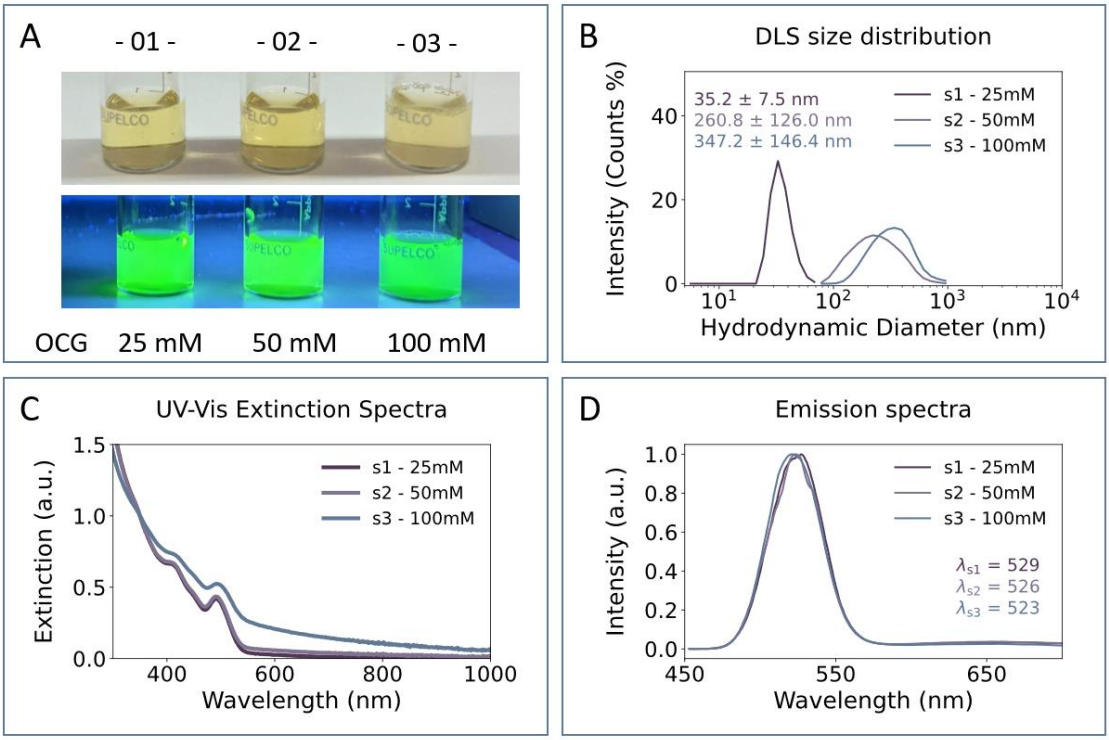

Figure 3.23 Visual appearance and optical characterization of spherical quantum wells (SQWs) encapsulated with increasing concentrations of β-D-octyl glucoside (OCG). (A) Photographs of samples containing 25 mM, 50 mM, and 100 mM OCG under ambient white light (top) and UV illumination (bottom). Samples with 25 mM and 50 mM OCG (samples 1 and 2) are optically clear with a slight yellow tint, while the 100 mM sample (sample 3) appears increasingly turbid due to light scattering. (B) Dynamic light scattering (DLS) analysis shows hydrodynamic diameters of 35.2 ± 7.5 nm, 260.8 ± 126.0 nm, and 347.2 ± 146.4 nm for the 25 mM, 50 mM, and 100 mM samples, respectively. (C) UV-Vis extinction spectra exhibit a concentration-dependent increase in baseline intensity, consistent with enhanced scattering in the 100 mM sample. (D) Emission spectra of the same samples display a blue shift in the photoluminescence maximum with increasing OCG concentration.

Despite the differences in the absorption spectra of sample 1 and sample 3, their photoluminescence lifetimes are notably similar (Figure 3.24). Both samples exhibit a bi-exponential decay profile, with components of 44.0 ± 1.0 ns and 6.0 ± 0.22 ns for sample 1, and 43.0 ± 1.1 ns and 9.1 ± 0.31 ns for sample 3. These correspond to average fluorescence lifetimes of 18.09 ns and 23.69 ns, respectively. Compared to SQWs dispersed in toluene (τ_1 = 44.0 ± 2.1 ns, τ_2 = 13.0 ± 0.79 ns), both encapsulated samples exhibit a shortened average lifetimes, more pronounced at the lowest OCG concentration. Interestingly, the sample with the lowest OCG concentration and smallest hydrodynamic diameter displays the shortest fluorescence lifetime. In smaller micelles, a higher surface-to-volume ratio places a greater fraction of SQWs near the micelle-water interface, increasing exposure to OCG headgroups and the aqueous phase. This proximity may enhance surface- or trap-mediated nonradiative relaxation, affecting the faster τ_2 component while leaving the long-lived component largely unchanged. This is a possible contributing factor, alongside other micellization-related effects

such as changes in local dielectric environment, interfacial strain, or surface ligand rearrangement.

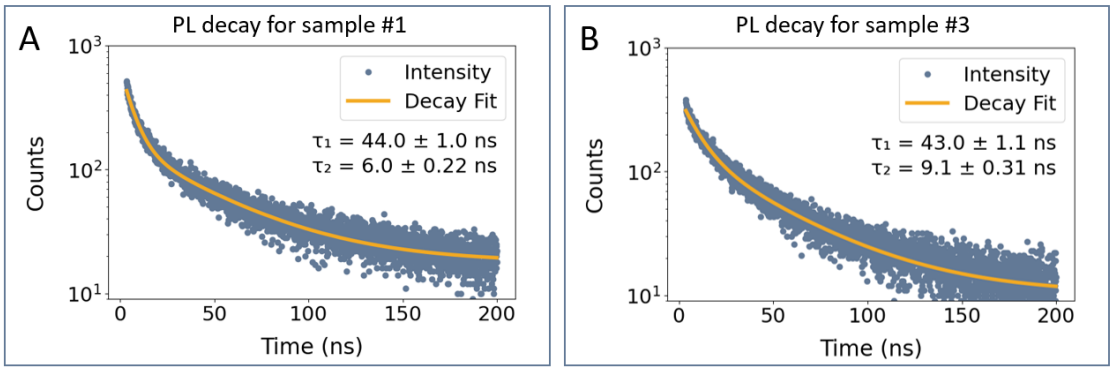

Figure 3.24. Photoluminescence lifetime analysis of encapsulated CdS/CdSe/CdS SQWs. (A) PL decay curve for sample 1, fitted with a biexponential model yielding lifetimes of τ_1 = 44.0 ± 1.0 ns and τ_2 = 6.0 ± 0.22 ns, corresponding to an average lifetime of 18.4 ns. (B) PL decay of sample 3, showing τ_1 = 43.0 ± 1.1 ns and τ_2 = 9.1 ± 0.31 ns, resulting in a longer average lifetime of 23.4 ns. The increased τ_2 component in sample 3 suggests improved passivation or altered surface dynamics.

Transmission electron microscopy analysis of the CdS/CdSe/CdS SQWs encapsulated in OCG micelles reveals that the micelles exhibit a spherical morphology with diameters ranging from approximately 20 to 100 nm (Figure 3.25 A). Higher-magnification imaging confirms that each micelle contains multiple SQWs densely packed within the micellar core (Figure 3.25 B). Statistical analysis of 250 micelles yields an average diameter of 44.3 ± 11.6 nm (Figure 3.25 C), which is larger than the average hydrodynamic diameter of 35.2 ± 7.5 nm determined by dynamic light scattering (Figure 3.23). The shift in distribution maximum between TEM and DLS measurements may result from population mismatch due to sample polydispersity or from drying-induced deformation of soft micelles during grid preparation.

Overall, the OCG micelle encapsulation method is an effective strategy for preserving the photophysical properties of nanocrystals during phase transfer, providing a rapid and practical route to obtain water-dispersible QDs while maintaining the original spectral features.

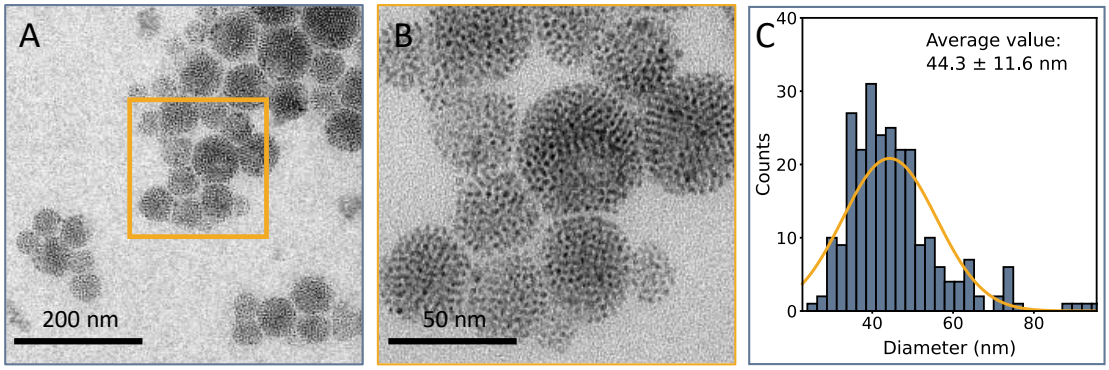

Figure 3.25 TEM analysis of CdS/CdSe/CdS spherical quantum wells encapsulated within OCG micelles. (A) Low-magnification TEM image showing SQWs encapsulated within micelles, with overall micelle sizes ranging from 20 to 100 nm. (B) Higher magnification image of the selected area in (A) reveals that individual micelles enclose multiple SQWs. (C) Histogram of micelle size distribution obtained from the analysis of 250 micelles based on TEM images. The average micelle diameter is 44.3 ± 11.6 nm.

2.2. Lipid Vesicles

Another widely employed strategy for transferring hydrophobic nanomaterials into aqueous environments involves their encapsulation within lipid bilayer vesicles, commonly referred to as liposomes. This method enables the transport of lipophilic, ligand-coated nanoparticles through water-based media while preserving their native surface chemistry.

Liposome formation reflects a general organizational principle observed in biological systems, where amphiphilic molecules spontaneously arrange into bilayer structures to form cell membranes, transport vesicles, and compartmentalized reaction spaces. Amphiphilic lipids contain polar headgroups and non-polar tails, and their assembly is driven primarily by the hydrophobic effect, supported by van der Waals forces, electrostatic interactions, and hydrogen bonding. Although each of these non-covalent interactions is individually weak, their combined effect yields stable bilayer membranes. Kinetic factors, such as mixing rate, can influence the assembly pathway, potentially leading to structural variations in membrane thickness or vesicle morphology.

Owing to their architecture and composition, liposomes can encapsulate both hydrophilic species in the aqueous core and hydrophobic species in the bilayer. These properties have enabled their widespread use as model systems for studying membrane-associated phenomena and as carriers for a broad range of substances, including therapeutic drugs and nanomaterials.[38,39] Encapsulation within liposomes can reduce nanoparticle cytotoxicity and improve stability, facilitating biomedical applications. [38,40] Examples include gold nanoparticles for stimuli-responsive release, [41] silver nanoparticles for antimicrobial treatments,[42,43] zinc

oxide[44,45] and cerium oxide[46] nanoparticles for cancer therapy, titanium dioxide nanotubes for sustained drug delivery, and superparamagnetic iron oxide nanoparticles in magnetoliposomes for hyperthermia, targeted chemotherapy, and magnetic resonance imaging (MRI).[47–50] Liposomes have also been used to encapsulate semiconductor quantum dots for bioimaging,[51,52] and hybrid systems combining liposomes with silica, polymers, or graphene-based materials have been developed to enhance encapsulation efficiency and enable stimuli-responsive release.[53,54]

Typically, the nanoparticles are co-dissolved with phospholipids in an organic solvent; after solvent evaporation and hydration, the lipids spontaneously self-assemble into bilayer vesicles, with the hydrophobic nanocrystals becoming embedded within the nonpolar region of the membrane.

We conducted a series of experiments to optimize the synthesis of phospholipid vesicles incorporating quantum dots within their lipid bilayers. The phospholipids used were selected based on their structural and functional properties, which support both stable vesicle formation and the potential for membrane fusion – an aspect relevant to our envisioned biomedical applications. A detailed justification for the lipid composition is provided in Section 3.2, *Fusosomes – Fusogenic Lipid Vesicles* (page 127). However, it is worth noting here that the molecular characteristics of these lipids were chosen to enhance the interaction of the vesicles with biological membranes, which is central to the aim of this study.

Preparation of lipid vesicles

Vesicles can be classified as unilamellar, bilamellar, or multilamellar based on the number of lipid bilayers they contain. Phospholipids, depending on their molecular size and three-dimensional arrangement, commonly form either small unilamellar vesicles or giant unilamellar vesicles.[55] To meet the central objectives of the present work, the goal was to produce small, unilamellar vesicles with minimal size variability.

The lipid composition used in these experiments was adapted from the work of G. Gopalkrishnan et al.[56] A lipid solution was prepared in chloroform at a total concentration of 1 mM, comprising 5% of the cationic lipid DOTAP, 0.5% DPPE-PEG2000, and 74.5% DMPC (see molecular structures in Figure 3.26 A) , and was mixed with 3×10^{-7} mmol of quantum dots. Once the mixture was thoroughly homogenized, the solvent was evaporated under a stream of nitrogen, and the resulting lipid film was further dried under vacuum for 2 hours. Following dehydration, 1 mL of PBS buffer was added to the vial, and the solution was vortexed to

redisperse the quantum dots. A magnetic stirrer was introduced to ensure thorough mixing. To facilitate complete dispersion, the vial was intermittently vortexed and briefly immersed in a hot water bath.

After obtaining a homogeneous mixture of lipids and quantum dots in PBS, a freeze-thaw cycle was performed by alternately placing the sample vial in a liquid nitrogen bath (~-200 °C) and a water bath maintained at 50 °C (Figure 3.26 B). This technique is closely tied to the lipids' phase transition temperature, often referred to as the melting temperature (T_m) – the point at which lipid molecules shift from a solid-like gel phase to a fluid-like liquid crystalline state. This transition plays a critical role in liposome preparation, as it influences membrane stability and permeability. Below the T_m, lipid bilayers are tightly packed with restricted molecular mobility; above the T_m, they become more fluid, allowing lateral diffusion of lipid molecules within the membrane. Repeated freeze-thaw cycles, commonly employed to transform multilamellar vesicles into unilamellar ones, leverage this phase behavior. During freezing, ice crystal formation disrupts the bilayers, breaking larger vesicles into smaller fragments; upon thawing, these fragments reassemble into unilamellar structures. The efficiency of this process depends on several factors, including lipid composition, ionic strength of the buffer, and the T_m, which is especially critical during the thawing phase when membrane fluidity is required for vesicle fusion. Properly optimizing these parameters leads to more uniform and stable vesicle populations, thereby improving the reliability and reproducibility of vesicle-based systems.[57,58]

DOTAP exhibits a transition temperature below 5 °C, DMPC has a well-characterized transition temperature of approximately 24 °C, and DSPE undergoes a phase transition at around 74 °C; while PEGylation may slightly alter this value, it is expected to remain relatively high.[59] All values are taken from data provided by Avanti Polar Lipids (https://avantiresearch.com/). To calculate the transition temperature of a mixed phospholipid system, we can use a weighted average approach based on the composition and individual transition temperatures of the lipids.

$$T_m(\text{mixture}) = (5\ °C \times 0.05) + (74\ °C \times 0.005) + (24°C \times 0.745) = 18.5\ °C \quad (3.1)$$

Therefore, the estimated transition temperature of the mixed phospholipid system is approximately 18.5 °C. It is important to note that this is a simplified calculation and the actual transition behavior of mixed lipid systems can be more complex. Factors such as lipid-lipid interactions, domain formation, and the presence of PEGylated lipids can affect the overall phase behavior. More accurate determinations would require experimental measurements using techniques such as differential scanning calorimetry (DSC) or nanoplasmonic sensing (NPS) as described in the literature.[57,60]

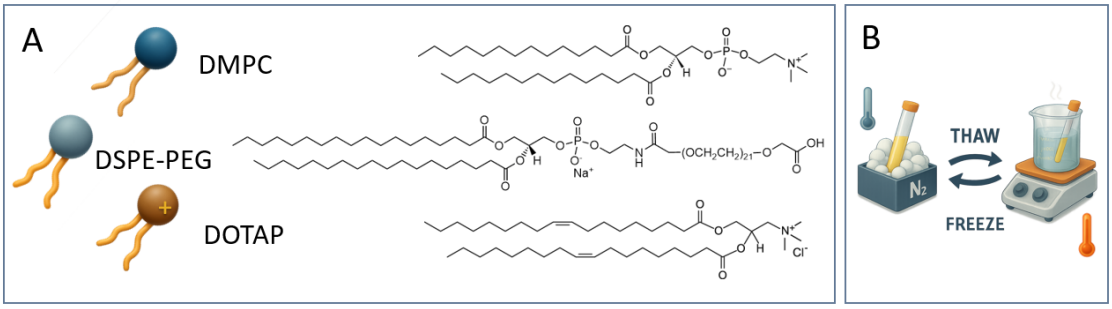

Figure 3.26 (A) Chemical structures and schematic representations of the lipid components used to prepare the lipid solution: 74.5% DMPC, 5% cationic lipid DOTAP, and 0.5% DSPE-PEG2000, yielding a total lipid concentration of 1 mM in PBS. (B) Schematic of the freeze-thaw procedure used to treat the lipid-quantum dot mixture. This method exploits the lipid phase transition temperature (T_m) to promote the transformation of multilamellar vesicles into unilamellar ones. Repeated freezing (in liquid nitrogen) and thawing (in a water bath at 50 °C) disrupt and reassemble the lipid bilayers, enhancing vesicle uniformity and stability.

Following established protocols, 10 freeze-thaw cycles were performed. The solution was transferred into 15 mL plastic tubes and sealed. Each cycle involved heating the tubes in a 50 °C water bath for 3 minutes to reach the lipid transition temperature, followed by freezing in liquid nitrogen for one minute. It is important to note that temperature and timing parameters may require adjustment depending on the specific lipid composition, solution volume, and experimental conditions.

After completing the freeze-thaw cycles, the lipid-quantum dot suspension was processed using a mini-extruder (Avanti Polar Lipids, USA), as illustrated in Figure 3.27. This device enables the production of unilamellar vesicles through sequential membrane extrusion. The extruder assembly consists of a stainless-steel outer casing, two internal membrane supports with O-rings, polycarbonate membranes of defined pore size, and porous filter supports that stabilize the membrane during extrusion. A retainer nut secures the internal components, while two gas-tight syringes are used to manually transfer the lipid suspension back and forth through the membrane. To ensure uniform thermal conditions, the entire assembly (including the syringes) was placed in a stabilizer block heated to 70 °C on a hot plate, maintaining the lipid mixture above its phase transition temperature (T_m) throughout the process. To minimize sample loss and facilitate a controlled reduction in vesicle size to the target diameter of 100 nm, the solution was extruded sequentially through polycarbonate membranes with pore sizes of 1000 nm (Extrusion I), 800 nm (Extrusion II), 400 nm (Extrusion III), and finally 100 nm (Extrusion IV). At each step, the sample was passed through the membrane ten times. This approach, combined with temperature control, supports the formation of stable, unilamellar vesicles suitable for later stages of the experimental workflow. Each batch of vesicles was characterized by

fluorescence microscopy and dynamic light scattering (DLS) before being used in further experiments.

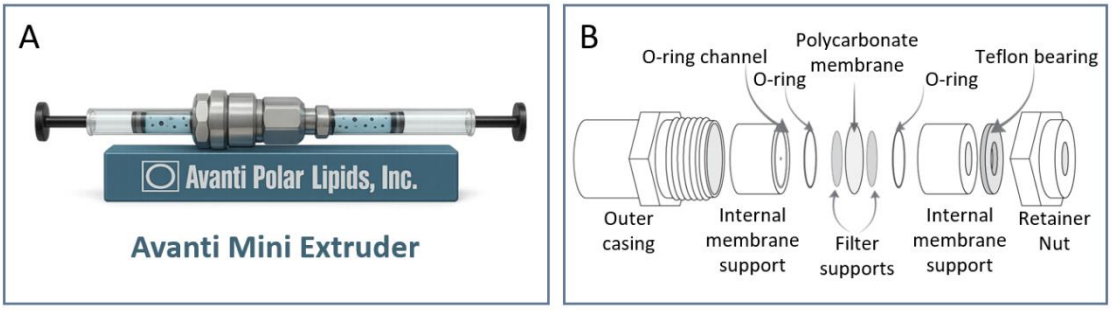

Figure 3.27 (A) Illustration of the Avanti Mini-Extruder system used for the preparation of unilamellar vesicles. (B) Detailed schematic of the mini-extruder extrusion chamber assembly, illustrating the main components: stainless steel outer casing, internal membrane supports with O-rings, polycarbonate membranes, porous filter supports, and Teflon bearing secured by a retainer nut. During extrusion, a lipid suspension is passed repeatedly between two gas-tight syringes through polycarbonate membranes of decreasing pore sizes. This configuration, combined with controlled heating, enables the consistent formation of size-homogeneous unilamellar vesicles suitable for downstream processing and functional characterization.

Characterization of lipid vesicles

During the preparation of the lipid vesicle solution, distinct visual changes were observed at various stages, as shown in Figure 3.28. Immediately after adding PBS to the dried lipid film (Stage 1, Figure 3.28 A), the solution appeared turbid, indicating incomplete dispersion of the lipids. After two minutes of vortexing (Stage 2, Figure 3.28 B), the solution began to clarify; however, bright fluorescent clumps were still present, suggesting partial clusters of lipids and quantum dots are still present in the mixture. With continued stirring (Stage 3, Figure 3.28 C),

the solution became fully homogeneous and uniformly fluorescent, indicating dispersion of the quantum dots.

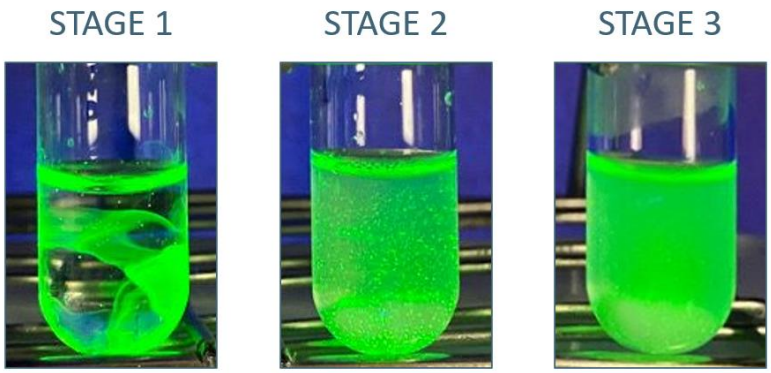

Figure 3.28 Visualization of lipid vesicle dispersion in PBS at three distinct stages. (A) Stage 1: Shortly after PBS is added, the lipid film remains mostly undispersed. (B) Stage 2: Following two minutes of vortexing, partial dispersion is observed, with visible fluorescent aggregates. (C) Stage 3: Complete dispersion is achieved, resulting in a uniform fluorescent solution suitable for further processing.

The extrusion process alters the appearance of the solutions. In the pre-extrusion stage (Figure 3.29 A), the solution appears foggy and milky, with significant light scattering. As it is sequentially extruded through membranes with decreasing pore sizes – 800 nm (Figure 3.29 B), 400 nm (Figure 3.29 C), and 100 nm (Figure 3.29 D) the solution gradually becomes more transparent, suggesting the reduction in vesicle size. The reduced fluorescence intensity of the solution after extrusion process indicates partial sample loss.

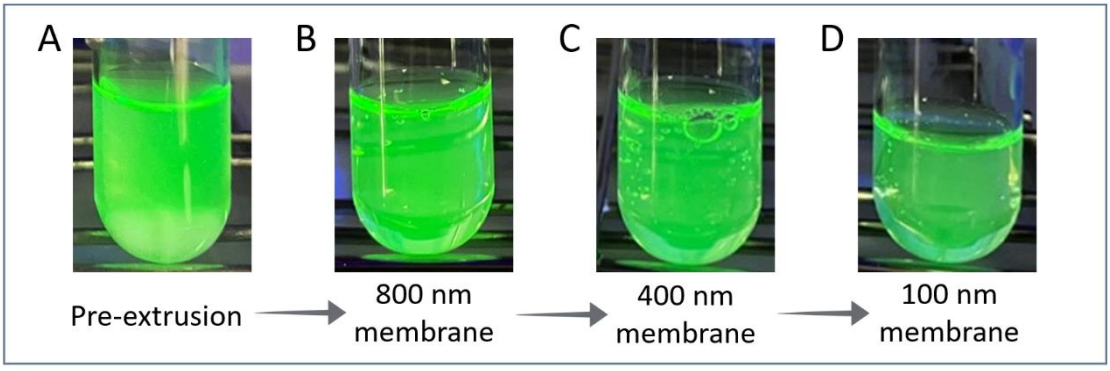

Figure 3.29 Visual progression of the lipid vesicle extrusion process. (A) Prior to extrusion, the sample appears turbid and milky due to light scattering by larger vesicles. (B) Following extrusion through an 800 nm polycarbonate membrane, partial clarification of the solution is observed, indicating initial size reduction. (C) Further extrusion through a 400 nm membrane results in increased optical clarity, consistent with a narrower vesicle size distribution. (D) Final extrusion through a 100 nm membrane results in a visibly clear solution, reflecting successful formation of uniformly sized vesicles.

The dispersion of quantum dots (QDs) in chloroform, mixture containing QDs and lipids in chloroform, and liposomes (extruded through 100 nm membrane filter) encapsulating QDs were characterized by fluorescence spectroscopy. (Figure 3.30 A). The consistent peak shapes and

positions across all three spectra suggest that the quantum dots largely retain their optical properties throughout the encapsulation process. However, a slight redshift in the emission maximum is observed – from 542 nm to 544 nm, and finally to 546 nm. While changes in the local refractive index – from chloroform ($n \approx 1.44$) to lipid bilayers ($n \approx 1.48$-1.50) – can contribute to such spectral shifts, the magnitude of this effect is typically modest, often resulting in shifts of only 1-2 nm. Therefore, the additional redshift observed is likely influenced by other factors, including alterations in the ligand shell environment and potential interactions with the lipid bilayer. These combined effects can modulate the electronic structure of the QDs, leading to the observed spectral changes.

Dynamic light scattering (DLS) measurements were conducted after each extrusion step to monitor changes in vesicle size distribution (Figure 3.30 B). The measured vesicle diameters were smaller than the nominal pore sizes of the extrusion membranes. Extrusion through membranes with progressively smaller pores resulted in a gradual reduction of the average hydrodynamic diameter: 238.8 ± 0.3 nm after extrusion through a 1000 nm membrane, 207.5 ± 0.2 nm at 800 nm, and 165.7 ± 0.2 nm at 400 nm, accompanied by a decrease in the polydispersity index (Figure 3.31). Final extrusion through a 100 nm membrane produced a narrower size distribution, with an average diameter of 97.11 ± 0.1 nm (Figure 3.31).

A comparison of the emission spectra for vesicles extruded through 800 nm, 400 nm, and 100 nm membranes (Figure 3.30 C) shows a marked decrease in fluorescence intensity with decreasing vesicle size. This reduction is likely due to the loss of nanocrystals that adhere to the membrane filters during extrusion, as observed under UV light following each membrane change (Figure 3.29). Additionally, quenching effects may contribute to the decreased signal, as the quantum dots experience changes in their local environment – particularly in smaller vesicles compared to their original dispersion in organic solvents.

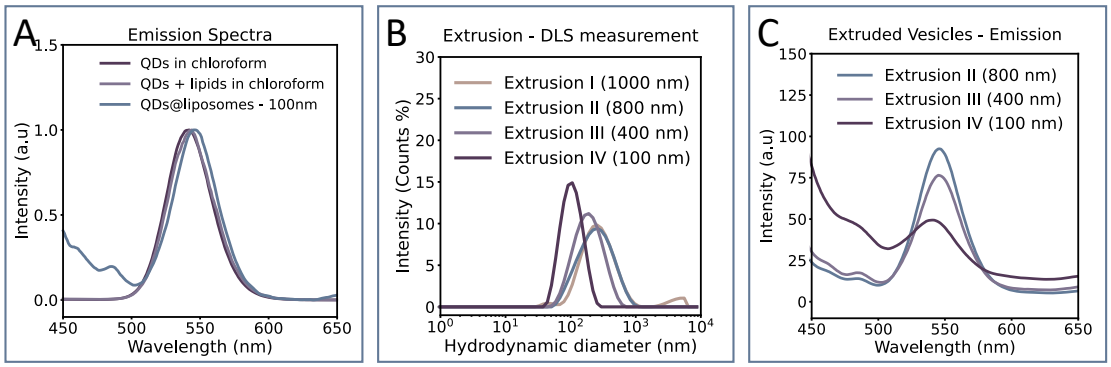

Figure 3.30 (A) Emission spectra of quantum dots (QDs) in chloroform, a QD-lipid mixture, and freshly prepared 100 nm liposomes. The spectra show consistent peak shapes with a slight redshift from 542 nm to 546 nm, reflecting changes in the QDs' environment. (B) DLS measurements of freshly prepared vesicles, demonstrating the decrease in vesicle size during extrusion, with average diameters reducing from 238.8 nm (1000 nm membrane) to 97.11 nm (100 nm membrane), confirming successful production of smaller, more uniform vesicles. (C) Comparison of emission spectra of three extrusion steps (through membrane 800 nm, 400 nm, and 100 nm), showing variations in fluorescence behavior.

Membrane Size	Vesicle diameter (nm)	Polydispersity Index (PdI)
Extrusion I 1000 nm	238.8	0.3
Extrusion II 800 nm	207.5	0.2
Extrusion III 400 nm	165.7	0.2
Extrusion IV 100 nm	97.1	0.1

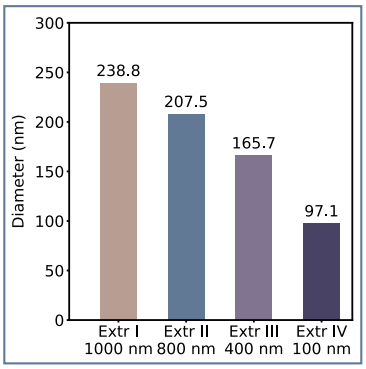

Figure 3.31 Z-average of hydrodynamic diameter and Polydispersity Index (PdI) of vesicles at each extrusion step, as measured by DLS. Vesicle size decreases from 238.8 nm to 97.1 nm as the membrane pore size reduces from 1000 nm to 100 nm, with a corresponding decrease in PdI, indicating improved uniformity in vesicle size.

The sample after full extrusion process was further analyzed using cryogenic transmission electron microscopy (cryoTEM). The cryoTEM images (Figure 3.32) display vesicles obtained through Extrusion IV using a 100 nm membrane filter and reveal a heterogeneous population with diameters ranging from 20 to 110 nm, with an average of 59.6 ± 23.2 nm, calculated from approximately 150 vesicles. Both unilamellar and multilamellar vesicles are evident, suggesting variability in vesicle formation. The average membrane thickness, determined from measurements at approximately 400 randomly selected positions, was 3.2 ± 0.7 nm (Figure 3.33). It is important to note that the average diameter obtained from cryoTEM is smaller than that measured by dynamic light scattering (DLS), which is expected since DLS measures

the hydrodynamic diameter and does not resolve smaller vesicles enclosed within multilamellar structures, leading to an overestimation of size.

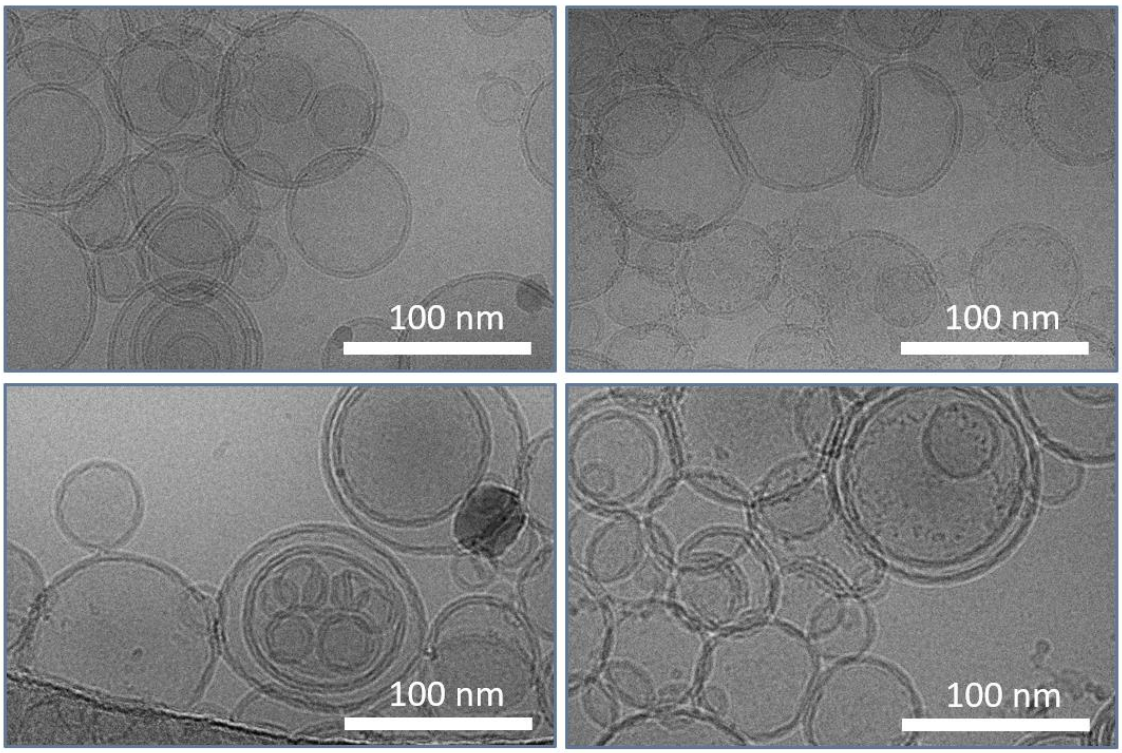

Figure 3.32 CryoTEM images showing a mixture of unilamellar and multilamellar vesicles. The images reveal vesicle sizes after Extrusion IV through 100 nm membrane. The bilayer membranes are clearly visible.

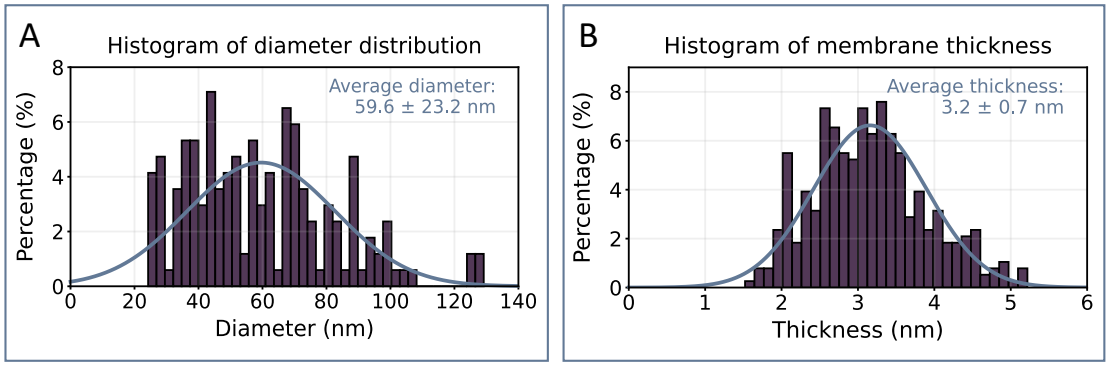

Figure 3.33 Histograms illustrating the size distribution of lipid vesicles (left) and membrane thicknesses (right), obtained from cryoTEM images. The average vesicle diameter was determined to be 59.6 ± 23.2 nm, and the average membrane thickness was 3.2 ± 0.7 nm.

Stability study

The visual inspection of the solutions containing vesicles and QDs revealed slight haze under white light Figure 3.34 and bright fluorescence under UV illumination (λex = 365 nm) indicating homogenous distribution of quantum dots (Figure 3.19).

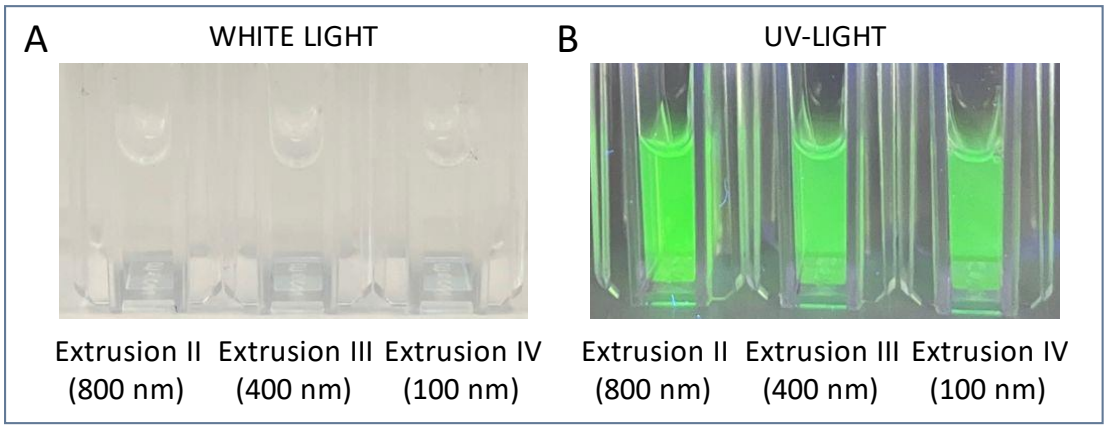

Figure 3.34 Visual comparison of vesicle solutions at three different extrusion stages under (A) white light and (B) UV irradiation.

To evaluate long-term stability of vesicle, we monitored the change of hydrodynamic diameter of samples extruded through 100 nm (Extrusion IV), 400 nm (Extrusion III), and 800 nm (Extrusion II) membranes over a five-day period. The results are presented in Figure 3.35 which includes extinction spectra (A, B, C), emission spectra (D, E, F), and dynamic light scattering (DLS) data (G, H, I) for each vesicle size. The extinction spectra (Figure 3.35 A, B, C) remain largely unchanged throughout the observation period, suggesting structural integrity are well preserved. In the emission spectra (Figure 3.35 D, E, F), the fluorescence profile remains consistent over five days; however, a gradual decrease in intensity is observed. This decline may result from factors such as vesicle aggregation, partial degradation of quantum dots in the aqueous environment, or minor sample dilution during repeated handling.

Dynamic light scattering (DLS) measurements of the vesicles from Extrusion IV, Extrusion III, and Extrusion II, which represent progressively larger average vesicle sizes, were performed over a five-day period to provide insights into their stability. For the smallest vesicles from Extrusion IV (Figure 3.35 G) the Z-average diameter decreased from 116.4 nm on day 1 to 109.4 nm on day 5 (-6%), accompanied by a modest increase in the polydispersity index from 0.129 to 0.158 (Figure 3.36).

Vesicles extruded through 400 nm membranes (Extrusion III, Figure 3.35 H) showed no notable change after 5 days of incubation, with differences below 2%: the Z-average diameter decreased from 203.8 nm to 201.2 nm, while the PdI showed a slight drop from 0.216 to 0.210 (Figure

3.36). The largest vesicles from Extrusion II, obtained using an 800 nm-pore membrane (Figure 3.35 I), exhibited an increase in Z-average diameter from 256.8 nm to 269.6 nm (+5%), accompanied by a rise in PdI from 0.247 to 0.270 (Figure 3.36). The DLS profile broadened significantly by day 5, indicating increased heterogeneity.

These results suggest a tendency toward vesicle fusion or aggregation over time, highlighting the comparatively lower structural stability of larger vesicles during prolonged storage. Vesicles subjected to three or four extrusion cycles through smaller-pore membranes (400 nm and 100 nm) maintained relatively stable diameters over the first two days, with changes below 1% (116.4 to 115.3 nm and 203.8 to 203.7 nm, respectively). However, all three vesicle populations exhibited measurable size or PdI variations over five days, indicating that the dispersions are most reliable when used immediately after preparation or within a short time frame, preferably within 24 hours.

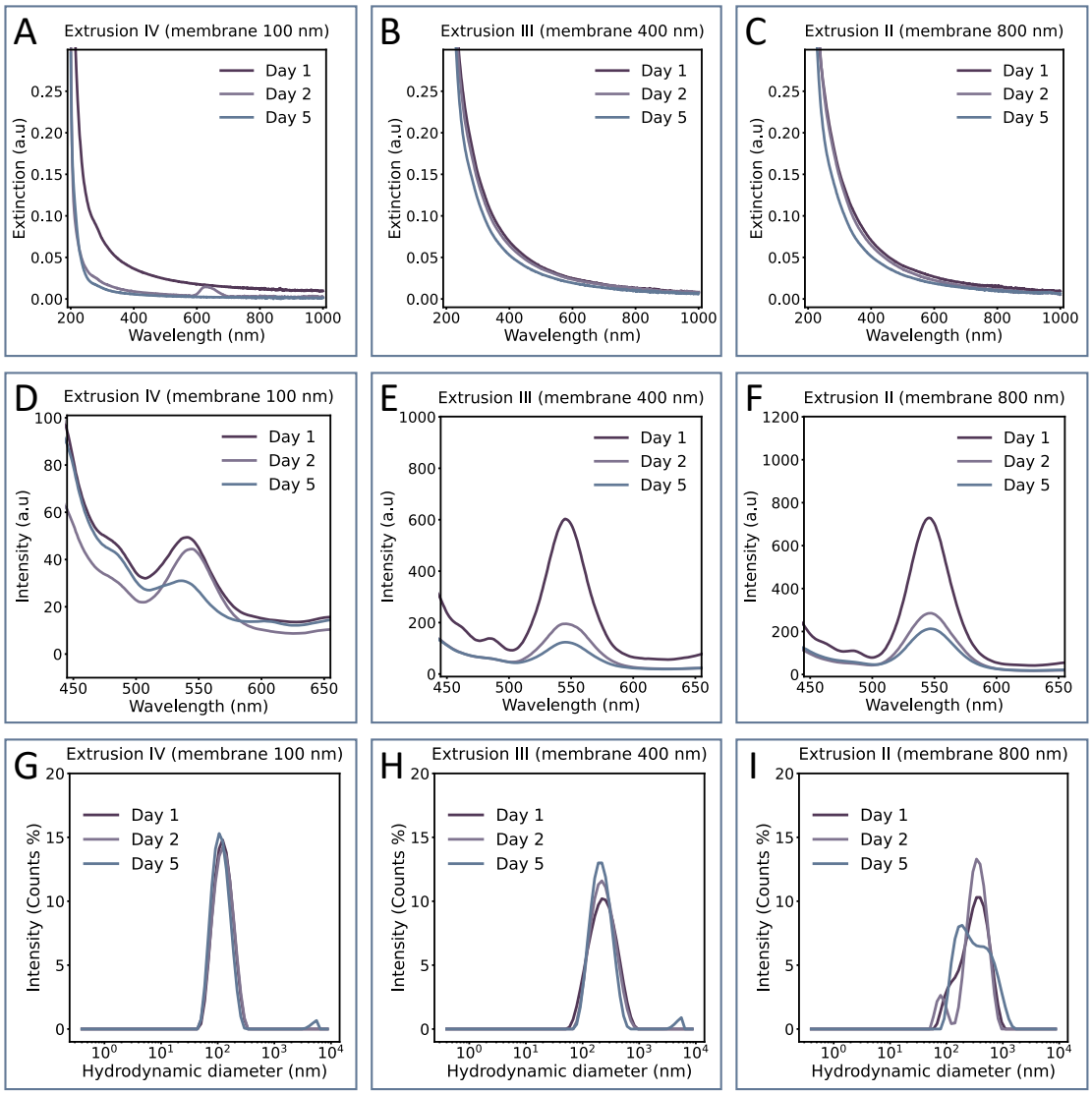

Figure 3.35 Stability assessment of vesicles extruded through membranes of 100 nm (Extrusion IV; A, D, G), 400 nm (Extrusion III; B, E, H), and 800 nm (Extrusion II; C, F, I) over a five-day period. Extinction spectra (A, B, C) show minimal changes. Emission spectra (D, E, F) reveal a gradual decrease in fluorescence intensity, possibly due to aggregation or QD degradation. DLS measurements (G, H, I) indicate a slight increase in vesicle size, particularly in the 800 nm samples, suggesting some degree of aggregation or fusion over time.

Day	Membrane Size	Diameter Z-average (nm)	Polydispersity Index (PdI)
Day 1	100 nm (Ex IV)	116.4	0.129
Day 1	400 nm (Ex III)	203.8	0.216
Day 1	800 nm (Ex II)	256.8	0.247
Day 2	100 nm (Ex IV)	115.3	0.114
Day 2	400 nm (Ex III)	203.7	0.198
Day 2	800 nm (Ex II)	270.7	0.246
Day 5	100 nm (Ex IV)	109.4	0.158
Day 5	400 nm (Ex III)	201.2	0.21
Day 5	800 nm (Ex II)	269.6	0.27

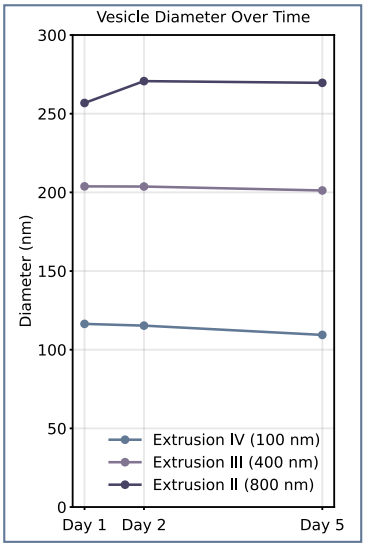

Figure 3.36 Summary of DLS measurement of vesicles extruded through 100 nm (Extrusion IV), 400 nm (Extrusion III), and 800 nm (Extrusion II) membranes over a five-day period. The table summarizes Z-average diameters and polydispersity indices obtained from dynamic light scattering measurements on days 1, 2, and 5. The graph illustrates temporal changes in average vesicle diameter for the three samples, showing minor variations for Extrusion IV and Extrusion III vesicles and an increase Extrusion II vesicles.

Fluorescence lifetime measurements were conducted to gain deeper insight into the photophysical behavior of the vesicle samples over time. Measurements were performed on vesicles obtained after extrusion through 100 nm-, 400 nm-, and 800 nm-pore membranes on days 1, 2, and 5. The resulting fluorescence decay curves were fitted using a triple exponential model, a commonly applied approach for describing complex, multi-component decay processes (Appendix, Figure A.2). The functional form of the model is shown below:

$$f(t) = H + A_1 e^{\left\{-\frac{t}{\tau_1}\right\}} + A_2 e^{\left\{-\frac{t}{\tau_2}\right\}} + A_3 e^{\left\{-\frac{t}{\tau_3}\right\}} \quad (3.2)$$

Here, f(t) represents the fluorescence intensity at time t; H is the baseline offset; A_1, A_2, and A_3 are the amplitudes of the three decay components; and τ_1, τ_2, τ_3 are the corresponding lifetimes. This model accounts for multiple emissive species or environments contributing to the overall decay profile. Although the fit quality showed minor deviations beyond 100 ns in some cases, this had little effect on the analysis, as the majority of photon counts occurred within the first 40 ns – the time window most critical for accurate lifetime determination.

A comparative analysis of the fitted decay curves is shown in the following Figure 3.37, highlighting changes in the average fluorescence lifetimes (τ_{av}), calculated as:

$$\tau_{av} = \frac{A_1\tau_1 + A_2\tau_2 + A_3\tau_3}{A_1 + A_2 + A_3} \quad (3.3)$$

across the different days of measurement. The model incorporates two exponential decay components, each characterized by a distinct lifetime τ_1, τ_2, and τ_3. The pre-exponential factors, A_1, A_2, A_3, represent the relative contributions of these two decay processes to the overall fluorescence intensity.

The average fluorescence lifetime of vesicles extruded through 100 nm membranes dropped markedly over time, from 2.1 ± 3.0 ns on day 1 to just 0.5 ± 0.2 ns by day 5, indicating a substantial rise in non-radiative decay processes. This rapid decrease aligns with mechanisms such as trap-assisted recombination and Auger-type interactions, both of which can become more prominent when become surface-charged or develop new trap states.[61] A likely contributing factor is curvature-induced stress in the lipid membrane: at higher curvature, as seen in smaller vesicles, the lipid bilayer may exhibit packing defects and transient permeability to water, oxygen, and ions. This increased permeability can facilitate oxidative damage or trion formation, both of which degrade photophysical performance over time.[62,63] Even though bilayer thickness and lipid composition are identical across all batches, the smaller radius amplifies surface-to-volume ratio and membrane tension, accelerating these degradation pathways. By contrast, vesicles extruded through 400 nm and 800 nm membranes, whose hydrodynamic diameters are around 200 nm, maintained stable lifetimes (Figure 3.37). The modestly larger radius lowers curvature stress, reduces defect density, and limits solvent/ion ingress, thereby suppressing the creation of surface traps and keeping Auger recombination rates near their initial values. Collectively, the results reveal a curvature-dependent photostability: smaller vesicles experience faster lifetime erosion owing to curvature-induced membrane leakiness, while slightly larger vesicles (< 200 nm) preserve QD optical integrity over several days. For experiments requiring consistent optical output, vesicles should ideally be used shortly after preparation; however, extrusion through membranes ≥ 400 nm and keeping the diameter of a vesicle slightly larger presents a straightforward strategy for improving formulation robustness.

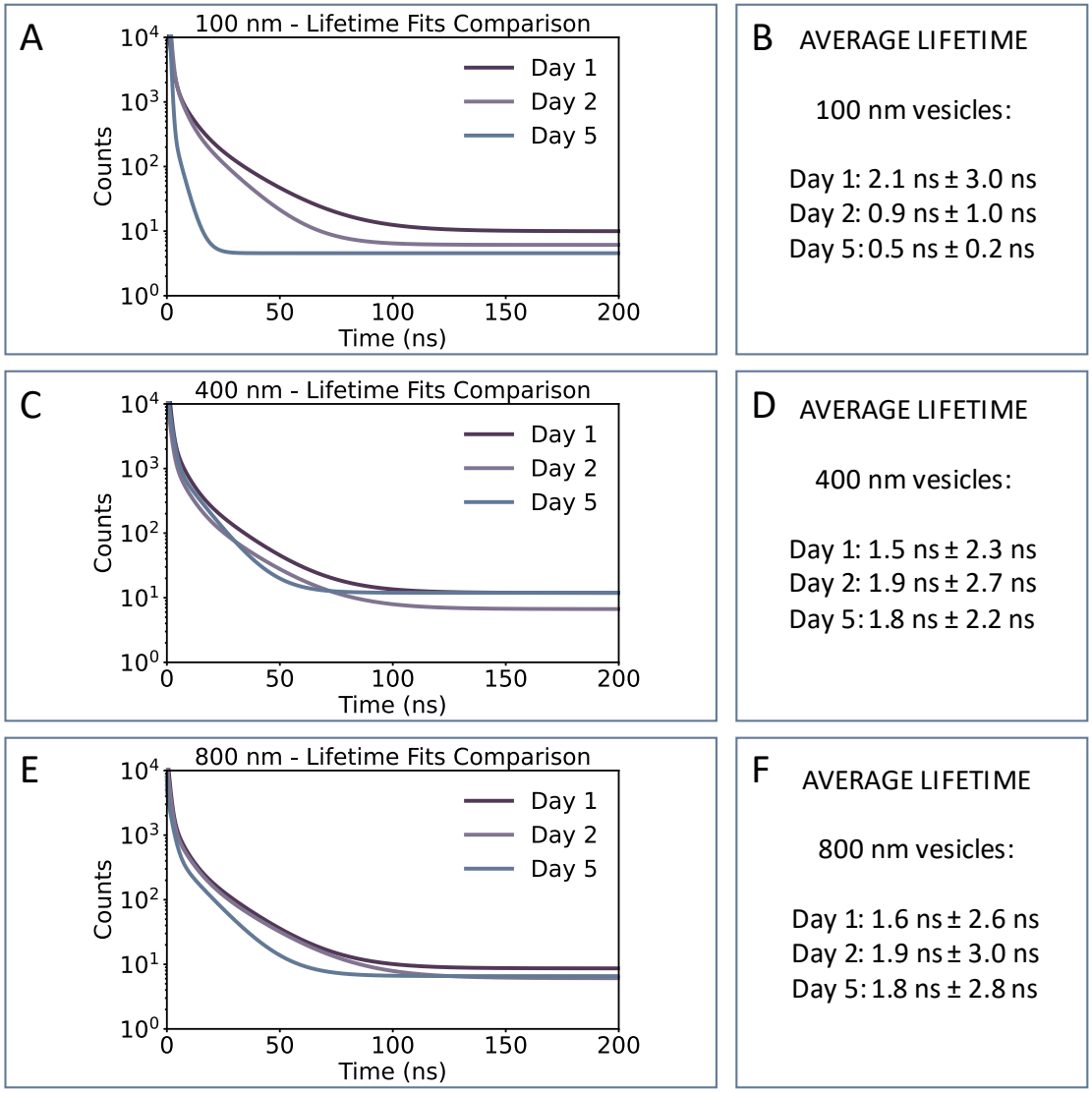

Figure 3.37 Time-resolved fluorescence decay analysis of lipid vesicles with different diameters: 100 nm (A, B), 400 nm (C, D), and 800 nm (E, F), measured on Day 1, Day 2, and Day 5 post-synthesis. Panels A, C, and E present the fitted fluorescence decay curves showing how fluorescence lifetimes evolve over time for each vesicle size. The corresponding average lifetimes are summarized in panels B, D, and F, respectively. Notably, 100 nm vesicles exhibit a marked decrease in fluorescence lifetime over time, indicating reduced photophysical stability, while larger vesicles (400 nm and 800 nm) maintain more consistent lifetimes over the five-day period. This suggests that vesicle size plays a role in the temporal stability of encapsulated fluorophores or quantum dots.

PLQY in the presence of lipids

The initial phase of our work on optimizing lipid vesicle preparation was conducted using commercially available CdSe/ZnS core/shell quantum dots (QDs) functionalized with trioctylphosphine oxide (TOPO). Given their low cost and wide availability, these QDs served as an ideal system for preliminary protocol development and optimization of the experimental workflow. Throughout these early experiments, we observed that the fluorescence of the

commercial QDs remained stable in lipid environments, with any minor decrease attributed primarily to material loss during the extrusion process. However, achieving the broader objectives of this research required transitioning to our material of choice: CdS/CdSe/CdS spherical quantum wells (SQWs), synthesized in Jonathan Owen's laboratory. These more sensitive nanostructures are better suited for future applications due to their unique optical and electronic properties.

The incorporation of SQWs into lipid systems revealed displayed a sharp decline in photoluminescence almost immediately upon mixing with lipids in non-polar solvents. This effect was especially pronounced in the presence of cationic lipids like DOTAP, suggesting that surface polarization might be triggering enhanced non-radiative recombination pathways. To preserve fluorescence, surface passivation must be improved to mitigate quenching effects. Several approaches for controlling surface chemistry were implemented. SQWs functionalized with Cd-oleate were evaluated first. This system, however, proved to be highly vulnerable to lipid-induced fluorescence loss, with PLQY values dropping from 31.6% in DCM to just 2.2% and 0.25% in the presence of DOTAP and DSPE-PEG, respectively (Figure 3.38). We then explored fluorinated passivation using CdF_2 combined with octylamine. Although these nanoparticles exhibited a high initial PLQY of 94.0% in DCM, they too experienced quenching in lipidic environments, highlighting the insufficient photostability of this passivation strategy (Figure 3.39).

The surface treatment with Zn-oleate ligands showed improved resistance to quenching, with PLQY values remaining relatively stable at 51% in DCM in the presence of DMPC and dropping to 10-12% in DOTAP and DSPE-PEG solutions. This effect can be attributed to the stronger affinity of Zn-oleate to anionic sulfur compared to Cd-oleate, which leads to more robust binding of Zn-oleate ligands to the nanocrystal surface and more effective passivation of surface states.[64] We further introduced a ZnS shell to form a robust core/shell structure, which markedly enhanced the optical stability of the SQWs. ZnS is particularly effective because undercoordinated sulfur atoms at the nanocrystal surface act as trap sites that promote nonradiative recombination; overcoating with ZnS suppresses these defect-related pathways and passivates surface states, thereby stabilizing the emission. In addition, the wider bandgap of ZnS relative to CdS or CdSe increases carrier confinement within the CdSe core and mitigates Auger recombination, further improving both photoluminescence efficiency and stability.[11,65] As a result, these ZnS-shelled SQWs stabilized with Zn-oleate ligands maintained high PLQY values (~54%) across all lipid formulations tested, including DMPC, DOTAP, and DSPE-PEG, and retained a notable 29% PLQY even in aqueous PBS vesicle suspensions (Figure 3.40). This final system

demonstrated that with the right combination of inorganic shell and surface ligands, SQWs can be effectively shielded from environmental perturbations, paving the way for their reliable use in biological applications.

Extinction and emission spectra corresponding to each studied system (System I – IV) are provided in the Appendix (Section 3.3, Figure A.3).

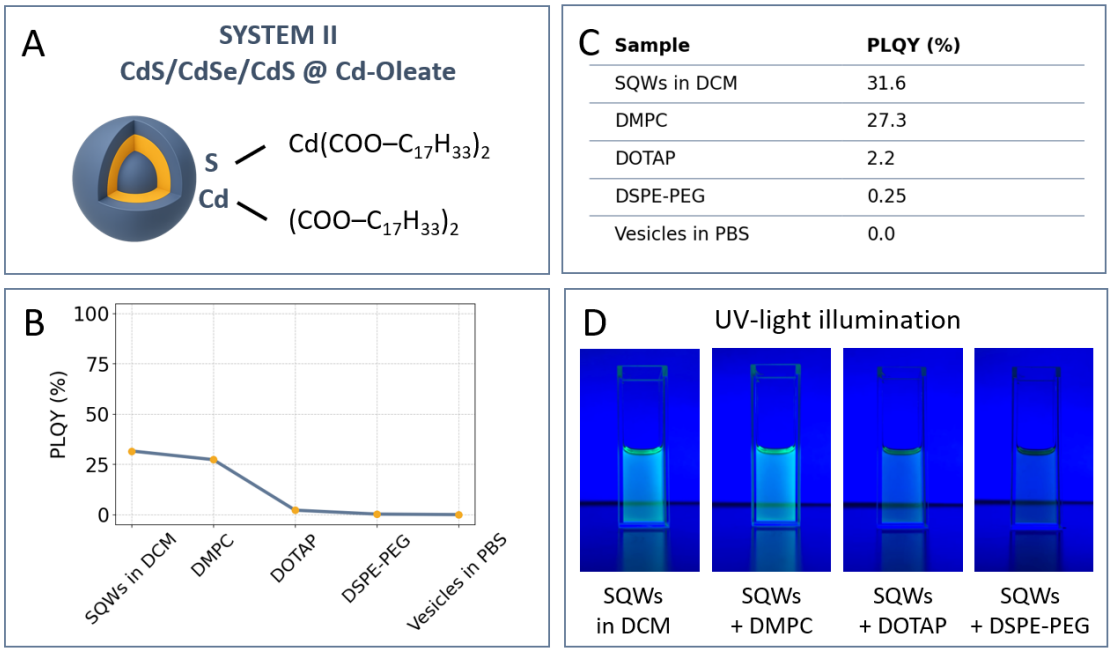

Figure 3.38 Photoluminescence response of CdS/CdSe/CdS spherical quantum wells (SQWs) functionalized with Cd-oleate upon exposure to lipid environments. (A) Schematic of SQW surface functionalization with cadmium oleate ligands. (B) Photoluminescence quantum yield (PLQY) measurements of SQWs in various media, demonstrating significant fluorescence quenching upon mixing with lipid components, particularly DOTAP and DSPE-PEG. (C) Summary of PLQY values corresponding to the samples shown in panel B. (D) Digital images of SQW samples under UV-light illumination, visually confirming the fluorescence loss in lipid-containing environments.

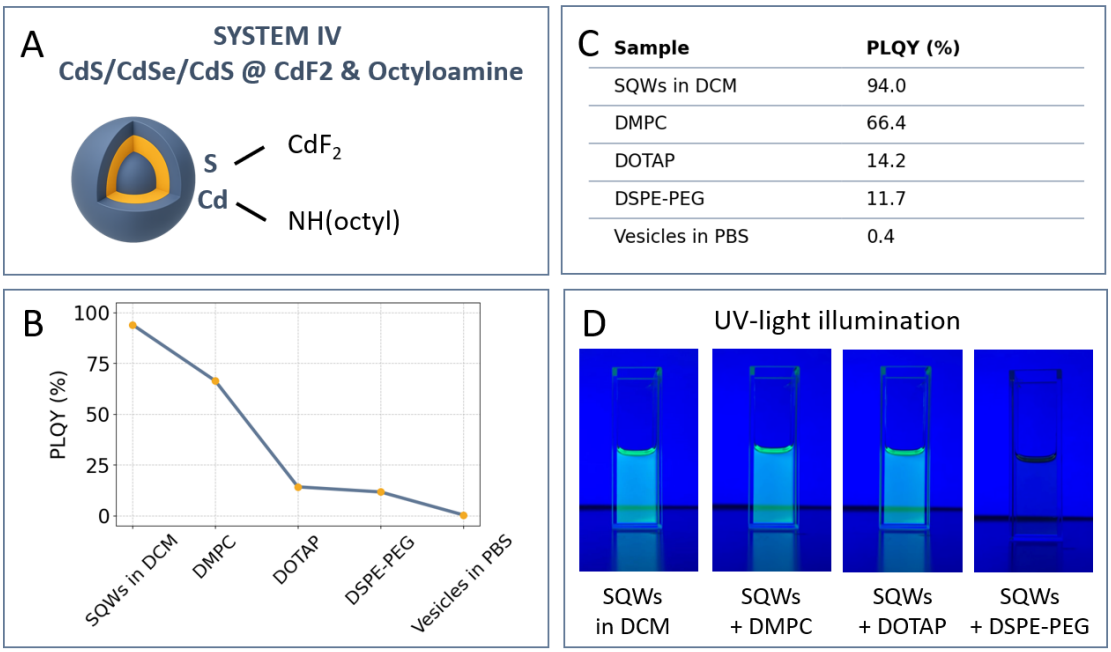

Figure 3.39 Photoluminescence of CdS/CdSe/CdS functionalized with CdF_2 and octylamine in lipid environments. (A) Illustration of SQW surface passivation (B) PLQY measurements showing a sharp decline in emission upon exposure to lipid components, particularly DOTAP and DSPE-PEG, and near-total quenching in PBS vesicles. (C) PLQY values from B. (D) Digital images of SQW samples under UV irradiation.

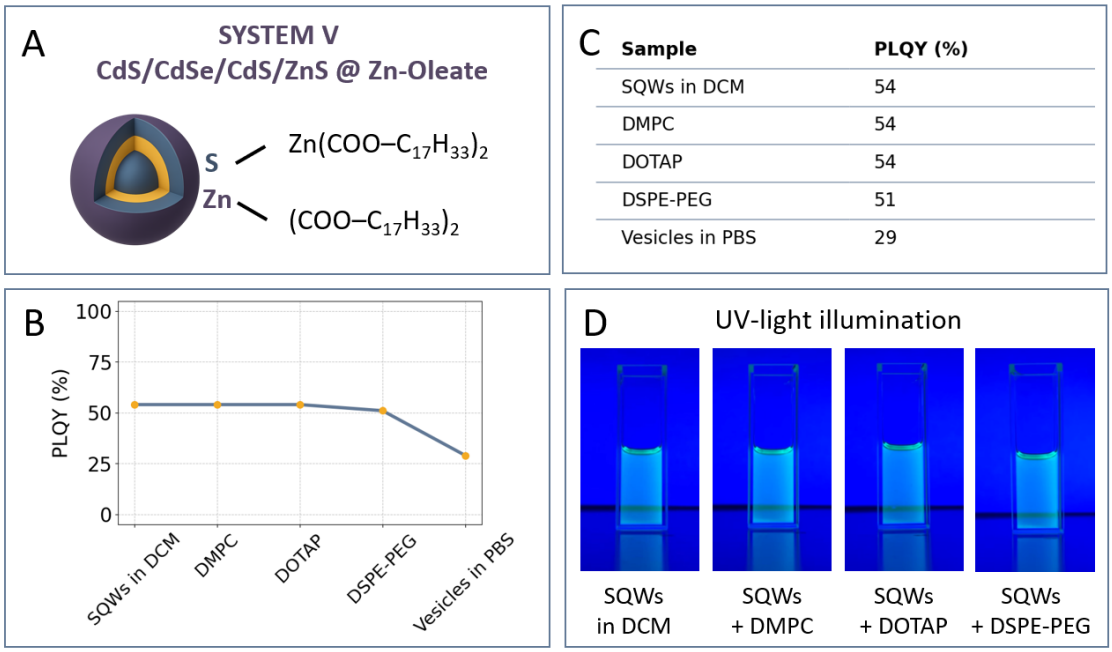

Figure 3.40 Photoluminescence stability of passivated CdS/CdSe/CdS/ZnS stabilized with Zn-oleate in lipid environments. (A) Schematic representation of the nanocrystal featuring a ZnS outer shell. (B) PLQY measurements showing consistent emission in lipids, with only a modest decrease observed in PBS. (C) PLQY values for each condition as shown in B. (D) Digital images of the SQW samples under UV-light irradiation, confirm fluorescence retention in all lipid media tested, and underscoring the effectiveness of the ZnS/Zn-oleate surface passivation strategy.

3. Cell Membrane Insertion

The next step was to assess their ability of SQWs to interface with biological membranes – an essential requirement for their intended use in detecting neuronal activity. This section focuses on the membrane insertion capabilities of SQWs delivered via the two strategies previously developed: OCG micelles and lipid vesicles. The primary objective was to evaluate whether these delivery systems could successfully embed SQWs into cell membranes in a manner compatible with their photoluminescent function and biological stability.

To validate membrane insertion in a biologically relevant context, we employed cultured HEK cells as a model system. Human embryonic kidney (HEK293-T) cells provide a robust and well-characterized platform for initial biological validation. In some experiments, unmodified HEK293-T cells were used to study fundamental membrane interactions. In others, we utilized self-spiking HEK cells transfected with voltage-gated sodium and potassium channels, providing a dynamic model for testing activity-dependent fluorescence responses. Details of the cell line used are provided in the description of each experimental result.

The experiments presented in the following subsections aim to assess both the membrane integration of SQWs and their functional responsiveness under conditions of real-time neuronal activity, establishing a foundation for their future use in all-optical electrophysiology, as detailed later in Subchapter 4*, Recordings of Spiking HEK Cells with Spherical Quantum Dots* (page 153).

3.1. OCG Micelles

We began by evaluating the membrane insertion capabilities of SQWs encapsulated within OCG micelles. The central question was whether these micelles could bring SQWs into close apposition with the plasma membrane of live cells without compromising cell viability – critical prerequisites for optical sensing applications.

Initial experiments were conducted using a specialized HEK cell line obtained from ATCC (CRL-3479), originally developed by Adam Cohen's laboratory.[66] This Tet-On "spiking" HEK cell line is genetically engineered to constitutively express the voltage-gated sodium channel NaV1.5, while the inward-rectifier potassium channel Kir2.1 is placed under doxycycline-inducible control. The Kir2.1 channel is also fused to cyan fluorescent protein (CFP), which emits fluorescence with an excitation peak around 456 nm and an emission peak near 480 nm. Upon addition of doxycycline (typically 1-2 µg/mL), Kir2.1-CFP is robustly expressed, leading to membrane hyperpolarization. In combination with NaV1.5, this enables the cells to generate

spontaneous, synchronized action potentials once a confluent monolayer is formed. The co-expression of CFP also allows for real-time tracking of Kir2.1 induction via fluorescence in the cyan channel, providing a convenient visual marker for identifying cells that are electrically competent.

However, an important technical consideration emerged during initial imaging: due to the spectral proximity of the CFP emission to that of the GFP channel – commonly used for visualizing SQWs – we observed detectable signal bleed-through. To minimize such optical interference in future experiments, later we switched to an equivalent spiking HEK cell line lacking the CFP tag. This modification is expected to eliminate the potential for spectral overlap and ensure a cleaner imaging channel for SQW emission, particularly important when tracking dynamic fluorescence signals with high temporal precision. Nevertheless, for the purposes of these preliminary membrane insertion studies, we proceeded with the available CFP-expressing line.

We first tested the as-prepared SQWs encapsulated in OCG micelles, using the crude dispersion exactly as it emerged from the encapsulation step. After a 1 to 5 dilution in our standard extracellular recording buffer (final concentration 20% of the stock), confluent HEK monolayers were incubated with the mixture for 15-20 minutes. To enhance membrane permeability and potentially facilitate SQW insertion, 1% (v/v) of a 10% (w/v) Pluronic F-127 solution was included in each sample during incubation. Following incubation, the samples were gently washed, and the solution was replaced with fresh, SQW-free recording buffer before imaging.

Bright-field microscopy prior to incubation revealed a uniform, polygonal monolayer with well-defined cell-cell contacts, indicative of a healthy and confluent culture (left panel of Figure 3.41). However, post-incubation images showed a dramatic shift in morphology (right panel of Figure 3.41). The monolayer appeared fragmented, with individual cells rounding up and displaying prominent membrane blebbing (protrusions of the cell membrane) – hallmarks of acute cellular stress and early stages of cell death. Notably, these changes progressed during imaging, suggesting that cytotoxic effects were rapid and severe.

Fluorescence images taken in the GFP channel reinforce this conclusion. Prior to incubation (left panel of Figure 3.41), only the faint cyan bleed-through from the Kir2.1-CFP tag was visible. After incubation, the field was dotted with numerous fluorescent spots, randomly distributed and showing no association with the cell membrane (right panel of Figure 3.41). The apparent overlap between these puncta and regions of cellular debris reflects monolayer retraction and increased endocytic activity in dying cells, rather than true selective staining.

The likely explanation for the observed cytotoxicity lies in the presence of residual free surfactant and the high micelle concentration in the unpurified dispersion. Surfactants are well-documented to disrupt lipid bilayers by intercalating into the membrane, increasing permeability, and ultimately compromising cell viability. In addition, polymer-based micelles can deliver concentrated surfactant loads directly to the membrane surface, exacerbating damage and triggering processes such as membrane blebbing and detachment. Although quantum dots themselves can contribute to cytotoxicity, the severity and rapid onset of cellular damage observed here suggest that the primary cause is the excess surfactant present in the crude micelle formulation. Based on these observations, we chose to purify the micellar solution prior to incubation with living cells, aiming to reduce the surfactant load while preserving the colloidal stability of the SQWs.

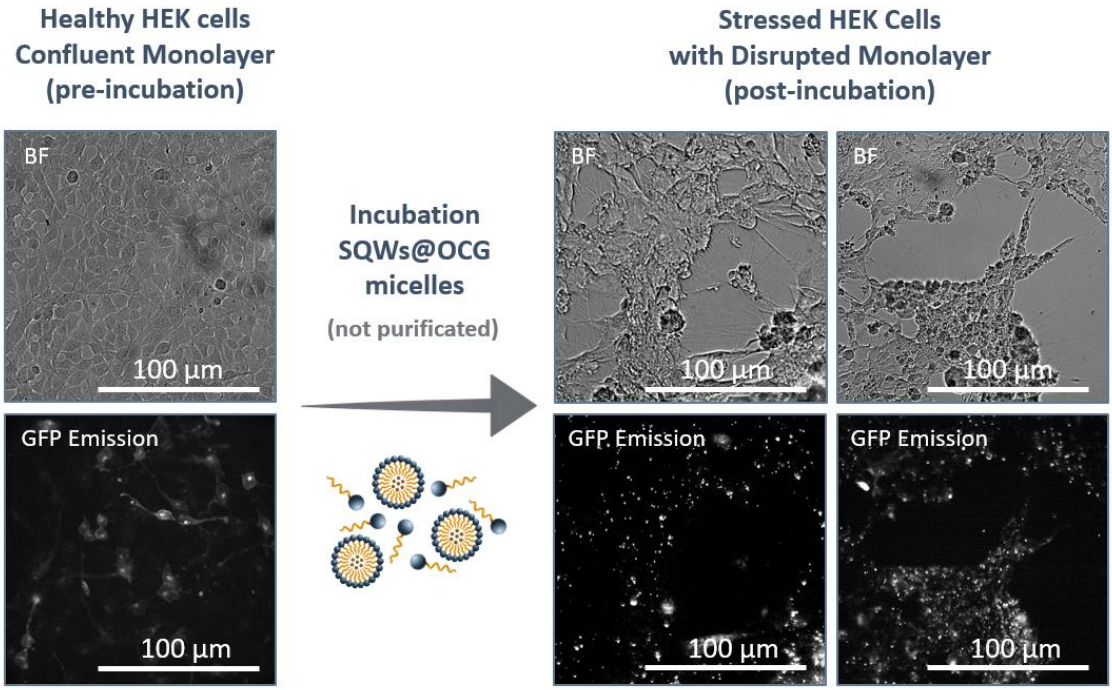

Figure 3.41 Exposure to unpurified SQWs@OCG micelles induces acute cytotoxicity and monolayer disruption in HEK cells. Bright-field (BF) and GFP-channel fluorescence images of HEK monolayers before (left) and after (right) incubation with unpurified SQWs encapsulated in OCG micelles. Prior to treatment, cells display a healthy, confluent monolayer with defined morphology and minimal background fluorescence. Post-incubation, marked cellular stress is evident, including monolayer disruption, cell rounding, and membrane blebbing. GFP images show numerous bright spots across the field, likely representing intact or aggregated micelles adhering nonspecifically to cell surfaces or substrate. The lack of membrane-localized fluorescence and rapid cell deterioration suggest that excess surfactant in the crude dispersion compromises membrane integrity rather than enabling targeted staining.

To reduce surfactant-related toxicity, the crude SQWs@OCG micelle solution was subjected to a two-step purification process. First, the dispersion was centrifuged using an Amicon Ultra-0.5 centrifugal filter unit with a 100 kDa molecular weight cutoff for 10 minutes at 10,000 rpm. This

step served to remove excess free surfactant and concentrate the micelles. The retained fraction was then redispersed in phosphate-buffered saline (PBS) to restore the original volume. To further refine the sample, it was centrifuged through a 200 nm membrane filter under the same conditions. This final step was intended to remove larger aggregates, which are less likely to interact with cell membranes in a controlled or effective manner and tend to introduce imaging artifacts – appearing as oversized fluorescent spots that obscure the finer signal distribution across the sample.

Application of the two-step purification protocol markedly improved the biocompatibility of the SQWs@OCG formulation. Bright-field images taken before incubation again show a uniform, confluent HEK monolayer with crisp cell-cell contacts; after a 15-20 min incubation with the purified micelles, monolayer remains intact, with no evidence of detachment, rounding, or membrane blebbing (Figure 3.42). Cells retain their typical polygonal morphology for the full 1-1.5 h imaging session on the microscope stage, indicating that removal of excess surfactant and large aggregates is sufficient to avert the acute cytotoxicity observed with the crude dispersion.

The GFP channel now displays a dense layer of fluorescent spots that are evenly distributed across the field (Figure 3.42). Although the bright spots corresponding to quantum dots are homogenously distributed, the observed fluorescence does not outline cellular perimeters, nor is it concentrated at cell-cell junctions, suggesting that the particles remain suspended in the medium rather than inserting into, or diffusing within, the plasma membrane.

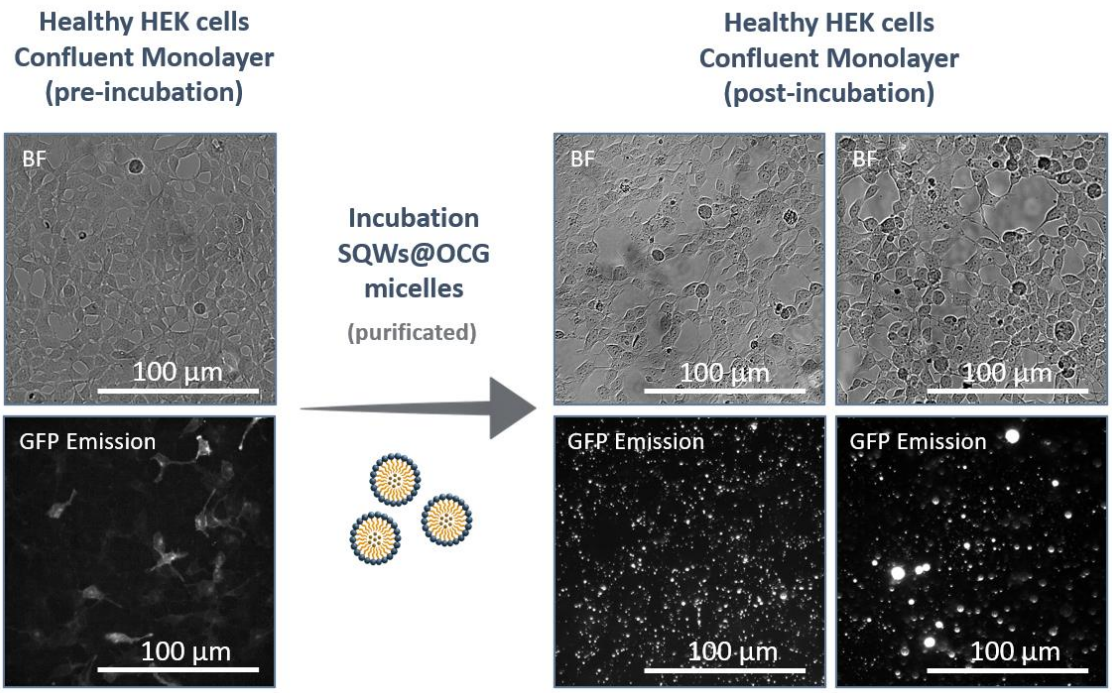

Figure 3.42 Bright-field and GFP fluorescence images of HEK cells before and after incubation with purified SQWs@OCG micelles. Pre-incubation images (left panels) show a healthy, confluent HEK monolayer with tight cell-cell contacts and minimal background fluorescence (limited to faint bleed-through from Kir2.1-CFP). Following a 15-20 min incubation with purified SQWs@OCG micelles (right panels), the monolayer remains intact with preserved cell morphology and no signs of acute cytotoxicity. GFP channel images reveal numerous, uniformly distributed fluorescent spots of diffraction-limited size and consistent intensity, consistent with individual micelles or small micelle clusters. These do not localize to cell membranes or junctions, suggesting that the particles are loosely surface-bound or suspended in the medium, rather than integrating into the plasma membrane.

Despite the improved biocompatibility achieved after purification, detailed imaging revealed that the SQWs@OCG micelles still failed to produce the continuous membrane staining we sought (Figure 3.43 and Figure 3.44). In bright-field mode (Figure 3.43 A and Figure 3.44 A) the HEK monolayer remains confluent and morphologically normal, confirming that the new formulation no longer compromises cell health. However, fluorescence images (Figure 3.43 C and Figure 3.44 C) are dominated by innumerable sub-micron emission spots that appear randomly distributed across the field rather than outlining the plasma membrane.

The spatial distribution of fluorescence confirms that the purified micelles preferentially adsorb to the coverslip rather than to the cell surface. In the first data set (Figure 3.43), regions of bare poly-D-lysine-coated glass, highlighted by dashed circles, are peppered with bright emission dots, whereas proximal areas occupied by a continuous cell sheet appear markedly darker, without characteristic fluorescence of nanocrystals. This inverse contrast points to preferential adsorption of SQWs@OCG micelles onto the positively charged substrate rather than the plasma membrane. A second set of data (Figure 3.44) offers complementary evidence: when the

monolayer is particularly dense, the fluorescent puncta accumulate in the narrow gaps between neighboring cells – locations where the underlying glass remains exposed – while the cell bodies themselves show little or no signal. Together, these observations indicate that even after purification, the micelles do not integrate into the membrane but instead settle onto the substrate wherever it is accessible.

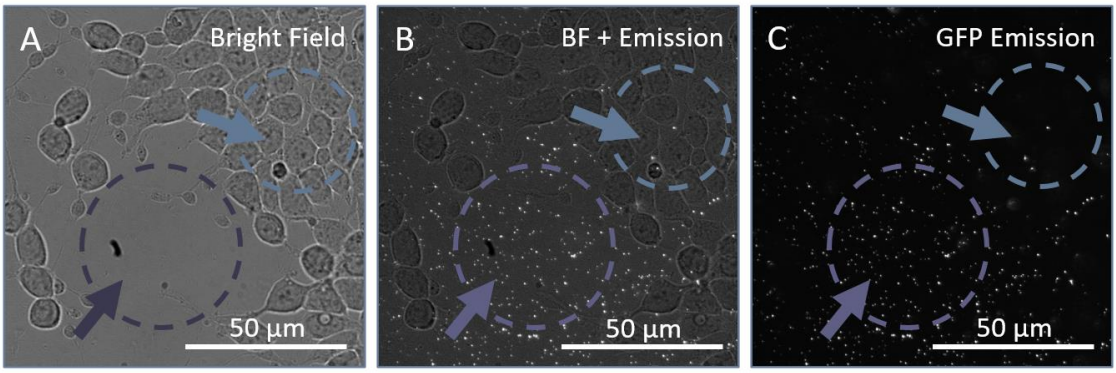

Figure 3.43 Spatial distribution of SQWs@OCG micelles relative to HEK cell coverage and exposed substrate. (A) Bright-field image of a microscopy frame intersecting a confluent HEK monolayer (blue dashed circle) and an adjacent region of bare poly-D-lysine-coated glass (purple dashed circle). (B) Overlay of bright-field and GFP fluorescence reveals abundant, punctate emission in the substrate-exposed area (purple), with markedly fewer fluorescent spots over the cell-covered region (blue). (C) GFP emission alone highlights preferential adsorption of micelles to the bare glass: high density of sub-micron fluorescent puncta in the purple-circled substrate area versus low signal in the blue-circled cell region.

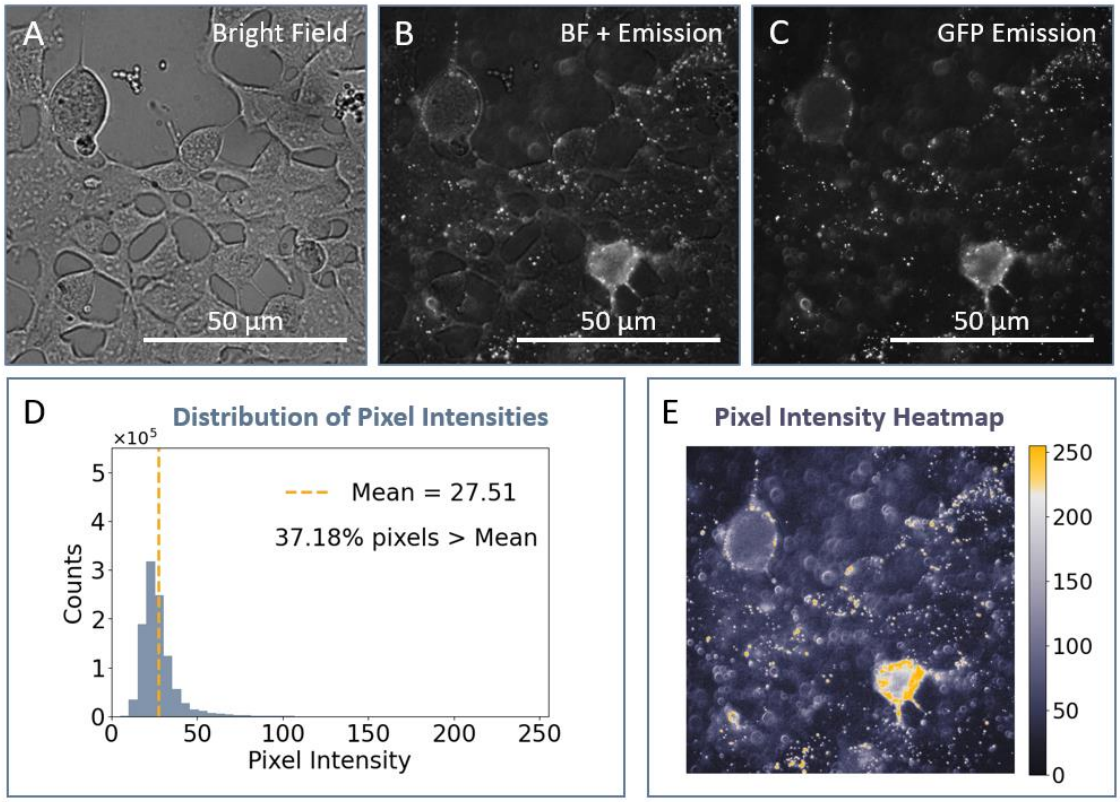

Figure 3.44 Representative example of staining HEK cells with purified OCG-encapsulated SQWs. (A) Bright-field image of a nearly confluent HEK monolayer following 20 min incubation, showing intact cell morphology. (B) Overlay of bright-field and GFP emission reveals numerous sub-micron fluorescent puncta dispersed across the field. (C) GFP emission alone highlights these discrete bright spots rather than a continuous membrane signal. (D) Histogram of pixel intensities from (C) indicates a mean intensity of 27.51 (yellow dashed line), with 37.18% of pixels exceeding this threshold – demonstrating that intense fluorescence is confined to a small fraction of the image. (E) The pixel intensity heatmap highlights concentrated fluorescence hotspots (yellow/white) localizing to narrow intercellular gaps and cell edges – areas where the substrate is exposed – while the interior of the cell bodies remains largely low-intensity (dark), indicating that purified OCG-encapsulated SQWs micelles accumulate in these extracellular spaces rather than coating the membrane uniformly.

Overlay of bright-field and GFP fluorescence (Panel B of Figure 3.44), alongside GFP emission alone (Panel C on the Figure 3.44), reveals a clear departure from the anticipated uniform membrane labeling. Rather than outlining the plasma membrane, the fluorescence signal appears as discrete, sub-micron spots scattered across the field, with the brightest points concentrated along intercellular gaps and at cell edges – areas where the substrate remains exposed. This distribution is quantified in Panel D of Figure 3.44, where a pixel intensity histogram of Panel C shows a strong skew toward low-intensity values, with a mean of 27.51 and only 37.18% of pixels exceeding this threshold, indicating that bright emission is restricted to a small subset of the image. The heatmap in Panel E (Figure 3.44) reinforces this interpretation, with high-intensity pixels (yellow/white) localized primarily to peripheral extracellular regions, while the cell interiors remain largely non-fluorescent (dark).

The unusually bright cell in the lower-right corner is most likely attributable to spectral bleed-through from CFP, as previously noted.

Across multiple replicates and experimental conditions, this punctate, extracellular accumulation pattern was consistently observed, even when micelle formulations were supplemented with additives such as Lipofectamine or Pluronic F-127 – neither of which altered the distribution or promoted membrane integration. These results suggest that although the purified OCG micelles are biocompatible and capable of approaching the cell surface, their structural and chemical properties are insufficient to support efficient insertion of SQWs into the lipid bilayer. This limitation prompted a strategic shift toward alternative delivery platforms, specifically lipid vesicles, which offer a more membrane-compatible interface for SQW incorporation, as described in the following sections.

3.2. Fusosomes – Fusogenic Lipid Vesicles

In an earlier chapter (2.2 *Lipid Vesicles*, page 102), when introducing the preparation of lipid vesicles and the encapsulation of quantum dots, the specific choice of lipids was deliberately left without detailed justification. The vesicles described so far were not designed merely as carriers for solubilizing hydrophobic quantum dots in aqueous media. Their formulation was driven by enabling them a fusion with biological membranes. Through careful selection of lipid components, a conventional liposome can be transformed into a fusosome – a vesicle with the intrinsic ability to merge with cellular membranes and deliver its contents directly into the membrane or the cytosol.

Fusogenic liposomes, or fusosomes, are lipid-based nanocarriers engineered to merge directly with cellular membranes, enabling efficient cytosolic delivery of therapeutic or diagnostic cargo. These systems often incorporate viral fusion peptides or synthetic ligands to improve target specificity and enhance membrane fusion efficiency.

Membrane fusion itself is a fundamental biological process in which two lipid bilayers merge to form a continuous membrane, allowing the contents of previously distinct compartments to mix. This mechanism underlies essential cellular activities, including endocytosis, exocytosis, synaptic vesicle release, and intracellular vesicle trafficking. Fusion proceeds through a series of orchestrated steps: membrane recognition, docking, local bilayer destabilization, hemifusion (outer leaflet merging), and finally full fusion, characterized by pore formation and content mixing.

General frameworks for designing fusosomes should consider few crucial elements:

1. Building-Block Lipids
    - Structural scaffold: A zwitterionic phosphatidylcholine (PC) lipid (e.g. POPC) provides a stable bilayer "skeleton" that maintains vesicle integrity and fluidity under physiological conditions.[67]
    - Curvature modulators: Cone-shaped lipids such as phosphatidylethanolamine (PE) or high-curvature POPC enrich the bilayer with the necessary negative curvature, helping to stabilize the structure of vesicle and maintain membrane integrity.[67]
    - Membrane stiffeners: Cholesterol intercalates between phospholipids, increasing bilayer order and rigidity to prevent premature cargo leakage without abolishing fusogenicity (membrane-fusion capacity).[67]
    - Charge anchors: Cationic lipids (e.g. DOTAP) enhance electrostatic attraction to the typically anionic cell surface, promoting vesicle docking and fusion initiation.[68,69]
2. Fusogenic Triggers
    - Aromatic lipids: Lipids bearing aromatic headgroups (e.g. fluorescent BODIPY- or rhodamine-tagged PE) intercalate into membranes, locally perturbing lipid packing and reducing the activation energy for stalk formation; they also serve as built-in tracers for imaging. [68,70,71]
    - Conical lipids: In addition to their role as key curvature-inducing building blocks in the bilayer, their pronounced cone shape actively drives fusion by creating local membrane strain that stabilizes hemifusion intermediates and promotes pore opening.
    - Fusogenic peptides: Short peptides derived from viral fusion proteins insert into and destabilize target bilayers; studies show they induce liposome shrinkage and local lipid rearrangements that prime membranes for fusion.[72,73]
3. Application Specific Surface Modifications:
    - Antifouling zwitterions: Inclusion of additional zwitterionic lipids (e.g. DOPC) resists serum-protein adsorption, preserving fusogenic activity in complex media.[74]
    - PEGylation: Grafting PEG chains (via DSPE-PEG) further reduces nonspecific interactions, enhances colloidal stability in serum, and extends circulation time in vivo, with minimal impact on fusion when optimized at low molar ratios.[56,74]

- Targeting and reporting: Introduce reactive headgroups for antibody or ligand conjugation,[69,70,72,75], fluorescent lipids for imaging,[70,71] or stimuli-responsive lipids for controlled cargo release[52].
- Incorporate lipids bearing hydrophobic anchors (e.g., cholesterol or tocopherol) to secure fusosomes onto target membranes or solid supports.[76]

By balancing these elements – structural lipids, active fusogens, and adaptive surface modifications – fusosomes can be rationally tuned to achieve rapid, efficient, and specific membrane fusion for cytosolic delivery of drugs, nucleic acids, proteins, or imaging agents.[77]

The fusosome composition in this study consisted of DMPC (1,2-dimyristoyl-sn-glycero-3-phosphocholine), DOTAP (1,2-dioleoyl-3-trimethylammonium-propane), and DPPE-PEG2000 (1,2-distearoyl-sn-glycero-3-phosphoethanolamine-N-methoxy(polyethylene glycol)-2000).[56] At physiological temperature (37 °C), DMPC exists in a fluid, liquid-crystalline phase (T_m ≈ 24 °C), providing a flexible and stable bilayer structure that supports the dynamic membrane rearrangements required for fusion. The addition of 5 mol% DOTAP, a cationic lipid, introduces a positive surface charge that facilitates strong electrostatic interactions with negatively charged cellular membranes. This enhances membrane binding and lowers the energetic barrier to initial bilayer destabilization and hemifusion.[56,70,77] An important component is DPPE-PEG2000 that plays a multifaceted role. While PEGylation is traditionally associated with providing steric stabilization and reducing aggregation in serum-containing environments, at low concentrations it also supports fusion.[56,76] The PEG chains help exclude interfacial water, reducing hydration repulsion between bilayers – a phenomenon often referred to as “PEG-induced dehydration”.[78,79] In addition, the bulky PEG headgroups introduce lateral pressure at the membrane interface, generating packing defects and localized curvature that can serve as nucleation sites for lipid mixing.[80] This effect is particularly beneficial when used alongside fusogenic or cationic lipids, as it promotes closer membrane apposition without completely shielding the surface charge. Together, this carefully balanced combination of lipids ensures both colloidal stability and high fusogenic potential, enabling the vesicles to function effectively as fusosomes for direct membrane interaction and intracellular delivery.[56]

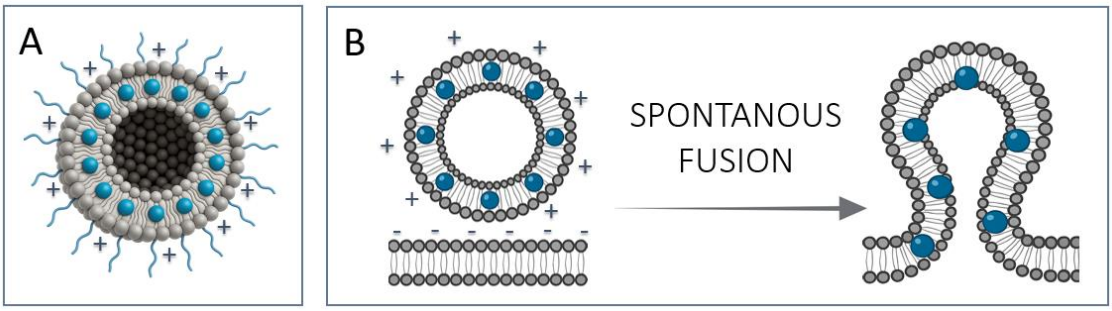

Figure 3.45 Schematic representation of fusosome structure and fusion mechanism. (A) Cross-sectional view of a fusosome composed of 74.5 mol% DMPC, 5 mol% DOTAP, and 0.5 mol% DPPE-PEG2000, with nanocrystals embedded between the lipid bilayers. The bilayer architecture is stabilized by DMPC, which exists in a fluid, liquid-crystalline phase at physiological temperature (37 °C). Surface-exposed DOTAP introduces a net positive charge, enhancing electrostatic interactions with negatively charged cellular membranes. PEGylated lipids (depicted with extended blue chains) contribute steric stabilization and promote membrane fusion by facilitating interfacial dehydration and inducing packing defects. (B) Upon contact with a negatively charged cellular membrane, the positively charged fusosome engages in electrostatic interactions, resulting in spontaneous membrane fusion. This process is driven by reduced hydration repulsion and membrane curvature stress induced by the PEGylated lipids, promoting lipid mixing and direct bilayer merger. The embedded nanocrystals are transferred directly into the target membrane, where they remain localized within the energetically favorable hydrophobic environment of the lipid tails.

In order to confirm the fusogenic capability of the liposome formulation, we performed a series of in-vitro experiments using liposomes labeled with the lipophilic fluorescent dye DiI (1,1'-Dioctadecyl-3,3,3',3'-Tetramethylindocarbocyanine Perchlorate). DiI is a highly hydrophobic, cationic indocarbocyanine dye that anchors into lipid bilayers via its two long C18 alkyl chains and serves as a highly sensitive probe for membrane fusion. Notably, DiI exhibits minimal fluorescence in aqueous environments due to aggregation and intramolecular flexibility, which favor non-radiative decay. Upon insertion into a lipid bilayer, the dye becomes brightly fluorescent as its chromophore is stabilized within the ordered, low-polarity membrane environment. This transition disrupts aggregate formation, restricts torsional motion of the polymethine chain, and significantly enhances its quantum yield – making fluorescence effectively gated by membrane embedding. The chemical structure of the dye is shown in Figure 3.46 A, and its spectroscopic profile after incorporation into vesicle membranes (Figure 3.46 B) reveals a distinct absorption peak near 550 nm and an emission centered at 570 nm. This environment-induced fluorescence makes DiI an ideal tracer for detecting lipid mixing and vesicle-cell fusion events.

In this set of experiments, we varied amounts of PEGylated lipid (DSPE-PEG2000) and kept constant DMPC and DOTAP. To assess how PEG density influences membrane fusion efficiency, we systematically adjusted the PEG content to 0.5 mol%, 1.0 mol%, 2.5 mol%, and 5.0 mol%. This concentration range was established based on previous findings by Gopalakrishnan et al.[56]

To visualize fusion events, we added 10 mol% of the fluorescent lipid DiI to each formulation. The remaining 90 mol% was used to preserve the original DMPC/DOTAP ratio (approximately 74.5:25), with the specified amount of PEG-lipid incorporated into this fraction. While the addition of DiI slightly reduced the absolute percentages of the other components, their relative proportions remained consistent across samples. This design ensured that any differences in fusion behavior could be attributed to the PEG content, without introducing variability from changes in the core lipid composition.

Panels C and D (Figure 3.46) display cuvettes containing the DiI-labeled vesicle suspensions under daylight and UV illumination, respectively. In white light, all samples look nearly identical, showing only a faint pink tint from the incorporated DiI, whereas UV excitation reveals the expected uniform orange-red fluorescence across every formulation.

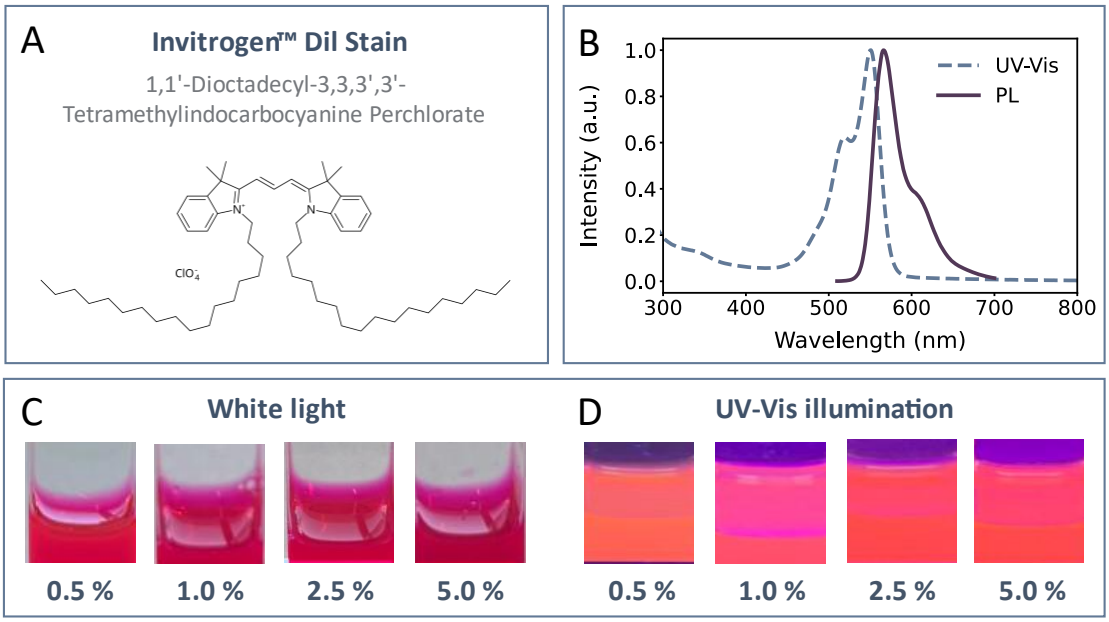

Figure 3.46 Characterization of DiI-labeled control liposomes used to evaluate vesicle-cell fusion. (A) Chemical structure of DiI [1,1'-dioctadecyl-3,3,3',3'-tetramethylindocarbocyanine perchlorate], a lipophilic cationic carbocyanine bearing two C18 alkyl tails that anchor stably into lipid bilayers. (B) Absorption (dashed blue) and photoluminescence (solid purple) spectra of DiI-labeleld liposomes. The dye, embedded within the vesicle membrane, exhibits a strong, narrow absorption peak centered at 550 nm and a fluorescence emission maximum at 570 nm, resulting in intense red-orange fluorescence. (C, D) Photographs of liposome suspensions containing 10 mol% DiI and increasing fractions of DSPE-PEG2000 (0.5, 1.0, 2.5, and 5.0 mol%). Images were taken under ambient white light (C) and UV illumination (D). Uniform bright-red fluorescence confirms successful incorporation of DiI in all formulations, enabling visual tracking of vesicle fusion in subsequent cell assays.

Fusion experiments were performed on spiking HEK293 monolayers, and the extent of membrane staining was evaluated via fluorescence microscopy and quantitative intensity profiling (Figure 3.47). At low PEG concentrations (0.5 mol% and 1.0 mol%), DiI fluorescence appeared sparse and punctate, with intensity profiles characterized by narrow, isolated peaks

and overall lower signal levels. This contrasts with the higher PEG conditions, reflecting more robust and continuous membrane labeling. This pattern is indicative of limited lipid mixing, suggesting incomplete hemifusion without substantial membrane incorporation. In contrast, at higher PEG concentrations (2.5 mol% and 5.0 mol%), the intensity profiles showed a continuous and uniform distribution of DiI along the cell periphery. The signal remained elevated across the scan, with minimal fluctuations toward lower intensity values. These trends paralleled the qualitative differences observed in the fluorescence images, confirming that vesicle fusion efficiency increases in a PEG-dependent manner. Across all conditions, bright-field images confirmed intact cell morphology, indicating no cytotoxic effects. Together, these data validate the functional integrity and fusogenic design of the liposomes proposed here.

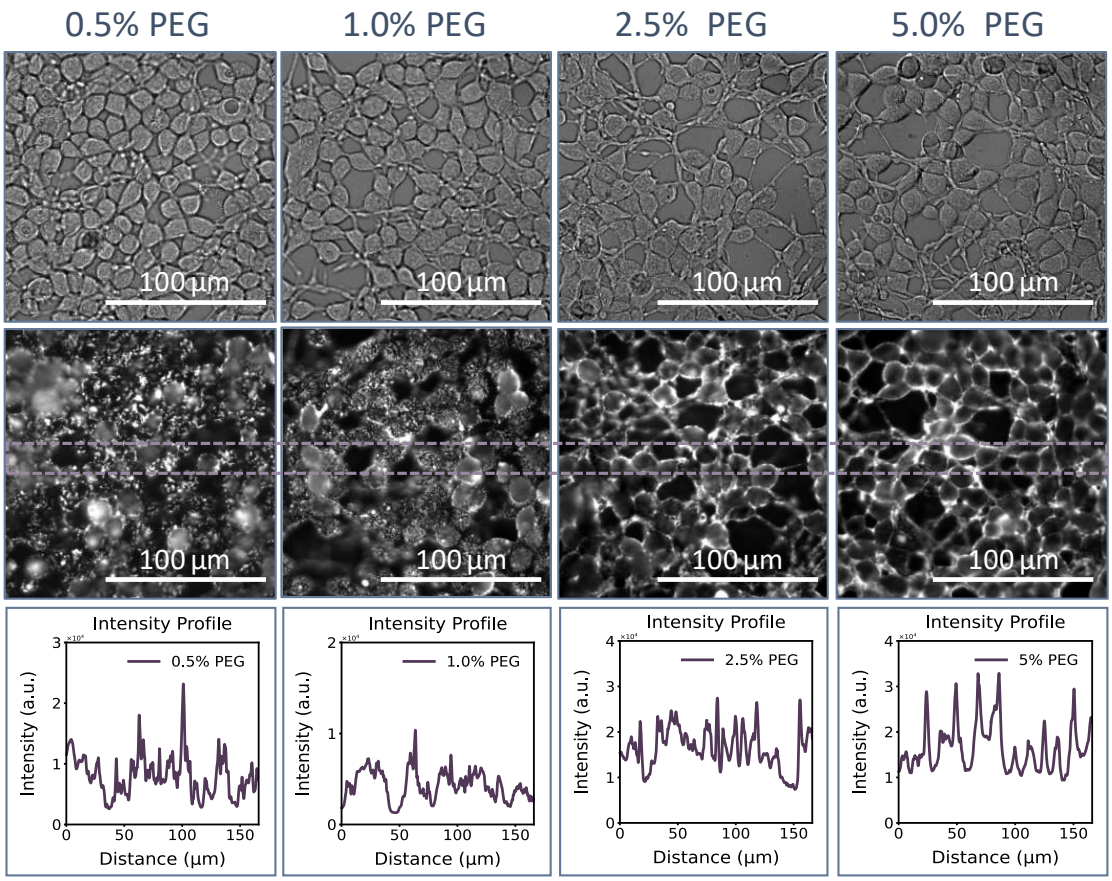

Figure 3.47 PEG-dependent fusion of DiI-labeled control liposomes with HEK293 cells. Bright-field (top row) and corresponding fluorescence (middle row) microscopy images acquired after 30 minutes of incubation with liposomes containing 0.5, 1.0, 2.5, or 5.0 mol% DSPE-PEG2000. All liposomes were labeled with 10 mol% DiI to track lipid mixing with the plasma membrane. Intensity profiles (bottom row) across the dashed purple lines reveal sparse, low-intensity, punctate signal at 0.5% and 1.0% PEG, and progressively stronger, more continuous fluorescence at 2.5% and 5.0% PEG, consistent with efficient membrane labeling.

Given the high efficiency of membrane fusion observed with DiI-labeled vesicles containing 5 mol% PEG-lipid, we next examined the minimum incubation time required to achieve detectable lipid mixing at the cell surface. This is an important experimental parameter since the fusion time constrains the time window needed to obtain representative data. That is, one needs to obtain fast fusogenesis that prolongate as long as possible to assure constant conditions for analysis of spikes dynamics. We tested durations range from 5 to 30 min to assess the kinetics of fusion under optimized conditions. As shown in Figure 3.48, membrane-associated DiI fluorescence was already detectable after just 5 minutes, with a continuous outline marking the cell periphery. However, the signal at this early time point appeared noticeably dimmer compared to longer incubations. By 10 and 15 minutes, the fluorescence intensity increased compared to the 5-minute time point and closely resembled the pattern observed at 30 minutes, although with slightly lower overall brightness. This suggests that membrane fusion initiates rapidly and progressively intensifies over time. Bright-field images confirmed preserved cell morphology throughout the time course, indicating that rapid fusion does not compromise membrane integrity. These results demonstrate that fusion occurs within minutes under optimal conditions, and confirm that 30-minute time window is sufficient to ensure complete and uniform membrane labeling.

In the following sections of this work, the terms vesicle, liposome, and fusosome will be used interchangeably, each referring specifically to the DMPC/DOTAP/DPPE-PEG2000-based vesicular structures described above (unless specified otherwise).

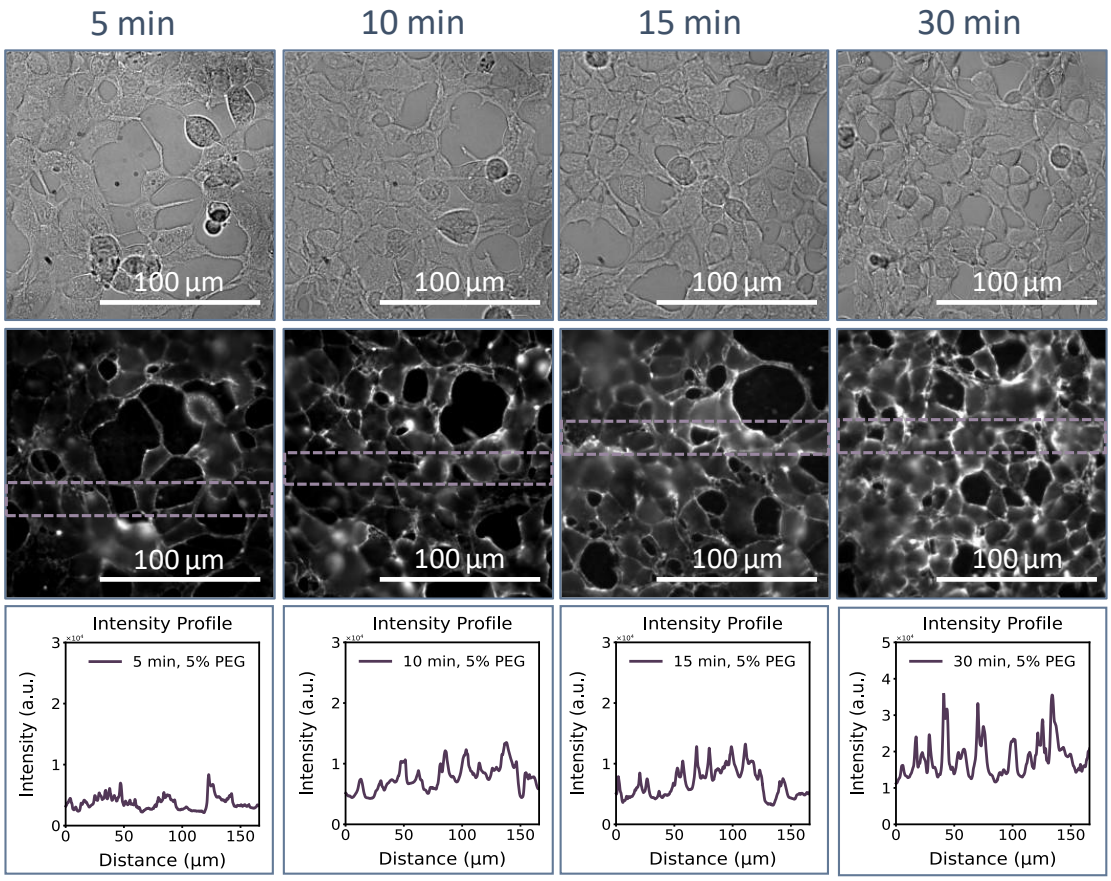

Figure 3.48 Time-course analysis of membrane fusion using DiI-labeled liposomes (5 mol% PEG). Bright-field (top row) and corresponding fluorescence (middle row) images of HEK293 cells incubated with DiI-labeled vesicles for 5, 10, 15, 30 minutes. A continuous fluorescent outline is visible as early as 5 minutes, indicating rapid initiation of lipid mixing. Intensity profiles (bottom row) show progressive increases in signal amplitude and uniformity over time, with the 30-minute trace reaching the highest and most consistent values, reflecting efficient and widespread membrane labeling. Cell morphology remains preserved at all time points, confirming that fusion proceeds without compromising membrane integrity.

Membrane staining

Building on the six nanocrystal systems introduced in 3.1.1 *Overview of Quantum-dot-based Platforms* and illustrated in Figure 3.17 (page 87), this section examines their interaction with cell membranes. The series includes one commercially available CdSe/ZnS reference (System I) and four custom-designed spherical quantum wells (Systems III-VI), each developed iteratively in response to experimental challenges encountered throughout the study. With aqueous transfer procedures in place, the next step is to evaluate how effectively these quantum dots associate with fusogenic vesicles. The membrane-staining results assessment of labeling performance and serve as a functional presented here provide a comparative, qualitative prelude to the fusion behavior explored.

System I

To evaluate the fusion capacity of the formulated fusosomes, we first examined vesicles incorporating commercially available CdSe/ZnS quantum dots capped with TOPO – referred to as System I (Figure 3.49, Panels A and B) – on HEK293 cell monolayers. Confocal fluorescence microscopy was used to monitor vesicle-cell interactions in real time, with the goal of determining whether fusion with the plasma membrane occurred and whether the quantum dots became incorporated into the membrane structure. The emission spectrum of the quantum dots showed a peak at 542 nm (Figure 3.49 B), enabling clear visualization of membrane-associated fluorescence. These experiments served as an initial validation of vesicle-cell fusion and provided a basis for evaluating the membrane integration of the quantum dots.

To systematically explore the variables influencing fusion efficiency, we investigated a range of parameters: cell seeding density (which affects monolayer confluency at the time of imaging), cell age (number of days post-seeding), the medium used during fusion (growth medium vs. PBS), fusion duration, time spent outside the incubator, and the volume of fusosomes suspension applied.

A critical challenge during imaging was the presence of cellular autofluorescence, which can obscure weak signals from membrane-bound quantum dots. This endogenous background signal arises from naturally fluorescent biomolecules such as NADH, flavins, and aromatic amino acids, and tends to intensify as cells age or undergo stress. The cellular autofluorescence can contribute background signals that may be mistakenly interpreted as probe-derived emission. Therefore, we carefully assessed imaging parameters to minimize such interference and ensure accurate evaluation of fusosome-mediated membrane staining.

Under the optimized conditions established through parameter screening, the most consistent and robust membrane labelling was achieved approximately 25-30 minutes after vesicle application. As shown in Figure 3.49 (Panels C-E), confocal fluorescence imaging of HEK293 cell monolayers (80% confluent, 24 hours post-seeding) incubated with quantum dot-loaded liposomes revealed a distinct green fluorescence outlining the cell periphery, accompanied by a limited number of bright intracellular puncta.

For these experiments, 500 µL of liposome suspension – DMPC, DOTAP, and DSPE-PEG2000 at a 74.5:25:0.5 molar ratio and extruded through a 100 nm membrane – was added directly to 2 mL of complete culture medium (DMEM supplemented with 10 % FBS) in each well. This gentle delivery strategy was chosen to preserve cell viability and minimize stress by avoiding abrupt

changes to the environment. Cells were incubated with the liposomes for 10-30 minutes, with optimal membrane-associated signal observed consistently at the 25-30-minute time point.

Imaging was performed using a Leica TCS SP5 confocal microscope with 458 nm laser excitation set to 30% of maximum power. Emission was collected using standard settings optimized for membrane-associated fluorescence. Full acquisition parameters are provided in the Appendix (Section 3.2.3).

The resulting images, presented on Figure 3.49, exhibit a largely continuous membrane-localized fluorescence signal, strongly suggestive of quantum dot integration into or association with the plasma membrane. The occasional presence of bright intracellular spots may arise from fused vesicle aggregates or local QD accumulation. However, the lack of extensive cytoplasmic or perinuclear fluorescence argues against large-scale internalization as the dominant mechanism.

The intensity plot profiles corresponding to the fluorescence micrographs within yellow rectangles (Fig. 3.31, panels C and D) provide further support for the membrane-associated localization of quantum dots. These profile scans show distinct peaks in fluorescence intensity at positions aligning with the cell periphery, indicating a higher concentration of fluorescent signal at the plasma membrane compared to the cell interior. The dual-peak pattern observed across individual cell profiles is consistent with fluorescence arising from left and right side of the membrane. The distance between the peaks corresponds to the diameter of HEK-293 cells, typically 10–15 μm, further confirming their assignment to cell boundaries. Background fluorescence remained stable at approximately 10 a.u., whereas membrane-associated regions reproducibly reached values two- to three-fold higher. Quantification across a population of approximately 30 cells confirmed this observation: statistics of fluorescence intensities measured at the cell outline and in the cytoplasm showed clearly separated distributions, with a calculated membrane-to-cytoplasm ratio (MCR) of 2.79 (Fig. 3.31 E). Overall, these spatial intensity profiles align with the interpretation that quantum dot-labeled vesicles preferentially associate with, or integrate into, the plasma membrane rather than being internalized.

While definitive distinction between fusion, adsorption, and endocytosis would require colocalization with membrane or endosomal markers, the overall fluorescence pattern demonstrates effective membrane staining and confirms that the liposome formulation reached and interacted extensively with the plasma membrane under the tested conditions.

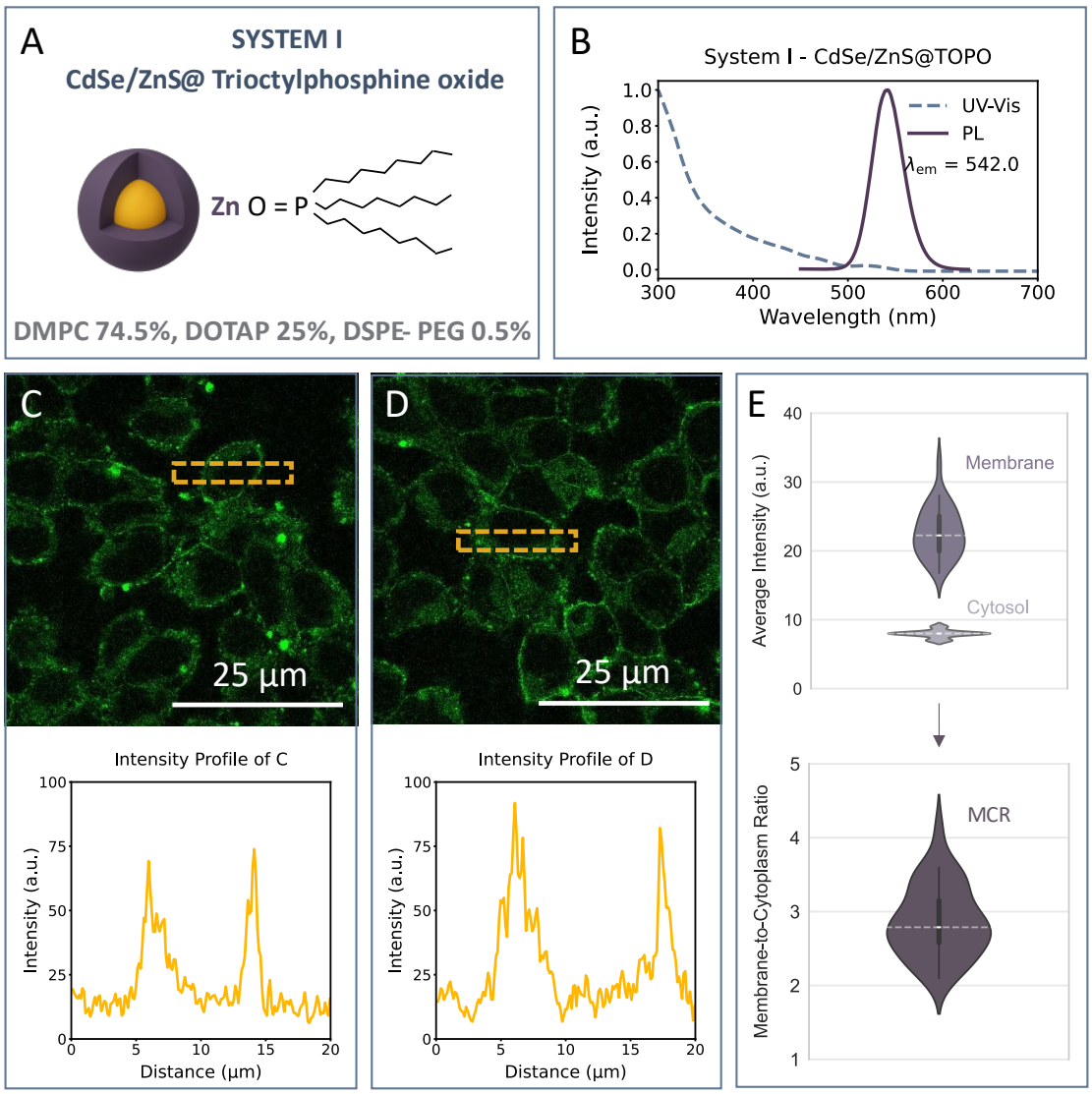

Figure 3.49 System I quantum-dot liposomes and membrane labelling of HEK-293 cells. (A) Schematic representation of System I: a CdSe/ZnS core-shell quantum dot capped with trioctylphosphine oxide (TOPO) and embedded in DMPC/DOTAP/DSPE-PEG2000 liposomes (74.5:25:0.5 mol%). (B) Absorption (dashed) and photoluminescence (solid) spectra of the QDs (λ_{em} = 542 nm). (C, D) Confocal micrographs of separate regions of a HEK-293 monolayer imaged 30 min after introduction QD-loaded liposomes. Yellow dashed rectangles indicate regions from which fluorescence-intensity profiles were extracted. Green fluorescence delineates the cell periphery, giving a continuous membrane outline. Background signals (~10 a.u.) are similar across all images, whereas the stained regions show recurrent peaks 2-3 times higher that coincide with the plasma membrane, consistent with uniform membrane-associated fluorescence throughout the sample. (E) Violin plots of average fluorescence intensities measured at the membrane and in the cytoplasm of approximately 30 cells. The derived membrane-to-cytoplasm ratio (MCR) is plotted below, showing a median value of 2.79. The distribution confirms preferential membrane-associated fluorescence with no significant intracellular staining.

To confirm that the membrane-associated fluorescence observed in the initial experiment was not an incidental or experiment-specific artefact, the staining protocol was repeated using an independently prepared HEK-293 cell culture. This replicate used a later-passage sample, imaged two days post-seeding to allow the monolayer to reach ~90% confluency. This replicate experiment was performed on a later-passage sample, imaged two days after seeding to allow

the monolayer to reach a slightly higher confluency (approximately 90%). Cells were treated under the same staining conditions as in the initial experiment.

Bright-field and fluorescence images were acquired sequentially at the same stage position using 458 nm excitation (argon laser at 30%, gain 50%, pinhole diameter 100 µm), allowing direct correlation between cellular morphology and fluorescence signal (Figure 3.50 A-C). To evaluate the contribution of endogenous cellular autofluorescence, an unstained control sample was imaged under identical optical settings. Intensity profiles across the dashed rectangles revealed consistent baseline levels of ~10 arbitrary units across all samples (Figure 3.50 D and E). In the control, the signal remained narrowly confined around this baseline, whereas in the stained samples (Areas #1 and #2), the profiles exhibited distinct peaks reaching intensities 2-3 times higher than the background. These elevated signals coincided with clear peripheral fluorescence outlining the cell boundaries in the stained images, indicating that the fluorescence arises from an external indicator rather than autofluorescence. The distance between peaks corresponds to the cell size (~10 µm). Collectively, these findings demonstrate that the signal enhancement is specific to the presence of quantum dot-loaded liposomes and that the observed labelling pattern is reproducible across independent experiments.

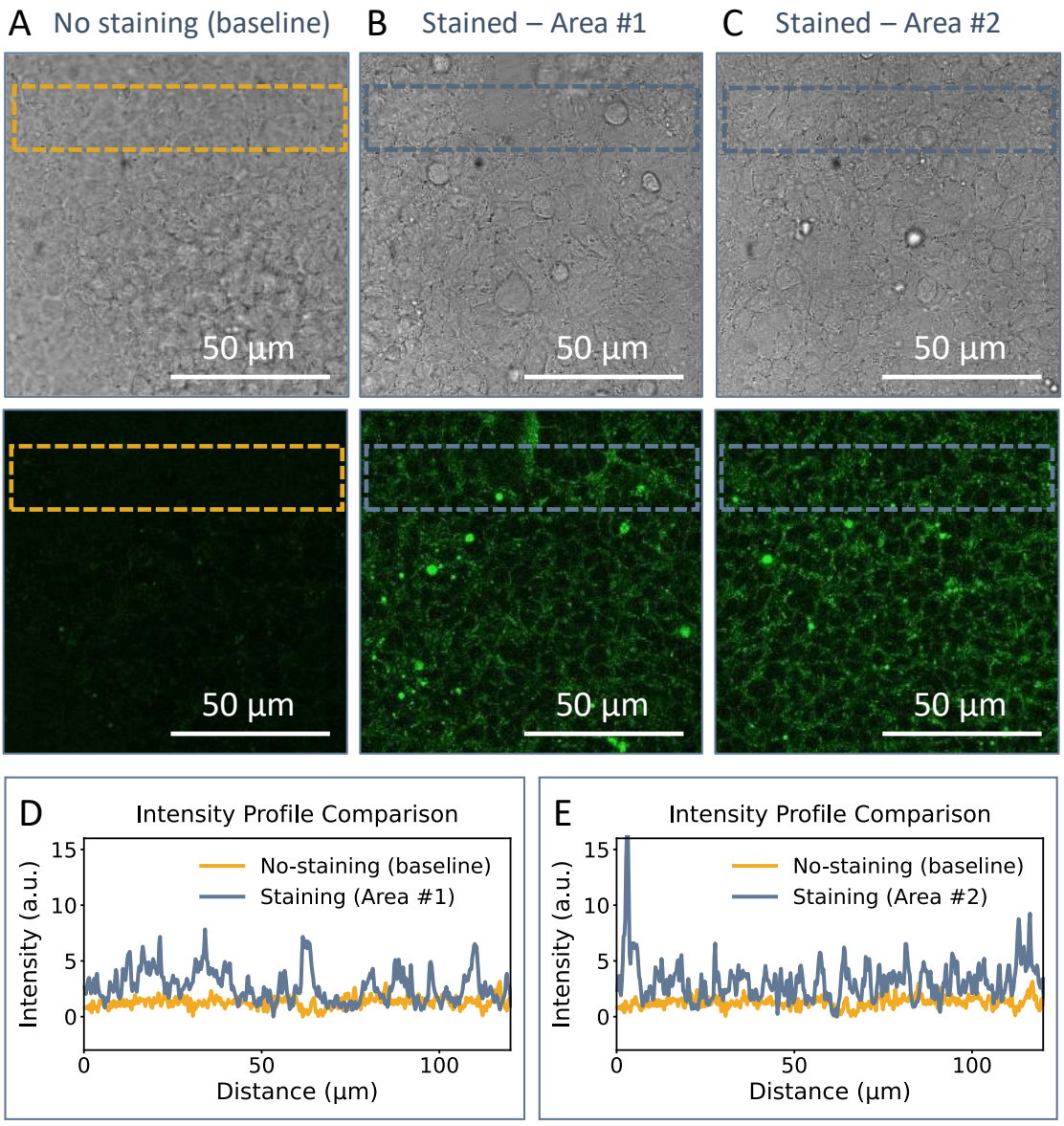

Figure 3.50 Reproducible membrane labelling of HEK-293 monolayers with quantum-dot (QD) liposomes. (A) Unstained control, (B) stained – Area 1, (C) stained – Area 2. Each panel shows a bright-field image (top) and the corresponding fluorescence image acquired with 458 nm excitation (argon laser 30%, gain 50%, pinhole 100 µm). Cells were imaged 30 min after addition of DMPC/DOTAP/DSPE-PEG2000 (74.5:25:0.5 mol%) liposomes (100 nm extrusion; 500 µL in 2 mL DMEM + 10% FBS). Green QD fluorescence is predominantly localized at the cell periphery, tracing a largely continuous outline of the membrane with sporadic brighter spots, whereas the baseline shows only low autofluorescence. (D, E) Fluorescence intensity profiles across the dashed rectangles in A-C show similar background levels (~10 a.u.), but stained areas (B and C) display peaks with 2-3-fold higher intensity, consistent with membrane-associated fluorescence.

Systems III-V

Having established the behavior of fusosomes incorporating commercial TOPO-stabilized quantum dots, we next turned our attention to custom-engineered nanocrystals with refined structural and surface properties. The following experiments focused on Systems III-V, marking the beginning of our investigations into liposomes containing spherical quantum wells and their interaction with a specialized spiking HEK cell model (Chapter 2 *Self Spiking HEK cells*).

System II, spherical quantum wells stabilized with cadmium oleate, served as the initial material for this set of experiments. However, as previously discussed (see *PLQY in the presence of lipids*, page 116), these nanocrystals exhibited a pronounced loss of fluorescence upon mixing with lipids. As a result, the vesicles prepared with this formulation were non-emissive, making it impossible to detect membrane fusion events. Given the limitations in optical signal detection, the system II was discarded from further study.

We replaced the native cadmium oleate ligands with zinc oleate, generating a new formulation – System III. This adjustment preserved the structural and optical integrity of the CdS/CdSe/CdS spherical quantum wells, which exhibited stable dispersion in non-polar solvents and retained bright, spectrally narrow green emission (λ_{em} = 530 nm, Figure 3.51 B) after incorporation into liposomes. Unlike System II, these vesicles remained fluorescent throughout their incubation with HEK293 cells, indicating that the Zn-oleate surface effectively prevented photoluminescence quenching in the lipid matrix. However, imaging revealed that this optical improvement did not translate into successful membrane staining. The fluorescent signal appeared as scattered, punctate spots, often detached from the cell membrane or localized within the cytoplasm, with no evidence of the continuous peripheral signal characteristic of uniform membrane labeling (Figure 3.51). These results imply that while Zn-oleate capping improves photostability, it may hinder the lipid mixing or membrane anchoring required for efficient nanocrystal delivery. The same fluorescence pattern was consistently observed across multiple independent samples, indicating a reproducible yet unsuccessful membrane staining outcome. This prompted a further reevaluation of the surface ligand architecture, with a focus on maintaining high quantum yield while enabling closer interaction with the lipid bilayer to facilitate effective vesicle-membrane fusion.

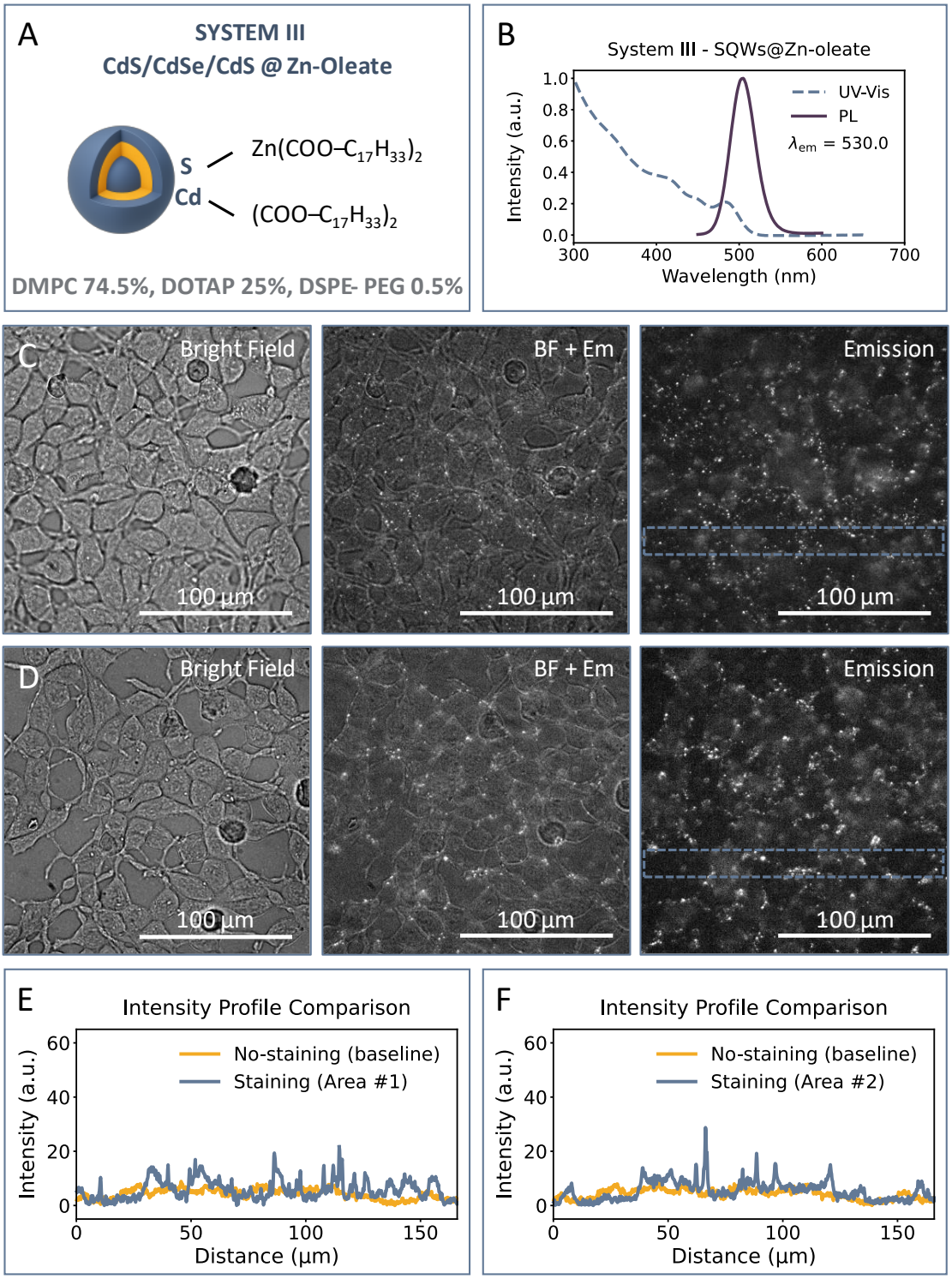

Figure 3.51 Representative results for System III: CdS/CdSe/CdS SQWs capped with Zn-oleate. (A) Nanocrystal structure schematic; lipid formulation: DMPC 74.5%, DOTAP 25%, DSPE-PEG2000 0.5%. (B) UV-Vis and PL spectra in hexane; emission peak at 530 nm. (C-D) HEK293 imaging after 30 min incubation with SQW-loaded liposomes shows scattered puncta without continuous membrane signal. (E-F) Intensity profiles from marked regions in C and D display irregular peaks near baseline, indicating non-membrane-localized fluorescence.

Panels E and F on Figure 3.51 present fluorescence intensity profiles corresponding to the blue rectangular regions marked in panels C (Area #1) and D (Area #2), respectively. In both cases, the profiles are plotted alongside a baseline trace obtained from a non-stained control sample of the same cell model (Appendix, Figure A.4), confirming minimal background signal under identical imaging conditions. System III samples exhibit multiple sharp, localized peaks that rise above the baseline, consistent with the presence of discrete fluorescent spots within the scanned regions. However, the profiles lack the dual-peak pattern typically associated with membrane-localized labeling, and the signal between peaks returns to levels comparable to those of the control. These features suggest that the observed fluorescence does not correspond to a uniform membrane-associated distribution, but rather to isolated accumulations, possibly reflecting vesicles loosely associated with the membrane or internalized structures. The overall similarity between the two profiles supports the reproducibility of this spatial pattern across different areas and different samples, reinforcing the conclusion that while the Zn-oleate surface maintains photoluminescence in the presence of lipids, it does not facilitate consistent membrane labeling under the tested conditions.

To rule out any uncertainty about PEG density as a limiting factor, we repeated the fusion assay with vesicles containing 5 mol% DSPE-PEG2000 while keeping the DMPC/DOTAP scaffold unchanged. Under these conditions, System III [CdS/CdSe/CdS SQWs, $\lambda_{em} \approx 530$ nm] (Figure 3.52). The fluorescence images are dominated by large, irregular aggregates dispersed throughout the field of view, while true membrane-associated fluorescence remains undetectable. No continuous rim of fluorescence tracing the cell perimeter was detected. Many bright spots appeared, but these were randomly distributed and not spatially correlated with cell outlines. Figure 3.55 Bright-field images confirmed that the HEK293 monolayers remained morphologically intact, indicating that the cells remained healthy.

We attribute the persistent lack of membrane staining to inherent limitations of the nanocrystals – specifically, their low brightness, limited stability in biological media, and surface chemistry that likely hinders efficient lipid mixing.

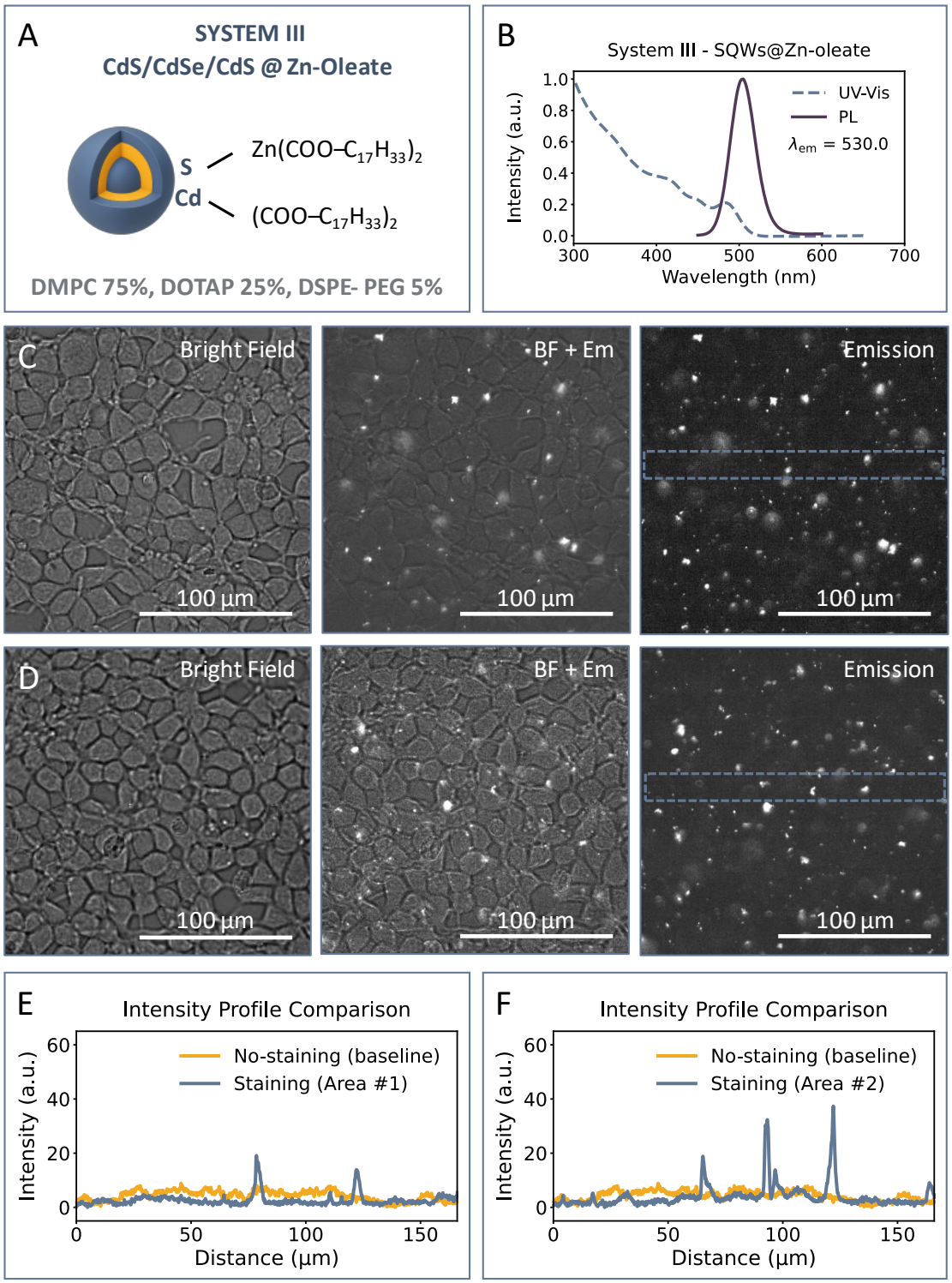

Figure 3.52 Representative results for System III (CdS/CdSe/CdS SQWs) delivered using vesicles containing 5 mol% PEG-lipid. (A) Schematic of SQW structure with Zn-oleate ligands; lipid mix: DMPC 75%, DOTAP 25%, DSPE-PEG2000 5%. (B) UV-Vis (dashed blue) and PL (solid purple) spectra; λ_{em} = 530 nm. (C-D) Fluorescence remains punctate and non-membrane-associated despite increased PEG concentration. (E-F) Intensity profiles from Areas #1 and #2 (C and D respectively) show sparse, narrow peaks near control levels, confirming lack of membrane labeling.

Replacing the oleate shell with a mixed cadmium-fluoride/octylamine passivation layer (System IV) produced colloidal SQWs that retained the archetypal CdS/CdSe/CdS architecture (Figure 3.53 A) while emitting a narrow green band centered at 541 nm (Figure 3.53 B). The new ligand set improved the interaction between the nanocrystal-loaded vesicles and the plasma membrane. In both presented regions (Figure 3.53, panels C and D), the fluorescence channel revealed pattern coincident with the cell boundaries seen in bright-field mode. Only a few discrete intracytoplasmic spots were detected, and extracellular aggregates were largely absent. The merged BF + Em overlays further confirm that the photoluminescent signal is confined to the cell perimeter, indicating that the liposome cargoreachedthe outer leaflet of the HEK293 membrane. The absence of diffuse cytosolic glow argues against vesicle endocytosis, whereas the uniform rim suggests lipid-to-lipid fusion rather than adsorption.

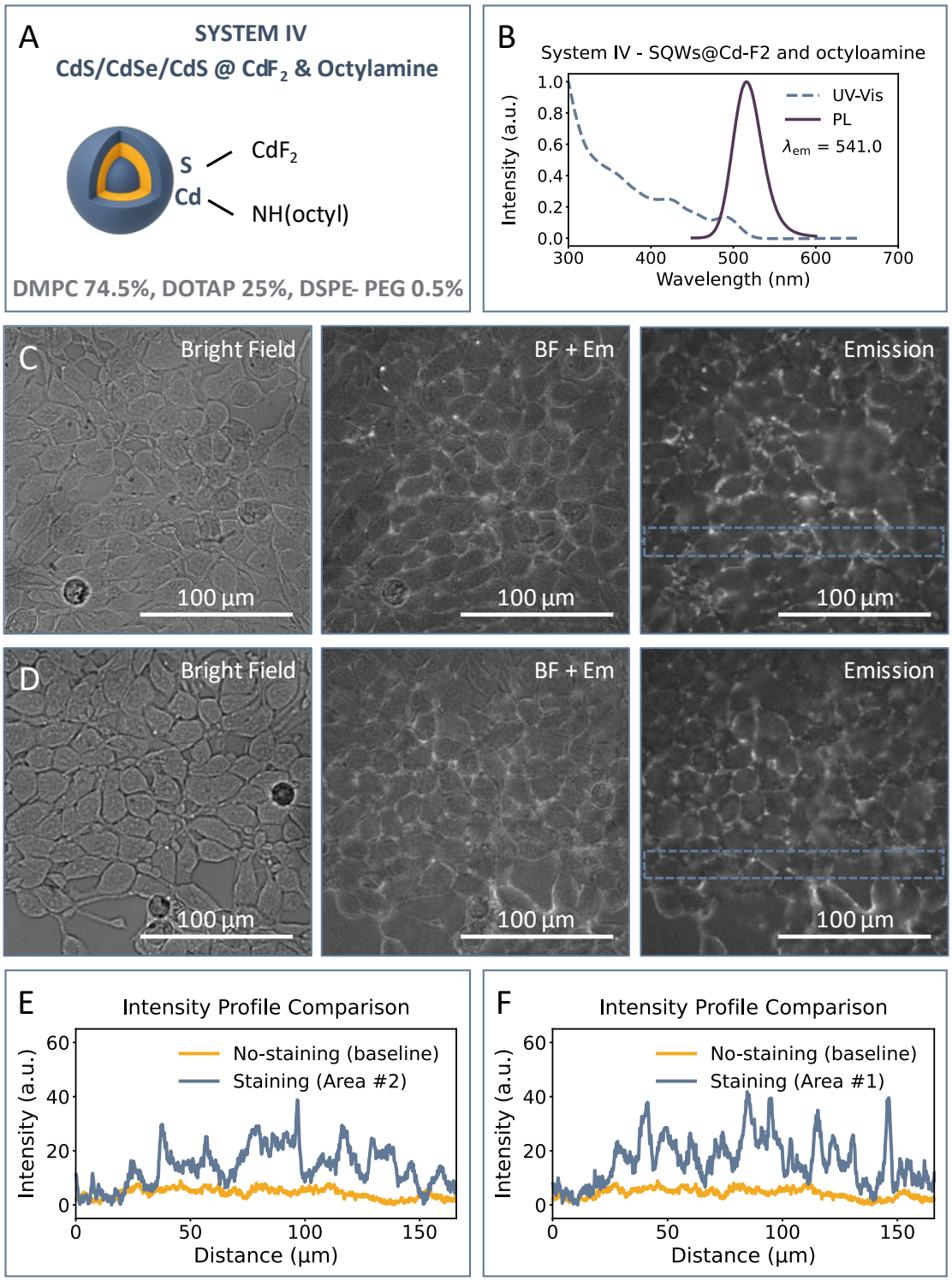

Figure 3.53 Representative membrane staining with System IV liposomes loaded with CdS/CdSe/CdS SQWs capped by CdF_2/octylamine. (A) Schematic of SQW structure and ligand composition. Lipid mix: DMPC 74.5%, DOTAP 25%, DSPE-PEG2000 0.5%. (B) Optical spectra showing UV-Vis (dashed blue) and PL (solid purple), λ_{em} = 541 nm. (C-D) Fluorescence microscopy of HEK293 cells after 30 min incubation shows uniform membrane-associated signal. (E-F) Intensity profiles reveal consistent signal above baseline with regularly spaced peaks, indicating effective membrane localization.

This interpretation is further supported by the fluorescence intensity profiles shown in panels E and F, corresponding to the emission regions from Areas #1 and #2. In both traces, the signal remains above the baseline obtained from an unstained control (Appendix, Figure A.4), with a series of peaks indicative of fluorescence along the cell periphery. This pattern stands in contrast to the profiles observed for System III, which exhibited irregular spikes corresponding to puncta and showed no indication of membrane association. The broader peaks observed for System IV suggest homogeneous distribution of the fluorophores and association with the plasma membrane across different regions of the sample. These spatial profiles, in agreement with the imaging data, support the conclusion that the CdF_2/octylamine surface chemistry facilitates vesicle-membrane interaction while maintaining photoluminescence for imaging at 100 ms exposure. Compared to the discontinuous signal seen in System III, System IV achieves membrane-specific labeling, highlighting the importance of surface ligand composition in directing vesicle behavior at the cellular interface. However, while the signal is detectable under current conditions, the overall fluorescence intensity remains below the level required for high-speed imaging of neural dynamics. Our goal is to develop a labeling system that not only enables accurate membrane targeting but also exceeds the brightness of conventional indicators, allowing for shorter exposure times and higher frame rates.

To enhance signal intensity while maintaining resistance to lipid-induced quenching, we subsequently explored System V, which features a CdS/CdSe/CdS core-well structure further passivated with an outer ZnS shell. As described in Section 3.2.2 *PLQY in the presence of lipids,* this additional layer significantly improves optical performance, yielding a PLQY of approximately 50% in non-polar lipid-rich solutions and retaining around 30% in aqueous media – making it the most photostable and efficient formulation within our current nanocrystal library.

Despite this favorable photophysical profile, membrane staining using System V was less efficient than that achieved with the CdF_2/octylamine-capped SQWs of System IV. Also, no effect of PEG concentration was observed on the quality of staining. Fluorescent microscopy of samples revealed a punctate fluorescence pattern distributed sparsely throughout the sample, with no continuous membrane-associated signal, regardless of PEG amount. Emissive spots were frequently observed away from the cell periphery, either adjacent to or detached from the membrane, suggesting inefficient delivery of nanocrystals to the plasma membrane and an absence of clear evidence for membrane fusion. Several factors may contribute to this reduced fusogenic behavior. The addition of the ZnS shell increases the overall particle size, which may elevate the energetic barrier for lipid mixing and bilayer incorporation. Furthermore, the long

and conformationally rigid chain of Zn-oleate ligands may create a steric barrier that limits close contact between the SQWs and the cell membrane, potentially hindering effective mixing with the acyl chains of the lipid bilayer. These results underscore the delicate balance between optical optimization and membrane interaction, highlighting the need to tailor both surface chemistry and structural parameters to achieve efficient and bright membrane labeling.

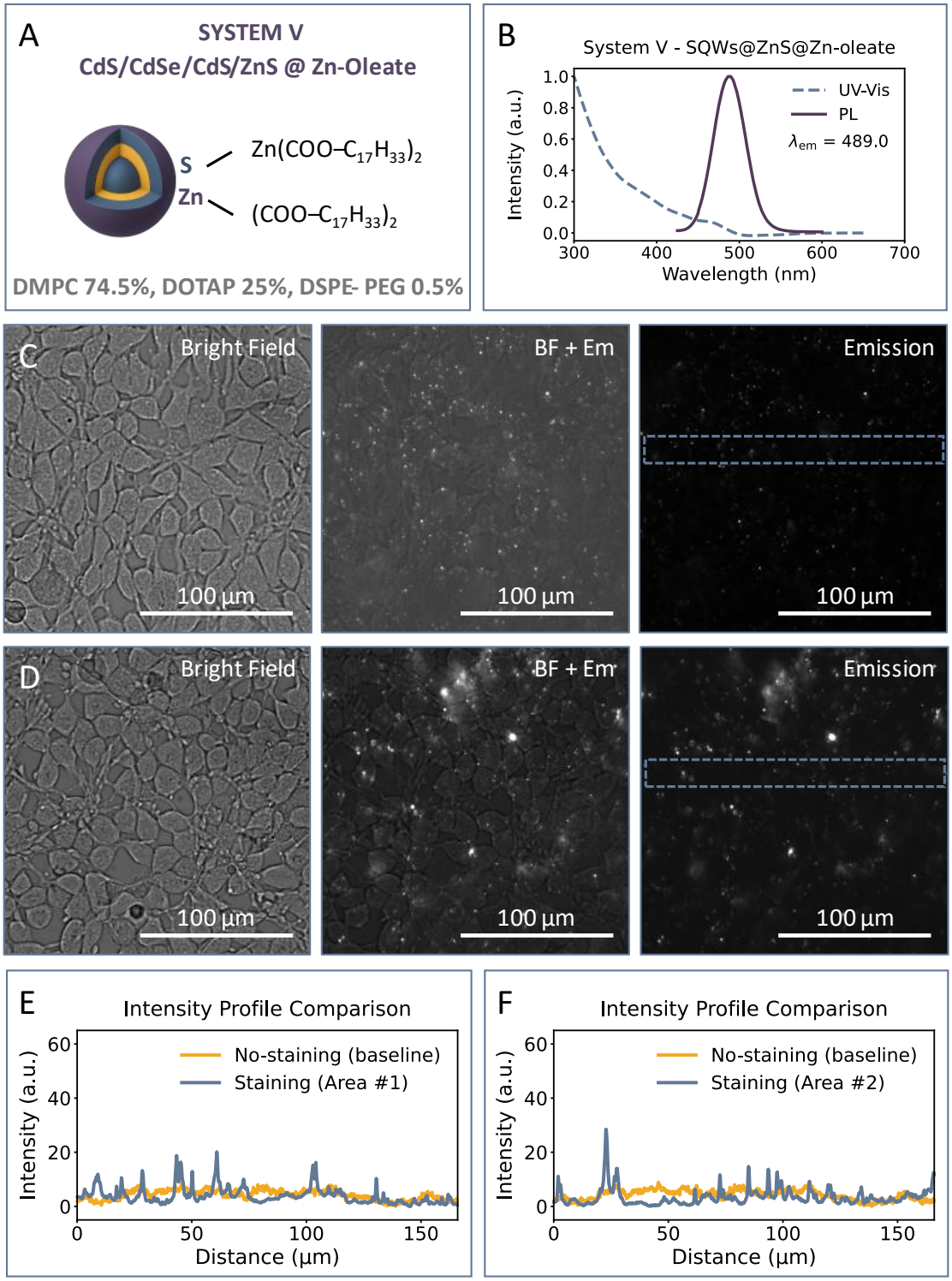

Figure 3.54 Fluorescence microscopy of System V: CdS/CdSe/CdS/ZnS SQWs with Zn-oleate ligands. (A) Schematic of nanocrystal structure; lipid formulation: DMPC 74.5%, DOTAP 25%, DSPE-PEG2000 0.5%. (B) UV-Vis (dashed blue) and PL (solid purple) spectra in non-polar solvent; λem = 489 nm. (C-D) Imaging of HEK293 cells shows sparse spots with no clear membrane-associated signal. (E-F) Intensity profiles across blue rectangles in C and D reveal weak, irregular peaks near baseline, indicating poor membrane localization.

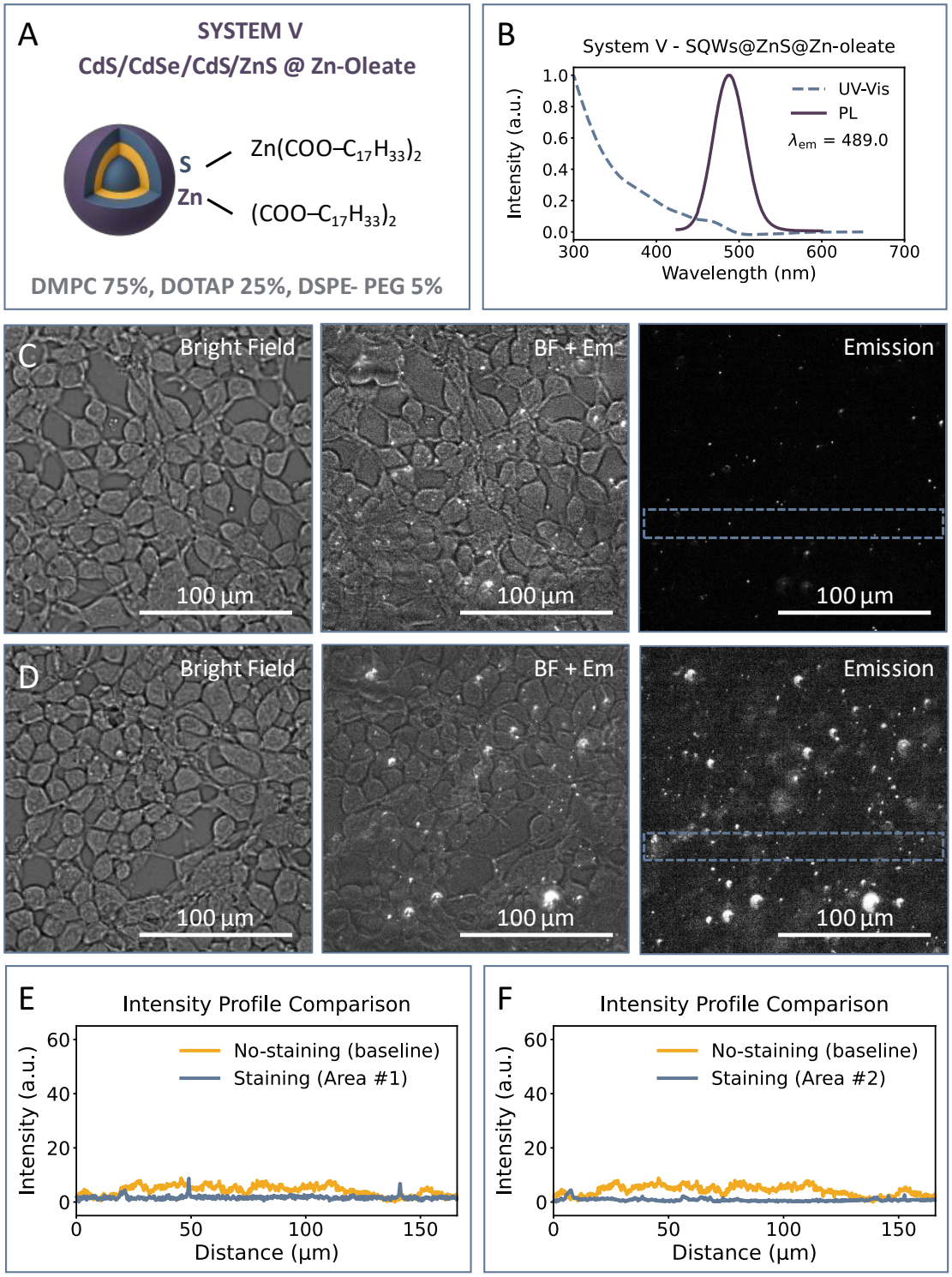

Figure 3.55 Representative results for System V (CdS/CdSe/CdS/ZnS SQWs) delivered using vesicles containing 5 mol% PEG-lipid. (A) SQW structure with Zn-oleate ligands and outer ZnS shell; lipid mix: DMPC 75%, DOTAP 25%, DSPE-PEG2000 5%. (B) UV-Vis (dashed blue) and PL (solid purple) spectra; λ_{em} = 489 nm. (C-D) Bright-field and fluorescence images show sparse, non-membrane-associated puncta despite increased PEG content. (E-F) Intensity profiles from Areas #1 and #2 (C and D respectively) remain near baseline, confirming lack of membrane staining.

System VI

To further optimize the surface chemistry of QD we performed a ligand exchange in which zinc bis(2-hexyldecanoate) [Zn(2-hexyldecanoate)$_2$] was used in place of Zn(oleate)$_2$ as the surface capping agent. In this configuration, Zn^{2+} ions coordinated by branched 2-hexyldecanoate ligands bind to surface chalcogenide (S^{2-}) sites, preserving electronic passivation while forming a more sterically bulky and loosely packed ligand shell. Compared to the linear C_{18} oleate, the secondary-alkyl branching of 2-hexyldecanoate disrupts efficient chain packing, reduces inter-ligand van der Waals interactions, and increases conformational entropy at the nanocrystal interface. These properties have been linked to significantly enhanced solubility, reduced aggregation, and improved film formation, as demonstrated by Yang et al., who described such ligands as "entropic" in their behavior.[81] Based on this, we hypothesized that the branched-ligand shell would facilitate lipid penetration and improve compatibility with the plasma membrane. To test this, SQW-loaded vesicles were prepared using 5 mol% DSPE-PEG2000 – an optimized formulation previously shown to support rapid and efficient fusion in DiI-labeled system – and evaluated for their ability to achieve uniform membrane staining.

The staining performance of System VI is presented in Figure 3.56. Panels A and B show the nanocrystal architecture and optical characterization, with the emission peak centered at approximately 495 nm. The lower panels display representative fluorescence and corresponding bright-field images acquired after a 30-minute incubation with HEK293 cells. Each column depicts a distinct field of view from separate samples, including two independent liposome batches prepared and imaged on different days. The consistency across these measurements confirms the reproducibility of the observed outcome.

In all samples, bright, continuous fluorescence clearly delineates the cell perimeter, indicating efficient delivery of SQWs to the plasma membrane via vesicle fusion (Figure 3.56). In each of the three analyzed regions, the fluorescence signal remains consistently elevated above the unstained control baseline (yellow trace; Appendix, Figure A.4) across nearly the full scan length, dipping only at locations corresponding to spaces between neighboring cells. The profiles exhibit broad, gradually rising and falling signal plateaus, in contrast to the narrow, irregular spikes characteristic of Systems III and V, confirming a uniform distribution of SQWs along the plasma membrane. Signal intensity and pattern are highly consistent across Areas #1, #2, and #3, underscoring the reproducibility of the staining achieved with independently prepared liposome batches on three independent samples. The corresponding bright-field images confirm the integrity and confluency of the HEK293 monolayer, indicating that both the fusogenic vesicle formulation and the modified SQWs are well-tolerated by the cells.

System VI yielded visibly stronger fluorescence and markedly higher membrane-to-background contrast. Notably, it supported shorter exposure times (as low as 30 ms), enabling frame rates up to ~33 Hz – beyond the capability of System IV under the same conditions. This represents an important step toward high temporal resolution, real-time imaging such as neuronal activity imaging, where temporal resolution is critical. Still, the achieved brightness remains below the potential of quantum dot-based probes, suggesting further optimization of ligand chemistry and nanocrystal architecture is needed to fully realize their performance in fast, high-resolution cellular imaging.

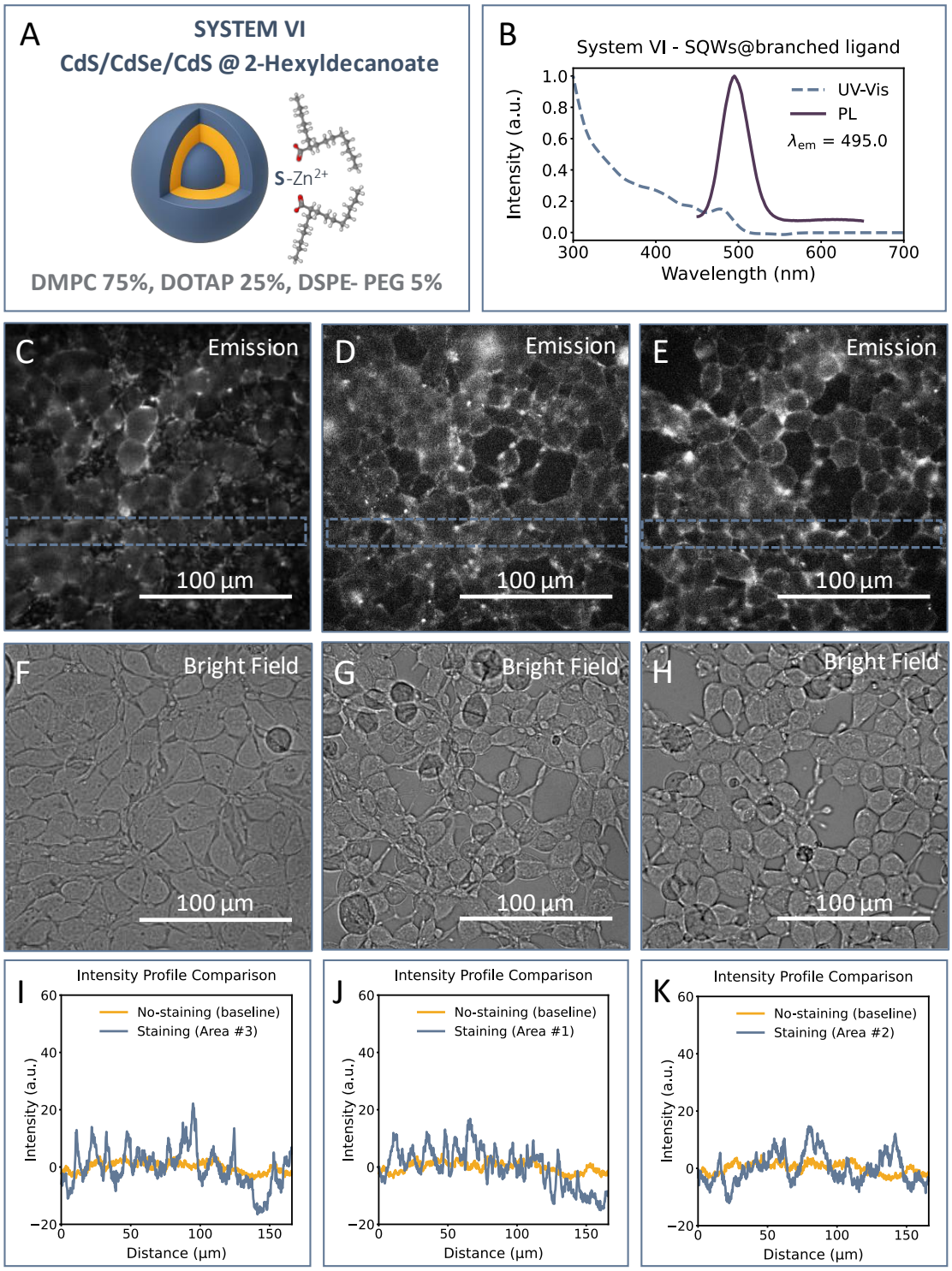

Figure 3.56 Representative membrane staining results for System VI: CdS/CdSe/CdS SQWs capped with branched 2-hexyldecanoate ligands. (A) Schematic of SQW structure; vesicles contained DMPC 75%, DOTAP 25%, DSPE-PEG2000 5%. (B) UV-Vis (dashed blue) and PL (solid purple) spectra; λ_{em} = 495 nm. (C-H) Fluorescence and bright-field images of HEK293 cells after 30 min incubation show strong, continuous membrane labeling. (I-K) Intensity profiles from Areas #1-3 confirm uniform fluorescence above baseline, supporting efficient and reproducible delivery to the plasma membrane.

4. Recordings of Spiking HEK Cells with Spherical Quantum Dots

Building on the advances presented in the previous chapter – where SQWs functionalized with branched ligands produced membrane staining bright enough to support high-speed imaging – this chapter evaluates the feasibility of using these nanocrystals as optical sensors of neuronal spiking. Inspired by the pioneering work of Park and Weiss, who demonstrated that peptide-coated CdSe/CdS nanorods could optically report spiking activity in self-firing HEK cells via the quantum-confined Stark effect (QCSE),[82] we explore whether spherical quantum wells (SQWs) offer advantages in signal quality and temporal resolution. In contrast to nanorods, which achieved promising but limited performance (~0.6% ΔF/F at 33 Hz)[82] due to suboptimal membrane insertion and fluorescence intermittency, SQWs provide symmetric three-dimensional confinement, near-unity quantum yield, and orientation-independent membrane interaction – features that may enhance spike detectability.

Our experimental workflow is outlined in Figure 3.57. Spontaneously spiking HEK cells, originally engineered by the Cohen lab, serve as the model system. These cells exhibit autonomous, periodic spiking behavior across the monolayer, with remarkably consistent frequency – effectively providing a convenient optical ground truth without the need for electrodes. Since experiments were conducted over multiple passages and across an extended period of time, careful records of passage number and culture conditions were maintained for each batch. For every sample prepared for SQW membrane staining and voltage imaging, a corresponding "twin" sample from the same batch (seeded under identical conditions) was prepared for calcium imaging with Calcium Green-1. This design ensures that the spiking behavior of each experimental batch is validated in parallel, and provides a reference for the expected spiking frequency during SQW recordings.

The following section describe the data analysis workflow, including signal processing, spike detection, and frequency-domain characterization, with the goal of determining the practical usability of SQWs as a tool for real-time optical voltage imaging.

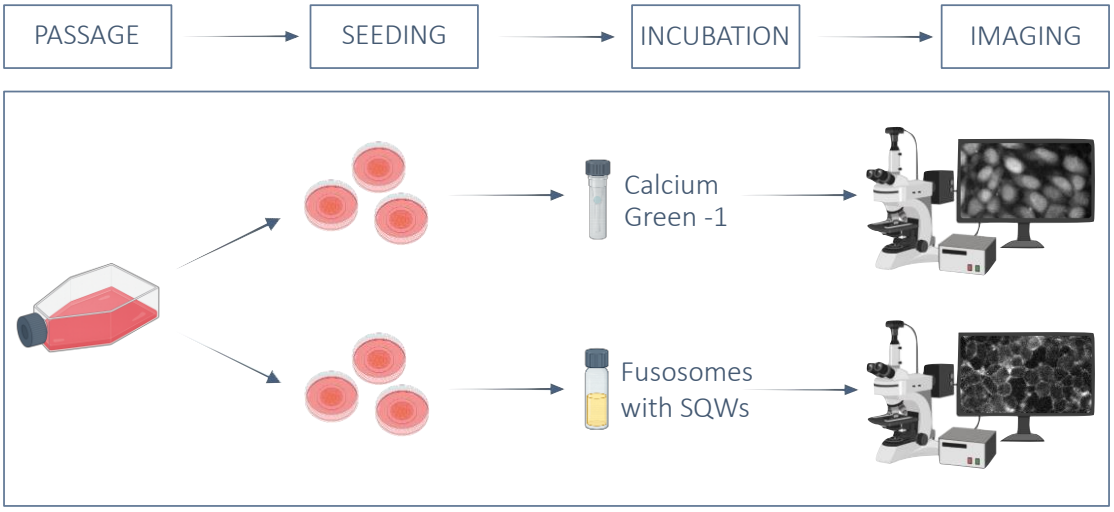

Figure 3.57 Experimental workflow for imaging spiking HEK cells. HEK cells were maintained in continuous culture and expanded through serial passaging. For each experimental set, cells from the same culture batch were seeded under controlled and identical conditions (seeding density, medium composition, incubation parameters). To validate spiking behavior and to establish a reference for expected spiking frequency, each sample subjected to membrane staining with spherical quantum wells (SQWs) was paired with a corresponding control sample stained with Calcium Green-1. Both SQW-labelled and calcium-labelled samples were imaged using wide-field fluorescence microscopy, with acquisition settings optimized for each probe. This parallel design allows direct comparison of SQW-derived signals with calcium transients from matched experimental conditions.

Data acquisition and processing

Fluorescence image sequences were acquired using a Hamamatsu ORCA-Flash 4.0 scientific CMOS camera (model C11440-22CU), operated through HCImage Live software (Hamamatsu Photonics). Imaging was performed with a 40×/0.8 NA water-immersion objective at 33.33 fps (30 ms exposure time). To enhance signal-to-noise ratio, hardware binning was set to 4 × 4 for voltage imaging with SQWs. Each SQWs recording was acquired at a frame size of 256 × 256 pixels, corresponding to a calibrated field of view of approximately 166.4 µm × 166.4 µm. For calcium imaging, for higher spatial resolution, images were acquired at 1024 × 1024 pixels with no binning at 10 fps rate (100 ms exposure). Raw image data were saved in Olympus ".cxd" format, which preserves both image stacks and acquisition metadata.

For data analysis, ".cxd" files were imported into Fiji (ImageJ) using the Bio-Formats importer. Regions of interest (ROIs), defined cellular regions or smaller (5 × 5 pixels) bright spots within the cell membrane, were manually selected from the image stacks. To correct for camera-induced electronic bias during 4 × 4 binning, a fixed baseline offset of 1600 analog-to-digital units (ADU), as specified by the manufacturer and confirmed in the acquisition metadata, was

subtracted from each pixel across all frames. For each defined ROI, the mean fluorescence intensity was calculated for every frame, resulting in a time-series trace representing the fluorescence dynamics of that region. These intensity traces were then exported from Fiji as "csv" files and further analyzed in Python, where additional processing steps – including baseline correction and signal filtering – were performed (Table 3.4).

These pre-processed fluorescence traces were first corrected for slow baseline drifts, which could arise from residual photobleaching, mechanical instability, fluctuations in illumination, or gradual changes in the sample environment. An asymmetric least-squares (ALS) algorithm was employed for this purpose. While originally optimized for calcium imaging data, the same correction was applied to SQW recordings. In an ideal case, minimal signal processing would be required, and spike-related transients would be clearly visible both in the raw fluorescence traces and directly observable during video playback. In practice, however, the current signal-to-noise ratio of the recordings is too low to distinguish spikes from background fluctuations without additional processing steps. To enhance the detection of fast transient events, the traces were subsequently smoothed using a Savitzky-Golay filter and processed with a Butterworth band-pass filter, effectively preserving spike-like features while suppressing high-frequency noise and low-frequency drift. The processed and raw signals were then examined using Welch's method, which provides an estimate of the power spectral density (PSD) and enables assessment of the dominant frequency components within the data. Unlike a standard Fourier transform, which applies a single transform to the entire trace and can produce highly variable spectral estimates in noisy, finite-length signals, Welch's method divides the time series into shorter, overlapping segments. Each segment is windowed to reduce edge artefacts, and the resulting periodograms are averaged to produce a smoother and more reliable PSD. This approach is particularly well suited to the fluorescence recordings used in this study, where the signals are relatively short in duration and subject to both biological and instrumental noise. In the last step, automated peak detection was performed (on both raw and filtered data) to extract quantitative parameters, including number of detected peaks, average frequency and standard deviation, which formed the basis for the subsequent statistical analyses. Because quasi type-II spherical quantum wells respond to changes in the transmembrane field primarily through dimming, analysis of minima in the fluorescence traces would in principle be sufficient. However, both maxima and minima were evaluated to ensure robust detection of periodic modulation. This approach accounts for field polarity reversals during action potentials and minimizes the influence of baseline fluctuations, allowing reliable extraction of the dominant oscillation frequency for comparison with calcium imaging data.

Table 3.4 Data analysis workflow for processing fluorescence time-series from SQW-labelled cells. Overview of key processing steps applied to ROI-based fluorescence traces extracted from Fiji.

	STEP	PURPOSE	KEY CODE BLOCKS / FUNCTIONS
1	**Load ROI tables**	Each CSV exported by Fiji (ImageJ) is read into a Pandas DataFrame; the first column is *frame number*; the remaining columns are individual ROIs.	`pd.read_csv( … )`
2	**Convert to time axis**	Frame index → seconds using the acquisition rate (fs ≈ 33.33 Hz).	`df['t'] = df['frame']/fs;` `add_time_column( … )`
3	**Baseline (bleaching) correction**	Removes slow photobleaching / drift with asymmetric least-squares (ALS) regression of Eilers & Boelens.	`baseline_als(trace, lam, p)` with typical values lam=1e4, p=0.5
4	**Temporal smoothing + band-pass filtering**	Two-stage filter to preserve spike-like transients while suppressing noise	*Savitzky-Golay* → `apply_savgol(trace, window=7, polyorder=2)` followed by *Butterworth band-pass* → `apply_butter(trace, order=3, lowcut=0.3, highcut=3.0, fs=fs_trace)`
5	**Spectral & statistical diagnostics**	Welch PSD plot (grid for many ROIs), frequencies histogram (global or grid for ROIs), histograms for dominant frequencies, etc.	`scipy.signal.welch`, custom matplotlib helpers
6	**Peak detection**	Detects both types of peaks - min and max; thresholds defined by mean and standard deviations.	`scipy.signal.find_peaks;` `find_peaks(−trace, height, distance)`
7	**Export of numeric summary**	Comaprison between raw and processed data peak detection, gathered in the table.	`summary_df( … ),` `results_orig` and `results_proc`

To establish a single, evidence-based preprocessing pipeline, we implemented a hierarchical parameter-scanning strategy to evaluate the optimal filtering approach across all data types. After fixing the sampling rate from the camera exposure, we first screened Savitzky-Golay (SG) smoothers over window lengths 5-11 and polynomial orders 2-4. Three criteria guided the choice: (1) maximize signal-to-noise ratio (SNR), (2) preserve native spike shape, latency and width, and (3) avoid ringing from high polynomial orders. The scan showed that window = 7, polyorder = 2 yielded the largest SNR gain with no detectable spike broadening, while its nearest runner-up (window = 7 with polyorder = 3) occasionally introduced mild edge wiggles. We next varied Butterworth band-pass order (2-5) inside the physiological 0.3-3 Hz band. Because *filtfilt* applies the filter forward and backward in time to achieve zero-phase distortion (i.e., no temporal shift of features), filter order primarily controls the trade-off between noise

rejection and the risk of ringing: order 2 left residual high-frequency noise, orders 4-5 introduced ringing around fast events, while order 3 provided the best noise suppression without distorting spike shape.

These scans were repeated at three spatial levels – full-frame averages, individual-cell outlines and small ROIs – and for three experimental classes: SQW-stained fluorescence, Ca^{2+} imaging, and an unstained baseline. For Ca^{2+} traces the dominant improvement arose from SG smoothing itself; Butterworth order had little impact, and combining SG with Butterworth produced a waveform almost identical to SG alone. In contrast, SQW traces benefitted strongly from SG (clarifying the baseline) and from the subsequent Butterworth step, which further suppressed high-frequency residue while preserving peak integrity; Butterworth alone, however, lost fine structure. The baseline control behaved similarly to SQWs.

Overall, the results supported the use of a common two-stage filtering approach across all data types: Savitzky-Golay (window = 7, polyorder = 2) → Butterworth (order = 3, 0.3-3 Hz, fs = trace-specific). This setting maximized SNR, preserved true transients, avoided ringing and, importantly, provided a uniform preprocessing standard across SQWs, Ca^{2+} and control recordings for all subsequent quantitative analyses.

Recording for system VI SQWs-stained spiking HEK cells

Figure 3.58 presents fluorescence data from HEK cells stained with System VI SQWs, showing both unprocessed and processed signals averaged over the entire imaging frame. It illustrates how the preprocessing pipeline transforms frame-averaged SQW fluorescence of HEK cells. The key point is that temporal smoothing and band-pass filtering suppress broadband noise and make the fluctuations appear regular, which concentrates spectral power near a narrow frequency band.

In Panel A, the bright-field image depicts a confluent monolayer of cells; Panel B shows the corresponding wide-field fluorescence image, in which cell membranes are clearly outlined against a low-background field. Panels C and D display time-series traces of mean fluorescence intensity averaged across all pixels in each frame. In Panel C, the raw trace – corrected only for baseline drift – exhibits substantial high-frequency fluctuations overlaid on slower variations. Panel D shows the same data after applying temporal smoothing and band-pass filtering, revealing more pronounced, regularly spaced fluctuations. This behavior should be interpreted as a consequence of filtering at this stage, not as evidence for a cellular activity.

Panels E and F present frequency-domain analyses of the processed trace. These plots show how filtering shapes the signal spectrum and quantifies the dominant frequency component. Panel E shows the Welch power spectral density (PSD), with a prominent peak at approximately 1.25 Hz. Panel F displays a histogram of peak frequencies obtained from Welch-estimated PSD values, indicating an average dominant frequency near 1.31 Hz.

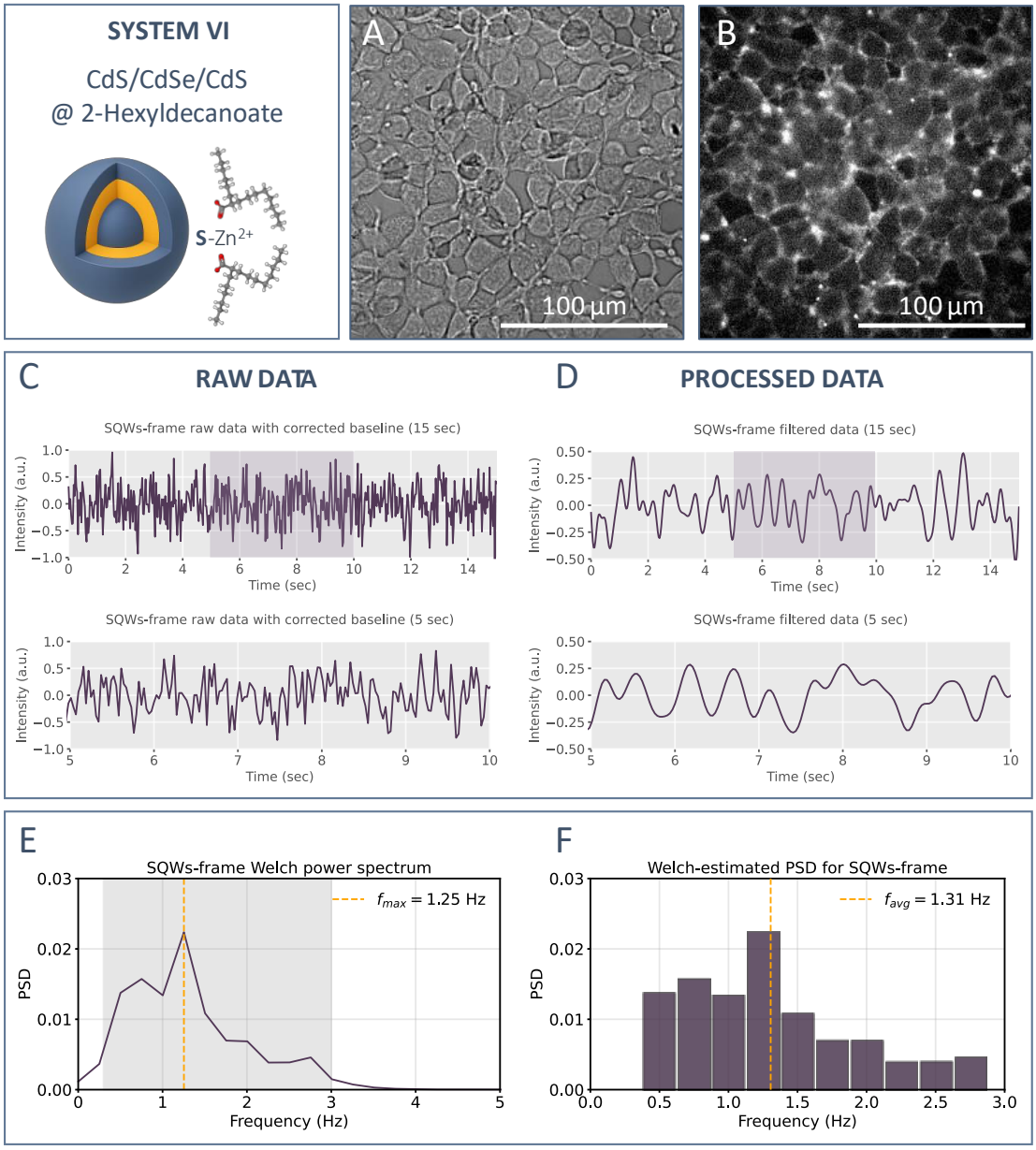

Figure 3.58 Whole-frame fluorescence recordings from HEK cells stained with System VI SQWs. (A) Bright-field image of a confluent HEK monolayer; (B) corresponding fluorescence image showing membrane-localized SQW. (C) Raw fluorescence intensity time series, averaged over whole frame (baseline-corrected only), shown for the full 15 s recording (top) and zoomed-in 5-10 s window (bottom). (D) Corresponding processed traces after temporal smoothing and band-pass filtering (same time windows as in (C)), highlighting more distinct oscillatory features. (E) Welch power spectral density (PSD) estimate computed from the processed trace, with the dominant frequency marked (f_{max} = 1.25 Hz). (F) Histogram of peak frequencies obtained from Welch-estimated PSDs, indicating an average dominant frequency of ≈ 1.31 Hz.

Figure 3.59 compares spike detection in whole-frame SQW fluorescence traces before and after filtering. In Panel A, the raw, band-passed trace is shown with detected maxima (yellow dots) and minima (blue dots). Many rapid fluctuations are evident, leading to a higher count of detected peaks (26 maxima and 25 minima) but with irregular spacing. After applying temporal smoothing and a more stringent band-pass filter (Panel B), the processed trace appears smoother, and the detection algorithm identifies fewer events (20 maxima and 19 minima). This

reduction reflects the removal of high-frequency noise and small transients that did not correspond to true spike-like oscillations. The table in Panel C quantifies these changes: the mean peak frequency for maxima shifts from 1.93 Hz (raw) to 1.76 Hz (processed), while minima shift from 1.85 Hz to 1.39 Hz. Standard deviations of peak frequencies also change (maxima: 0.60 Hz raw → 0.75 Hz processed; minima: 0.59 Hz raw → 0.49 Hz processed). These differences arise from the combined effects of filtering and peak detection thresholds. In the minima, the removal of spurious, closely spaced noise peaks results in a narrower frequency spread. In the maxima, selective elimination of smaller peaks alters the distribution of inter-peak intervals, leading to a broader spread. Thus, signal processing not only reduces the number of detected events, but also reshapes the apparent frequency structure of the recorded signal.

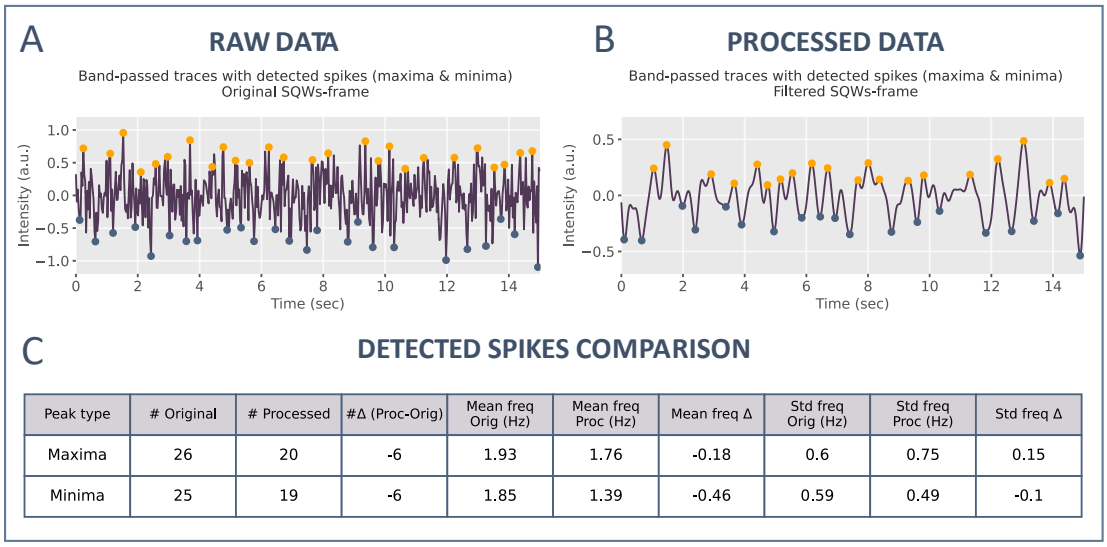

Peak type	# Original	# Processed	#Δ (Proc-Orig)	Mean freq Orig (Hz)	Mean freq Proc (Hz)	Mean freq Δ	Std freq Orig (Hz)	Std freq Proc (Hz)	Std freq Δ
Maxima	26	20	-6	1.93	1.76	-0.18	0.6	0.75	0.15
Minima	25	19	-6	1.85	1.39	-0.46	0.59	0.49	-0.1

Figure 3.59 Peak detection in whole-frame SQW fluorescence traces before and after signal processing. (A) Raw baseline-corrected trace, band-pass filtered, with detected maxima (yellow) and minima (blue) marked. (B) Corresponding trace after temporal smoothing and refined filtering, with updated peak detection. Filtering reduces high-frequency noise and sharpens the dominant oscillatory pattern. (C) Summary table comparing the number of detected peaks, mean peak frequencies, and standard deviations for maxima and minima in original versus processed traces. Filtering reduces peak count and shifts mean frequencies toward values consistent with the expected periodic spiking of the HEK model.

To further investigate the spatial characteristics of the signal and assess whether spike-like events are more pronounced at the single-cell level, a cell-based ROI analysis was performed. For this, 20 individual cells were selected across the imaging frame (Figure 3.60), and the same signal processing pipeline described for the whole-frame data was applied to each cell's fluorescence trace. To further characterize the frequency content of the signals at the single-cell level, Welch power spectra and Welch-based frequency histograms were computed for each cell. The resulting spectra (Figure 3.61) and histograms (Figure 3.62) are presented as grids, allowing direct visual comparison across all 20 cells.

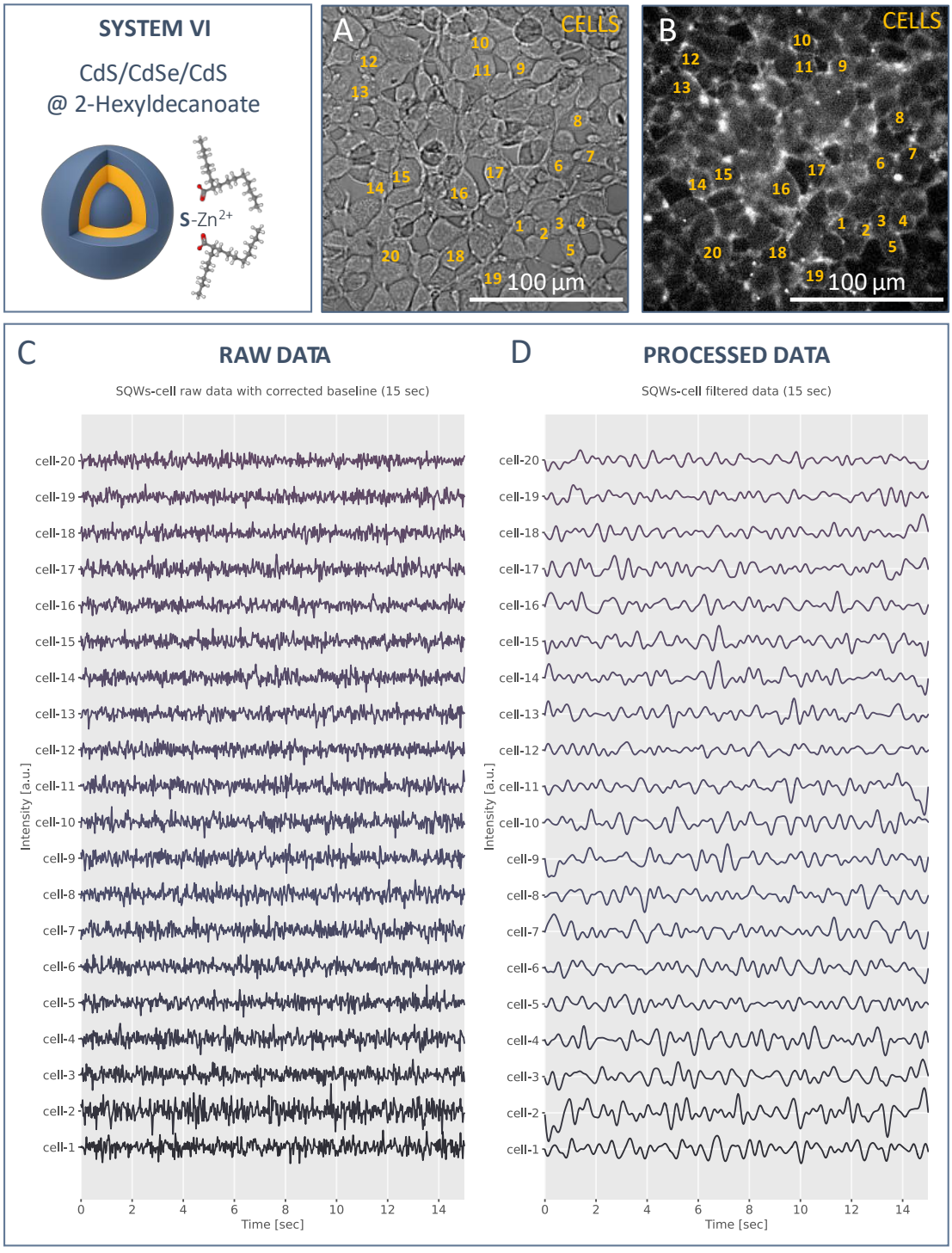

Figure 3.60 Cell-based fluorescence traces from 20 selected HEK cells stained with System VI SQWs. (A) Bright-field image and (B) corresponding fluorescence image with numbered ROIs marking the 20 selected cells. (C) Raw, baseline-corrected fluorescence traces for each cell (15 s recording). (D) Corresponding processed traces after temporal smoothing and band-pass filtering, revealing clearer oscillatory patterns across individual cells.

To summarize these results across the dataset, two aggregate distributions were generated: (1) a histogram of dominant frequencies, determined from the peak frequency (f_{max}) identified in each Welch power spectrum (Figure 3.63, panel A), and (2) a histogram of average frequencies (f_{avg}), computed from the PSD-weighted frequency histograms of each ROI (Figure 3.63, panel B). Gaussian fits were applied to both distributions to extract the overall mean and spread of frequencies across the population of analyzed cells. This provides a quantitative comparison of the dominant oscillatory components at the single-cell level, complementing the whole-frame analysis and allowing assessment of variability between cells. This approach is justified by the known behavior of the spiking HEK model used here, in which spontaneous firing is synchronized across the monolayer. Under these conditions, all cells are expected to oscillate at the same dominant frequency, allowing direct comparison of single-cell frequency components with the whole-frame analysis.

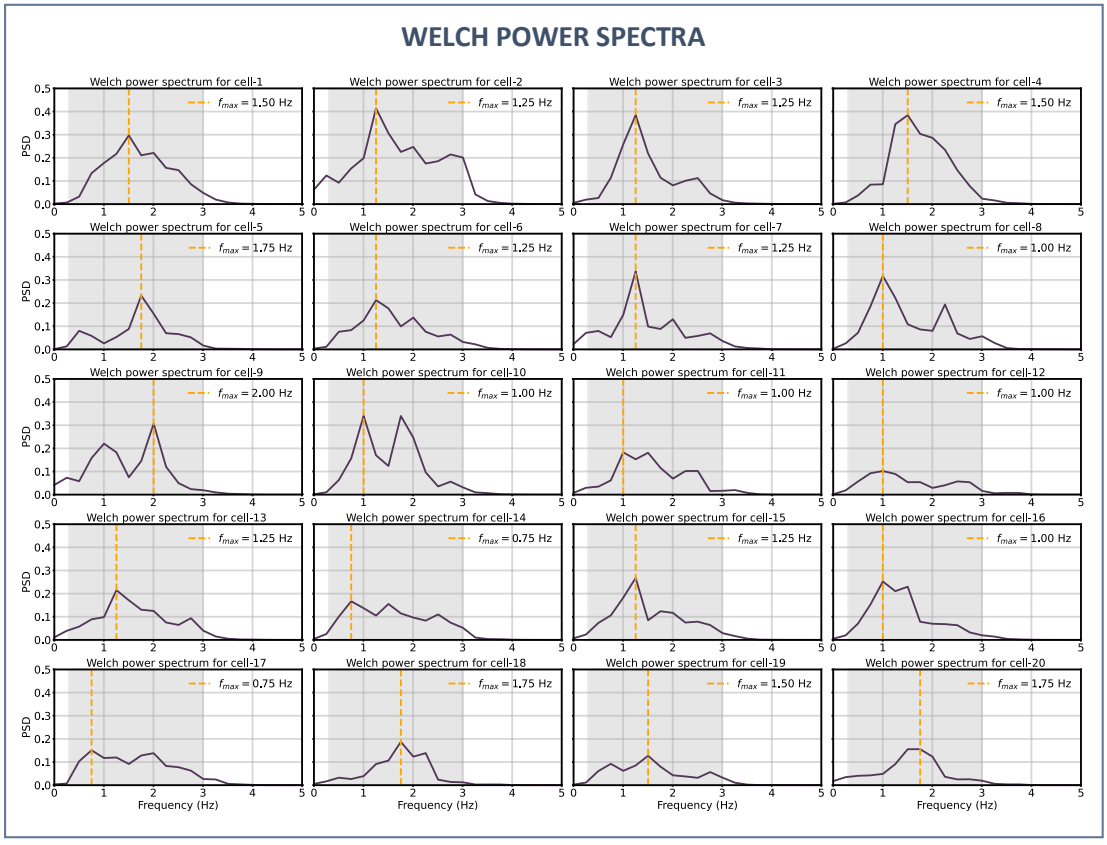

Figure 3.61 Welch power spectra of processed fluorescence traces for 20 individual cells. Dominant frequencies (fmax) for each cell were extracted from the highest peak of the corresponding Welch power spectral density (PSD) curve.

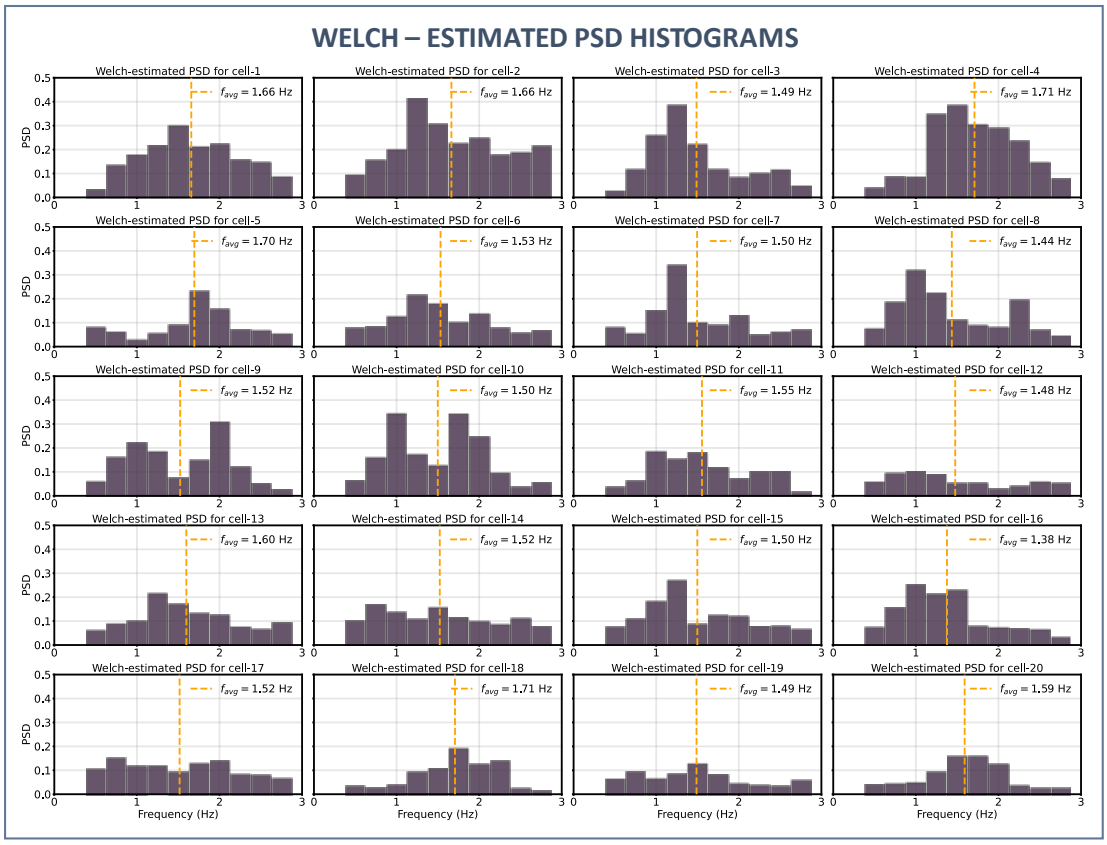

Figure 3.62 Welch-estimated frequency histograms for 20 individual cells. Average frequencies (f_{avg}) were computed for each cell from the PSD-weighted frequency distribution.

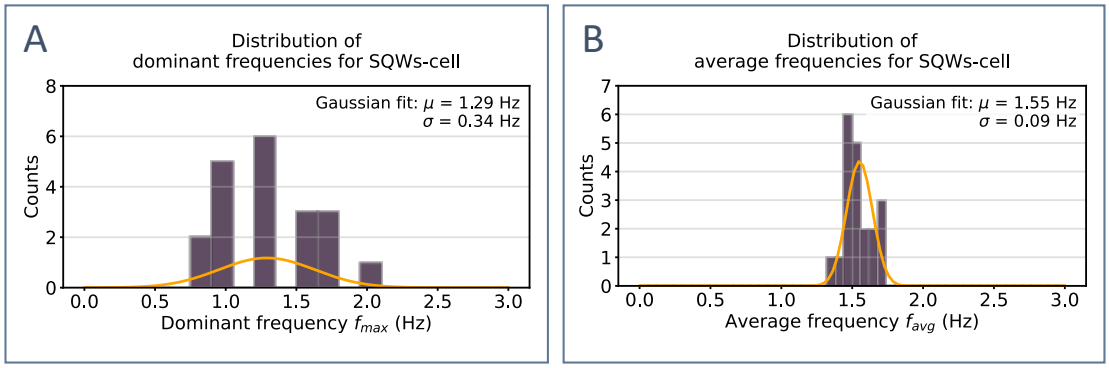

Figure 3.63 Summary of dominant and average frequencies across all analyzed cells. (A) Distribution of dominant frequencies (f_{max}) extracted from Welch power spectra. (B) Distribution of average frequencies (f_{avg}) from Welch-estimated PSD histograms. Gaussian fits were used to determine overall mean and standard deviation for each distribution.

The distribution of dominant frequencies (f_{max}), derived from the peak maximum of each cell's Welch power spectrum (Figure 3.63, panel A), shows a Gaussian-fit mean of 1.29 Hz with a standard deviation of 0.34 Hz. The distribution is relatively broad, reflecting variability in the exact location of the dominant peak across individual cells. In contrast, the distribution of average frequencies (f_{avg}), calculated from the PSD-weighted frequency histograms (Figure 3.63,

panel B), is notably narrower, with a mean of 1.55 Hz and a standard deviation of 0.09 Hz. This difference in spread arises from the method of calculation: while f_{max} reflects a single spectral feature (which slightly vary between cells), f_{avg} represents an average over the entire frequency content of each cell's trace, thus reducing sensitivity to local fluctuations and providing a more general estimate of the underlying oscillatory behavior.

Following the same analysis pipeline used for whole-frame intensity traces, peak detection was also performed on individual cell traces, both before and after signal processing with the selected filters. For each cell, both maxima and minima were identified. The resulting traces, with detected peaks overlaid, are presented as a grid of plots (Figure 3.64, Figure 3.65), providing a visual overview of the temporal dynamics and peak distribution across the analyzed cell set. A corresponding summary table (Figure 3.66) compiles key quantitative metrics from the analysis, including the number of detected peaks, the mean peak frequency within each cell trace (with standard deviation), and how these values change following signal processing.

These figures are included here in the main text to illustrate and support the key conclusions drawn from the individual-cell analysis. However, to maintain clarity and focus in the following sections, detailed per-cell and per-ROI plots will be provided in the Appendix (Section 5 *Data and Code Repository*). From this point forward, only summary analyses will be presented here.

Figure 3.64 Peak detection in raw individual cell traces. Unprocessed (raw) fluorescence traces for 20 individual SQW-labelled cells, with detected maxima (yellow) and minima (blue) overlaid. This visualization illustrates the noisier baseline prior to signal processing.

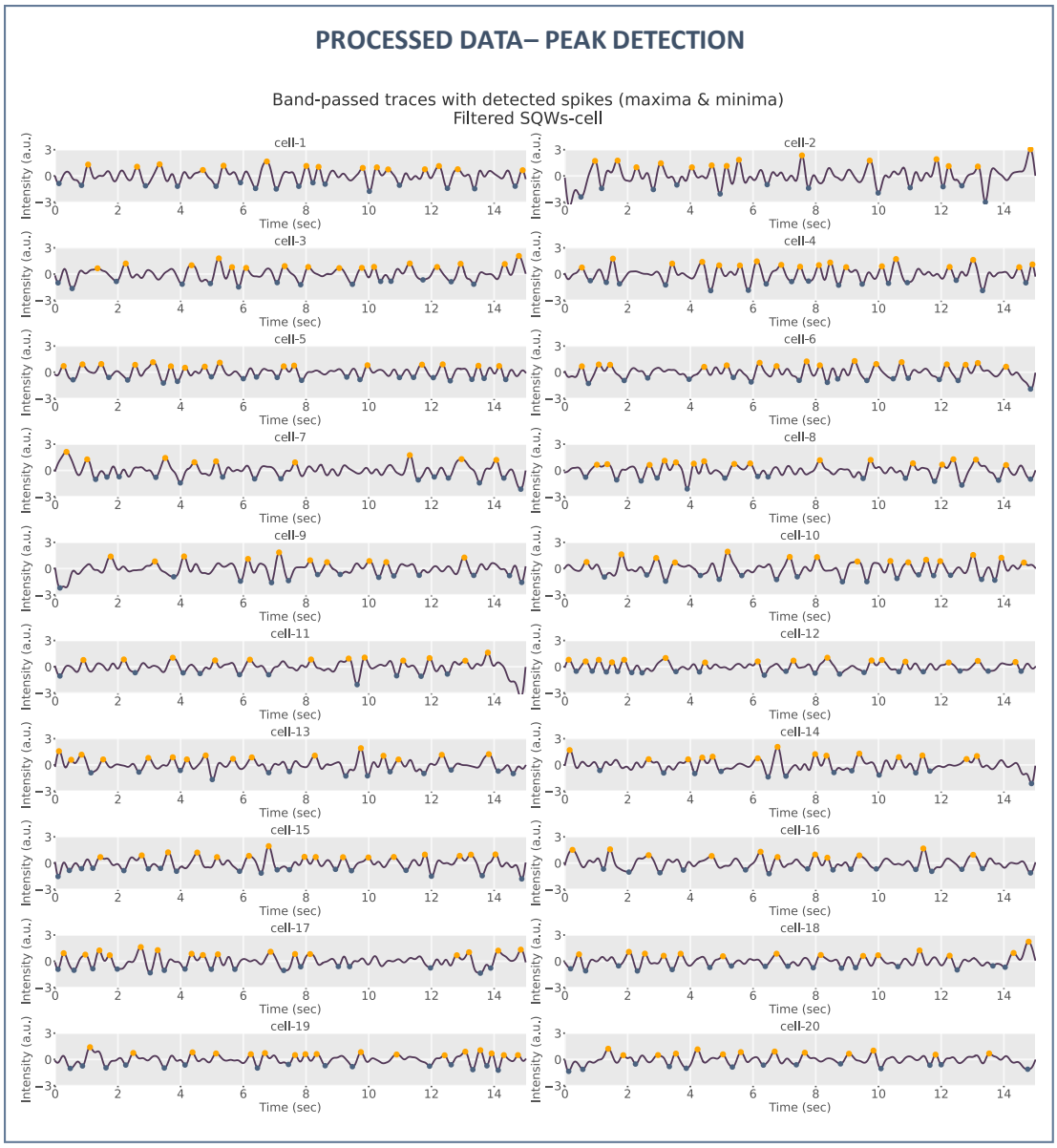

Figure 3.65 Peak detection in processed individual cell traces. Filtered fluorescence traces for 20 individual SQW-labelled cells, with detected maxima (yellow) and minima (blue) overlaid. This visualization highlights spike-like transients following signal processing.

DETECTED SPIKES COMPARISON

Cell	Peak type	# Original	# Processed	#Δ (Proc-Orig)	Mean freq Orig (Hz)	Mean freq Proc (Hz)	Mean freq Δ	Std freq Orig (Hz)	Std freq Proc (Hz)	Std freq Δ
cell-1	Maxima	29	15	-14	1.98	1.08	-0.9	0.24	0.52	0.28
cell-1	Minima	28	16	-12	1.89	1.1	-0.79	0.17	0.44	0.27
cell-2	Maxima	30	14	-16	2.03	1.01	-1.02	0.17	0.65	0.48
cell-2	Minima	28	13	-15	1.89	0.98	-0.91	0.2	0.51	0.31
cell-3	Maxima	27	16	-11	1.86	1.19	-0.67	0.16	0.44	0.27
cell-3	Minima	27	14	-13	1.86	1.06	-0.8	0.2	0.46	0.26
cell-4	Maxima	28	18	-10	1.95	1.25	-0.7	0.15	0.45	0.3
cell-4	Minima	28	16	-12	1.9	1.15	-0.75	0.17	0.38	0.2
cell-5	Maxima	28	16	-12	1.94	1.15	-0.79	0.17	0.6	0.44
cell-5	Minima	29	19	-10	2.0	1.38	-0.62	0.14	0.32	0.18
cell-6	Maxima	28	16	-12	1.93	1.18	-0.75	0.17	0.63	0.46
cell-6	Minima	28	15	-13	1.94	1.06	-0.88	0.17	0.5	0.32
cell-7	Maxima	27	9	-18	1.91	0.66	-1.25	0.13	1.01	0.88
cell-7	Minima	31	14	-17	2.09	1.03	-1.06	0.15	1.01	0.85
cell-8	Maxima	28	16	-12	1.94	1.23	-0.71	0.16	0.54	0.38
cell-8	Minima	31	14	-17	2.1	0.99	-1.11	0.11	0.62	0.51
cell-9	Maxima	28	10	-18	1.9	0.89	-1.02	0.14	0.62	0.47
cell-9	Minima	27	13	-14	1.84	0.88	-0.95	0.19	0.87	0.68
cell-10	Maxima	30	15	-15	2.1	1.08	-1.02	0.15	0.42	0.27
cell-10	Minima	26	16	-10	1.83	1.29	-0.55	0.21	0.3	0.1
cell-11	Maxima	26	12	-14	1.81	0.93	-0.88	0.19	0.38	0.19
cell-11	Minima	26	11	-15	1.82	0.75	-1.08	0.21	0.75	0.54
cell-12	Maxima	29	16	-13	1.95	1.12	-0.83	0.2	0.43	0.23
cell-12	Minima	27	18	-9	1.85	1.27	-0.58	0.19	0.4	0.21
cell-13	Maxima	30	16	-14	2.05	1.17	-0.89	0.18	0.49	0.31
cell-13	Minima	31	13	-18	2.13	0.97	-1.17	0.12	0.44	0.32
cell-14	Maxima	29	14	-15	1.99	1.08	-0.91	0.16	0.6	0.44
cell-14	Minima	27	12	-15	1.85	0.87	-0.98	0.19	0.78	0.58
cell-15	Maxima	29	16	-13	2.0	1.27	-0.73	0.16	0.26	0.1
cell-15	Minima	28	18	-10	1.89	1.22	-0.68	0.17	0.53	0.37
cell-16	Maxima	23	11	-12	1.62	0.86	-0.76	0.26	0.52	0.26
cell-16	Minima	25	15	-10	1.68	1.1	-0.58	0.25	0.39	0.14
cell-17	Maxima	29	16	-13	2.0	1.1	-0.9	0.17	1.05	0.88
cell-17	Minima	31	16	-15	2.12	1.16	-0.96	0.14	0.58	0.44
cell-18	Maxima	25	14	-11	1.71	0.98	-0.73	0.17	0.52	0.34
cell-18	Minima	29	16	-13	2.01	1.15	-0.86	0.13	0.39	0.26
cell-19	Maxima	29	17	-12	2.0	1.25	-0.76	0.23	0.49	0.26
cell-19	Minima	29	15	-14	1.96	1.1	-0.86	0.17	0.63	0.46
cell-20	Maxima	30	13	-17	2.21	1.07	-1.14	0.18	0.45	0.28
cell-20	Minima	26	13	-13	1.79	0.89	-0.9	0.15	0.63	0.48

Figure 3.66 Comparison of detected spikes in raw and processed traces for individual cells. Summary of peak detection results (maxima and minima) for 20 individual SQW-labelled cells. The table reports the number of detected peaks before and after signal processing, changes in peak count (#Δ), mean peak frequency (Hz) and corresponding standard deviations, allowing quantitative assessment of how filtering affects spike detection.

For ease of interpretation, summary statistics were calculated by taking the mean of the individual mean frequencies extracted from each cell (or ROI), separately for maxima and minima peaks (data shown in Figure 3.66). In other words, for each peak type, the "mean of means" was computed across all traces, along with the standard deviation of these mean values

("std of means"), providing an overall measure of central tendency and variability for the dataset. These values are presented in Table 3.5. For the maxima peaks, the mean frequency decreased from 1.94 Hz in the original traces to 1.08 Hz after processing (Δ = -0.87 Hz), with a standard deviation of means of 0.13 Hz (original) and 0.15 Hz (processed). For minima peaks, the mean frequency similarly decreased from 1.92 Hz to 1.07 Hz (Δ = -0.85 Hz), with corresponding standard deviations of 0.12 Hz (original) and 0.16 Hz (processed). The substantial drop in mean frequency after filtering indicates that many of the peaks initially detected in the raw traces were due to high-frequency noise or artefacts, which were effectively suppressed by the filtering process. The low standard deviations of the mean frequencies suggest that the average spike frequencies were consistent across different cells, with no large variation between traces.

Table 3.5 Summary of spike detection metrics for SQW-labelled HEK cells (System VI), whole-cell ROI analysis. Mean of average spike frequencies ("mean of means") and corresponding standard deviations for maxima and minima peaks, comparing raw and processed traces.

Peak type	Avg# for Original	Avg# for Processed	#Δ (Proc-Orig)	Mean freq Orig (Hz)	Mean freq Proc (Hz)	Mean freq Δ	Std of Mean freq Orig	Std of Mean freq Proc	Std of Mean freq Δ
Maxima	28.1	14.5	-13.6	1.94	1.08	-0.87	0.13	0.15	0.16
Minima	28.1	14.85	-13.25	1.92	1.07	-0.85	0.12	0.16	0.18

Finally, we extended the analysis to the highest spatial resolution by performing peak detection and frequency-domain analysis on small ROIs (5 × 5 pixels) selected from individual SQW-labelled cells. Each ROI was positioned on the cell membrane to focus on localized membrane regions containing fewer total quantum dots, but with higher local concentration, with the goal of enhancing signal-to-noise ratio. For this analysis, three ROIs were manually defined per cell across five different cells, as illustrated in Panel A of Figure 3.67. The complete processing pipeline described previously was applied to each ROI trace.

Panels B and C of Figure 3.67 present the raw and processed fluorescence traces from the selected small ROIs. Despite the reduced spatial averaging, raw ROI traces exhibit pronounced high-frequency noise and lack clearly distinguishable spike events. In contrast, the processed traces reveal well-defined spike-like transients with consistent temporal patterns across different ROIs and cells. To quantitatively characterize these signals, dominant frequencies and average spike frequencies were extracted from the processed traces and summarized as histograms (Figure 3.68). The distribution of dominant frequencies (Panel A) and the distribution of average frequencies (Panel B) both displays pronounced peaks centered around ~1.6 Hz.

A summary of spike detection metrics for the small-ROI analysis is presented in Table 3.6. Similar to the whole-cell results, a substantial reduction in detected peak frequency is observed after

processing, with mean frequencies for maxima decreasing from 1.9 Hz to 1.15 Hz, and for minima from 1.94 Hz to 1.10 Hz. The standard deviations of the mean frequencies remain low across ROIs, confirming good consistency of spike detection at this finer spatial scale.

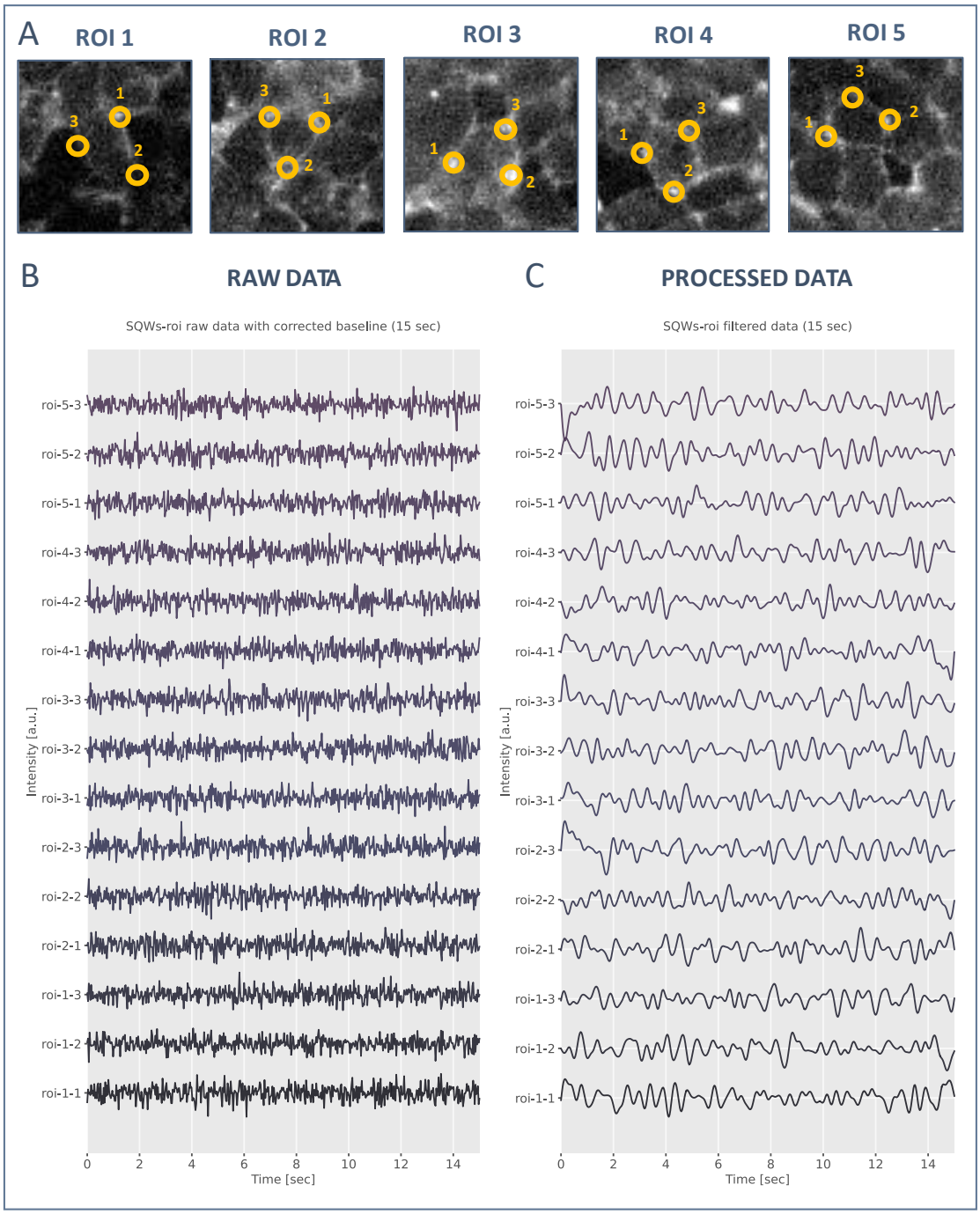

Figure 3.67 Small-ROI analysis of SQW-labelled cell membrane regions. (A) Example membrane regions from five different cells, with three manually selected 5 × 5 pixel ROIs per cell (yellow circles). (B) Raw fluorescence traces from each ROI after baseline correction. (C) Corresponding processed traces, showing enhanced visibility of spike-like transients.

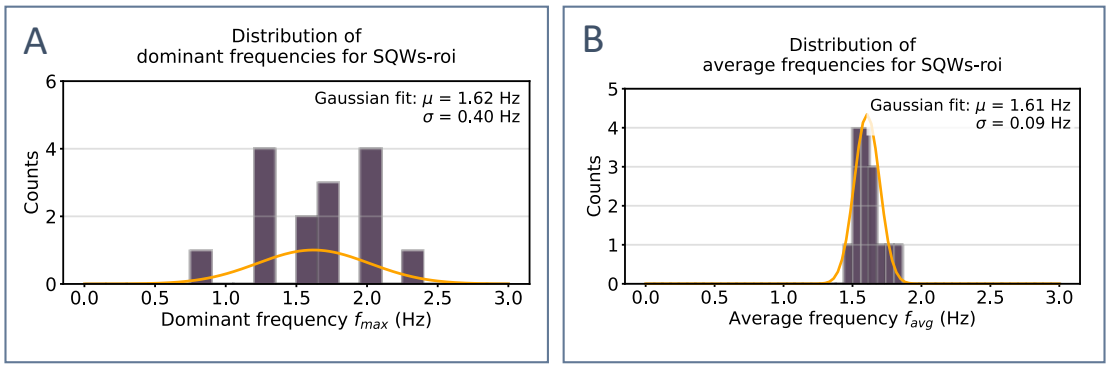

Figure 3.68 Frequency analysis of spike-like transients in small ROIs. (A) Distribution of dominant frequencies (f_{max}) extracted from processed ROI traces. (B) Distribution of average spike frequencies (f_{avg}). Both distributions show peaks centered around ~1.6 Hz.

Table 3.6 Summary of spike detection metrics for small-ROI analysis (SQW-labelled HEK cells). Mean of average spike frequencies and corresponding standard deviations for maxima and minima peaks, comparing raw and processed traces across all small ROIs.

Peak type	Avg# for Original	Avg# for Processed	#Δ (Proc-Orig)	Mean freq Orig (Hz)	Mean freq Proc (Hz)	Mean freq Δ	Std of Mean freq Orig	Std of Mean freq Proc	Std of Mean freq Δ
Maxima	27.8	15.27	-12.53	1.9	1.15	-0.76	0.14	0.11	0.14
Minima	28.13	14.87	-13.27	1.94	1.1	-0.84	0.11	0.19	0.22

To conclude, the analysis of SQW-labelled spiking HEK cells across multiple spatial scales demonstrates that periodic components are present in the recorded fluorescence signals, particularly when the analysis is localized to individual cells or small membrane ROIs. In these smaller spatial domains, frequency estimates obtained from Welch analysis and peak detection show closer agreement, likely due to reduced contributions from spatially uncorrelated noise. In contrast, whole-frame peak detection tends to overestimate spike rates, likely reflecting the inclusion of non-physiological fluctuations when averaging over the entire field of view.

While dominant and average frequencies derived from Welch-based methods remain relatively consistent across scales, substantial discrepancies persist between Welch-derived and peak-detection-derived frequencies, particularly when compared against the narrow physiological frequency band of interest (0.3-3 Hz). For instance, whole-frame peak detection reports frequencies around 1.8 Hz, whereas Welch analysis centers closer to 1.3 Hz – a divergence of approximately 40%. Even at the single-cell and small-ROI levels, peak-derived frequencies remain ~0.4-0.5 Hz lower than Welch estimates, corresponding to relative errors of 25-30%. These differences likely reflect the differing sensitivities of the analytical methods to signal quality. Welch analysis identifies dominant periodic components even when their amplitude is small, while peak detection requires transients to exceed amplitude and separation thresholds.

As a result, genuine spike-related fluctuations near the noise floor may either be missed or overcounted by the peak detection pipeline, particularly because the amplitude threshold had to be set low to accommodate the high noise level in these recordings. At the same time, non-spike-related periodic noise can still contribute to the Welch spectrum. The divergence between methods therefore underscores the impact of limited signal-to-noise ratio on the accuracy and reliability of spike detection in the current dataset.

Overall, while the data confirm the presence of recurring oscillatory components, the lack of convergence across analytical approaches indicates that the current signal quality is not sufficient for reliable and unambiguous spike detection. Enhancing the brightness of the SQW probes, and thereby improving the signal-to-noise ratio, will be critical for reducing this analytical uncertainty. In addition, further optimization of filtering parameters and validation against electrophysiological ground truth will be required before SQW-based recordings can support quantitative membrane-voltage spike detection.

Table 3.7 Overview of frequency estimates obtained from SQW-labelled spiking HEK cell recordings. Comparison of dominant frequencies (Welch spectra), average frequencies (Welch histogram), and spike-detection-derived frequencies (maxima and minima) across whole-frame, cell-level, and small-ROI analyses.

SQWs	Welch spectra (dominant frequency)	Welch histogram (average frequency)	Detected spikes from processed traces	
			max peak	min peak
frame	1.25 Hz	1.31 Hz	1.76 ± 0.75 Hz	1.39 ± 0.49 Hz
cells	1.29 ± 0.34 Hz	1.55 ± 0.09 Hz	1.08 ± 0.15 Hz	1.07 ± 0.16 Hz
small ROI	1.62 ± 0.40 Hz	1.61 ± 0.09 Hz	1.15 ± 0.11 Hz	1.10 ± 0.19 Hz

Experiment with tetrodotoxin

To assess whether the oscillatory components observed in the SQW recordings reflect genuine sodium channel-dependent activity or arise from residual noise, the same sample analyzed in the previous section was treated with tetrodotoxin (TTX) to block voltage-gated Na^+ channels and suppress spiking behavior. Fluorescence recordings were acquired 10 minutes after TTX addition, when spiking should be fully inhibited, using the same imaging conditions. The complete analysis pipeline (baseline correction, filtering, Welch analysis, and peak detection across whole frame, selected cells, and small ROIs) was then applied to the TTX-treated data. The presence of persistent oscillatory components or detected peaks would suggest contributions from noise or non-voltage-dependent fluctuations, while their suppression would support the interpretation that the original SQW signals were associated with spike activity.

The TTX-treated recording produced raw and processed traces that closely resembled those of the untreated sample. The Welch power spectrum exhibited a noticeably flatter profile compared to the original whole-frame trace, yet we identified a dominant frequency of 1.25 Hz (Figure 3.69 C). Similarly, the Welch-estimated PSD histogram peaked at 1.42 Hz (Figure 3.69 D), only slightly higher than the 1.31 Hz observed prior to TTX application. Peak detection applied to the same frame yielded mean frequencies of 1.44 ± 0.59 Hz for maxima and 1.57 ± 0.50 Hz for minima, both with substantial standard deviations. This pattern remained consistent at higher spatial resolutions: for individual-cell outlines, Welch analysis yielded 1.39 ± 0.42 Hz (dominant) and 1.56 ± 0.10 Hz (average), while for 5 × 5-pixel membrane ROIs, the corresponding values were 1.07 ± 0.19 Hz and 1.05 ± 0.17 Hz. The summary histograms for cell and ROI-based analysis are visualized on Figure 3.71. The full set of results is summarized in Table 3.8 and shows only minor differences from the untreated SQW recordings.

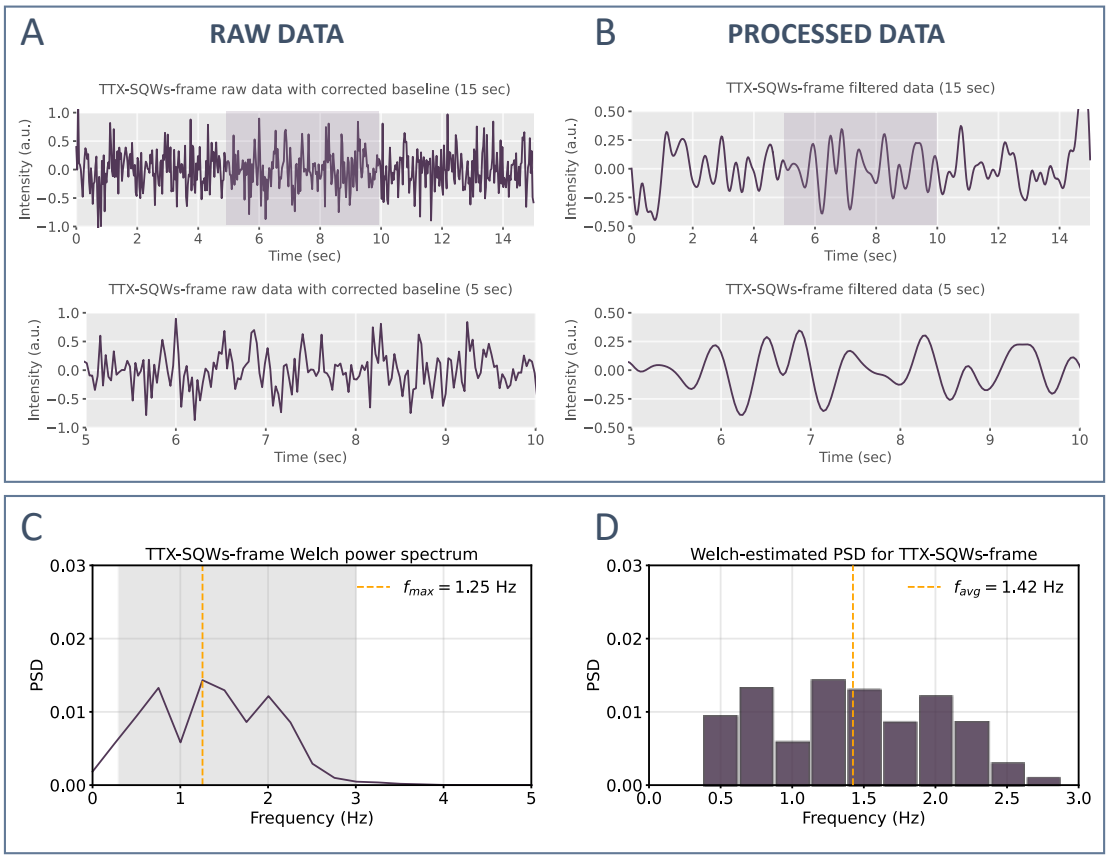

Figure 3.69 Whole-frame analysis of SQW-labelled HEK cells after TTX treatment. (A) Raw fluorescence traces after baseline correction. (B) Corresponding processed traces after filtering. (C) Welch power spectrum of the processed trace, with dominant frequency indicated. (D) Welch-estimated power spectral density (PSD) histogram, showing average frequency.

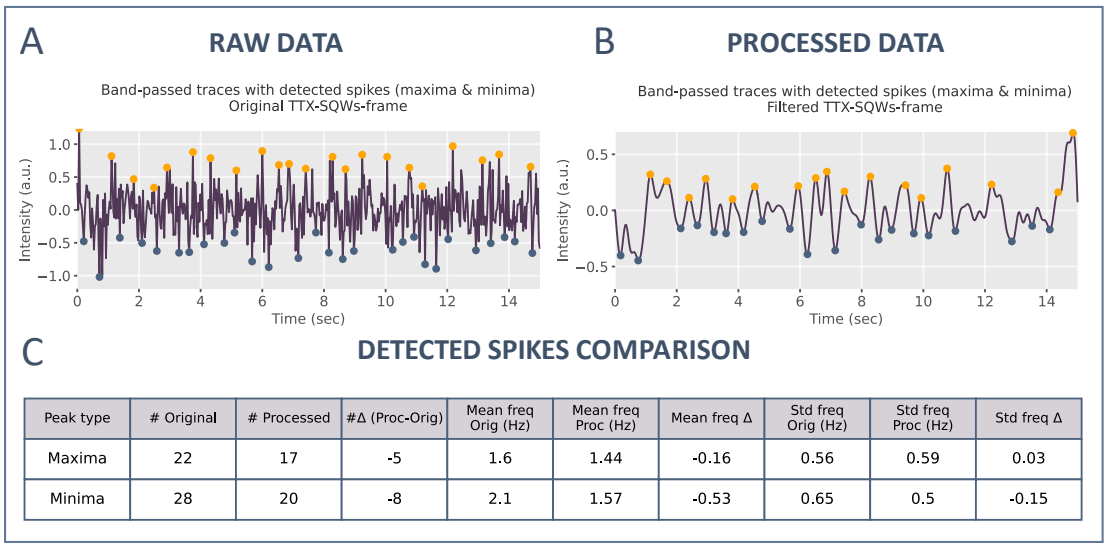

Peak type	# Original	# Processed	#Δ (Proc-Orig)	Mean freq Orig (Hz)	Mean freq Proc (Hz)	Mean freq Δ	Std freq Orig (Hz)	Std freq Proc (Hz)	Std freq Δ
Maxima	22	17	-5	1.6	1.44	-0.16	0.56	0.59	0.03
Minima	28	20	-8	2.1	1.57	-0.53	0.65	0.5	-0.15

Figure 3.70 Peak detection analysis of SQW-labelled HEK cells after TTX treatment (whole-frame). (A) Raw fluorescence trace with detected maxima (yellow) and minima (blue). (B) Processed trace after filtering with detected peaks. (C) Comparison of peak detection results before and after processing, showing number of detected peaks and corresponding frequency statistics.

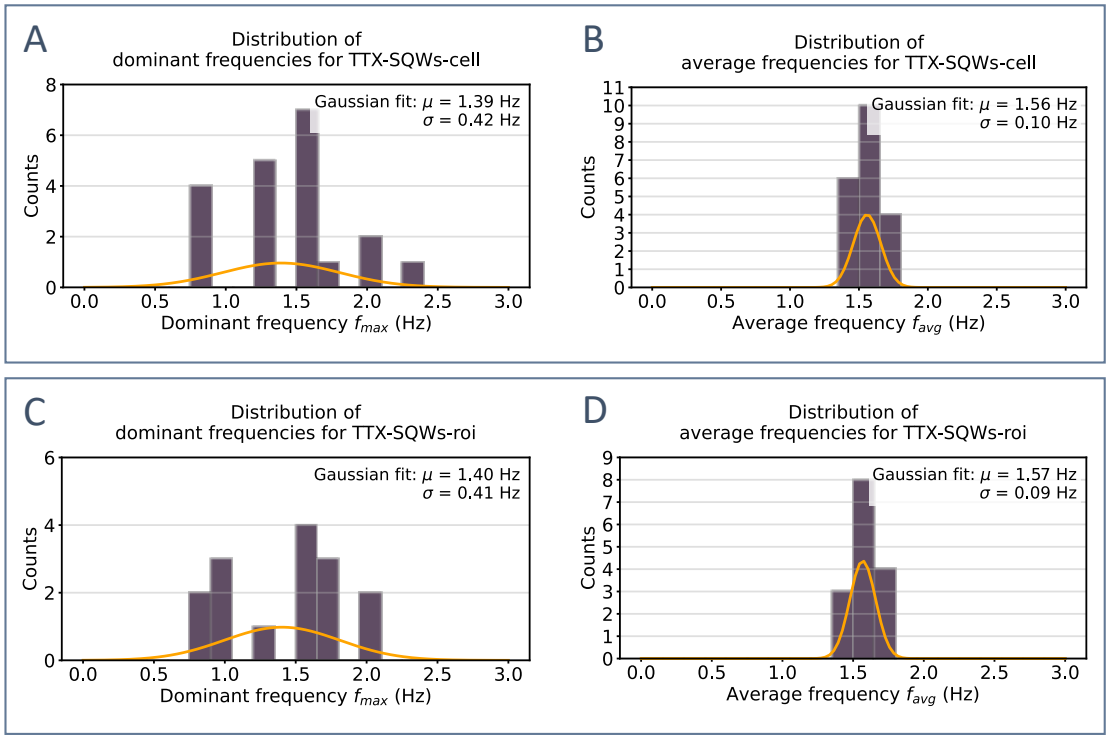

Figure 3.71 Welch frequency analysis of SQW-labelled HEK cells after TTX treatment. (A, B) Distributions of dominant frequencies (A) and average frequencies (B) for individual-cell outlines. (C, D) Distributions of dominant frequencies (C) and average frequencies (D) for small membrane ROIs. Gaussian fits are overlaid (yellow) to illustrate the spread of frequency components.

Table 3.8 Overview of frequency estimates obtained from of SQW-labelled HEK cells after TTX treatment recordings. Comparison of dominant frequencies (Welch spectra), average frequencies (Welch histogram), and spike-detection-derived frequencies (maxima and minima) across whole-frame, cell-level, and small-ROI analyses.

TTX-SQWs	Welch spectra (dominant frequency)	Welch histogram (average frequency)	Detected spikes from processed traces	
			max peak	min peak
frame	1.25 Hz	1.42 Hz	1.44 ± 0.59 Hz	1.57 ± 0.5 Hz
cells	1.39 ± 0.42 Hz	1.56 ± 0.10 Hz	1.04 ± 0.18 Hz	1.0 ± 0.6 Hz
small ROI	1.40 ± 0.41 Hz	1.57 ± 0.09 Hz	1.07 ± 0.19 Hz	1.05± 0.17 Hz

The lack of a clear frequency shift following sodium-channel blockage, combined with the broad, low-contrast Welch spectra and the large variability in peak-derived frequencies, suggests that the periodic components identified in both datasets likely reflect noise or other non-voltage-dependent fluctuations, rather than true spiking activity.

However, to test whether any subregion within the field of view exhibited a spike-related response, a large-scale membrane-ROI analysis was performed on the same sample before and after tetrodotoxin addition. Three hundred ROIs were defined as 3 × 3-pixel windows positioned on the membranes of 60 cells in the field of view, five ROIs per cell. Each ROI trace was processed with the same pipeline, including baseline correction, temporal smoothing, band-pass filtering, and Welch spectral analysis. For every ROI, two frequency metrics were extracted: the dominant frequency from the maximum of the Welch power spectrum (f_{max}) and the average frequency from the PSD-weighted Welch histogram (f_{avg}). Summary histograms for f_{max} and f_{avg} were then constructed for the datasets prior and post TTX addition (Figure 3.72).

The distributions were statistically indistinguishable across conditions. Gaussian fits to the f_{max} histograms yielded nearly identical means and widths for the both recordings (μ = 1.51 Hz, σ = 0.46 Hz versus μ = 1.48 Hz, σ = 0.44 Hz; Δμ = 0.03 Hz, Figure 3.72 A and B). To express the magnitude of this difference relative to the variability of the data, the mean shift (Δμ) was normalized to the pooled standard deviation of the two distributions, calculated as:

$$\Delta_{\text{norm}} = \frac{\Delta\mu}{\sqrt{\frac{\sigma_1^2+\sigma_2^2}{2}}} \tag{3.4}$$

This yielded a value of approximately 0.07, indicating that the observed difference in means is small compared to the overall spread of the distributions. Such a low normalized difference supports the conclusion that the two conditions are statistically indistinguishable. The f_{avg} distributions overlapped almost completely, with identical fitted means and standard deviations

(μ = 1.59 Hz, σ = 0.10 Hz in both datasets, Figure 3.72 C and D). Importantly, in both conditions the extracted frequencies lie outside the calcium-spike band determined independently from calcium imaging of a twin sample, marked as the shaded region in Figure 3.72. Taken together, these results indicate that no statistically significant spike-correlated signal is present anywhere within the frame and that the periodic components observed in SQW fluorescence originate from noise or non-voltage-dependent fluctuations rather than from sodium-channel mediated activity.

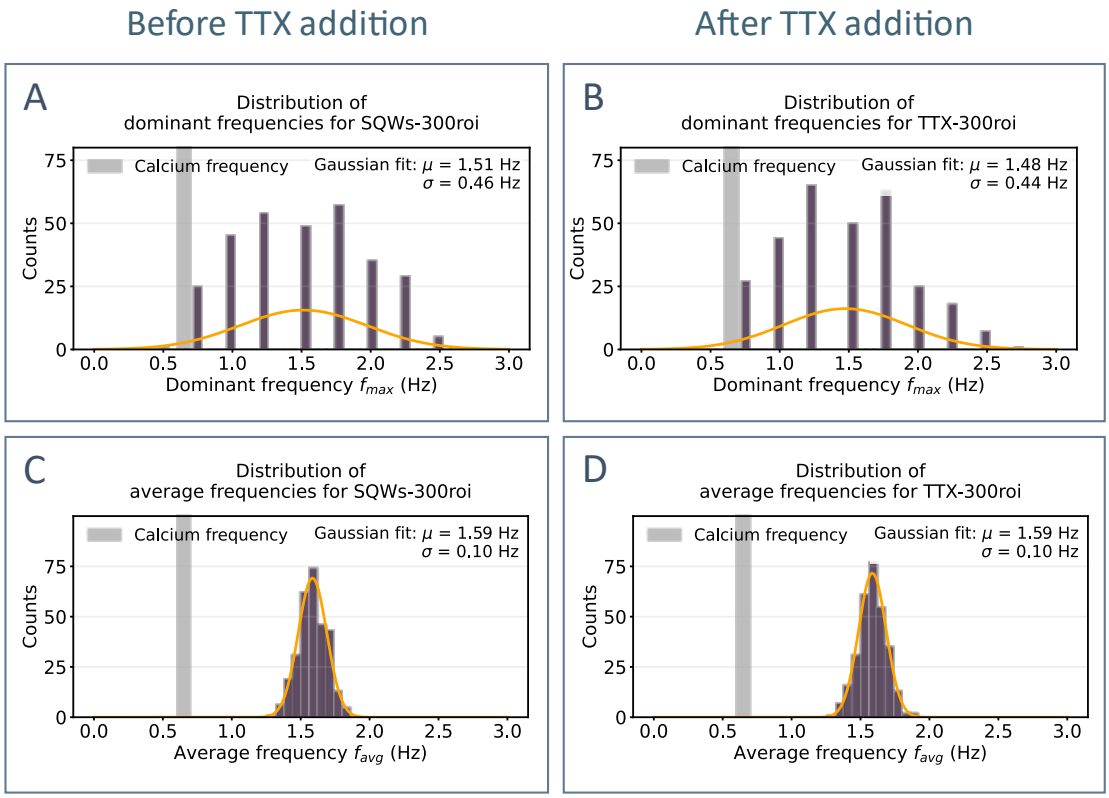

Figure 3.72 Frequency distributions from 300 membrane-localized ROIs (3 × 3 pixels) before (A, C) and after (B, D) TTX addition. Panels A-B show dominant frequencies (f_{max}) extracted from the peak of the Welch spectrum; panels C-D show average frequencies (f_{avg}) computed from PSD-weighted histograms. Gaussian fits (yellow) indicate mean (μ) and standard deviation (σ) for each distribution. The shaded area marks the calcium spiking frequency (0.6-0.75 Hz) determined from a corresponding sample. Distributions are statistically similar across conditions, supporting the interpretation that detected oscillations are unrelated to sodium-channel mediated activity.

Reference recording: unstained spiking HEK cells

The control (baseline) recording, acquired from unstained HEK cells under identical illumination and acquisition settings, serves as a reference for the intrinsic optical noise of the setup. At the whole-frame level, the filtered trace displays reduced oscillatory character, with much of the high-frequency noise smoothed out. The Welch power spectrum shows a pronounced peak at 0.75 Hz (Figure 3.73 E), while the Welch-estimated PSD histogram yields a higher average frequency of 1.26 Hz (Figure 3.73 F), reflecting the broad distribution of spectral components. Peak-detection analysis shows only modest changes after filtering: maxima decrease from 1.85 ± 0.63 Hz to 1.62 ± 0.81 Hz, and minima from 1.80 ± 0.60 Hz to 1.71 ± 0.76 Hz (Figure 3.74 B and C). In both cases, the large standard deviations indicate substantial variability from frame to frame, consistent with the expectation that these detected "peaks" reflect random noise rather than coherent biological events.

At finer spatial scales, the results remain dispersed and inconsistent. For individual-cell outlines, Welch analysis yields a dominant frequency of 1.52 ± 0.50 Hz and an average frequency of 1.54 ± 0.09 Hz (Figure 3.75 A and B). For 5 × 5-pixel membrane ROIs, the corresponding values are 1.05 ± 0.29 Hz (dominant) and 1.46 ± 0.11 Hz (average) (Figure 3.76 A and B). Peak-detection-derived frequencies at the cell level (1.08 ± 0.15 Hz for maxima and 1.04 ± 0.15 Hz for minima,

Table 3.9) and ROI level (1.03 ± 0.17 Hz and 1.07 ± 0.15 Hz, Table 3.10) are more internally consistent, and notably lower than the unprocessed values – reduced by approximately 1 Hz after filtering.

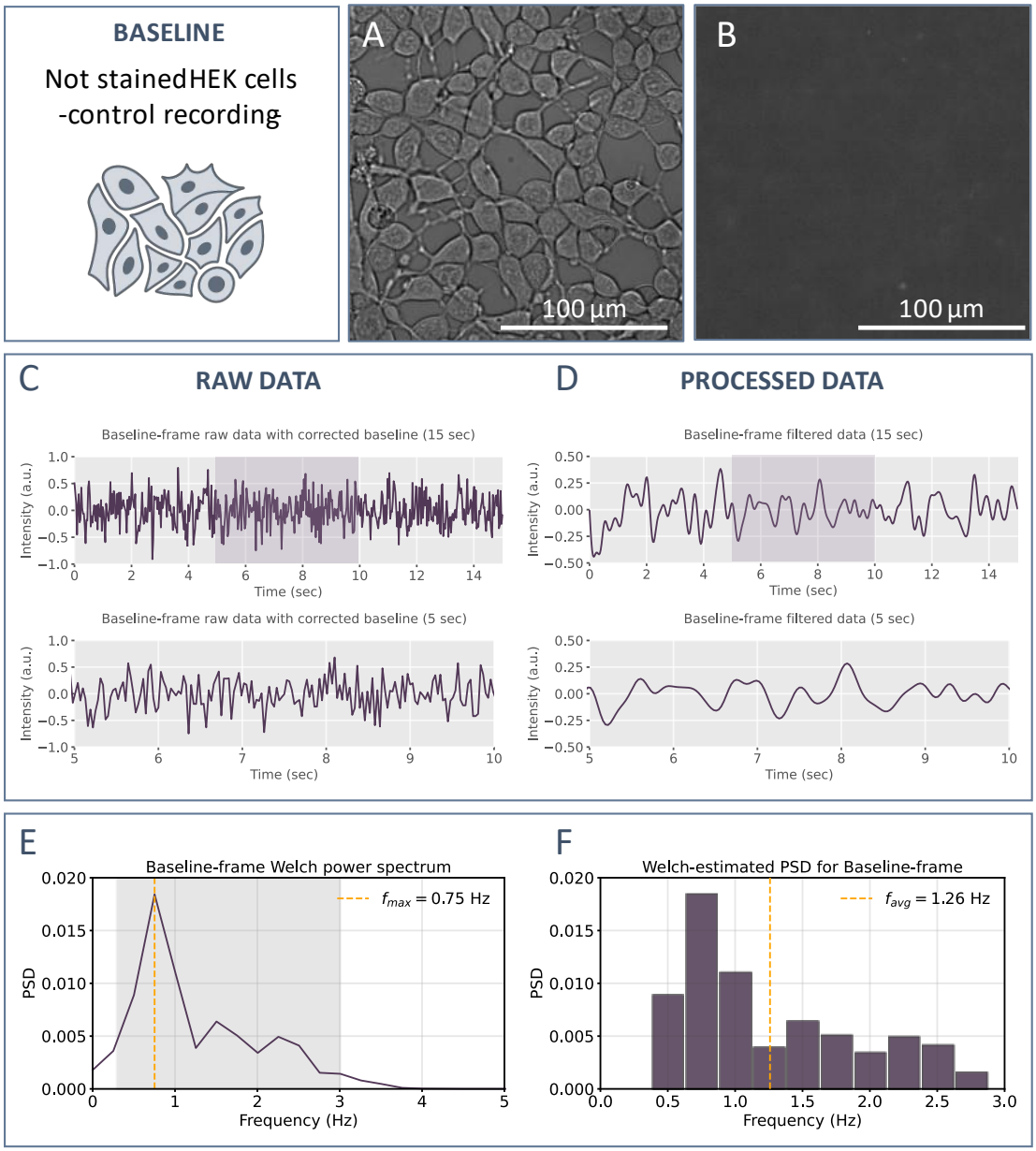

Figure 3.73 Whole-frame analysis of control baseline recording (unstained HEK cells). (A) Brightfield image of HEK cell monolayer; (B) corresponding fluorescence image under identical acquisition settings. (C) Raw fluorescence traces after baseline correction. (D) Processed traces after filtering. (E) Welch power spectrum of the processed trace, with dominant frequency indicated. (F) Welch-estimated power spectral density (PSD) histogram, showing average frequency.

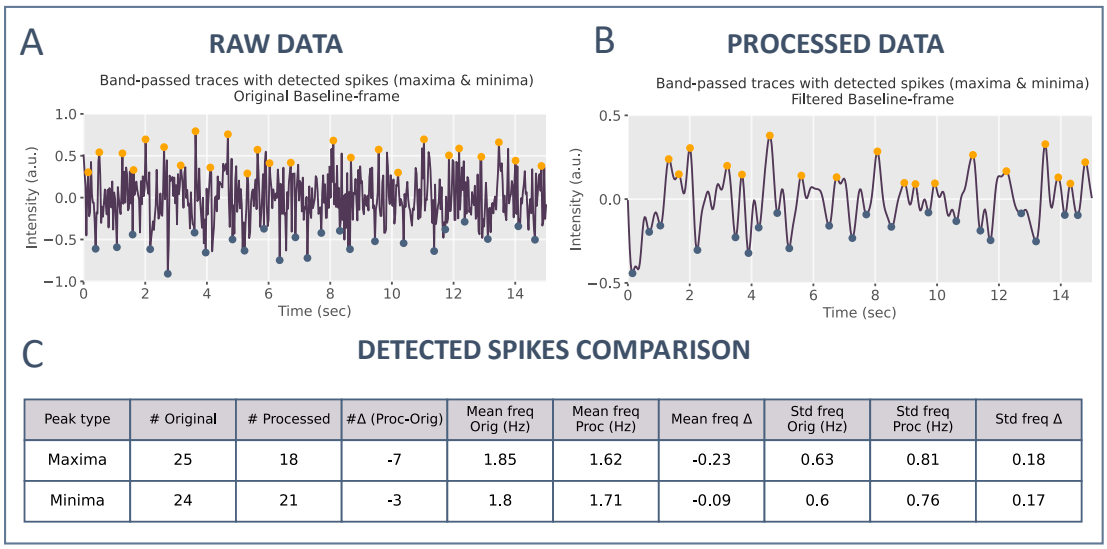

Peak type	# Original	# Processed	#Δ (Proc-Orig)	Mean freq Orig (Hz)	Mean freq Proc (Hz)	Mean freq Δ	Std freq Orig (Hz)	Std freq Proc (Hz)	Std freq Δ
Maxima	25	18	-7	1.85	1.62	-0.23	0.63	0.81	0.18
Minima	24	21	-3	1.8	1.71	-0.09	0.6	0.76	0.17

Figure 3.74 Peak-detection analysis of control baseline recording (unstained HEK cells, whole-frame). (A) Raw fluorescence trace with detected maxima (yellow) and minima (blue). (B) Corresponding processed trace after filtering, with peaks again highlighted. (C) Summary table comparing the number of detected peaks and their mean frequencies before and after processing, including associated standard deviations.

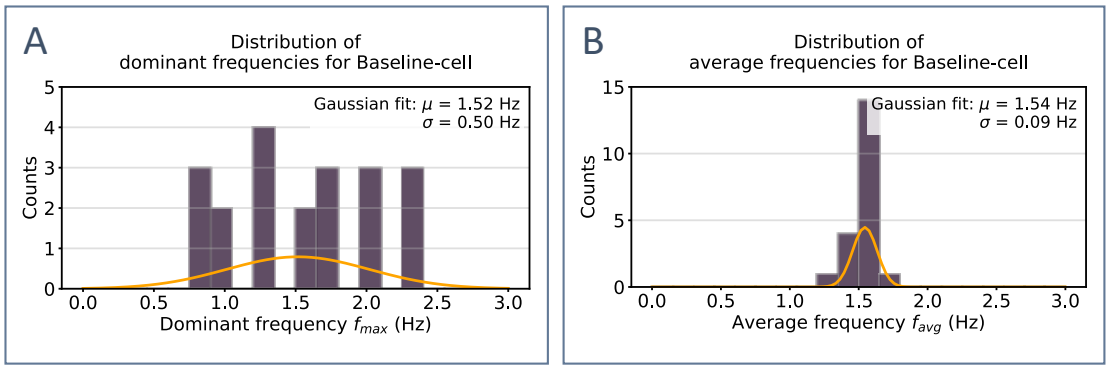

Figure 3.75 Frequency distributions for control baseline recording at the individual-cell level. (A) Histogram of dominant frequencies (f_{max}) obtained from Welch analysis of each cell outline; Gaussian fit overlaid in yellow. (B) Histogram of average frequencies (f_{avg}) derived from the same Welch analysis, again with Gaussian fit.

Table 3.9 Summary of peak-detection metrics for baseline recording at the individual-cell level. Average number of detected peaks (before and after processing), mean peak frequencies, and corresponding standard deviations for maxima and minima detected across selected cells.

Peak type	Avg# for Original	Avg# for Processed	#Δ (Proc-Orig)	Mean freq Orig (Hz)	Mean freq Proc (Hz)	Mean freq Δ	Std of Mean freq Orig	Std of Mean freq Proc	Std of Mean freq Δ
Maxima	28.3	14.25	-14.05	1.94	1.08	-0.87	0.1	0.15	0.18
Minima	27.7	14.3	-13.4	1.91	1.04	-0.87	0.14	0.15	0.21

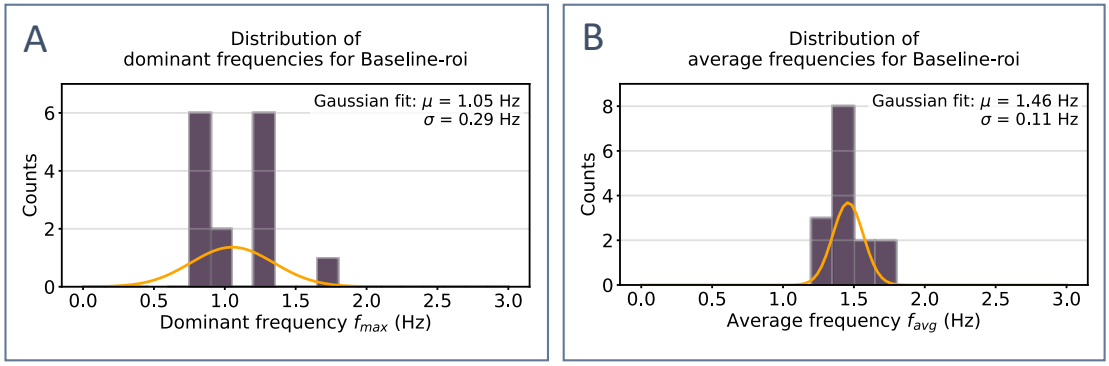

Figure 3.76 Frequency distributions for baseline recording at the ROI level. (A) Histogram of dominant frequencies (f_{max}) obtained from Welch analysis of small ROIs (5 × 5 pixels), with Gaussian fit overlaid. (B) Histogram of average frequencies (f_{avg}) for the same ROIs, with corresponding Gaussian fit.

Table 3.10. Summary of peak-detection metrics for baseline recording at the ROI level.

Peak type	Avg# for Original	Avg# for Processed	#Δ (Proc-Orig)	Mean freq Orig (Hz)	Mean freq Proc (Hz)	Mean freq Δ	Std of Mean freq Orig	Std of Mean freq Proc	Std of Mean freq Δ
Maxima	28.13	14.13	-14.0	1.95	1.03	-0.92	0.07	0.17	0.2
Minima	27.73	14.87	-12.87	1.91	1.07	-0.84	0.08	0.14	0.15

Taken together, the control baseline data demonstrate that frequency estimates vary substantially between analytical methods and remain highly variable across different levels of spatial resolution, from whole-frame averages to individual cells and small membrane ROIs (

Table 3.11). The clear 0.75 Hz peak in the Welch spectrum, the broader 1.3-1.8 Hz distribution in the histogram, and the variability in peak-detection results all suggest that the observed periodic components reflect stochastic intensity fluctuations rather than coordinated electrical activity. These findings reinforce the conclusion drawn from the TTX control: under the current signal-to-noise conditions, the periodic components detected in SQW recordings cannot yet be reliably attributed to membrane-voltage spiking. Further improvements in probe brightness and noise suppression will be required before spectral and peak-based analyses can yield consistent, biologically meaningful spike detection.

Table 3.11 Comparison of frequency estimates for baseline recording (unstained HEK cells), from whole-frame, individual-cell, and small-ROI analyses using three methods: dominant frequency from Welch spectrum, average frequency from Welch-estimated PSD histogram, and peak-detection-derived mean frequencies (maxima and minima). The table highlights variability across methods and spatial scales in the control sample (baseline, noise-only) condition.

Baseline (control sample)	Welch spectra (dominant frequency)	Welch histogram (average frequency)	Detected spikes from processed traces	
			max peak	min peak
frame	0.75 Hz	1.26 Hz	1.62 ± 0.81 Hz	1.71 ± 0.76 Hz
cells	1.52 ± 0.5 Hz	1.54 ± 0.09 Hz	0.60 ± 0.07 Hz	0.59 ± 0.05 Hz
small ROI	1.05 ± 0.29 Hz	1.46 ± 0.11 Hz	1.03 ± 0.17 Hz	1.07 ± 0.14 Hz

Reference recording: calcium imaging of corresponding sample

Having established through the TTX control and baseline recordings that the periodic components observed in the SQW-labelled samples could not be conclusively attributed to membrane-voltage spikes, it is essential to demonstrate that the HEK cells used in these experiments were indeed exhibiting spiking behavior under the given culture conditions. For this purpose, calcium imaging was performed on a corresponding "twin" sample from the same experimental batch, prepared in parallel with the SQW-labelled cultures, following the workflow described in Figure 3.57. In each batch, at least one set of cells was stained with Calcium Green-1 to monitor intracellular Ca^{2+} transients, providing an independent reference for spiking activity, while the matched sample was used for SQW-based voltage imaging. In the following section, we present the results of this calcium imaging, including raw and processed traces at the whole-frame, cell, and ROI levels, and corresponding frequency analyses.

In the calcium-imaging control, the presence of periodic activity is evident even prior to signal processing. Averaging the fluorescence intensity across the entire field of view (Figure 3.77 C, left) produces a raw trace in which well-resolved calcium transients are clearly visible at regular intervals. The filtering pipeline (Figure 3.77 D, right) further smooths the traces without altering the underlying temporal pattern. Consistent with this visual impression, Welch analysis of the processed trace yields a single, narrow peak at approximately 0.75 Hz (Figure 3.77 E), while the histogram of peak frequencies extracted from individual Welch windows is tightly clustered around 0.66 Hz (Figure 3.77 F). The close agreement between the dominant frequency and the histogram average, along with the absence of side-bands or broadband spectral power, indicates a stable and coherent spiking rhythm across the cell monolayer.

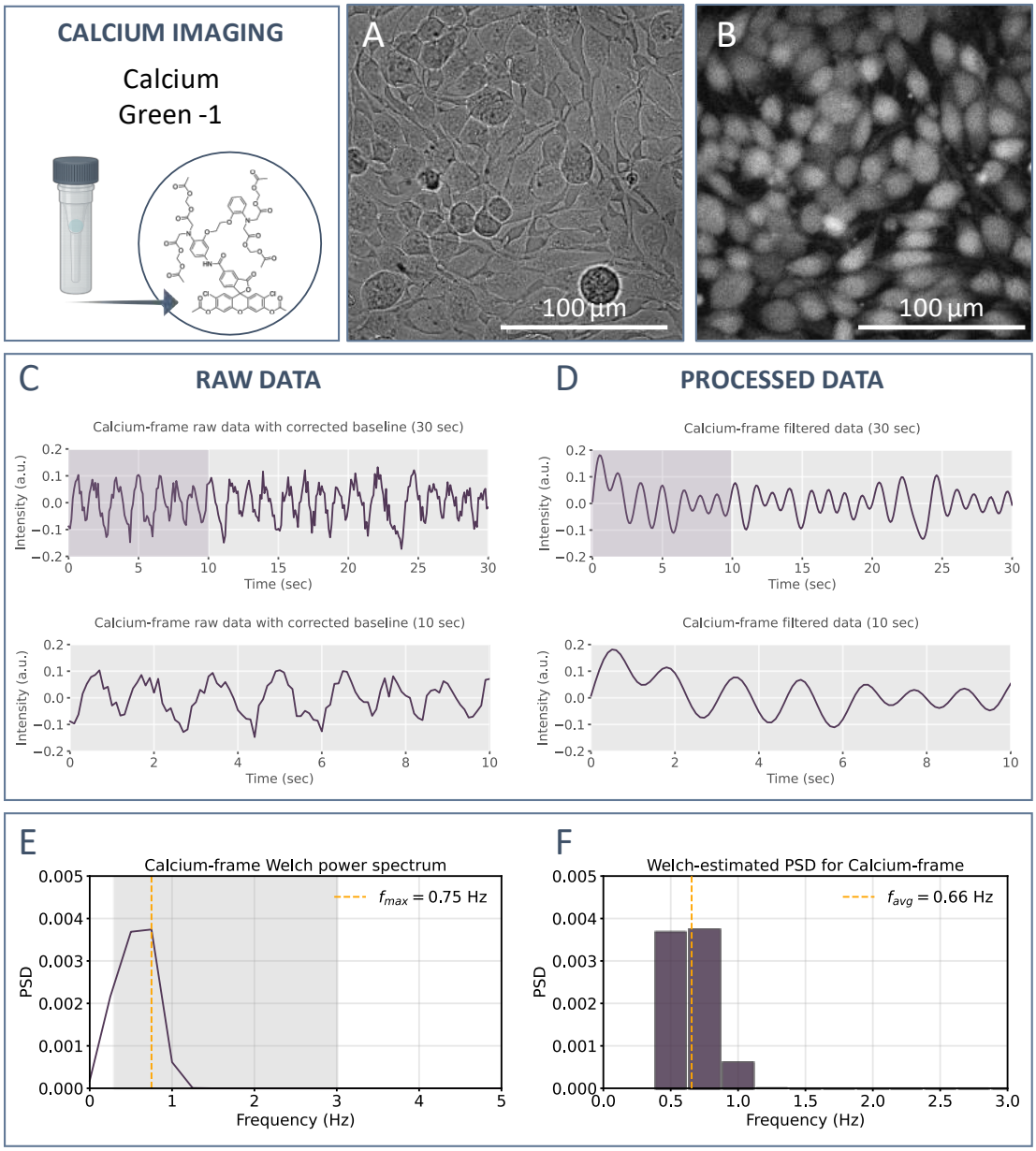

Figure 3.77 Whole-frame analysis of calcium imaging in spiking HEK cells. (A) Brightfield image of the HEK cell monolayer. (B) Corresponding fluorescence image following Calcium Green-1 staining. (C) Raw fluorescence traces after baseline correction. (D) Processed fluorescence traces after filtering. (E) Welch power spectrum of the processed trace, with dominant frequency indicated. (F) Welch-estimated power spectral density (PSD) histogram, showing average frequency.

Whole-frame peak detection further confirms the presence of rhythmic Ca^{2+} activity observed in the preceding Welch analysis. In the unprocessed trace (Figure 3.78 A), 28 maxima and 28 minima were detected, yielding mean peak frequencies of 1.25 Hz and 1.24 Hz, respectively, though both exhibited large standard deviations (~0.8-0.9 Hz). The high peak count in the raw data can be attributed to sharp local fluctuations, which frequently resulted in multiple peaks being identified within a single calcium transient. Following filtering (Figure 3.78 B), the number of detected events decreased modestly to 22 maxima and 17 minima. Importantly, the mean

frequencies after filtering dropped to 0.75 Hz (maxima) and 0.66 Hz (minima), with substantially lower standard deviations (0.12-0.17 Hz), as shown in Figure 3.78, panel C. These results align closely with the ≈0.75 Hz dominant frequency obtained from the Welch power spectrum. Thus, the filtering process effectively suppressed noise-induced false positives, resulting in a peak count and frequency estimate that corresponds well with the visually observed spiking rhythm in the trace.

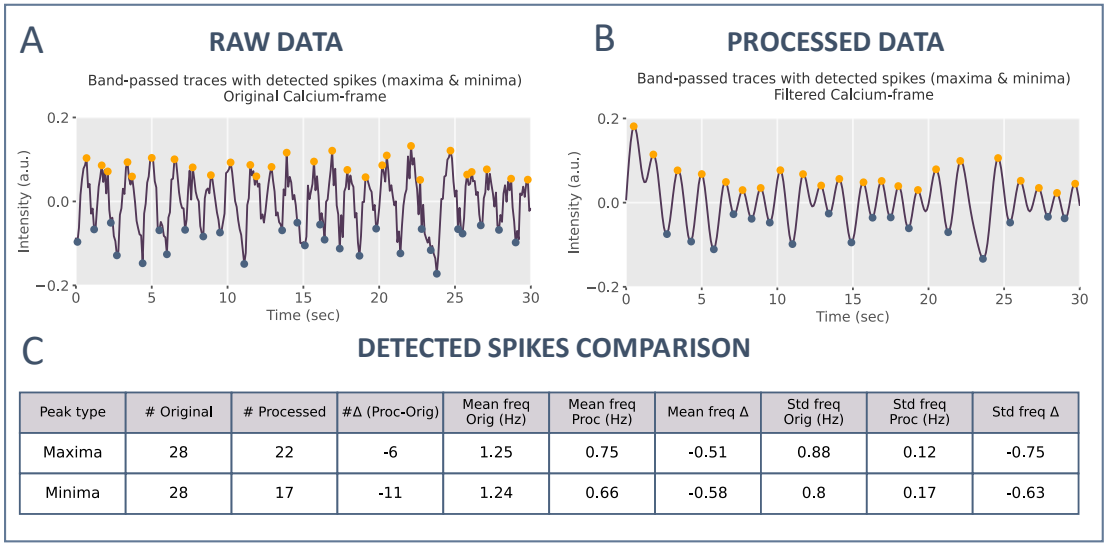

Peak type	# Original	# Processed	#Δ (Proc-Orig)	Mean freq Orig (Hz)	Mean freq Proc (Hz)	Mean freq Δ	Std freq Orig (Hz)	Std freq Proc (Hz)	Std freq Δ
Maxima	28	22	-6	1.25	0.75	-0.51	0.88	0.12	-0.75
Minima	28	17	-11	1.24	0.66	-0.58	0.8	0.17	-0.63

Figure 3.78 Peak-detection analysis of calcium imaging (whole-frame). (A) Raw fluorescence trace with detected maxima (yellow) and minima (blue). (B) Corresponding processed trace after filtering, with detected peaks highlighted. (C) Summary table comparing the number of detected peaks and mean frequencies before and after processing, with associated standard deviations for maxima and minima.

At the individual-cell level, calcium imaging reveals a highly consistent and well-defined spiking rhythm across the HEK cell monolayer. The selected twenty cells (Figure 3.79 A, B) display clear periodic activity, with calcium transients readily visible in the raw fluorescence traces (Figure 3.79 C), despite the presence of high-frequency noise. After baseline correction and filtering (Figure 3.79 D), the traces resolve into smooth, regular oscillations with highly uniform periodicity across all cells, consistent with globally synchronous spiking behavior. This visual impression is strongly supported by quantitative frequency analysis: Welch-derived dominant frequencies are centered at 0.56 ± 0.11 Hz (Figure 3.80 A), while the average frequencies exhibit an even tighter distribution around 0.65 ± 0.02 Hz (Figure 3.80 B). Peak-detection analysis yields consistent results, with mean processed frequencies of 0.6 Hz for maxima and 0.59 Hz for minima, accompanied by low variability across cells (Table 3.12).

These consistent results, summarized in Table 3.13, confirm that under the given culture conditions, the spiking HEK cells exhibit stable and coherent calcium dynamics across the monolayer, providing a reliable benchmark for comparison with SQW-based recordings. Given

that the SQW-labelled sample was prepared from the same cell batch and under identical experimental conditions, it is reasonable to expect that those cells were exhibiting similar spiking behavior during recording. Therefore, if the SQW-based method were capable of reliably detecting membrane-voltage spikes, corresponding activity should have been observable in the previously analyzed SQW recordings, with an expected frequency in the range of approximately 0.5 to 0.8 Hz.

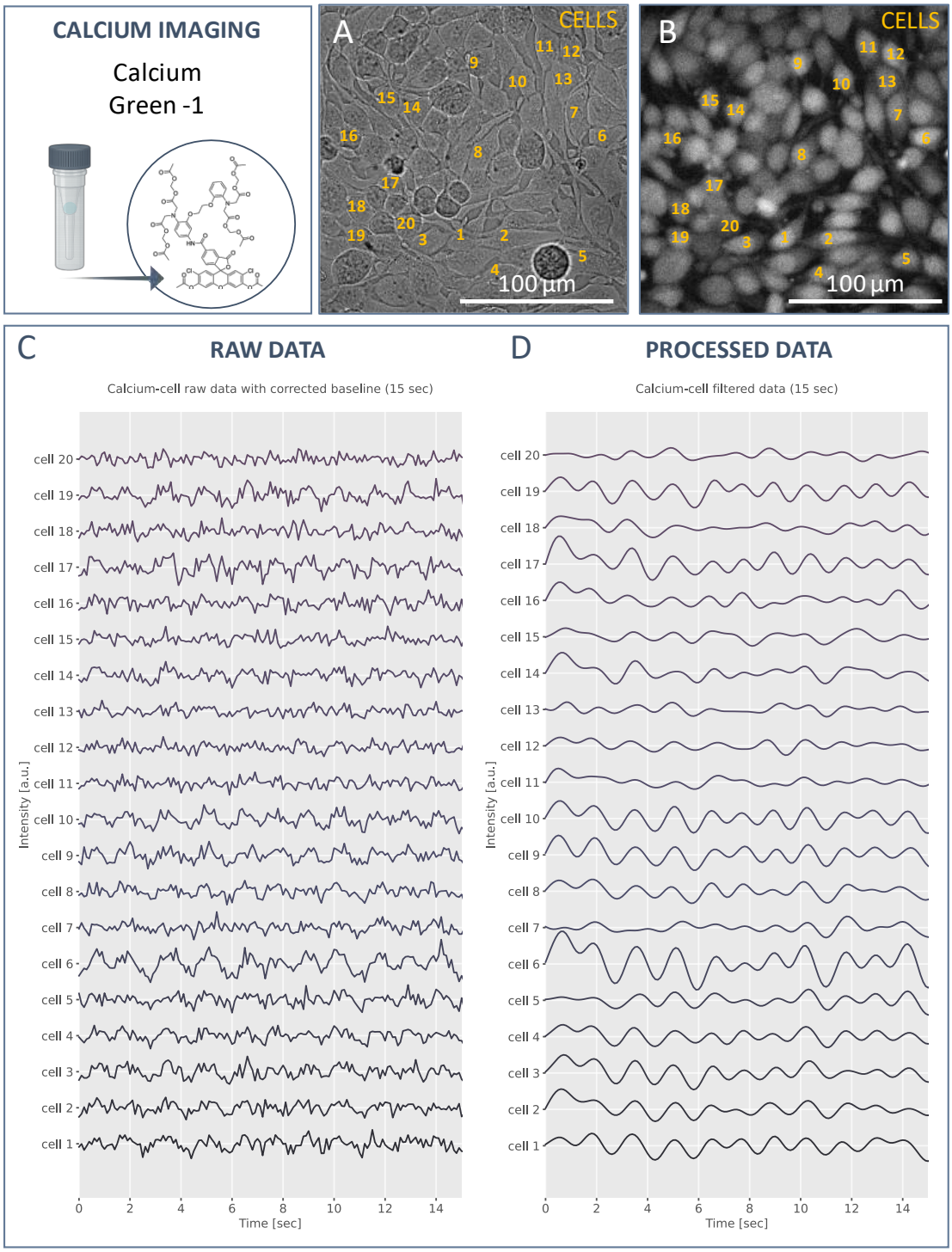

Figure 3.79 Cell-based calcium imaging analysis of spiking HEK cells. (A) Brightfield image of the HEK cell monolayer with selected cell ROIs (numbered 1-20). (B) Corresponding fluorescence image following Calcium Green-1 staining. (C) Raw fluorescence traces for individual cells after baseline correction. (D) Processed traces after filtering, showing consistent and synchronous calcium transients across cells.

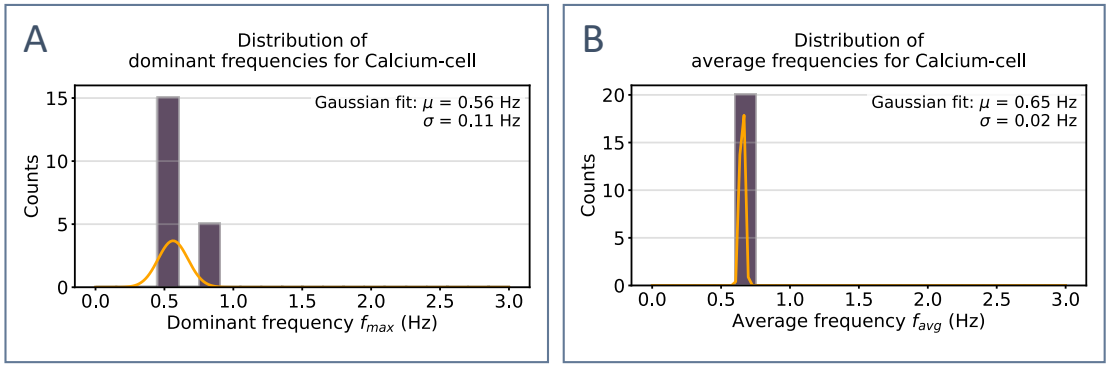

Figure 3.80 Frequency distributions for calcium imaging at the individual-cell level. (A) Histogram of dominant frequencies (f_{max}) obtained from Welch analysis of individual cell traces, with Gaussian fit overlaid. (B) Histogram of average frequencies (f_{avg}) for the same cells, showing a narrow and well-defined frequency distribution.

Table 3.12 Summary of peak-detection metrics for calcium imaging at the individual-cell level. Average number of detected peaks (before and after processing), mean peak frequencies, and corresponding standard deviations for maxima and minima detected across selected cells.

Peak type	Avg# for Original	Avg# for Processed	#Δ (Proc-Orig)	Mean freq Orig (Hz)	Mean freq Proc (Hz)	Mean freq Δ	Std of Mean freq Orig	Std of Mean freq Proc	Std of Mean freq Δ
Maxima	30.65	16.6	-14.05	1.08	0.6	-0.48	0.09	0.07	0.12
Minima	31.15	15.2	-15.95	1.09	0.59	-0.51	0.13	0.05	0.13

Table 3.13 Summary of frequency estimates for calcium imaging. Comparison of frequencies obtained from whole-frame and individual-cell analyses using three methods: dominant frequency from Welch spectrum, average frequency from Welch-estimated PSD histogram, and peak-detection-derived mean frequencies (maxima and minima).

Calcium	Welch spectra (dominant frequency)	Welch histogram (average frequency)	Detected spikes from processed traces	
			max peak	min peak
frame	0.75 Hz	0.66 Hz	0.75 ± 0.12 Hz	0.66 ± 0.17 Hz
cells	0.56 ± 0.11 Hz	0.65 ± 0.02 Hz	0.6 ± 0.07 Hz	0.59 ± 0.05 Hz

5. Chapter Summary

In this chapter, we explored the potential of spherical quantum-well (SQW) nanocrystals as voltage-sensitive optical probes for neuronal activity. Our work encompassed the complete development process, from nanocrystal synthesis and photophysical characterization, through water transfer and surface functionalization, to membrane targeting and in vitro live-cell voltage imaging.

A key outcome of this study is the establishment of an effective membrane delivery strategy for SQWs, based on engineered fusogenic liposomes. This approach enabled bright, uniform membrane staining of live HEK cells with excellent biocompatibility. It represented a substantial improvement over earlier methods such as micelle encapsulation or linear ligand exchange, which often suffered from poor targeting and cytotoxic effects. The ability to reproducibly localize SQWs at the plasma membrane provides a robust platform for further development of these nanomaterials as voltage sensors.

However, the functional imaging experiments did not yet yield reliable detection of membrane potential dynamics. Wide-field recordings of spiking HEK cells labelled with SQWs exhibited fluorescence fluctuations that did not correlate with true electrical activity. Signal profiles remained largely unchanged after pharmacological blockade of action potentials with tetrodotoxin (TTX), and similar noise features were observed in unstained control samples. Furthermore, the dominant frequency components extracted from SQW recordings were inconsistent across different analytical methods and did not match the spike patterns observed via calcium imaging in paired control samples. These observations indicate that the current system lacks sufficient sensitivity for robust voltage detection under the tested conditions.

Several factors are likely to contribute to this limitation. First, the fluorescence signal intensity may be insufficient to support spike-resolved imaging at the required frame rates. Second, the acquisition speed (~33 frames per second) may be inadequate to capture the intrinsically fast voltage response of SQWs. Third, the optical detection setup may require further optimization; for example, the use of more sensitive detectors such as back-illuminated sCMOS, EMCCD, or single-photon-counting systems could substantially improve signal-to-noise ratio.

In conclusion, this chapter demonstrates significant progress in the bio-integration of SQWs for membrane targeting, establishing an essential foundation for further voltage imaging work. At the same time, it identifies critical areas for future optimization. These include fluorescence brightness, detection sensitivity, and imaging speed. Addressing these factors is essential to fully realize the potential of SQWs as practical tools for all-optical electrophysiology.

6. References for Chapter 3

(1) Jeong, B. G.; Park, Y.-S.; Chang, J. H.; Cho, I.; et al. Colloidal Spherical Quantum Wells with Near-Unity Photoluminescence Quantum Yield and Suppressed Blinking. *ACS Nano* **2016**, *10* (10), 9297–9305. https://doi.org/10.1021/acsnano.6b03704.

(2) Chu, A.; Livache, C.; Ithurria, S.; Lhuillier, E. Electronic Structure Robustness and Design Rules for 2D Colloidal Heterostructures. *J. Appl. Phys.* **2018**, *123* (3), 035701. https://doi.org/10.1063/1.5003289.

(3) Allemand, A.; Kulzer, F.; Mahler, B.; Dujardin, C.; et al. Optical Properties of Individual CdS/CdSe/CdS Nanocrystals: Spherical Quantum Wells as Single-Photon Sources. *Nanotechnology* **2022**, *33* (27), 275703. https://doi.org/10.1088/1361-6528/ac5ee3.

(4) Nagamine, G.; Jeong, B. G.; Ferreira, T. A. C.; Chang, J. H.; et al. Efficient Optical Gain in Spherical Quantum Wells Enabled by Engineering Biexciton Interactions. *ACS Photonics* **2020**, *7* (8), 2252–2264. https://doi.org/10.1021/acsphotonics.0c00812.

(5) Xu, J.; Xiao, M.; Battaglia, D.; Peng, X. Exciton Radiative Recombination in Spherical CdS⁄CdSe⁄CdS Quantum-Well Nanostructures. *Appl. Phys. Lett.* **2005**, *87* (4), 043107. https://doi.org/10.1063/1.2001731.

(6) Battaglia, D.; Li, J. J.; Wang, Y.; Peng, X. Colloidal Two-Dimensional Systems: CdSe Quantum Shells and Wells. *Angew. Chem. Int. Ed.* **2003**, *42* (41), 5035–5039. https://doi.org/10.1002/anie.200352120.

(7) Marder, A. A.; Cassidy, J.; Harankahage, D.; Beavon, J.; et al. CdS/CdSe/CdS Spherical Quantum Wells with Near-Unity Biexciton Quantum Yield for Light-Emitting-Device Applications. *ACS Mater. Lett.* **2023**, *5* (5), 1411–1419. https://doi.org/10.1021/acsmaterialslett.3c00110.

(8) Xiang, W.; Bai, C.; Zhang, Z.; Gu, B.; et al. Modulation of High-Intensity Optical Properties in CdS/CdSe/CdS Spherical Quantum Wells by CdSe Layer Thickness. *Nanomaterials* **2024**, *14* (19), 1568. https://doi.org/10.3390/nano14191568.

(9) Toscano-Negrette, R. G.; León-González, J. C.; Vinasco, J. A.; Morales, A. L.; et al. Optical Properties in a ZnS/CdS/ZnS Core/Shell/Shell Spherical Quantum Dot: Electric and Magnetic Field and Donor Impurity Effects. *Nanomaterials* **2023**, *13* (3), 550. https://doi.org/10.3390/nano13030550.

(10) Jo, D.-Y.; Kim, H.-M.; Park, G. M.; Shin, D.; et al. Unity Quantum Yield of InP/ZnSe/ZnS Quantum Dots Enabled by Zn Halide-Derived Hybrid Shelling Approach. *Soft Sci.* **2024**, *4* (3), N/A-N/A. https://doi.org/10.20517/ss.2024.19.

(11) Talapin, D. V.; Mekis, I.; Götzinger, S.; Kornowski, A.; et al. CdSe/CdS/ZnS and CdSe/ZnSe/ZnS Core−Shell−Shell Nanocrystals. *J. Phys. Chem. B* **2004**, *108* (49), 18826–18831. https://doi.org/10.1021/jp046481g.

(12) Diroll, B. T.; Chen, M.; Coropceanu, I.; Williams, K. R.; et al. Polarized Near-Infrared Intersubband Absorptions in CdSe Colloidal Quantum Wells. *Nat. Commun.* **2019**, *10* (1), 4511. https://doi.org/10.1038/s41467-019-12503-z.

(13) Meng, Z.; Mahler, B.; Houel, J.; Kulzer, F.; et al. Perspectives for CdSe/CdS Spherical Quantum Wells as Rapid-Response Nano-Scintillators. *Nanoscale* **2021**, *13* (46), 19578–19586. https://doi.org/10.1039/D1NR04781G.

(14) Quesada-González, D.; Merkoçi, A. Quantum Dots for Biosensing: Classification and Applications. *Biosens. Bioelectron.* **2025**, *273*, 117180. https://doi.org/10.1016/j.bios.2025.117180.

(15) Li, X.; Van Embden, J.; Chon, J. W. M.; Gu, M. Enhanced Two-Photon Absorption of CdS Nanocrystal Rods. *Appl. Phys. Lett.* **2009**, *94* (10). https://doi.org/10.1063/1.3100196.

(16) García de Arquer, F. P.; Talapin, D. V.; Klimov, V. I.; Arakawa, Y.; et al. Semiconductor Quantum Dots: Technological Progress and Future Challenges. *Science* **2021**, *373* (6555), eaaz8541. https://doi.org/10.1126/science.aaz8541.

(17) Cragg, G. E.; Efros, A. L. Suppression of Auger Processes in Confined Structures. *Nano Lett.* **2010**, *10* (1), 313–317. https://doi.org/10.1021/nl903592h.

(18) Giansante, C.; Infante, I. Surface Traps in Colloidal Quantum Dots: A Combined Experimental and Theoretical Perspective. *J. Phys. Chem. Lett.* **2017**, *8* (20), 5209–5215. https://doi.org/10.1021/acs.jpclett.7b02193.

(19) Marshall, J. D.; Schnitzer, M. J. Optical Strategies for Sensing Neuronal Voltage Using Quantum Dots and Other Semiconductor Nanocrystals. *ACS Nano* **2013**, *7* (5), 4601–4609. https://doi.org/10.1021/nn401410k.

(20) Park, K.; Weiss, S. Design Rules for Membrane-Embedded Voltage-Sensing Nanoparticles. *Biophys. J.* **2017**, *112* (4), 703–713. https://doi.org/10.1016/j.bpj.2016.12.047.

(21) Efros, A. L.; Delehanty, J. B.; Huston, A. L.; Medintz, I. L.; et al. Evaluating the Potential of Using Quantum Dots for Monitoring Electrical Signals in Neurons. *Nat. Nanotechnol.* **2018**, *13* (4), 278–288. https://doi.org/10.1038/s41565-018-0107-1.

(22) Hendricks, M. P.; Campos, M. P.; Cleveland, G. T.; Jen-La Plante, I.; et al. A Tunable Library of Substituted Thiourea Precursors to Metal Sulfide Nanocrystals. *Science* **2015**, *348* (6240), 1226–1230. https://doi.org/10.1126/science.aaa2951.

(23) Campos, M. P.; Hendricks, M. P.; Beecher, A. N.; Walravens, W.; et al. A Library of Selenourea Precursors to PbSe Nanocrystals with Size Distributions near the Homogeneous Limit. *J. Am. Chem. Soc.* **2017**, *139* (6), 2296–2305. https://doi.org/10.1021/jacs.6b11021.

(24) Bar, L.; Perissinotto, F.; Redondo-Morata, L.; Giannotti, M. I.; et al. Interactions of Hydrophilic Quantum Dots with Defect-Free and Defect Containing Supported Lipid Membranes. *Colloids Surf. B Biointerfaces* **2022**, *210*, 112239. https://doi.org/10.1016/j.colsurfb.2021.112239.

(25) Koyasu, S.; Ikeda, H.; Ishigaki, T. Exchange of Thiol Ligands on CuInS2 Quantum Dots in High Boiling Solvents. *Langmuir* **2024**, *40* (35), 18466–18472. https://doi.org/10.1021/acs.langmuir.4c01475.

(26) Calzada, R.; Thompson, C. M.; Westmoreland, D. E.; Edme, K.; et al. Organic-to-Aqueous Phase Transfer of Cadmium Chalcogenide Quantum Dots Using a Sulfur-Free Ligand for Enhanced Photoluminescence and Oxidative Stability. *Chem. Mater.* **2016**, *28* (18), 6716–6723. https://doi.org/10.1021/acs.chemmater.6b03106.

(27) Lee, K. H.; Noesges, B. A.; McPherson, C.; Khan, F.; et al. Oxidation of Quantum Dots Encapsulated in Block Copolymer Micelles as a Function of Polymer Terminal Charge. *Nanoscale* **2022**, *14* (32), 11779–11789. https://doi.org/10.1039/D2NR00778A.

(28) Lee, S. M.; Jung, H.; Park, W. I.; Lee, Y.; et al. Preparation of Water-Soluble CsPbBr3 Perovskite Quantum Dot Nanocomposites via Encapsulation into Amphiphilic

Copolymers. *ChemistrySelect* **2018**, *3* (40), 11320–11325. https://doi.org/10.1002/slct.201802237.

(29) Carrillo-Carrion, C.; Bocanegra, A. I.; Arnaiz, B.; Feliu, N.; et al. Triple-Labeling of Polymer-Coated Quantum Dots and Adsorbed Proteins for Tracing Their Fate in Cell Cultures. *ACS Nano* **2019**, *13* (4), 4631–4639. https://doi.org/10.1021/acsnano.9b00728.

(30) Nakane, Y.; Sasaki, A.; Kinjo, M.; Jin, T. Bovine Serum Albumin-Coated Quantum Dots as a Cytoplasmic Viscosity Probe in a Single Living Cell. *Anal. Methods* **2012**, *4* (7), 1903–1905. https://doi.org/10.1039/C2AY25318F.

(31) Zhang, B.; Wang, X.; Liu, F.; Cheng, Y.; et al. Effective Reduction of Nonspecific Binding by Surface Engineering of Quantum Dots with Bovine Serum Albumin for Cell-Targeted Imaging. *Langmuir* **2012**, *28* (48), 16605–16613. https://doi.org/10.1021/la302758g.

(32) Morandat, S.; El Kirat, K. Solubilization of Supported Lipid Membranes by Octyl Glucoside Observed by Time-Lapse Atomic Force Microscopy. *Colloids Surf. B Biointerfaces* **2007**, *55* (2), 179–184. https://doi.org/10.1016/j.colsurfb.2006.11.039.

(33) Walter, A.; Kuehl, G.; Barnes, K.; VanderWaerdt, G. The Vesicle-to-Micelle Transition of Phosphatidylcholine Vesicles Induced by Nonionic Detergents: E°ects of Sodium Chloride, Sucrose and Urea.

(34) Vinson, P. K.; Talmon, Y.; Walter, A. Vesicle-Micelle Transition of Phosphatidylcholine and Octyl Glucoside Elucidated by Cryo-Transmission Electron Microscopy. *Biophys. J.* **1989**, *56* (4), 669–681. https://doi.org/10.1016/S0006-3495(89)82714-6.

(35) Rasch, M. R.; Rossinyol, E.; Hueso, J. L.; Goodfellow, B. W.; et al. Hydrophobic Gold Nanoparticle Self-Assembly with Phosphatidylcholine Lipid: Membrane-Loaded and Janus Vesicles. *Nano Lett.* **2010**, *10* (9), 3733–3739. https://doi.org/10.1021/nl102387n.

(36) Sharma, H.; Sharma, S. N.; Kumar, U.; Singh, V. N.; et al. Formation of Water-Soluble and Biocompatible TOPO-Capped CdSe Quantum Dots with Efficient Photoluminescence. *J. Mater. Sci. Mater. Med.* **2009**, *20* (1), 123–130. https://doi.org/10.1007/s10856-008-3494-2.

(37) Jasieniak, J.; Smith, L.; Van Embden, J.; Mulvaney, P.; et al. Re-Examination of the Size-Dependent Absorption Properties of CdSe Quantum Dots. *J. Phys. Chem. C* **2009**, *113* (45), 19468–19474. https://doi.org/10.1021/jp906827m.

(38) De Leo, V.; Maurelli, A. M.; Giotta, L.; Catucci, L. Liposomes Containing Nanoparticles: Preparation and Applications. *Colloids Surf. B Biointerfaces* **2022**, *218*, 112737. https://doi.org/10.1016/j.colsurfb.2022.112737.

(39) Ianiro, A.; Wu, H.; van Rijt, M. M. J.; Vena, M. P.; et al. Liquid–Liquid Phase Separation during Amphiphilic Self-Assembly. *Nat. Chem.* **2019**, *11* (4), 320–328. https://doi.org/10.1038/s41557-019-0210-4.

(40) Parchekani, J.; Allahverdi, A.; Taghdir, M.; Naderi-Manesh, H. Design and Simulation of the Liposomal Model by Using a Coarse-Grained Molecular Dynamics Approach towards Drug Delivery Goals. *Sci. Rep.* **2022**, *12* (1), 2371. https://doi.org/10.1038/s41598-022-06380-8.

(41) Mathiyazhakan, M.; Wiraja, C.; Xu, C. A Concise Review of Gold Nanoparticles-Based Photo-Responsive Liposomes for Controlled Drug Delivery. *Nano-Micro Lett.* **2017**, *10* (1), 10. https://doi.org/10.1007/s40820-017-0166-0.

(42) Liu, J.; Li, X.; Liu, L.; Bai, Q.; et al. Self-Assembled Ultrasmall Silver Nanoclusters on Liposome for Topical Antimicrobial Delivery. *Colloids Surf. B Biointerfaces* **2021**, *200*, 111618. https://doi.org/10.1016/j.colsurfb.2021.111618.

(43) Eid, K. A.; and Azzazy, H. M. Sustained Broad-Spectrum Antibacterial Effects of Nanoliposomes Loaded with Silver Nanoparticles. *Nanomed.* **2014**, *9* (9), 1301–1310. https://doi.org/10.2217/nnm.13.89.

(44) Youssef, Z.; Vanderesse, R.; Colombeau, L.; Baros, F.; et al. The Application of Titanium Dioxide, Zinc Oxide, Fullerene, and Graphene Nanoparticles in Photodynamic Therapy. *Cancer Nanotechnol.* **2017**, *8* (1), 6. https://doi.org/10.1186/s12645-017-0032-2.

(45) Tripathy, N.; Ahmad, R.; Ko, H. A.; Khang, G.; et al. Enhanced Anticancer Potency Using an Acid-Responsive ZnO-Incorporated Liposomal Drug-Delivery System. *Nanoscale* **2015**, *7* (9), 4088–4096. https://doi.org/10.1039/C4NR06979J.

(46) Das, S.; Dowding ,Janet M; Klump ,Kathryn E; McGinnis ,James F; et al. Cerium Oxide Nanoparticles: Applications and Prospects in Nanomedicine. *Nanomed.* **2013**, *8* (9), 1483–1508. https://doi.org/10.2217/nnm.13.133.

(47) Heidari Khoee, M.; Khoee, S.; Lotfi, M. Synthesis of Titanium Dioxide Nanotubes with Liposomal Covers for Carrying and Extended Release of 5-FU as Anticancer Drug in the Treatment of HeLa Cells. *Anal. Biochem.* **2019**, *572*, 16–24. https://doi.org/10.1016/j.ab.2019.02.027.

(48) Wu, S.; Weng, Z.; Liu, X.; Yeung, K. W. K.; et al. Functionalized TiO_2 Based Nanomaterials for Biomedical Applications. *Adv. Funct. Mater.* **2014**, *24* (35), 5464–5481. https://doi.org/10.1002/adfm.201400706.

(49) Liao, Z.; Wang, H.; Lv, R.; Zhao, P.; et al. Polymeric Liposomes-Coated Superparamagnetic Iron Oxide Nanoparticles as Contrast Agent for Targeted Magnetic Resonance Imaging of Cancer Cells. *Langmuir* **2011**, *27* (6), 3100–3105. https://doi.org/10.1021/la1050157.

(50) Thébault, C. J.; Ramniceanu, G.; Boumati, S.; Michel, A.; et al. Theranostic MRI Liposomes for Magnetic Targeting and Ultrasound Triggered Release of the Antivascular CA4P. *J. Controlled Release* **2020**, *322*, 137–148. https://doi.org/10.1016/j.jconrel.2020.03.003.

(51) Aizik, G.; Waiskopf, N.; Agbaria, M.; Ben-David-Naim, M.; et al. Liposomes of Quantum Dots Configured for Passive and Active Delivery to Tumor Tissue. *Nano Lett.* **2019**, *19* (9), 5844–5852. https://doi.org/10.1021/acs.nanolett.9b01027.

(52) Awad, N. S.; Haider, M.; Paul, V.; AlSawaftah, N. M.; et al. Ultrasound-Triggered Liposomes Encapsulating Quantum Dots as Safe Fluorescent Markers for Colorectal Cancer. *Pharmaceutics* **2021**, *13* (12), 2073. https://doi.org/10.3390/pharmaceutics13122073.

(53) Reina, G.; González-Domínguez, J. M.; Criado, A.; Vázquez, E.; et al. Promises, Facts and Challenges for Graphene in Biomedical Applications. *Chem. Soc. Rev.* **2017**, *46* (15), 4400–4416. https://doi.org/10.1039/C7CS00363C.

(54) Othman, A. K.; Kurdi, R. E.; Badran, A.; Mesmar, J.; et al. Liposome-Based Nanocapsules for the Controlled Release of Dietary Curcumin: PDDA and Silica Nanoparticle-Coated DMPC Liposomes Enhance the Fluorescence Efficiency and Anticancer Activity of Curcumin. *RSC Adv.* **2022**, *12* (18), 11282–11292. https://doi.org/10.1039/D2RA00071G.

(55) Sapala, A. R.; Dhawan, S.; Haridas, V. Vesicles: Self-Assembly beyond Biological Lipids. *RSC Adv.* **2017**, *7* (43), 26608–26624. https://doi.org/10.1039/C7RA02746J.

(56) Gopalakrishnan, G.; Danelon, C.; Izewska, P.; Prummer, M.; et al. Multifunctional Lipid/Quantum Dot Hybrid Nanocontainers for Controlled Targeting of Live Cells. *Angew. Chem. Int. Ed.* **2006**, *45* (33), 5478–5483. https://doi.org/10.1002/anie.200600545.

(57) Chen, W.; Duša, F.; Witos, J.; Ruokonen, S.-K.; et al. Determination of the Main Phase Transition Temperature of Phospholipids by Nanoplasmonic Sensing. *Sci. Rep.* **2018**, *8* (1), 14815. https://doi.org/10.1038/s41598-018-33107-5.

(58) Traïkia, M.; Warschawski, D. E.; Recouvreur, M.; Cartaud, J.; et al. Formation of Unilamellar Vesicles by Repetitive Freeze-Thaw Cycles: Characterization by Electron Microscopy and 31P-Nuclear Magnetic Resonance. *Eur. Biophys. J.* **2000**, *29* (3), 184–195. https://doi.org/10.1007/s002490000077.

(59) Viitala, L.; Pajari, S.; Gentile, L.; Määttä, J.; et al. Shape and Phase Transitions in a PEGylated Phospholipid System. *Langmuir* **2019**, *35* (11), 3999–4010. https://doi.org/10.1021/acs.langmuir.8b03829.

(60) Losada-Pérez, P.; Mertens, N.; de Medio-Vasconcelos, B.; Slenders, E.; et al. Phase Transitions of Binary Lipid Mixtures: A Combined Study by Adiabatic Scanning Calorimetry and Quartz Crystal Microbalance with Dissipation Monitoring. *Adv. Condens. Matter Phys.* **2015**, *2015* (1), 479318. https://doi.org/10.1155/2015/479318.

(61) Hou, X.; Kang, J.; Qin, H.; Chen, X.; et al. Engineering Auger Recombination in Colloidal Quantum Dots via Dielectric Screening. *Nat. Commun.* **2019**, *10* (1), 1750. https://doi.org/10.1038/s41467-019-09737-2.

(62) Brown, M. F. Curvature Forces in Membrane Lipid-Protein Interactions. *Biochemistry* **2012**, *51* (49), 9782–9795. https://doi.org/10.1021/bi301332v.

(63) van der Pol, R. W. I.; Brinkmann, B. W.; Sevink, G. J. A. Analyzing Lipid Membrane Defects via a Coarse-Grained to Triangulated Surface Map: The Role of Lipid Order and Local Curvature in Molecular Binding. *J. Chem. Theory Comput.* **2024**, *20* (7), 2888–2900. https://doi.org/10.1021/acs.jctc.4c00082.

(64) Xiao, P.; Zhang, Z.; Ge, J.; Deng, Y.; et al. Surface Passivation of Intensely Luminescent All-Inorganic Nanocrystals and Their Direct Optical Patterning. *Nat. Commun.* **2023**, *14* (1), 49. https://doi.org/10.1038/s41467-022-35702-7.

(65) Wang, X.; Yu, J.; Chen, R. Optical Characteristics of ZnS Passivated CdSe/CdS Quantum Dots for High Photostability and Lasing. *Sci. Rep.* **2018**, *8* (1), 17323. https://doi.org/10.1038/s41598-018-35768-8.

(66) Park, J.; Werley, C. A.; Venkatachalam, V.; Kralj, J. M.; et al. Screening Fluorescent Voltage Indicators with Spontaneously Spiking HEK Cells. *PLOS ONE* **2013**, *8* (12), e85221. https://doi.org/10.1371/journal.pone.0085221.

(67) Cavalcanti, R. R. M.; Lira, R. B.; Riske, K. A. Membrane Fusion Biophysical Analysis of Fusogenic Liposomes. *Langmuir* **2022**, *38* (34), 10430–10441. https://doi.org/10.1021/acs.langmuir.2c01169.

(68) Kolašinac, R.; Kleusch, C.; Braun, T.; Merkel, R.; et al. Deciphering the Functional Composition of Fusogenic Liposomes. *Int. J. Mol. Sci.* **2018**, *19* (2), 346. https://doi.org/10.3390/ijms19020346.

(69) Scheeder, A.; Brockhoff, M.; Ward, E. N.; Kaminski Schierle, G. S.; et al. Molecular Mechanisms of Cationic Fusogenic Liposome Interactions with Bacterial Envelopes. *J. Am. Chem. Soc.* **2023**, *145* (51), 28240–28250. https://doi.org/10.1021/jacs.3c11463.

(70) Csiszár, A.; Hersch, N.; Dieluweit, S.; Biehl, R.; et al. Novel Fusogenic Liposomes for Fluorescent Cell Labeling and Membrane Modification. *Bioconjug. Chem.* **2010**, *21* (3), 537–543. https://doi.org/10.1021/bc900470y.

(71) Kleusch, C.; Hersch, N.; Hoffmann, B.; Merkel, R.; et al. Fluorescent Lipids: Functional Parts of Fusogenic Liposomes and Tools for Cell Membrane Labeling and Visualization. *Mol. Basel Switz.* **2012**, *17* (1), 1055–1073. https://doi.org/10.3390/molecules17011055.

(72) Nomura, F.; Inaba, T.; Ishikawa, S.; Nagata, M.; et al. Microscopic Observations Reveal That Fusogenic Peptides Induce Liposome Shrinkage Prior to Membrane Fusion. *Proc. Natl. Acad. Sci.* **2004**, *101* (10), 3420–3425. https://doi.org/10.1073/pnas.0304660101.

(73) Daudey, G. A.; Shen, M.; Singhal, A.; Van Der Est, P.; et al. Liposome Fusion with Orthogonal Coiled Coil Peptides as Fusogens: The Efficacy of Roleplaying Peptides. *Chem. Sci.* **2021**, *12* (41), 13782–13792. https://doi.org/10.1039/D0SC06635D.

(74) Kong, H.; Zheng, C.; Yi, K.; Mintz, R. L.; et al. An Antifouling Membrane-Fusogenic Liposome for Effective Intracellular Delivery in Vivo. *Nat. Commun.* **2024**, *15* (1), 4267. https://doi.org/10.1038/s41467-024-46533-z.

(75) Bruun, K.; Hille, C. Study on Intracellular Delivery of Liposome Encapsulated Quantum Dots Using Advanced Fluorescence Microscopy. *Sci. Rep.* **2019**, *9* (1), 10504. https://doi.org/10.1038/s41598-019-46732-5.

(76) Karmacharya, M.; Kumar, S.; Cho, Y.-K. Tuning the Extracellular Vesicles Membrane through Fusion for Biomedical Applications. *J. Funct. Biomater.* **2023**, *14* (2), 117. https://doi.org/10.3390/jfb14020117.

(77) Nag, O. K.; Oh, E.; Delehanty, J. B. Fusogenic Liposomes for the Intracellular Delivery of Phosphocreatine. *Pharmaceuticals* **2024**, *17* (10), 1351. https://doi.org/10.3390/ph17101351.

(78) MacDonald, R. I. Membrane Fusion Due to Dehydration by Polyethylene Glycol, Dextran, or Sucrose. *Biochemistry* **1985**, *24* (15), 4058–4066. https://doi.org/10.1021/bi00336a039.

(79) Lehtonen, J. Y.; Kinnunen, P. K. Changes in the Lipid Dynamics of Liposomal Membranes Induced by Poly(Ethylene Glycol): Free Volume Alterations Revealed by Inter- and Intramolecular Excimer-Forming Phospholipid Analogs. *Biophys. J.* **1994**, *66* (6), 1981–1990. https://doi.org/10.1016/S0006-3495(94)80991-9.

(80) Shi, S.; Markl, A. M.; Lu, Z.; Liu, R.; et al. Interplay of Fusion, Leakage, and Electrostatic Lipid Clustering: Membrane Perturbations by a Hydrophobic Antimicrobial Polycation. *Langmuir* **2022**, *38* (7), 2379–2391. https://doi.org/10.1021/acs.langmuir.1c03445.

(81) Yang, Y.; Qin, H.; Jiang, M.; Lin, L.; et al. Entropic Ligands for Nanocrystals: From Unexpected Solution Properties to Outstanding Processability. *Nano Lett.* **2016**, *16* (4), 2133–2138. https://doi.org/10.1021/acs.nanolett.6b00730.

(82) Park, K.; Kuo, Y.; Shvadchak, V.; Ingargiola, A.; et al. Membrane Insertion of—and Membrane Potential Sensing by—Semiconductor Voltage Nanosensors: Feasibility Demonstration. *Sci. Adv.* **2018**.

Chapter 4

Plasmonic Nanocrystals for Photothermal Modulation of Neuronal Activity

1. Synthesis of Gold Nanocrystals

The fascination with gold extends back thousands of years. Its visual appeal led ancient cultures to associate it with the sun, often referring to it as the “essence of the sun”, while its resistance to corrosion made it a symbol of immortality.[1] These qualities made gold both culturally significant and practically valuable for millennia. In Ancient Egypt, gold was used in medical preparations intended for purification and longevity.[2] By the Roman period, its applications had expanded to include decorative materials - most notably in colored glass. The Lycurgus Cup, which changes color depending on lighting conditions, is an example of colloidal gold embedded in glass - a result of the optical behavior now known to arise from nanoscale phenomena.[3]

Scientific study of colloidal gold began in 1857, when Michael Faraday reduced gold salts with phosphorus to produce stable dispersions with a deep red color.[4] The optical response of these solutions was not fully understood until 1908, when Gustav Mie applied electromagnetic theory to explain how light interacts with small particles. His work demonstrated that absorption and scattering by sub-wavelength gold particles were responsible for the observed.[5]

Gold nanocrystals, being smaller than the diffraction limit of light, remained invisible to optical microscopes until the 1930s, when electron microscopy was invented by Ruska and Knoll.[4] Building on this, a major step forward came in 1951, when Turkevich and colleagues[6] developed a simple method for synthesizing spherical gold nanoparticles in water. Using citrate as both the reducing and stabilizing agent, they produced colloids with relatively uniform size and recorded the first electron micrographs of these particles.[6] This method became the basis for decades of colloidal gold research. In 1973, Frens modified the procedure to allow size tuning by adjusting the citrate-to-gold ratio, offering improved control over particle uniformity.[4]

Further developments emerged in the 1990s, when Brust and Schiffrin introduced a two-phase synthesis method that enabled the production of small, thiol-stabilized gold nanocrystals dispersed in organic solvents[4]. This approach significantly broadened the chemical flexibility and surface functionalization potential of gold nanoparticles. Around the same time, Masuda and Martin demonstrated the use of hard templates to fabricate anisotropic structures such as nanorods. This was soon followed by the development of colloidal, seed-mediated methods by El-Sayed, Murphy, and others.[4] By the early 2000s, a new era of shape-controlled colloid synthesis had begun, enabling precise morphological control and establishing fully solution-based strategies for producing anisotropic gold nanostructures.[7]

In the following section, we present three distinct synthetic routes used to obtain colloidal gold nanoparticles with controlled size and shape. The first involves the preparation of citrate-stabilized spherical particles. The second focuses on a multi-step, seed-mediated synthesis of size-tunable nanospheres using a CTAB-based approach. The third is a seed-mediated growth of pentatwinned gold bipyramids. These three systems represent the foundation for the experimental work that follows.

1.1.Synthesis of Citrate-Stabilized Gold Nanoparticles (Au NPs@citrate)

Citrate-stabilized gold nanoparticles were synthesized using the classical Turkevich method for preparing monodisperse spherical gold colloids in aqueous media.[6]

The process begins with heating a dilute aqueous solution of chloroauric acid ($HAuCl_4$) to its boiling point under vigorous stirring, ensuring uniform temperature distribution throughout the reaction vessel. At this stage, a pre-heated solution of trisodium citrate is injected rapidly into the boiling gold solution. The injection triggers the chemical reactions responsible for nanoparticle nucleation and growth.

Trisodium citrate plays a multifaceted role in this synthesis. It first acts as a mild reducing agent.[8] Upon injection, the pale-yellow solution turns colorless almost instantly. This indicates the rapid reduction of gold(III) chloride complexes ($AuCl_4^-$) to gold(I) ($AuCl_2^-$), which is colorless in solution. The yellow color originates from charge-transfer transitions in Au^{3+} species, and its disappearance marks their complete conversion. During this step, citrate is partially oxidized to acetone dicarboxylate (DC^{2-}), a more effective reducing agent that begins to accumulate. This sets the stage for the next reduction step and the formation of nanocrystals.[6,8]

After a short induction period (10-12 seconds), the solution takes on a bluish-grey shade. This transient color signals the onset of nucleation, during which DC^{2-} reduces Au^+ to elemental gold (Au^0). The spontaneous formation of gold nuclei at this stage is driven by favorable reaction thermodynamics. After the initial reduction, the resulting, the resulting DC^{2-} becomes the primary reductant. To donate an electron, DC^{2-} must first enolize and coordinate with Au^+ through its enolate form, enabling further electron transfer. This process introduces a kinetic barrier, making the second reduction step slower. The redox couple $AuCl_2^-/Au^0$ has a standard reduction potential of +0.99 V, while DC^{2-} oxidizes at approximately +0.50 V under reaction conditions. This creates a positive cell potential ($\Delta E° \approx +0.49$ V), which corresponds to a negative Gibbs free energy change ($\Delta G° \approx -47$ kJ mol^{-1} per electron). Such a large, negative ΔG makes the reduction of Au^+ to Au^0 energetically favorable. In contrast, citrate alone offers almost no driving

force ($\Delta G° \approx -2$ kJ mol^{-1}), which is why the reaction does not proceed efficiently until DC^{2-} builds up in sufficient concentration. The newly formed gold atoms rapidly collide and aggregate into small clusters. Once these clusters exceed a critical size, they become stable nuclei.[8,9]

As the reaction proceeds, the concentration of DC^{2-} decreases due to its consumption and partial decomposition. Once it falls below the threshold needed for continued nucleation, the rate of gold reduction slows. This decline in reduction kinetics marks the transition from nucleation to growth. Gold atoms (Au^0) continue to form, but now they deposit preferentially onto the surfaces of existing nuclei rather than initiating new ones. This surface-mediated growth is promoted by the catalytic properties of metallic gold and the strong adsorption of DC^{2-} and citrate onto nanoparticle surfaces. During this stage, the solution's color shifts from blueish to pink and ultimately to a deep ruby-red, which is an optical signature of colloidal gold nanoparticles.[6]

Throughout the process an excess of citrate ions also serves as stabilizing agents, coating the particle surfaces and imparting negative surface charge. This electrostatic repulsion prevents aggregation and ensures colloidal stability over time.

The reaction typically reaches completion within 15 minutes of continuous heating, at which point particle growth stabilizes and the optical properties remain constant. The resulting colloid contains uniform, spherical gold nanoparticles with diameters typically ranging from 10 to 20 nm, with an absorption peak near 520 nm in the UV-Vis spectrum. The dispersion remains stable in aqueous solution and is suitable for further characterization or functionalization.

To confirm the structural and optical features of the synthesized nanoparticles, we performed a series of characterization measurements. Transmission electron microscopy (TEM) imaging (Figure 4.81 A) confirmed spherical particles with uniform morphology. Particle size analysis based on TEM micrographs, processed using ImageJ software (Figure 4.81 B), showed a narrow size distribution centered at 13.5 ± 1.2 nm, measured from approximately 150 nanocrystals. UV-Vis-NIR spectroscopy (Figure 4.81 C), revealed a distinct surface plasmon resonance at 518 nm – what is expected for citrate-stabilized gold nanoparticles in this size range.

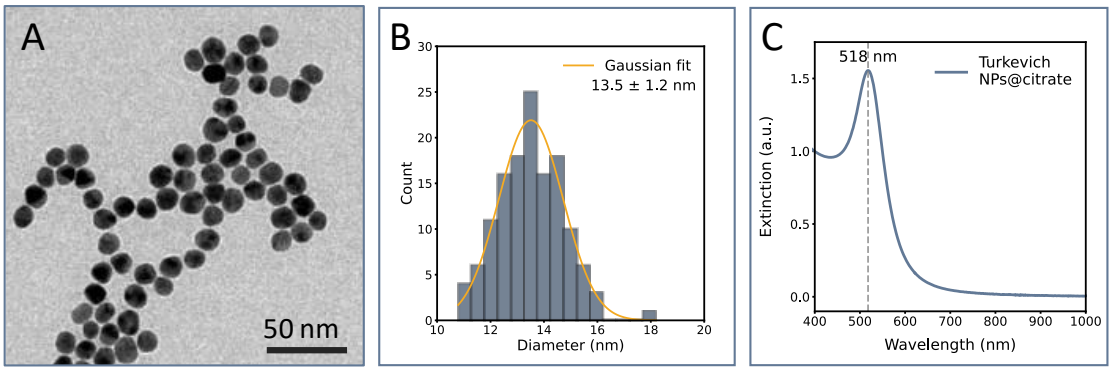

Figure 4.81 Characterization of citrate-stabilized gold nanoparticles synthesized by the Turkevich method. (A) TEM image showing uniform, spherical nanoparticles. (B) Size distribution obtained from TEM analysis, with a mean diameter of 13.5 ± 1.2 nm (Gaussian fit). (C) UV-Vis-NIR extinction spectrum with a surface plasmon resonance peak at 518 nm, consistent with the observed particle size.

1.2. Synthesis of Size-Controlled Spherical Gold Nanoparticles (Au NPs@CTAB)

The synthesis of 30 nm gold nanospheres was carried out using a three-step, seed-mediated approach that improves control over particle size and shape. By separating nucleation from growth and gradually expanding pre-formed seeds, this method enables the formation of single-crystal spheres with tunable diameters.

The process begins with the formation of small gold seeds (<2 nm) through the reduction of Au^{3+} ions by sodium borohydride ($NaBH_4$) in the presence of cetyltrimethylammonium bromide (CTAB), a cationic surfactant commonly used in noble metal nanoparticle synthesis. Prior to reduction, CTAB forms electrostatic ion-pair complexes with $AuCl_4^-$, confining the gold precursor within micelles. Bromide ions (Br^-) from CTAB gradually displace chloride ligands, forming tribromoaurate ($AuBr_4^-$), which shifts the redox potential of the complex to more negative values.[10] This shift renders the reduction of Au^{3+} less thermodynamically favorable, slowing the reaction and reducing the number of nuclei formed. The slower kinetics allow surface-bound gold atoms more time to diffuse before becoming fixed in the crystal lattice. This favors the formation of more spherical nanoparticles by guiding growth along a thermodynamically preferred pathway.

The reduction of Au^{3+} to Au^0 is initiated by the rapid injection of $NaBH_4$, resulting in a light-brown colloidal solution of seed particles. At this stage, CTAB acts as a stabilizing agent by forming a bilayer around the nanoparticle surface, preventing aggregation and limiting uncontrolled

growth. The resulting monocrystalline seeds are highly reactive but metastable, remaining suitable for further use only for several hours.

In the second stage, the gold seeds are grown to approximately 12 nm in diameter through a secondary reduction carried out in a trimethyloctylammonium chloride (CTAC) solution. CTAC, like CTAB, features a quaternary ammonium head group, but lacks strongly coordinating halide ions such as Br^- or I^-. The absence of these anions is essential to avoid facet-selective binding, which would otherwise promote anisotropic growth and lead to non-spherical morphologies such as cuboctahedra or octahedra. The $AuCl_4^-$ precursor is thoroughly mixed with CTAC, allowing for complexation analogous to that observed in CTAB-based systems. The reducing agent employed in this step is ascorbic acid (AA), a mild reductant chosen for its surface-selective behavior. When AA is added, followed immediately by the injection of the seed solution, the reduction of gold ions to metallic gold occurs exclusively at the surface of existing nanoparticles. This confines gold deposition to the seed particles, effectively suppressing secondary nucleation. As a result, gold atoms are deposited uniformly, preserving the single-crystalline structure of the growing nanospheres.

The final particle diameter after this step can be predicted and tuned by adjusting the ratio of gold atoms in the seed particles to those introduced in the growth solution, using the expression derived from mass conservation for spherical particles of uniform density:

$$D_f = D_n \left(\frac{Au_n + Au_g}{Au_n}\right)^{1/3} \quad (4.1)$$

where D_f the final particle diameter, D_n the seed diameter, Au_n the amount of gold in the seeds, and Au_g the amount of gold added during the growth step.[11]

In the final growth step, the particles were enlarged to 30 nm using benzyldimethylhexadecylammonium chloride (BDAC) as the capping agent. The aromatic headgroup in BDAC binds more strongly to the gold surface, forming a denser and less permeable surfactant layer.[12] This reduces the deposition rate of gold atoms by approximately an order of magnitude compared to CTAC, promoting more uniform growth and improved crystallinity.[13] A concentrated solution of 12 nm seeds was added to the BDAC medium, and after a 10-minute incubation, ascorbic acid and the gold precursor were rapidly injected in sequence. The reductant was used at low concentration to maintain a controlled deposition rate, allowing gold atoms to diffuse across the particle surface before incorporation. As in the previous stage, reduction occurred only on existing gold surfaces. The volume of seed solution added was calculated based on the desired final particle size. After the growth step, the particles were treated with a mild oxidant, 1% sodium hypochlorite solution, to selectively remove high-

curvature surface irregularities and enhance sphericity. This was followed by the addition of a small amount of gold precursor, triggering a surface-mediated disproportionation reaction ($Au^{3+} + 2\ Au^{0} \rightleftharpoons 3\ Au^{+}$). This redox process promotes further gentle etching and redistribution of gold atoms across the nanoparticle surface. This final touch improves the uniformity and monodispersity of the final product.[14]

The structural and optical properties of the final 30 nm gold nanospheres stabilized with CTAB were evaluated by transmission electron microscopy, image-based size analysis, and UV-Vis-NIR spectroscopy. TEM imaging (Figure 4.82 A) confirmed the formation of uniform, well-defined spherical particles with smooth surfaces. The narrow size distribution obtained by the analysis of approximately 500 nanocrystals from TEM micrographs (Figure 4.82 B) yielded an average particle diameter of 29.1 ± 0.9 nm, consistent with the targeted dimensions from the seeded growth protocol. The extinction spectrum (Figure 4.82 C) exhibited a well-defined surface plasmon resonance (SPR) peak at 522 nm, which aligns with values expected for spherical gold nanoparticles of this size and further indicates high monodispersity and colloidal stability. The narrow plasmon band reflect both the uniformity in particle size and the absence of aggregation, confirming that the multi-step growth and post-synthesis refinement procedures produced high-quality, monodisperse nanospheres suitable for subsequent surface modification.

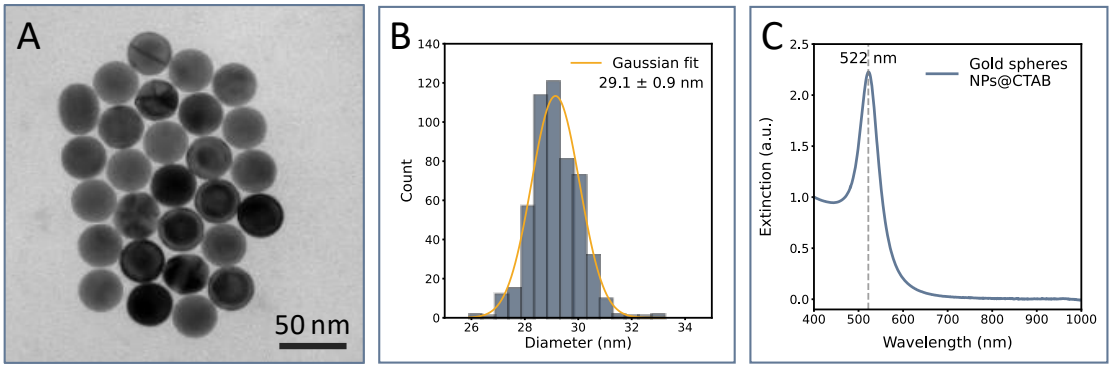

Figure 4.82 Characterization of 30 nm spherical gold nanoparticles stabilized with CTAB. (A) TEM image showing uniform, well-dispersed nanospheres. (B) Size distribution based on TEM analysis, with an average diameter of 29.1 ± 0.9 nm (Gaussian fit). (C) UV-Vis-NIR extinction spectrum displaying a surface plasmon resonance band with maximum at 522 nm, consistent with the measured particle size.

1.3.Seed-Mediated Synthesis of Gold Bipyramids

The synthesis of gold bipyramids was also carried out employing a seeded growth approach.[15] This method relies on the use of preformed gold seeds to direct the anisotropic deposition of gold atoms during the growth stage. In the previous protocol, to obtain larger monocrystalline nanospheres, we used monocrystalline seeds. Those could be used for growth of anisotropic single-crystal nanorods with octagonal cross section. But in order to achieve a pentatwinned symmetry to grow pentatwinned nanorods, bipyramids or decahedra - we need to prepare citrate-capped gold nanoparticles that exhibit a pentagonal cross-section and five-fold twinning. Ensuring that twinning is introduced before the growth step is the most effective way for improving the efficiency of gold-bipyramid preparations.[15]

Gold seeds were initially prepared by the rapid chemical reduction of $HAuCl_4$ in the presence of stabilizing and shape-directing agents. An aqueous solution of CTAC and $HAuCl_4$ was first combined at room temperature. Citric acid was then added, turning the solution colorless, followed immediately by the addition of freshly prepared $NaBH_4$ under vigorous stirring. This led to an immediate color change to bright brown, indicating the formation of small gold nanoclusters. At this stage, the particles are typically below 2 nm in diameter and do not exhibit a localized surface plasmon resonance (LSPR) band. The complete reduction of Au(III) to Au(0) was confirmed spectroscopically by an extinction value of 0.6 at 400 nm (for 0.25 mM of gold atoms).

To induce the internal structure necessary for anisotropic growth, those freshly prepared seeds underwent a thermal aging process. The seed solution was heated at 80°C for 90 minutes under gentle stirring. During this treatment, atomic mobility increases sufficiently and enable surface diffusion, atom detachment and reattachment, and limited Ostwald ripening. These processes collectively drive the seeds toward a more thermodynamically favorable configuration. As a result, the initially disordered or single-crystalline clusters reorganize into more stable structures, growing in size to approximately 6 nm. At this scale, the surface energy minimization favors a decahedral geometry composed of ten {111} facets joined by five coherent twin boundaries. Although this configuration introduces internal strain, the energetic cost is offset by the stabilization provided through facet minimization, making the pentatwinned structure the preferred thermodynamic product. The presence of both citric acid and chloride ions is critical to this transformation. Citrate ions are known to direct growth towards {111} facets and induce twin defect transformation.[14,16] Chloride, in contrast to bromide or iodine that can strongly inhibit {111} facets, ensures sufficient surface accessibility and allows preferential growth in this

direction and ensures sufficient surface accessibility. Substitution of CTAC with CTAB or omission of citrate from the thermal treatment markedly suppresses twinning and diminishes the quality of the resulting anisotropic nanocrystals.[14] As the thermal treatment progresses, the proportion of pentatwinned seeds increases steadily, reaching approximately 90% after 90 minutes with no observable improvement upon prolonged heating. These aged seeds provide a well-defined structural template, essential for the controlled synthesis of high-purity anisotropic nanoparticles such as gold bipyramids.

For the growth of bipyramidal gold nanoparticles, a fresh solution was prepared containing CTAB, $HAuCl_4$, silver nitrate ($AgNO_3$), hydrochloric acid (HCl), and ascorbic acid (AA). CTAB again served a dual function, as a colloidal stabilizer and as a shape-directing surfactant. This behavior is primarily attributed to the selective adsorption of bromide ions onto specific crystallographic facets of gold, which in turn affects the relative growth rates of those surfaces.

Silver ions, introduced via $AgNO_3$ played a key role in directing anisotropic growth through underpotential deposition.[12] In this process, Ag^+ ions preferentially adsorb onto certain gold facets, effectively suppressing further gold deposition on those surfaces while allowing it to proceed on others. This inhibition is most pronounced on the {110} facets, followed by {100}, and least on {111}. The selectivity arises from the different coordination environments: silver atoms bind more strongly to {110} due to having five nearest-neighbor gold atoms, compared to four on {100} and three on {111}.[17] This facet-dependent binding enables directional growth, which is essential for the formation of bipyramidal morphologies.

Ascorbic acid was used as a mild reducing agent, converting Au(III) to Au(I) and yielding a clear, colorless solution. Importantly, this reduction is incomplete in the absence of a catalytic surface, ensuring that further reduction to metallic gold occurs selectively on the surface of the added seeds. This minimizes undesired secondary nucleation and promotes controlled, seed-mediated growth. The addition of HCl further modulates the reduction kinetics by adjusting the pH and shifting redox potential in the synthetic mixture. Its addition is known to favor anisotropic growth in the presence of surfactants like CTAB.[18]

Once CTAB and $HAuCl_4$ were thoroughly mixed at 30°C, the remaining components – $AgNO_3$, HCl, and ascorbic acid – were added in sequence under vigorous stirring, followed immediately by the thermally aged seed solution. The amount of seeds introduced directly influenced the final dimensions and aspect ratio of the bipyramids, thereby tuning the position of the longitudinal surface plasmon resonance.

After seed addition, the reaction mixture was left undisturbed at 30 °C for two hours. A sharp LSPR bands in the near-infrared range, typically between 700 and 1000 nm, were observed. The LSPR position depends on the seed concentration (Figure 4.83). When the seed concentration is reduced, gold bipyramids with higher aspect ratios are formed, and the LSPR red-shifts.

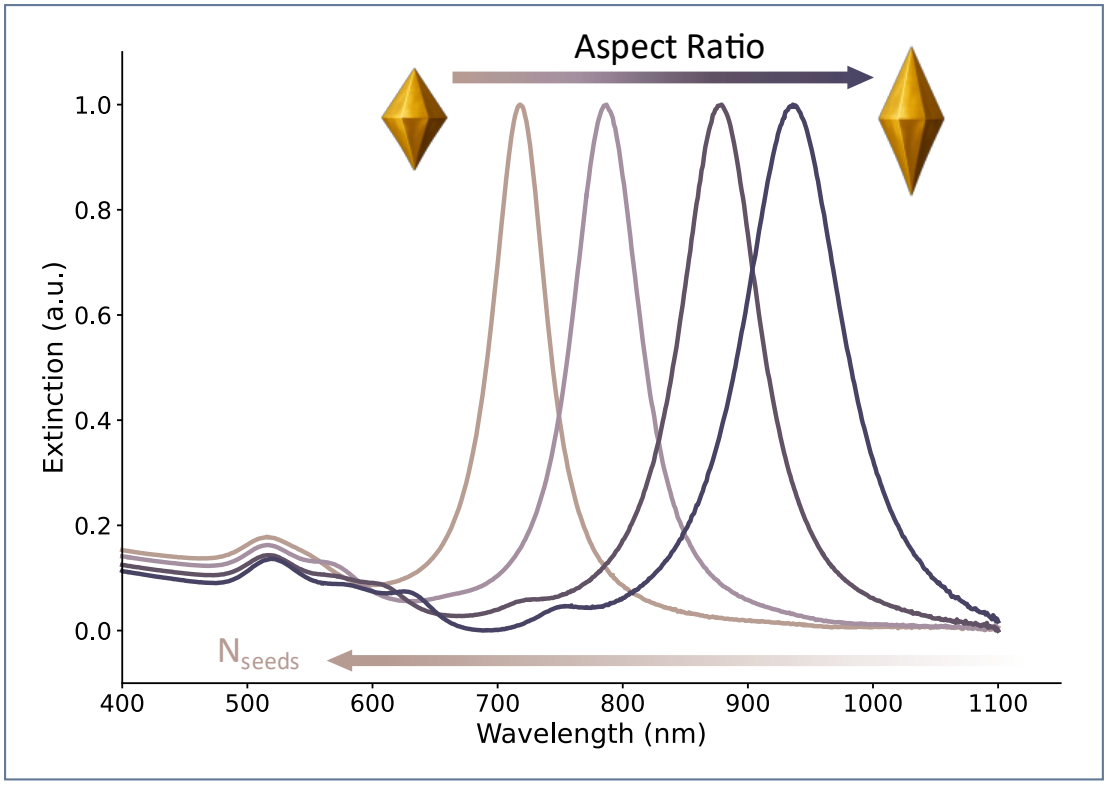

Figure 4.83. UV-Vis-NIR extinction spectra of gold bipyramids synthesized with decreasing seed concentrations. Lower seed amounts result in longer bipyramids with higher aspect ratios, leading to a red-shift of the LSPR.

Transmission electron microscopy (Figure 4.84 A) revealed uniform bipyramidal morphology. The image shows a monodisperse population of nanocrystals forming a well-aligned monolayer. Size analysis of approximately 150 nanocrystals based on TEM images (Figure 4.84 B) yielded an average length of 131.3 ± 5.8 nm and width of 39.4 ± 2.2 nm, of aspect ratio equal to 3.33. Optical characterization by UV-Vis-NIR spectroscopy (Figure 4.84 C) showed a prominent longitudinal surface plasmon resonance (LSPR) peak centered at 830 nm. The sharpness and intensity of the peak, with a full width at half maximum of 81.33 nm, indicate the uniformity of the sample and the absence of significant byproducts or shape impurities. These results confirm that the growth conditions produced structurally well-defined and optically responsive bipyramidal nanocrystals suitable for subsequent surface modification and functional studies.

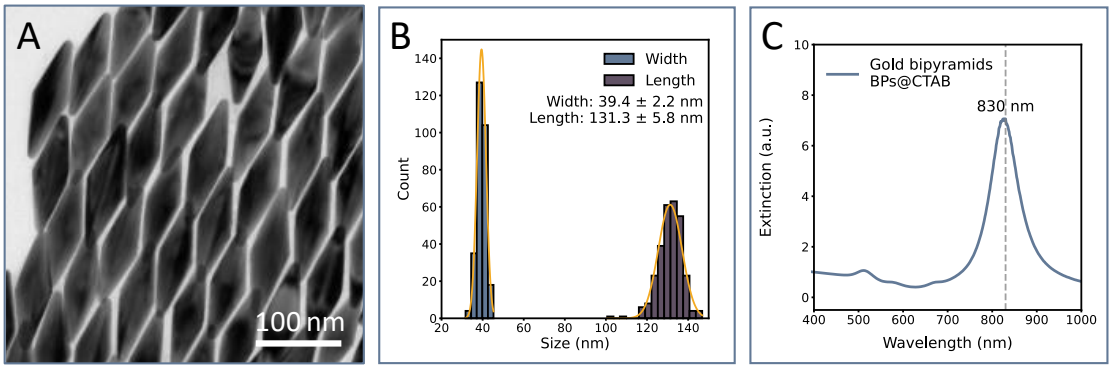

Figure 4.84 Characterization of gold bipyramids stabilized with CTAB. (A) TEM image showing anisotropic bipyramidal morphology with high uniformity. (B) Size distribution from TEM analysis, yielding an average width of 39.4 ± 2.2 nm and length of 131.3 ± 5.8 nm (Gaussian fits). (C) UV-Vis-NIR extinction spectrum with a longitudinal plasmon resonance band at 830 nm, characteristic of elongated bipyramidal morphology.

2. Biofunctionalization of Gold Nanocrystals

Proteins with highly specific binding abilities are particularly useful for nanoparticle functionalization, as they enable the selective targeting of specific biological structures, including membrane receptors and other biomolecular markers.[19] A prominent example is the group of biotin-binding proteins: avidin, NeutrAvidin, and streptavidin.[20] Each of these tetrameric proteins contain four binding pockets capable of capturing biotinylated ligands with femtomolar affinity, facilitating predictable assembly of nanoparticle systems for sensing, imaging, or therapeutic delivery. In 2018, de Boer and Yuste demonstrated the use of streptavidin- or NeutrAvidin-coated gold nanoparticles to selectively target neurons, enabling photoactivation through second-harmonic near-infrared absorption.[21]

Avidin, derived from egg white, exhibits the strongest biotin-binding strength among the three; however, its high positive charge and glycosylation can lead to increased non-specific interactions. NeutrAvidin (NeuAv), a chemically modified and deglycosylated form of avidin, retains high biotin affinity ($K_d \approx 10^{-15}$ M) while exhibiting minimal non-specific binding due to its near-neutral isoelectric point and absence of carbohydrate groups, effectively eliminating lectin-mediated interactions.[22,23]

The biofunctionalization of gold nanocrystals with proteins is guided by a careful balance of electrostatic interactions, surface chemistry, and colloidal stability to produce a consistent and robust protein layer. The detailed protocols for each type of nanocrystals can be found in the Appendix (Section 4.2.1).

To validate the biofunctionalization strategy, we first optimized protein adsorption on 13 nm citrate-capped gold nanospheres based on previous works.[24] The particles were incubated with either Avidin or NeutrAvidin at pH ≈ 11 and temperatures below 10 °C. The alkaline pH promotes deprotonation of amino acid residues in NeuAv, increasing its affinity for the gold surface through enhanced electrostatic attraction and reduced inter-protein aggregation.[19] Incubation at low temperature (<10 °C) slows adsorption kinetics, allowing controlled surface binding while preserving protein structure.[25]

These conditions were subsequently applied to all nanocrystal types. For CTAB-stabilized nanocrystals, preparatory washing steps were essential to remove excess surfactant, exposing the gold surface and minimizing interference with protein attachment. Centrifugation conditions were optimized to selectively remove unbound protein while maintaining nanocrystal integrity: spherical nanoparticles tolerated higher speeds (8k-10k RCF), whereas bipyramids, more prone to aggregation, required prolonged centrifugation at reduced speed. Final resuspension in alkaline water helped preserve colloidal stability by maintaining surface charge.

The extinction spectra in Figure 4.85 illustrate the optical response of citrate-capped gold nanoparticles before and after incubation with Avidin or NeutrAvidin. Upon protein adsorption, the surface plasmon resonance red-shifts from 519 nm (NPs@citrate) to 521 nm for NeuAv and 522 nm for Avidin, as shown in Figure 4.85 B. The spectra for Avidin- and NeutrAvidin-coated particles are nearly identical and overlap on the plot, indicating similar optical responses under the tested conditions. This 2-3 nm shift is consistent with the formation of a protein layer. Replacing the short citrate layer (~0.7 nm, refractive index n ≈ 1.49-1.51) with a thicker protein shell (~5 nm, n ≈ 1.45-1.6) increases the effective refractive index in the immediate vicinity of the nanoparticle surface.[24,26,27] Since the localized surface plasmon resonance is highly sensitive to changes in the dielectric environment within the electromagnetic decay length, this increase in local refractive index leads to a slight red-shift in the LSPR peak. The preserved band shape and intensity confirm that colloidal stability is maintained under the applied alkaline conditions.

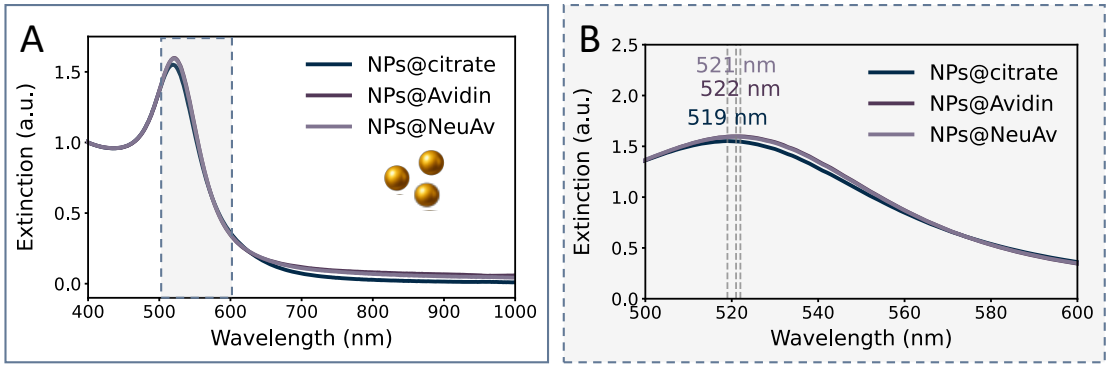

Figure 4.85 UV-Vis-NIR spectroscopy measurements of 13 nm citrate-capped gold nanoparticles before and after functionalization with Avidin or NeutrAvidin. (A) Extinction spectra over the full wavelength range confirm preserved colloidal stability following protein adsorption. (B) A zoomed-in view of the surface plasmon resonance region shows a red-shift from 519 nm (NPs@citrate) to 522 nm (NPs@Avidin) and 521 nm (NPs@NeuAv), consistent with change of refractive index due to protein adsorption.

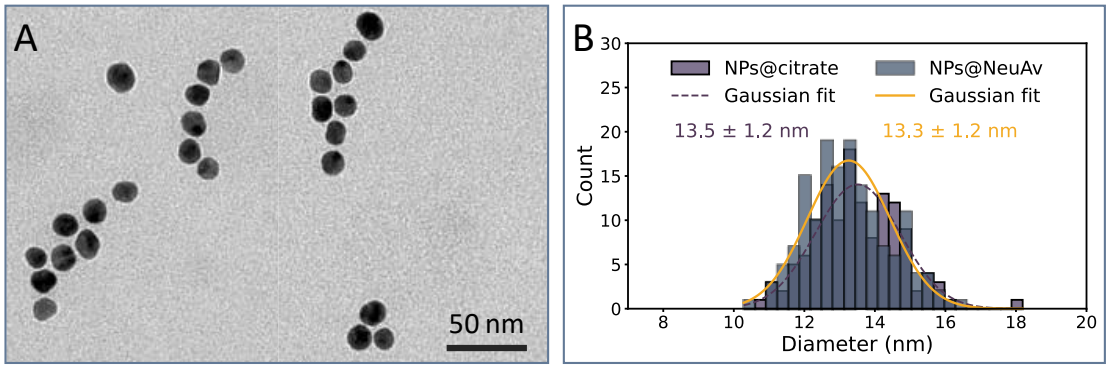

Figure 4.86 Transmission electron microscopy (TEM) analysis of gold nanoparticles before and after NeutrAvidin functionalization. (A) TEM image of NPs@NeuAv showing well-dispersed, spherical particles. (B) Diameter distributions for NPs@citrate and NPs@NeuAv, based on TEM measurements. The mean diameters were 13.5 ± 1.2 nm and 13.3 ± 1.2 nm, respectively, indicating no change in core size following ligand exchange.

To verify that ligand exchange does not alter nanoparticle size, we analyzed samples before and after NeutrAvidin functionalization by transmission electron microscopy. The TEM image in Figure 4.86 A reviels well defined spherical NPs@NeuAv. Diameter analysis (Figure 4.86 B) compares NPs@NeuAv to the initial citrate-stabilized particles. The average diameters were 13.5 ± 1.2 nm for NPs@citrate and 13.3 ± 1.2 nm for NPs@NeuAv, with the difference falling within the statistical uncertainty, indicating that the core size remained unchanged. This supports the interpretation that the red-shift observed in the extinction spectra arises from protein adsorption on the surface rather than any alteration in particle morphology.

Following successful optimization of the ligand exchange protocol, and guided by literature reporting a lower tendency for nonspecific binding, NeutrAvidin was selected for all subsequent

biofunctionalization steps. The near-neutral isoelectric point of NeutrAvidin minimizes background binding and improves targeting specificity in complex biological environments. For visualization purposes, NeutrAvidin can be conjugated to a fluorophore, enabling tracking of the functionalized nanoparticles. Commercial NeuAv conjugates labeled with fluorescein isothiocyanate (FITC) or DyLight 633 were purchased and used to functionalize 30 nm gold nanospheres and gold bipyramids. Figure 4.87 presents the structural dimensions of the NeuAv tetramer (~5 × 4 nm) along with the normalized excitation and emission spectra of the free dyes (FITC: max excitation at 498 nm, max emission at 517 nm; DyLight 633: max excitation at 638 nm, max emission at 658 nm).

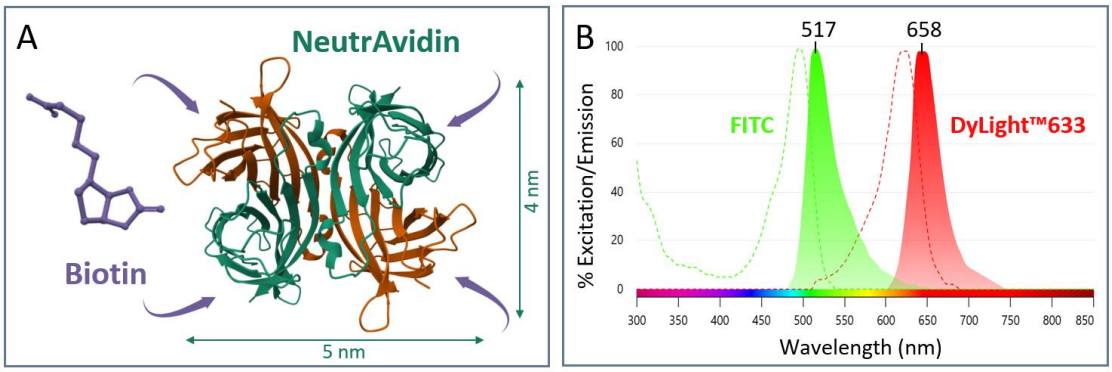

Figure 4.87 (A) Schematic structure of the NeutrAvidin (NeuAv) tetramer, approximately 5 nm × 4 nm in size, with four binding sites for biotin. (B) Normalized excitation and emission spectra of the commercial dyes used for nanoparticle functionalization. FITC (green) was used for gold bipyramids; it exhibits a maximum excitation at 498 nm and emission at 517 nm. DyLight™ 633 (red) was used for 30 nm gold nanospheres; maximum excitation at 638 nm and emission at 658 nm.

We characterized the optical properties of the nanoparticles before and after ligand exchange, as shown in Figure 4.88. Both nanocrystal types were initially stabilized with CTAB and subsequently functionalized with NeuAv, which altered their optical properties. For spherical NPs (Figure 4.88 A), the LSPR shifted from 522 nm (CTAB) to 525 nm (NeuAv), indicating an increase in the local refractive index. Fluorescence measurements of NPs@NeuAv*DyLight633 (Figure 4.88 B) showed an emission maximum at 646 nm. This 12 nm blue shift relative to the free dye (Ex 638 nm, Em 658 nm) reflects changes in the fluorophore's local environment at the nanoparticle surface.

Bipyramidal nanoparticles (Figure 4.88 C) exhibited two distinct plasmon resonances: a transverse mode near 520 nm and a longitudinal mode that shifted from 767 nm (CTAB) to 773 nm (NeuAv). For BPs@NeuAv*FITC, we recorded emission spectra at a fixed excitation of 480 nm (Figure 4.88 D). The emission profile peaked at 521 nm, aligning with expectations for surface-bound FITC.

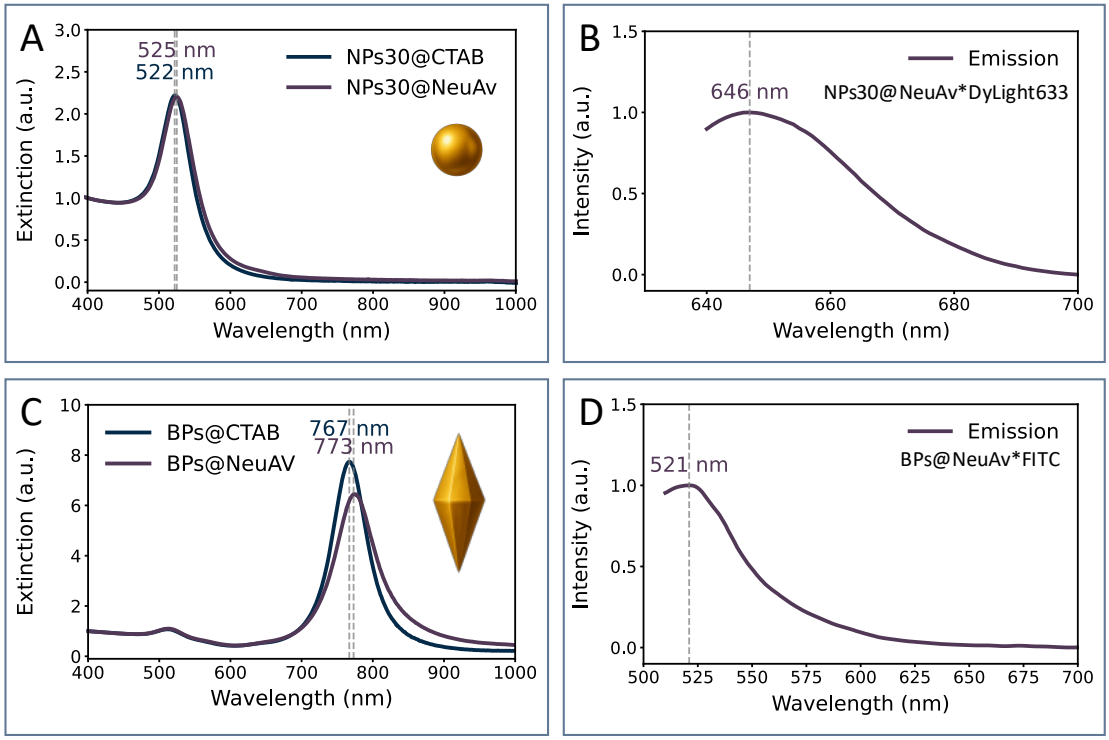

*Figure 4.88 Optical characterization of gold nanoparticles before and after functionalization with NeutrAvidin conjugated dyes. (A) Extinction spectra of 30 nm gold nanospheres show an LSPR red-shift from 522 nm (CTAB) to 525 nm (NeuAv). (B) Fluorescence spectra of NPs@NeuAv*DyLight633 with emission maximum at 646 nm. (C) Extinction spectra of gold bipyramids show a transverse mode near 520 nm and a longitudinal mode shifting from 767 nm (CTAB) to 773 nm (NeuAv). (D) Fluorescence spectra of BPs@NeuAv*FITC with emission maximum at 521 nm (excitation wavelength at 480 nm).*

3. Gold Nanocrystals in Neurobiological Research

3.1. Physicochemical Characterization of NPs in Biological Media

Nanocrystals that remain stable under controlled laboratory conditions often exhibit altered behavior when introduced into biological environments. In physiological fluids, parameters such as pH (typically 7.2-7.4), osmolarity (~300 mOsm), and ionic strength (dominated by Na^+, K^+, Ca^{2+}, Cl^-, and phosphate ions) differ significantly from those in standard aqueous buffers. More critically, biological media (like Neurobasal or DMEM) contain high concentrations of amphiphilic and zwitterionic biomolecules (primarily serum proteins) that can adsorb to nanoparticle surfaces, displace stabilizing ligands, and, in the absence of adequate surface protection, promote aggregation. Assessing the colloidal stability of nanocrystals under such conditions is a necessary step prior to any biological application.

To assess the colloidal stability of gold nanoparticles in biologically relevant conditions, we tracked UV-Vis-NIR spectra of 30 nm spherical gold nanoparticles stabilized with citrate.

The particles were redispersed in Neurobasal medium, commonly used for neuronal cell culture, and supplemented with increasing concentrations of fetal bovine serum (FBS, 0-20%). FBS, which contains approximately 37 mg/mL of total protein in its undiluted form, introduces a complex mixture of serum proteins capable of adsorbing to the nanoparticle surface and forming a protein corona - a factor known to affect both colloidal stability and biological interactions. Measurements were conducted at room temperature (25 °C) and physiological temperature (37 °C) to reflect standard handling and incubation conditions (Figure 4.89).

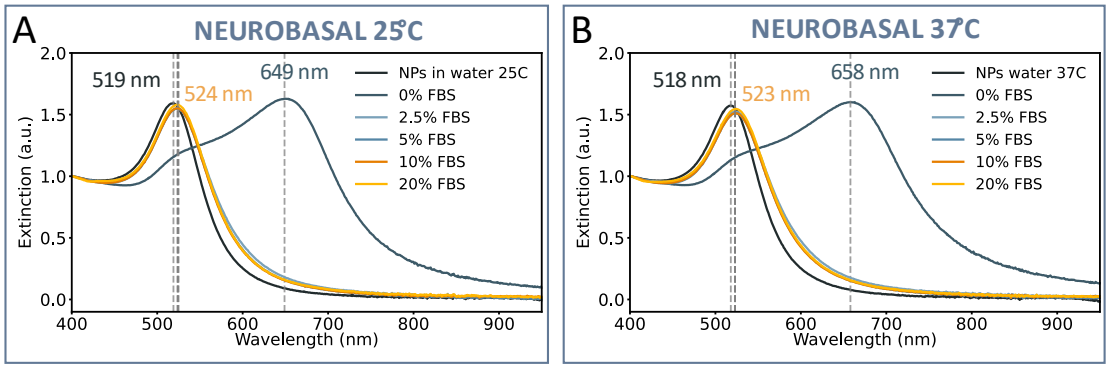

Figure 4.89 UV-Vis-NIR spectra of citrate-coated gold nanoparticles in Neurobasal with increasing FBS content. (A) At 25 °C, the LSPR peak shifts from 519 nm (water) to 524 nm with FBS, while an aggregation peak (649 nm) appears in 0 % FBS. (B) At 37 °C, similar trends are observed with LSPR shifting to 523 nm and aggregation seen in FBS-free medium (658 nm). FBS ≥2.5 % prevents aggregation at both temperatures.

In the absence of serum (0% FBS), the extinction spectra exhibited features characteristic of nanoparticle destabilization. Specifically, a broadened and red-shifted peak appeared at 649 nm at 25°C and 658 nm at 37°C, indicative of interparticle plasmon coupling likely resulting from clustering. The primary localized surface plasmon resonance (LSPR) peak - initially observed at 519 nm in water (25°C) and 518 nm in water (37°C) - decreased in intensity and became secondary relative to the newly formed maximum. These spectral changes are consistent with the loss of colloidal stability in protein-free Neurobasal medium, likely driven by ionic interactions, altered surface charge, and insufficient steric or electrostatic stabilization.

Upon addition of FBS at concentrations of 2.5% and above, the clustering-associated peak was no longer observed. Instead, the spectra displayed a modest but consistent red-shift of the LSPR band to 524 nm (25 °C) and 523 nm (37 °C). The absence of spectral broadening or secondary peaks under these conditions suggests that serum proteins adsorb onto the nanoparticle surface to form a stabilizing protein corona, effectively preventing further aggregation. Notably, no significant spectral differences were detected between 2.5%, 5%, 10%, and 20% FBS, indicating that even low serum concentrations are sufficient to saturate the particle surface and maintain dispersion. Temperature had only a limited effect on the optical response. The magnitude of the

LSPR red-shift (Δλ ≈ 5 nm) was comparable at both 25 °C and 37 °C. The consistent peak shape and intensity across temperatures further support the conclusion that FBS-mediated stabilization remains effective under physiologically relevant conditions.

To further examine the nature of this serum-induced stabilization and to verify the presence of a protein corona, we characterized the nanoparticles by transmission electron microscopy to visualize the inorganic cores and by dynamic light scattering to determine their hydrodynamic diameters, enabling an estimation of the thickness of the surface layer formed in the presence of FBS.

TEM grids were prepared from aqueous dispersions of citrate- and NeutrAvidin-functionalized nanoparticles. As shown in Figure 4.90 (Panels A and B), both samples displayed well-dispersed, spherical particles. Size distribution analysis of approximately 150 nanocrystals based on TEM images (Figure 4.90 C) revealed that the core diameters were the same within the statistical error of image-based measurement: 27.7 ± 1.4 nm for citrate-stabilized nanoparticles and 27.6 ± 1.7 nm for NeutrAvidin-functionalized particles, corresponding to core radii of 13.8 ± 0.7 nm and 13.8 ± 0.9 nm, respectively. These results confirm that surface modification does not affect the dimensions of the inorganic core.

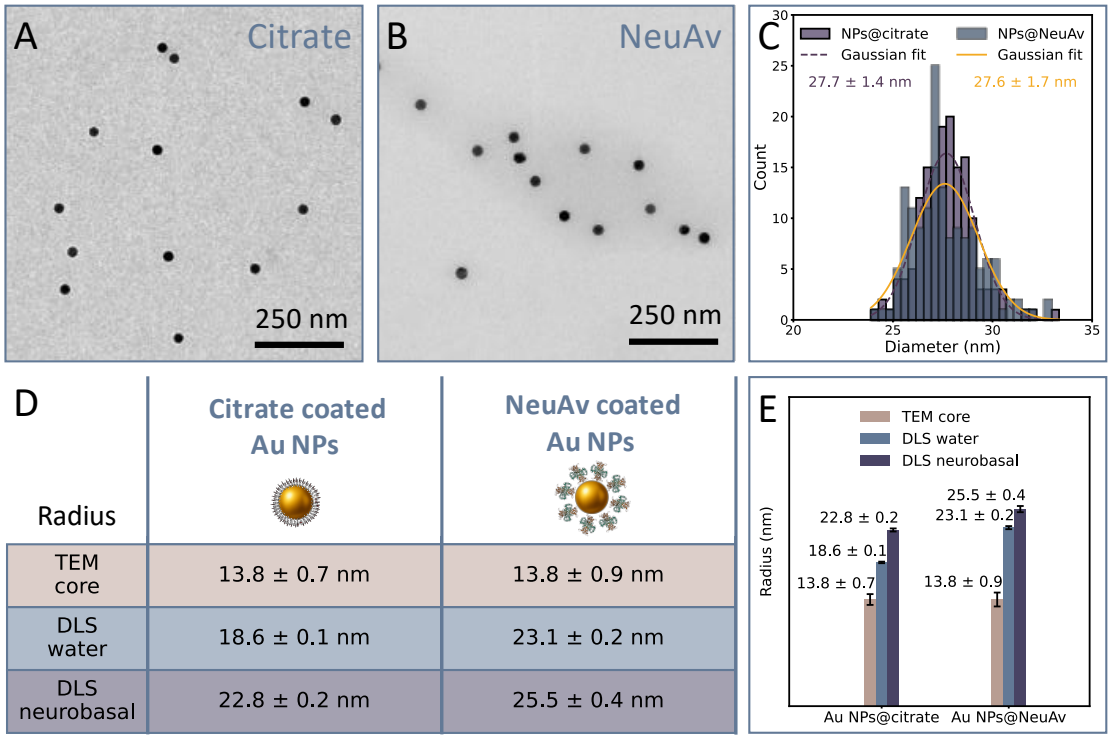

Figure 4.90 Core and hydrodynamic size characterization of citrate- and NeutrAvidin-coated gold nanoparticles. (A, B) TEM micrographs of 30 nm gold nanoparticles stabilized with citrate and with NeutrAvidin. (C) Diameter histograms obtained from TEM images (≈150 particles per sample) with Gaussian fits indicating mean core diameters of 27.7 ± 1.4 nm (citrate) and 27.6 ± 1.7 nm (NeutrAvidin). (D, E) Summary of size measurements by TEM and dynamic light scattering (DLS) in water and in Neurobasal medium with 10% FBS. The TEM core radius, obtained by dividing the mean diameter measured from TEM images by two, is ≈13.8 nm for both coatings. In contrast, DLS shows an increase in hydrodynamic radius from 18.6 ± 0.1 nm to 22.8 ± 0.2 nm for citrate-coated particles and from 23.1 ± 0.2 nm to 25.5 ± 0.4 nm for NeutrAvidin-coated particles (E), consistent with ligand shell formation and protein corona effects.

In water, citrate-stabilized particles exhibited a hydrodynamic radius of 18.6 ± 0.1 nm, while NeutrAvidin-functionalized particles measured 23.1 ± 0.2 nm (Figure 4.90 D and E). Assuming a core radius of approximately 14 nm, determined as half of the TEM-measured diameter, these values correspond to effective shell thicknesses of about 4 nm for citrate-capped nanoparticles and about 9 nm for NeutrAvidin-functionalized nanoparticles. Supporting DLS autocorrelation functions and the resulting hydrodynamic radius calculations are provided in the Appendix (Section 4.3, Figure A.11).

For citrate, the physical ligand layer alone cannot fully account for the observed 4 nm increase. Spectroscopic and computational studies have shown that citrate forms a compact inner monolayer on the gold surface, with the possibility of a loosely associated second layer formed through hydrogen bonding – resulting in a total thickness of up to 1-1.5 nm.[28] The remaining contribution to the hydrodynamic size arises from solvation and electrostatic effects intrinsic to dynamic light scattering (DLS) measurements in aqueous environments. Citrate-stabilized

nanoparticles carry a strong negative surface charge (ζ-potential ≈ -35 to -50 mV), which attracts a diffuse layer of counterions and solvating water molecules - known as the electrical double layer (EDL). Under low ionic strength conditions, this EDL can extend 1-3 nm from the particle surface. In addition, hydrogen bonding between citrate's carboxylate groups and water molecules forms a tightly bound hydration shell, typically contributing an additional 0.5-1 nm.[29]

For NeutrAvidin-functionalized nanoparticles, the larger hydrodynamic shell of ≈9 nm can be primarily attributed to the size of the protein itself. NeutrAvidin, a tetrameric protein approximately 4-5 nm across (Figure 4.87), forms a surface monolayer that accounts for most of the observed increase. While a single protein layer is the most likely configuration under the conditions used, multilayer formation has been reported in related systems and may contribute to the total shell thickness. Smaller contributions arise from structured hydration layers (approximately 0.5-1.2 nm) and the electrical double layer (EDL, 1-3 nm), formed by counterions associated with charged amino acid residues on the protein.[30,31]

In biological medium, both samples exhibited an increase in hydrodynamic radius: from 18.6 ± 0.1 nm to 22.8 ± 0.2 nm for citrate-stabilized particles, and from 23.1 ± 0.2 nm to 25.5 ± 0.4 nm for NeutrAvidin-functionalized particles. These shifts likely reflect the formation of a protein corona, resulting from the adsorption of serum proteins and other medium components onto the nanoparticle surface. Notably, the relative increase was larger for citrate-coated particles (4.2 nm) than for NeutrAvidin-coated ones (2.4 nm), suggests that a more extensive corona forms on surfaces initially free of protein.

Because the hydrodynamic increases are modest and remain well below the particle diameter, aggregation can be ruled out. Together with the unchanged core size and stable UV-Vis-NIR spectra, these data confirm that both nanoparticle formulations remain individually dispersed in biologically relevant conditions, supporting their use in subsequent in-vitro experiments. However, citrate-coated nanoparticles are more prone to non-specific interactions with surrounding ions and biomolecules than NeutrAvidin-coated nanoparticles. For this reason, NeutrAvidin-functionalized nanoparticles were selected for subsequent experiments to ensure improved control over particle behavior in biological media.

The study presented above was performed on spherical nanocrystals because their geometry allows a reliable interpretation of hydrodynamic size from standard DLS measurements. In contrast, DLS was not applied to bipyramidal nanocrystals, as their anisotropic shape complicates data interpretation. For such particles, Brownian motion involves both translational and rotational diffusion, whereas conventional DLS analysis assumes spherical symmetry and

accounts only for translational motion. Accurate characterization of anisotropic particles, such as bipyramids, requires more advanced methods, including Depolarized Dynamic Light Scattering (DDLS), which employs polarized and depolarized light to separately determine translational and rotational diffusion coefficients.[32]

3.2. In Vitro Internalization Studies

As an initial cellular model, we selected SH-SY5Y human neuroblastoma cells, a widely used cancer cell line that expresses neuronal markers and serves as a model for neurodegenerative disease research and neuropharmacology.[33] The in-vitro analysis was performed by Ane Escobar Fernández at Biogipuzkoa. To visualize cell morphology, we performed multi-color confocal microscopy with DAPI staining of nuclei (blue) and Phalloidin-Texas Red labeling of actin filaments (red), while the nanoparticles were tracked via the FITC signal (green). Figure 4.91 illustrates the separate fluorescence channels and the resulting composite image used to assess nanoparticle localization within the cellular context.

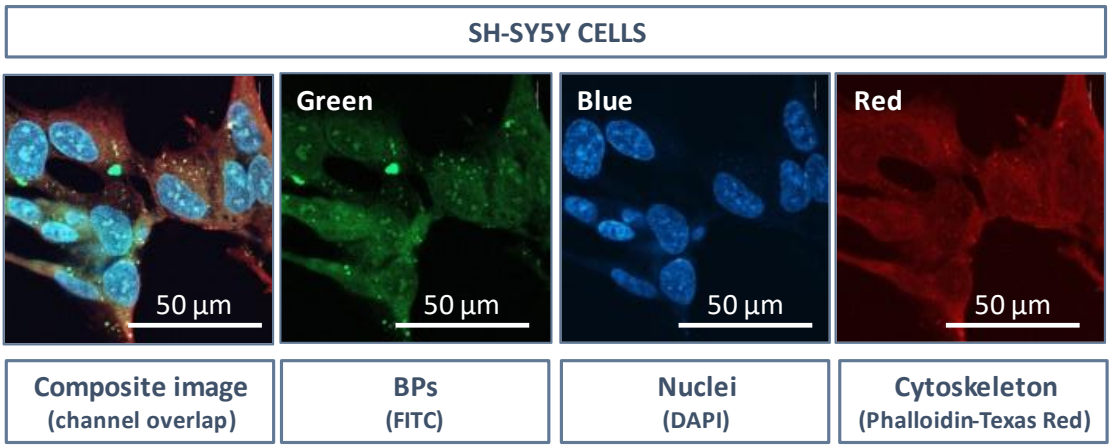

Figure 4.91 Fluorescence imaging of SH-SY5Y cells. Confocal microscopy images of SH-SY5Y neuroblastoma cells stained with DAPI (blue) for nuclei and Phalloidin-Texas Red (red) for actin filaments, followed by 1 h incubation with gold nanocrystals. Gold bipyramids functionalized with FITC-labeled NeutrAvidin (green) were used to visualize nanoparticle localization. Individual fluorescence channels are shown alongside a composite image with channel overlap.

SH-SY5Y cells exhibit a flat, spread-out morphology with broad extensions reaching into the surrounding space (Figure 4.91). The dense actin network, visualized in red, outlines both the cell perimeter and internal structure, aligning closely with the fluorescent signal of the nanoparticle conjugates.

Bipyramidal gold nanocrystals functionalized with FITC-labeled NeutrAvidin (BP@NeuAv*FITC) were incubated with cells for 1 h, followed by washing with PBS to remove unbound particles.

Cells were then maintained in fresh medium for 24h and 48h to assess nanoparticle internalization over time. To evaluate whether surface anchoring of the nanoparticles could be enhanced, we compared particles applied directly (BP@NeuAv*FITC) with those applied to cells that had been pre-incubated with a NHS-PEG-biotin linker (Figure 4.92). This approach was adapted from the strategy employed by Yuste et al., where biotinylated linkers were used to promote membrane retention of NeutrAvidin-coated nanoparticles.[21]

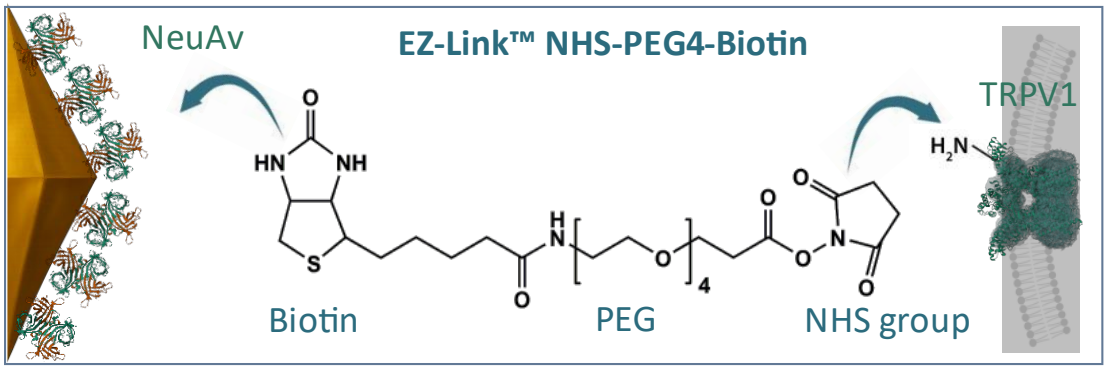

Figure 4.92 Schematic representation of the EZ-Link NHS-PEG4-Biotin Linker attaching NeutrAvidin-coated nanocrystals to membrane proteins. The NHS group reacts with primary amines on extracellular protein domains, anchoring the linker to the cell surface. The PEG spacer provides flexibility and separation, while the biotin moiety enables high-affinity binding to NeutrAvidin on the nanoparticle surface. Relative sizes are not depicted to scale.

The EZ-Link™ NHS-PEG4-Biotin linker serves as a molecular bridge between membrane proteins and NeutrAvidin-coated nanocrystals. The N-hydroxysuccinimide (NHS) ester group reacts covalently with primary amine groups (-NH_2), which are present on lysine amino acids or polypeptides sites within cell membrane proteins such as TRPV1. When the linker is incubated with cells, this reaction anchors it to the membrane proteins. The polyethylene glycol (PEG) spacer provides flexibility and spatial separation, which reduces steric hindrance. The biotin moiety remains exposed on the cell surface. Upon subsequent addition of nanoparticles coated with NeutrAvidin, the high-affinity biotin-NeutrAvidin interaction mediates attachment of the nanoparticles to the biotin-functionalized membrane proteins.

Confocal images from both experimental conditions, the linker-free and the linker-modified samples, revealed comparable patterns of nanoparticle uptake (Figure 4.93). In each case, the FITC signal appeared as distinct puncta localized within the cytoplasm, consistent with internalization through endocytic pathways. There was no substantial difference in the number or intensity of fluorescent signals between the two treatment groups. A modest increase in FITC signal was observed at 48 h compared to 24 h in both groups, indicating progressive uptake over

time; however, the spatial distribution of the signal remained unchanged. Fluorescent puncta are present near the nuclear envelope, which may suggest nanoparticle entry into the nucleus.

These results indicate that NeutrAvidin alone is sufficient to mediate nanoparticle interaction and internalization in SH-SY5Y cells. The presence of the biotin linker did not enhance surface retention or promote greater internalization under the tested conditions. This result supports the use of the linker-free formulation in subsequent in vitro studies, while keeping the linker strategy in reserve for targeted or receptor-mediated applications.

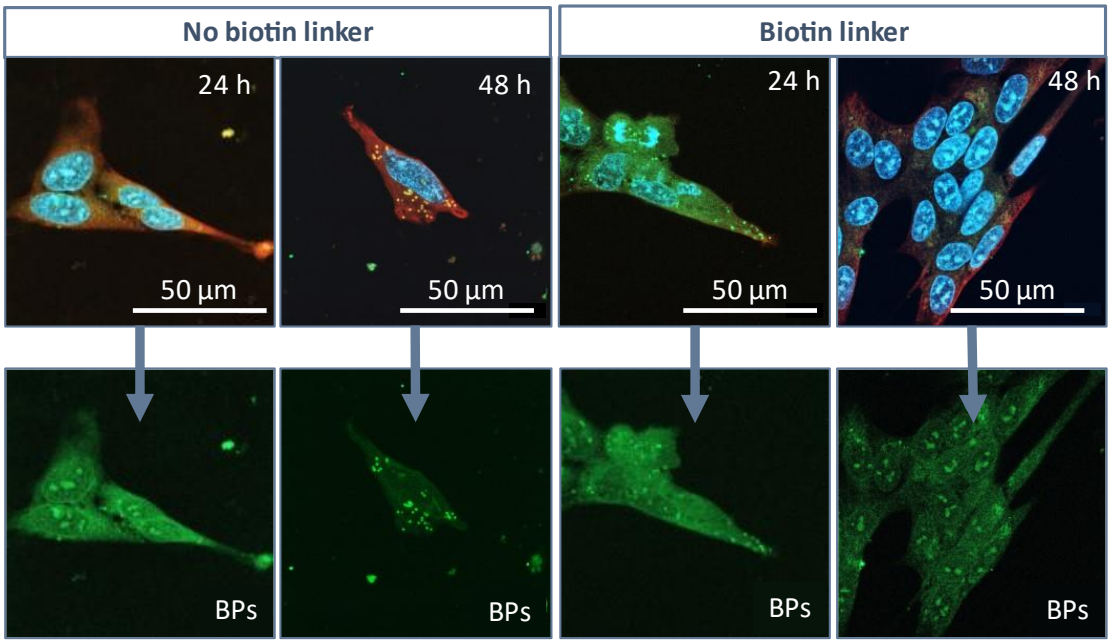

*Figure 4.93 Confocal fluorescence microscopy images of SH-SY5Y cells incubated with FITC-labeled NeutrAvidin-coated bipyramidal gold nanoparticles (BP@NeuAv*FITC) for 1 h. Two experimental conditions were compared: without biotin linker (left) and with pre-treatment using biotin-PEG linker (right). The upper row shows composite images with actin cytoskeleton (red), nuclei (blue), and nanoparticle signal (green). The lower row highlights FITC channel to visualize nanoparticle localization. No major differences in nanoparticle uptake or distribution were observed between the two conditions*

To further examine the time-dependent internalization dynamics of BP@NeuAv*FITC in SH-SY5Y cells, a series of incubation time points (1, 3, 6, and 48 hours) was analyzed using confocal microscopy (Figure 4.94). After 1 hour, the FITC signal was broadly distributed along the cell surface, particularly at the edges, where it overlapped with the actin signal to produce a yellow-orange shade. This pattern suggests that most bipyramids were surface-bound or undergoing early stages of internalization. By 3 hours, peripheral fluorescence remained visible, but small intracellular puncta began to appear, indicating the formation of endocytic vesicles. At 6 hours, these fluorescent aggregates became more distinct and concentrated closer to the nucleus, reflecting progressive intracellular trafficking. After 48 hours, the signal was primarily localized in large clusters within the perinuclear region, consistent with accumulation in endolysosomal

compartments. Throughout all time points, the actin cytoskeleton and nuclear morphology remained unchanged, confirming that nanoparticle exposure under these conditions did not compromise cell integrity. These results reinforce earlier findings and provide additional evidence of the cellular uptake and retention behavior of bipyramidal gold nanocrystals in SH-SY5Y cells.

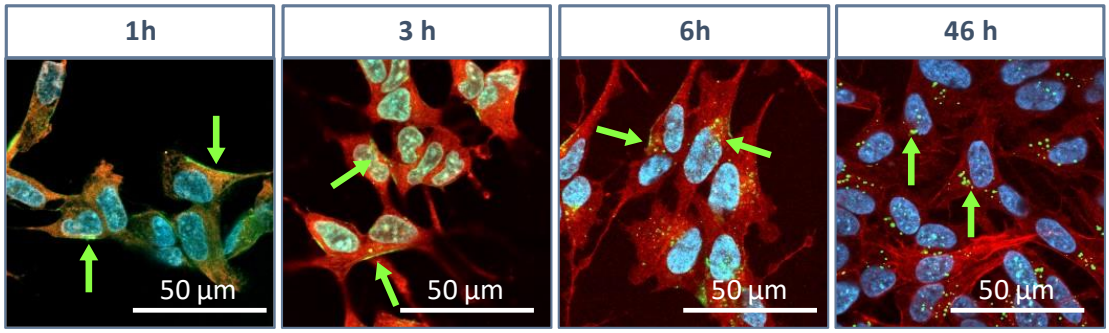

*Figure 4.94 Time-dependent internalization of BP@NeuAv*FITC in SH-SY5Y cells. Confocal images acquired after 1, 3, 6, and 48 hours of incubation show nuclei (DAPI, blue), actin filaments (Phalloidin-Texas Red, red), and nanoparticles (FITC, green).*

As the study progressed, our internalization experiments shifted from immortalized cell lines to primary neurons to better reflect the physiological context. Primary cortical neurons, commonly harvested from embryonic rodent brain tissue via enzymatic dissociation,[34] were cultured on poly-D-lysine-coated substrates in Neurobasal/B27 medium. Confocal microscopy was again used to visualize nanoparticle uptake, applying the same multicolor approach: DAPI staining for nuclei (blue), Phalloidin-Texas Red for F-actin (red), and FITC fluorescence to track bipyramidal gold nanocrystals functionalized with NeutrAvidin (green). Figure 4.95 illustrates the three channels and their overlap, highlighting the dense cytoskeletal structure and dispersed nanoparticle signal within the neuronal culture. Primary cortical neurons present a more intricate morphology and network formation compared to SH-SY5Y cells.

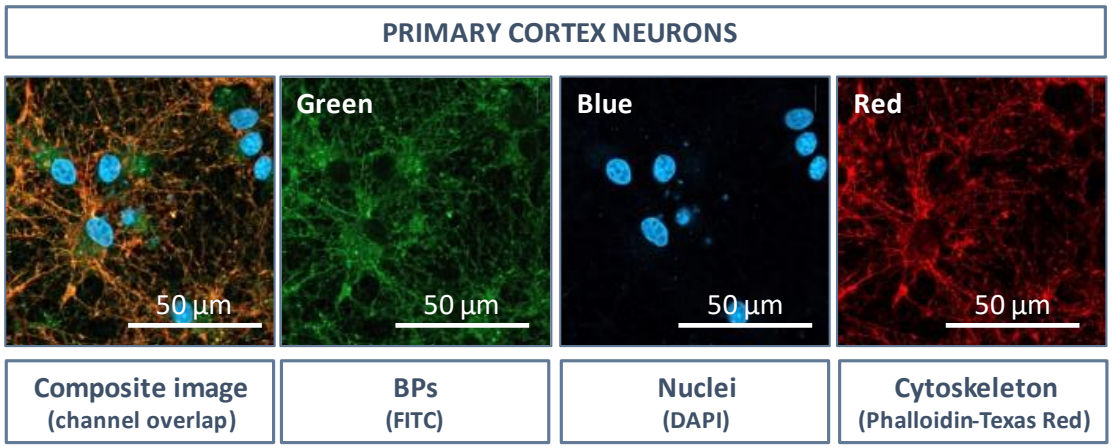

Figure 4.95 Fluorescence imaging of primary cortical neurons labeled for nanoparticle localization and cellular structure. Confocal microscopy images show primary cortical neurons stained with DAPI (blue) for nuclei and Phalloidin-Texas Red (red) for the actin cytoskeleton, incubated for 1h with gold nanocrystals. Gold bipyramids functionalized with FITC-labeled NeutrAvidin (green) were used to assess nanoparticle uptake. Individual fluorescence channels (green, blue, red) are presented alongside a composite image showing channel overlap.

The experiment presented in Figure 4.96 examines the time-dependent uptake of BP@NeuAv*FITC in primary cortical neurons at three post-incubation intervals: 1 h, 6 h, and 24 h. The control sample, which was not exposed to nanocrystals, displays only DAPI-stained nuclei (blue) and a well-organized Phalloidin-labeled actin network (red), with no detectable green fluorescence. This confirms the absence of background signal from FITC or autofluorescence and provides a reference for unaltered cell structure. One hour after nanoparticle exposure, discrete green fluorescent puncta appear along the cell extensions, including axons and dendrites, indicating initial surface binding and the onset of endocytic uptake. By six hours, the FITC signal becomes more intense and broadly distributed throughout the neuronal processes. Numerous yellow-orange puncta, resulting from the overlap of FITC and actin signals, suggest active intracellular transport of internalized particles along the cytoskeleton. After 24 hours, the FITC fluorescence further increases and becomes concentrated within the cell bodies and perinuclear regions, consistent with ongoing internalization and accumulation in endolysosomal compartments. Throughout the time course, the actin cytoskeleton and nuclear morphology remain intact, indicating that nanoparticle uptake under these conditions does not disrupt overall neuronal structure.

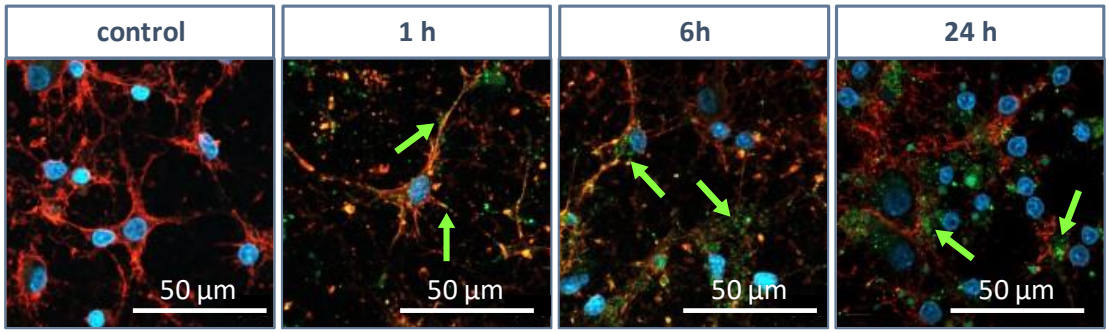

Figure 4.96 Time-dependent uptake of bipyramidal gold nanoparticles by primary cortical neurons. Confocal fluorescence images show primary cortical neurons after incubation with FITC-labeled NeutrAvidin-functionalized gold bipyramids (green) for 1 h, 6 h, and 24 h. At 1 h, green puncta appear along neuronal extensions, increasing in number and intensity over time. By 24 h, a strong FITC signal is visible throughout the cell bodies, indicating progressive internalization.

To complement the confocal microscopy results, we acquired TEM images to directly visualize the localization of bipyramidal gold nanocrystals in primary neurons. Panels A1-A3 show representative images from samples fixed after 1 hour of incubation. Neuronal projections, including axons and dendrites, are identifiable by their elongated morphology and bundled cytoskeletal filaments. In each image, small aggregates of bipyramids are seen adhered to the outer surface of the membrane, suggesting initial contact and anchoring. At this early time point, there is no clear evidence of internalization.

Panels B1-B3 present images from neurons fixed after 24 hours of incubation. In B1, both neuronal extensions and segments of the cell body are visible. Bipyramids are now observed not only at the membrane but also within intracellular vesicles, indicated by arrows. Higher-magnification images (B2 and B3) confirm the presence of nanoparticles inside membrane-bound compartments consistent with endosomes. These vesicles commonly contain multiple nanocrystals clustered together. Cellular structures appear preserved throughout, with no obvious signs of morphological damage, indicating that the nanocrystal uptake occurs without compromising neuronal integrity under the tested conditions.

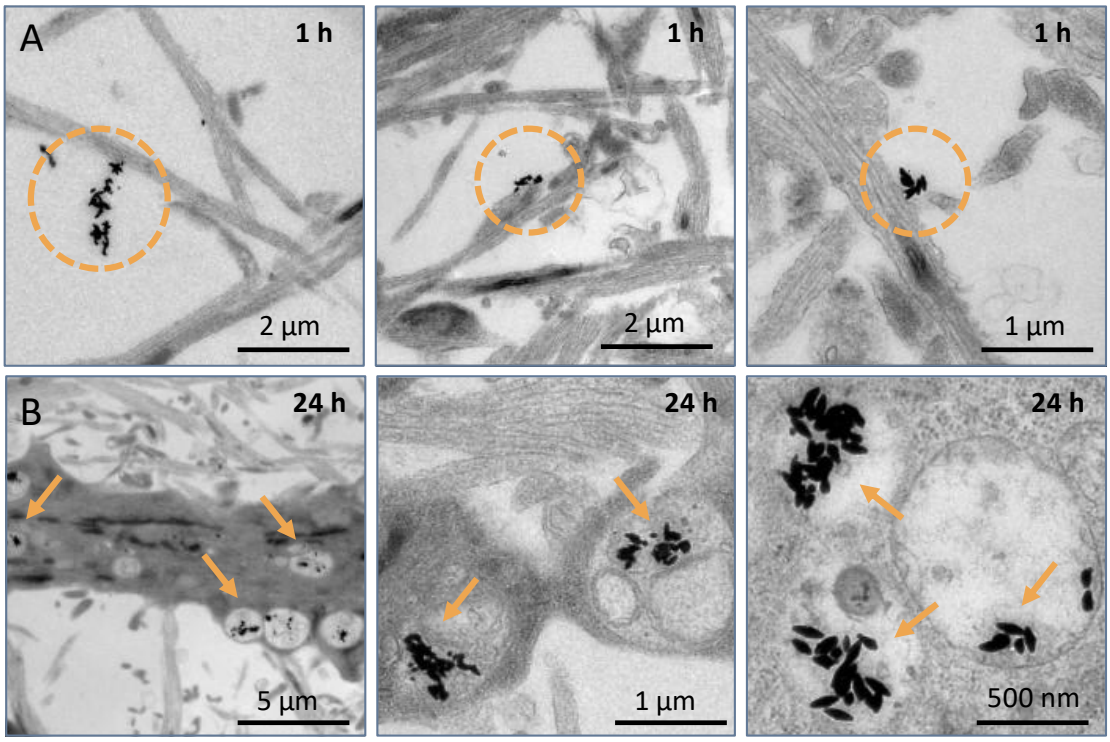

Figure 4.97 TEM images of primary neurons incubated with bipyramidal gold nanocrystals stabilized with NeutrAvidin. (A) Representative images taken after 1 hour of incubation show small aggregates of bipyramids (circled) adhering to the external surface of neuronal projections, such as axons and dendrites. No internalization is observed at this stage. (B) After 24 hours of incubation, bipyramids are clearly visible inside membrane-bound intracellular vesicles (arrows), consistent with endosomal uptake.

3.3. In Vitro Optical Modulation of Neuronal Activity with Au NPs

A central motivation throughout this work has been to explore whether gold nanocrystals can be used to optically modulate neuronal activity, with future applications in both in vitro and in vivo settings. As a first step in this direction, we began a collaborative effort to test whether introducing these nanocrystals into neurons could support light-driven activation under physiologically relevant conditions. The experiments are ongoing and part of a broader project carried out in collaboration with the Neurotechnology Center (Yuste Laboratory). Acute slices of mouse visual cortex were prepared by cardiac perfusion performed with sucrose-based solution (also used during slicing) and maintained in artificial cerebrospinal fluid. Patch-clamp recordings were by Teresa Celaya Garmendia.

The results presented in Figure 4.98 show how extracellularly delivered gold nanoparticles support light-driven modulation of neuronal activity under physiologically relevant conditions. A suspension of 30 nm spherical gold nanoparticles functionalized with NeutrAvidin was introduced in the proximity of patched cortical pyramidal neurons through the glass

micropipette, with mild positive pressure enabling cytosolic diffusion. For these experiments, spherical nanoparticles were used, as dictated by the constraints of the neuromodulation setup employing a 488 nm laser (Figure 4.98 A). The use of bipyramids for neuromodulation at laser of 785 nm is beyond the scope of the present work. Neuronal responses were recorded in current-clamp mode while the cells were exposed to 488 nm light pulses (200 ms, 1 Hz) at 11 mW and 25 mW, which correspond to estimated radiant flux of 4.4 mW and 10 mW at the sample plane, respectively. At lower power (panel B), each illumination event triggered a single, time-locked action potential, followed by a rapid repolarization and stable resting potential. No spontaneous activity was observed between pulses. Increasing the power to 25 mW (panel C) produced a markedly different response: each stimulus evoked a brief burst of 3-6 action potentials. With episodical (not statistically significant) spontaneous firing between stimulations. Panels D and E present overlays of 15 successive trials under each condition, showing high reproducibility. At 11 mW (panel D), single-spike responses were consistent, with the averaged trace peaking near 35 mV and returning to baseline within approximately 50 ms. In contrast, the averaged trace at 25 mW (panel E) displayed a broader depolarization profile, corresponding to the clustered spike bursts.

These recordings indicate that extracellular gold nanoparticles may effectively enable light-triggered excitation of neurons. The response is dependent on illumination power, with higher intensity producing stronger depolarization and burst firing.

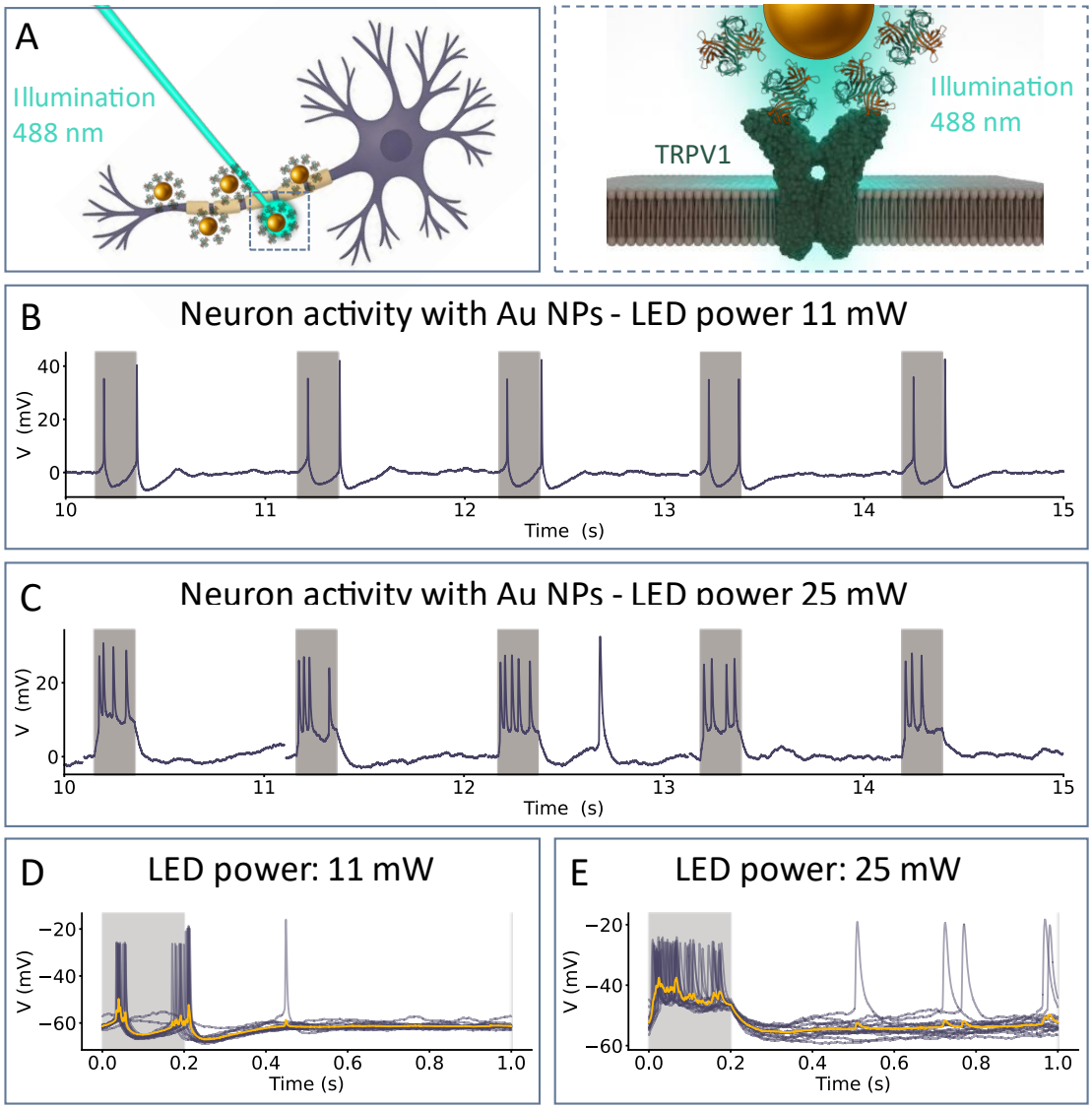

Figure 4.98 Light-induced neuronal responses mediated by intracellular Au-NeutrAvidin spherical nanoparticles. (A) Schematic representation of the experiment. Relative dimensions are not to scale. (B-C) Current-clamp recordings from a cortical pyramidal neuron filled with 30 nm gold NPs and stimulated with light pulses (200 ms, 1 Hz). LED powers of 11 mW (B) and 25 mW (C) correspond to estimated sample irradiance of 4.4 and 10 mW, respectively. Higher power elicited burst firing, while lower power triggered single spikes. (D-E) Same data aligned to light onset. Purple: individual sweeps; yellow: average trace. Data reproduced with permission from Celaya et al. (unpublished).

4. References for Chapter 4

(1) Kauffman, G. B. The Role of Gold in Alchemy. Part II. *Gold Bull.* **1985**, *18* (2), 69–78. https://doi.org/10.1007/bf03214689.

(2) Karnwal, A.; Kumar Sachan, R. S.; Devgon, I.; Devgon, J.; et al. Gold Nanoparticles in Nanobiotechnology: From Synthesis to Biosensing Applications. *ACS Omega* **2024**, *9* (28), 29966–29982. https://doi.org/10.1021/acsomega.3c10352.

(3) Gul, M.; Kashif, M.; Muhammad, S.; Azizi, S.; et al. Various Methods of Synthesis and Applications of Gold-Based Nanomaterials: A Detailed Review. *Cryst. Growth Des.* **2025**, *25* (7), 2227–2266. https://doi.org/10.1021/acs.cgd.4c01687.

(4) Dreaden, E. C.; Alkilany, A. M.; Huang, X.; Murphy, C. J.; et al. The Golden Age: Gold Nanoparticles for Biomedicine. *Chem. Soc. Rev.* **2012**, *41* (7), 2740–2779. https://doi.org/10.1039/C1CS15237H.

(5) Haiss, W.; Thanh, N. T. K.; Aveyard, J.; Fernig, D. G. Determination of Size and Concentration of Gold Nanoparticles from UV−Vis Spectra. *Anal. Chem.* **2007**, *79* (11), 4215–4221. https://doi.org/10.1021/ac0702084.

(6) Turkevich, J.; Stevenson, P. C.; Hillier, J. A Study of the Nucleation and Growth Processes in the Synthesis of Colloidal Gold. *Discuss. Faraday Soc.* **1951**, *11* (0), 55–75. https://doi.org/10.1039/DF9511100055.

(7) Liu, M.; Guyot-Sionnest, P. Mechanism of Silver(I)-Assisted Growth of Gold Nanorods and Bipyramids. *J. Phys. Chem. B* **2005**, *109* (47), 22192–22200. https://doi.org/10.1021/jp054808n.

(8) Gao, Y.; Torrente-Murciano, L. Mechanistic Insights of the Reduction of Gold Salts in the Turkevich Protocol. *Nanoscale* **2020**, *12* (4), 2740–2751. https://doi.org/10.1039/C9NR08877F.

(9) Doyen, M.; Bartik, K.; Bruylants, G. UV–Vis and NMR Study of the Formation of Gold Nanoparticles by Citrate Reduction: Observation of Gold–Citrate Aggregates. *J. Colloid Interface Sci.* **2013**, *399*, 1–5. https://doi.org/10.1016/j.jcis.2013.02.040.

(10) Rodríguez-Fernández, J.; Pérez-Juste, J.; Mulvaney, P.; Liz-Marzán, L. M. Spatially-Directed Oxidation of Gold Nanoparticles by Au(III)−CTAB Complexes. *J. Phys. Chem. B* **2005**, *109* (30), 14257–14261. https://doi.org/10.1021/jp052516g.

(11) Turkevich, J. Colloidal Gold. Part I. *Gold Bull.* **1985**, *18* (3), 86–91. https://doi.org/10.1007/BF03214690.

(12) Grzelczak, M.; Sánchez-Iglesias, A.; Heidari, H.; Bals, S.; et al. Silver Ions Direct Twin-Plane Formation during the Overgrowth of Single-Crystal Gold Nanoparticles. *ACS Omega* **2016**, *1* (2), 177–181. https://doi.org/10.1021/acsomega.6b00066.

(13) Tebbe, M.; Kuttner, C.; Mayer, M.; Maennel, M.; et al. Silver-Overgrowth-Induced Changes in Intrinsic Optical Properties of Gold Nanorods: From Noninvasive Monitoring of Growth Kinetics to Tailoring Internal Mirror Charges. *J. Phys. Chem. C* **2015**, *119* (17), 9513–9523. https://doi.org/10.1021/acs.jpcc.5b03155.

(14) Grzelczak, M.; Pérez-Juste, J.; Mulvaney, P.; Liz-Marzán, L. M. Shape Control in Gold Nanoparticle Synthesis. *Chem. Soc. Rev.* **2008**, *37* (9), 1783–1791. https://doi.org/10.1039/B711490G.

(15) Sánchez-Iglesias, A.; Winckelmans, N.; Altantzis, T.; Bals, S.; et al. High-Yield Seeded Growth of Monodisperse Pentatwinned Gold Nanoparticles through Thermally Induced

Seed Twinning. *J. Am. Chem. Soc.* **2017**, *139* (1), 107–110. https://doi.org/10.1021/jacs.6b12143.

(16) Nguyen, A. L.; Griffin, Q. J.; Wang, A.; Zou, S.; et al. Optimization of the Surfactant Ratio in the Formation of Penta-Twinned Seeds for Precision Synthesis of Gold Nanobipyramids with Tunable Plasmon Resonances. *J. Phys. Chem. C* **2025**, *129* (8), 4303–4312. https://doi.org/10.1021/acs.jpcc.4c08818.

(17) Liu, M.; Guyot-Sionnest, P. Mechanism of Silver(I)-Assisted Growth of Gold Nanorods and Bipyramids. *J. Phys. Chem. B* **2005**, *109* (47), 22192–22200. https://doi.org/10.1021/jp054808n.

(18) Sánchez-Iglesias, A.; Grzelczak, M. Expanding Chemical Space in the Synthesis of Gold Bipyramids. *Small* **2025**, *21* (2), 2407735. https://doi.org/10.1002/smll.202407735.

(19) Tebbe, M.; Kuttner, C.; Männel, M.; Fery, A.; et al. Colloidally Stable and Surfactant-Free Protein-Coated Gold Nanorods in Biological Media. *ACS Appl. Mater. Interfaces* **2015**, *7* (10), 5984–5991. https://doi.org/10.1021/acsami.5b00335.

(20) *Avidin and Streptavidin Conjugates—Section 7.6 - ES*. https://www.thermofisher.com/es/es/home/references/molecular-probes-the-handbook/antibodies-avidins-lectins-and-related-products/avidin-streptavidin-neutravidin-and-captavidin-biotin-binding-proteins-and-affinity-matrices.html (accessed 2025-08-11).

(21) Wieteke D. A. M. de Boer; Jan J. Hirtz; Antonio Capretti; Tom Gregorkiewicz; et al. Neuronal Photoactivation through Second-Harmonic near-Infrared Absorption by Gold Nanoparticles _ Enhanced Reader.

(22) Nguyen, T. T.; Sly, K. L.; Conboy, J. C. Comparison of the Energetics of Avidin, Streptavidin, NeutrAvidin, and Anti-Biotin Antibody Binding to Biotinylated Lipid Bilayer Examined by Second-Harmonic Generation. *Anal. Chem.* **2012**, *84* (1), 201–208. https://doi.org/10.1021/ac202375n.

(23) Jain, A.; Cheng, K. The Principles and Applications of Avidin-Based Nanoparticles in Drug Delivery and Diagnosis. *J. Controlled Release* **2017**, *245*, 27–40. https://doi.org/10.1016/j.jconrel.2016.11.016.

(24) D'Agata, R.; Palladino, P.; Spoto, G. Streptavidin-Coated Gold Nanoparticles: Critical Role of Oligonucleotides on Stability and Fractal Aggregation. *Beilstein J. Nanotechnol.* **2017**, *8* (1), 1–11. https://doi.org/10.3762/bjnano.8.1.

(25) You, Y.; Lim, S.; Gunasekaran, S. Streptavidin-Coated Au Nanoparticles Coupled with Biotinylated Antibody-Based Bifunctional Linkers as Plasmon-Enhanced Immunobiosensors. *ACS Appl. Nano Mater.* **2020**, *3* (2), 1900–1909. https://doi.org/10.1021/acsanm.9b02461.

(26) Bagheri, M.; Kiani, F.; Koohyar, F.; Khang, N. T.; et al. Measurement of Refractive Index and Viscosity for Aqueous Solution of Sodium Acetate, Sodium Carbonate, Trisodium Citrate, (Glycerol + Sodium Acetate), (Glycerol + Sodium Carbonate), and (Glycerol + Trisodium Citrate) at T = 293.15 to 303.15 K and Atmospheric Pressure. *J. Mol. Liq.* **2020**, *309*, 113109. https://doi.org/10.1016/j.molliq.2020.113109.

(27) Koushki, E. Effect of Conjugation with Organic Molecules on the Surface Plasmon Resonance of Gold Nanoparticles and Application in Optical Biosensing. *RSC Adv.* **2021**, *11* (38), 23390–23399. https://doi.org/10.1039/d1ra01842f.

(28) Park, J.-W.; Shumaker-Parry, J. S. Structural Study of Citrate Layers on Gold Nanoparticles: Role of Intermolecular Interactions in Stabilizing Nanoparticles. *J. Am. Chem. Soc.* **2014**, *136* (5), 1907–1921. https://doi.org/10.1021/ja4097384.

(29) Bian, T.; Gardin, A.; Gemen, J.; Houben, L.; et al. Electrostatic Co-Assembly of Nanoparticles with Oppositely Charged Small Molecules into Static and Dynamic Superstructures. *Nat. Chem.* **2021**, *13* (10), 940–949. https://doi.org/10.1038/s41557-021-00752-9.

(30) Mishra, N.; Wu, W. Y.; Srinivasan, B. M.; Hariharaputran, R.; et al. Continuous Shape Tuning of Nanotetrapods: Toward Shape-Mediated Self-Assembly. *Chem. Mater.* **2016**, *28* (4), 1187–1195. https://doi.org/10.1021/acs.chemmater.5b04803.

(31) Sotnikov, D. V.; Berlina, A. N.; Ivanov, V. S.; Zherdev, A. V.; et al. Adsorption of Proteins on Gold Nanoparticles: One or More Layers? *Colloids Surf. B Biointerfaces* **2019**, *173*, 557–563. https://doi.org/10.1016/j.colsurfb.2018.10.025.

(32) Wu, W.; Chittem, P. K.; Meißner, F.; Damm, C.; et al. Determination of Translational and Rotational Diffusivities of Anisotropic Nanoparticles by Heterodyne Polarized and Depolarized Dynamic Light Scattering. *J. Phys. Chem. C* **2024**, *128* (22), 9116–9129. https://doi.org/10.1021/acs.jpcc.4c00918.

(33) Kaya, Z. B.; Santiago-Padilla, V.; Lim, M.; Boschen, S. L.; et al. Optimizing SH-SY5Y Cell Culture: Exploring the Beneficial Effects of an Alternative Media Supplement on Cell Proliferation and Viability. *Sci. Rep.* **2024**, *14* (1), 4775. https://doi.org/10.1038/s41598-024-55516-5.

(34) Sahu, M. P.; Nikkilä, O.; Lågas, S.; Kolehmainen, S.; et al. Culturing Primary Neurons from Rat Hippocampus and Cortex. *Neuronal Signal.* **2019**, *3* (2), NS20180207. https://doi.org/10.1042/NS20180207.

Chapter 5

Summary and Outlook

1. Summary of Major Findings and Conclusions

This dissertation set out to explore how nanomaterials can be used to both monitor and control electrical activity in neurons, with the broader goal of addressing the need for minimally invasive, high-resolution tools at the interface of nanotechnology and neurobiology. In the introductory Chapter 1, we established the conceptual foundation by outlining how semiconductor and metallic nanocrystals, specifically, quantum dots and plasmonic gold nanoparticles, might be employed to interact with and influence neural systems at the nanoscale. These materials offer access to spatial and functional regimes that are difficult to reach using conventional electrodes or fluorescent dyes. We also identified key challenges that served as guiding principles for experimental work that followed, including targeted delivery, biocompatibility, and integration with living systems.

To establish a controlled and reproducible biological system for our experiments, in Chapter 2 we adopted a self-spiking HEK293 cell monolayer, previously engineered to exhibit spontaneous electrical activity. We optimized culture conditions and handling protocols to ensure consistent spiking behavior across experiments. This system functioned as a simplified yet stable cellular model, well-suited for assessing nanoscale voltage sensors and photothermal actuators. Rhythmic action potentials were reliably generated and confirmed through calcium imaging, while pharmacological suppression using sodium channel blockers verified their origin in genuine sodium-driven excitability.

In Chapter 3, we investigated spherical quantum well nanocrystals as a possible tool for voltage sensing. Our first delivery attempt relied on encapsulating hydrophobic dots in micelles. While this method achieved efficient delivery, the micelle-bound particles exhibited low affinity for the plasma membrane and imposed stress on the cells. We also explored membrane-fusion approach with fusogenic liposomes, which produced uniform surface labeling and maintained good biocompatibility. Photophysical characterization showed that, with appropriately engineered surface chemistry, the quantum dots exhibited high quantum yield and stability. The live-cell imaging revealed certain limitations. We were unable to resolve spike-correlated fluorescence changes above background noise, and similar signal fluctuations persisted even after spiking activity was pharmacologically suppressed, indicating that the observed variations remain below the threshold of detectable membrane voltage transients. This limitation was largely attributed to insufficient temporal resolution and poor signal-to-noise ratios in the recording setup. These findings underscore the need for improved imaging speed, enhanced probe sensitivity, and more effective signal processing methods. While the platform for delivery

and biocompatibility was established, reliable spike detection remained out of reach under our experimental conditions.

In parallel with our efforts to detect neural activity, we also investigated whether nanomaterials could be used to stimulate neurons in a controlled and targeted manner. In Chapter 4, we synthesized gold nanocrystals of spherical and bipyramid-like shapes, tuning their optical properties to enable light-to-heat transduction within the biological window. The particles were biofunctionalized with NeutrAvidin to enhance biocompatibility and facilitate targeted delivery. We confirmed their stability in physiological media and evaluated cellular uptake in both primary cortical (CTX) neurons and SH-SY5Y neuroblastoma cells. Short incubations led to surface association, while 24-hour exposure resulted in endocytic uptake without observable cytotoxicity. Surprisingly, the use of a biotin linker showed limited ability to retain nanoparticles at the cell membrane, thereby failing to prevent endocytosis as initially expected. Finally, preliminary photothermal stimulation experiments demonstrated that pulsed laser illumination of neurons containing 30 nm nanospheres could elicit time-locked spikes at moderate power, and burst firing at higher power, confirming the feasibility of gold nanocrystals for plasmonic neuromodulation.

In summary, these studies present a step toward an all-optical neural interface based on inorganic nanomaterials. While several technical and biological constraints limited the full realization of voltage sensing and photothermal control within a single platform, each experimental effort yielded essential insights. We identified the practical boundaries of current designs, clarified what remains technically feasible, and shaped an outcome that will inform further improvements in sensitivity, targeting, and temporal resolution.

2. Methodological Refinement for Future Studies

With the knowledge gained from our experiments, we now revisit our initial assumptions and outline several methodological improvements aimed at advancing future studies. To guide this process, we structured our reflection around a clear progression: Assumption → Lesson → Gap Identification. This framework revealed four gaps: three related to the challenges encountered in Chapter 3 concerning quantum-dot-based voltage detection, and one arising from Chapter 4, focused on plasmonic nanocrystal-based photothermal modulation. The following Table 5.14 summarizes these gaps and forms the foundation for the methodological refinements and technical tweaks discussed in the subsequent section. Those practical adjustments aim to

strengthen the experimental framework and map future development of reliable and effective nanoscale neural interfaces.

Table 5.14 Summary of key findings that support future methodological refinements.

Aspect	Assumption → Lesson → Gap		
Surface chemistry of quantum dots.	With optimized surface chemistry, standard micelle or liposome coatings could deliver QDs to the membrane without significant loss of brightness.	Fusogenic liposomes did achieve uniform membrane insertion, but maintaining QD brightness in the lipid bilayer proved challenging , some coatings caused quenching or aggregation.	Surface chemistry must ensure that QDs remain bright, stably anchored, and properly positioned for voltage sensing, depending on the chosen detection strategy.
Voltage sensing capability.	Membrane-embedded SQW QDs are sensitive and could produce spike-locked fluorescence via the Stark effect.	Live-cell recordings showed no resolvable spikes - fluorescence fluctuations persisted after blocking spiking, indicating true voltage signals were buried in noise.	Both per-particle voltage sensitivity and imaging SNR/time-resolution must be improved for reliable spike readout.
Self-spiking HEK assay.	The HEK293 monolayer would behave as a uniform pacemaker network under fixed culture protocols.	Even under tightly controlled conditions, dishes varied in frequency from batch to batch and dish to dish.	Each dish must be individually validated to confirm genuine activity and exact spiking frequency.
Surface chemistry of gold nanocrystals.	Neutravidin-coated particles targeted to biotinylated membranes were expected to improve surface retention, allowing sufficient time to perform stimulation experiments.	Particles were initially membrane-associated and non-toxic, but over time they were endocytosed, disable efficient near-membrane heating.	Surface coatings must be properly engineered to ensure targeted delivery and stable anchoring of nanoparticles at the cell membrane for a sufficient duration.

QUANTUM DOTS BASED DETECTION

Surface functionalization of quantum dots.

Assumption: We recognized that moving quantum dots from organic solvent into aqueous buffer and embedding them in a lipid membrane might impact their brightness and colloidal stability. Our goal was to tailor surface coatings that could mitigate these effects while still achieving robust membrane association.

Lesson: Fusogenic liposomes enabled the delivery of QDs to the plasma membrane. We tested six coating strategies, adjusting ligand types to improve colloidal stability within the lipid bilayer. These modifications reduced aggregation and enhanced membrane localization. However, a notable loss of the original quantum yield persisted; fluorescence quenching remained a challenge, highlighting the sensitivity of QD brightness to the local lipid environment. As a result, the reduced optical output impacted the sensitivity of voltage recording and raised the threshold required for reliable signal detection.

Gap #1: Surface chemistry should be precisely engineered to ensure that QDs remain stably anchored, optically bright, and positioned appropriately for voltage sensing, with placement tailored to the specific detection strategy.

Proposed refinement:

In our experiments, we observed a notable loss of brightness in membrane-localized QDs, which in turn limited sensitivity to the quantum-confined Stark effect (QCSE). This reduction in performance likely arises from two main factors: (1) aggregation of QDs around or within the membrane, and (2) the influence of surrounding lipid molecules on the QD surface, which may disrupt the optical properties or stability of the particles.

To address these issues, further optimization of surface chemistry is required. As a next step, we propose functionalizing the QD surface with specially designed organic ligands selected to reduce aggregation and minimize damaging interactions with lipids. When applied to compact (~3.5 nm) CdS/CdSe/CdS spherical quantum wells, passivated with an additional ZnS shell (as in system V, described in Chapter 3), this strategy may help preserve both structural integrity and fluorescence efficiency in the membrane environment.

The proposed SH-C8CP-PEG ligand (Figure 5.99) features a thiol group (-SH) on an octyl (C8) chain that forms a strong covalent bond with cadmium or zinc atoms on the quantum dot surface, creating a compact passivation layer that protects against oxidation and reduces photoluminescence quenching. Attached to this alkyl chain is a choline-phosphate (CP)

headgroup, a structural analogue of phosphatidylcholine (PC) with reversed charge orientation. Phosphatidylcholine (PC) is a major component of the cell membrane, and the CP headgroup interacts specifically with PC through electrostatic pairing. This interaction forms quadrupolar complexes that enable nanoparticle adhesion at the membrane interface. A terminal polyethylene- glycol (PEG, 2 kDa) segment, connected forms a shell that suppresses nonspecific interactions, prevents aggregation, and improves colloidal stability in biological environments. Together, these components are designed to preserve quantum dot brightness, minimize nonspecific interactions, and localize the particles near the membrane for voltage sensing applications.[1,2]

An alternative strategy involves modifying the inorganic core composition. Substituting the Cd-based structure with ZnS/ZnSe/ZnS heterostructures could enhance QCSE sensitivity due to their larger bandgap. Although protocols for synthesizing such structures are still under development, they are expected to emit in the blue spectral region, which is suboptimal for bioimaging. This limitation might be addressed by introducing Mn (manganese) doping to create dual-emitting nanocrystals via trap states. Such a system could enable ratiometric sensing by comparing blue and red emission channels or by exploiting voltage-sensitive trap-state emission directly, pending detailed characterization of its response.[3]

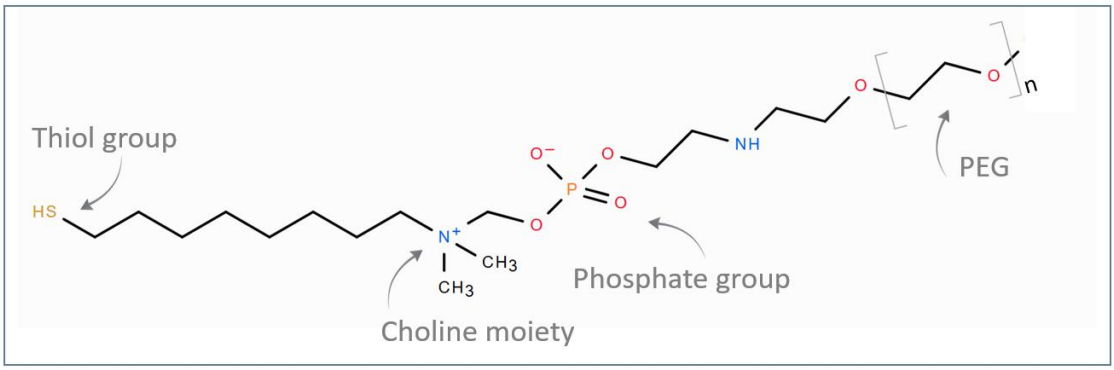

Figure 5.99 Molecular structure of the SH-C8-CP-PEG ligand, showing key functional domains: thiol anchor for quantum dot binding, choline-phosphate (CP) headgroup for membrane targeting via PC interactions, and PEG chain for colloidal stability and antifouling properties.

Voltage sensing capability.

Assumption: Membrane-embedded spherical quantum-well QDs are sensitive enough to produce detectable fluorescence changes correlated with neuronal spikes, based on the quantum-confined Stark effect.

Lesson: In vitro imaging failed to reveal spike-correlated signals. Fluorescence fluctuations persisted even after spiking activity was pharmacologically blocked, indicating that voltage-dependent signals were indistinguishable from background noise.

Gap #2: The optical signal-to-noise ratio and time resolution of the recording remain below the threshold required for reliable spike detection.

Proposed refinement:

This challenge can be addressed through two complementary strategies. The first is to increase the brightness and quantum efficiency of fluorescent probes, such as quantum dots, to improve the optical signal-to-noise ratio. This approach aligns with the solution proposed for Gap #1. The second is to enhance the sensitivity and temporal resolution of the detection hardware. Although the present work prioritized a simple setup accessible to most biological laboratories, commercially available high-performance detectors could substantially improve both sensitivity and frame rate.

For wide-field fluorescence measurements, back-illuminated scientific complementary metal-oxide-semiconductor (scientific CMOS or sCMOS) cameras offer an optimal balance of speed, sensitivity, and field of view. With quantum efficiencies approaching 85% and read noise below 2 e- RMS, these detectors can acquire multi-megapixel images at >100 frames/s, enabling the capture of rapid events in live-cell preparations. The Hamamatsu ORCA-Flash4.0, used in this work, provides performance well aligned with these requirements.

When signals are exceptionally weak, electron-multiplying charge-coupled device (EMCCD) cameras can provide an advantage through electron multiplication, effectively eliminating read noise and enabling single-photon detection. However, they operate at lower frame rates and typically have smaller sensor formats. The emerging quantitative CMOS (qCMOS) technology combines the speed and dynamic range of sCMOS with the ultra-low noise of EMCCDs, representing a promising future option for quantitative imaging in low-light conditions. The technical specification of sCMOS, EMCCD and qCMOS are listed in the Table 5.15.

Point detectors such as photomultiplier tubes (PMTs), avalanche photodiodes (APDs), or single-photon avalanche diodes (SPADs) are widely used in high-resolution scanning modalities, but their single-point acquisition makes them less effective for dim, wide-field systems. If quantum dot brightness and voltage response are sufficiently enhanced, such detectors could also become viable for nanoscale neural recordings.

Finally, temporal resolution is critical. Action potentials occur on the millisecond timescale, whereas quantum dots respond to local electric field changes within nanoseconds. Low frame

rates cause temporal averaging that obscures rapid fluorescence fluctuations. High-speed acquisition is therefore essential to resolve voltage-dependent transients and accurately capture the dynamics of neuronal activity in situ.

Table 5.15 Comparison of key performance specifications for representative sCMOS, EMCCD, and qCMOS camera models. Data listed in the table are based on technical specifications provided by the manufacturers in their respective technical notes.

Detector Type	sCMOS	sCMOS	EMCCD	qCMOS
Model	Andor Marana 4.2B-11	Hamamatsu ORCA-Flash4.0 V3	Andor iXon Ultra 897	Hamamatsu ORCA-Quest
Peak QE (%)	95	82	95	85
Max Frame Rate (fps)	2k	25k	11k	15k
Pixel Size (µm)	11x11	6.5x6.5	16x16	4.6x4.6
Max frame Size (pixels)	2048 x 2048	2048 x 2048	512 x 512	4096 x 2304
Read Noise (e-)	1.6	1.6	<1 (EM gain)	0.2
Dark Current (e-/pixel/s)	0.7	0.06	0.0003	0.006
Dynamic Range	53 000:1	37 000:1	-	26 000:1
Cooling	-45°C	-30°C	-100°C	-35°C
Digitization Depth (bit)	16	16	16	16

Self-spiking HEK assay.

Assumption: The engineered HEK293 monolayer would behave as a uniform pacemaker network, providing a stable platform for evaluating voltage sensors.

Lesson: Rhythmic spiking was generally observed under optimized conditions, but some preparations still showed little or no spontaneous activity. This variability occurred even when all efforts were made to maintain consistent culture protocols, timing, and handling. Differences in spiking frequency and synchrony were observed not only between batches but also between samples within the same batch, underscoring that even simplified biological systems can exhibit unpredictable behavior. These findings reinforced the need to validate network activity in each preparation using established reference methods.

Gap #3: Each sample, meaning each culture dish, must be independently validated to confirm the presence and frequency of spiking activity. Relying on parallel or “twin” preparations introduces additional uncertainty, as biological variability between nominally identical samples can lead to divergent behavior.

Proposed refinement:

To ensure scientific rigor and interpretability, validation of electrical activity should be performed directly on the same sample used for optical measurements. Simultaneous confirmation using an independent method is essential to avoid ambiguity, particularly given the variability observed across individual cultures. While this added complexity was not implemented in the preliminary studies due to experimental constraints, future experiments in optimized systems should incorporate such dual validation. Co-recording using patch-clamp electrophysiology or two-color imaging (e.g., calcium or voltage-sensitive dyes in parallel with QD emission) would provide critical ground-truth correlation. This approach would offer a more definitive demonstration that quantum dot fluorescence changes are indeed linked to voltage dynamics in spiking HEK monolayers.

PLASMONIC NANOCRYSTALS BASED MODUALTION

Surface functionalization of gold nanocrystals.

Assumption: Functionalizing gold nanocrystals with Neutravidin and immobilizing them using a biotinylated linker was expected to improve surface retention in-vitro, keeping the particles near the membrane for a longer duration than without the linker. This extended retention was considered crucial to enable stimulation within the timeframe required for longer experiments or treatments.

Lesson: Although the particles were non-toxic and initially associated with the membrane, prolonged exposure led to internalization and accumulation in endosomal compartments. This reduced their effectiveness for near-membrane heating.

Gap #4: Surface coatings must be optimized to ensure that nanocrystals remain anchored at the membrane for the duration of the experiment or treatment period. Appropriate targeting strategies should also be explored to enhance localization and functional efficacy.

Proposed refinement:

To extend the membrane residency of gold nanocrystals and improve the reliability of photothermal stimulation, three complementary surface-engineering strategies may be considered. The first involves directional anchoring by converting bipyramidal nanocrystals into Janus particles. This is achieved by selectively attaching a phospholipid-PEG segment (e.g., DSPE-PEG) to one facet of the nanocrystal, while passivating the remaining surface with a

dense PEG or zwitterionic layer. The phospholipid moiety inserts shallowly into the outer leaflet of the plasma membrane, anchoring the particle at the cell surface. Meanwhile, the opposing protein-repellent coating presents a sterically bulky interface that hinders membrane wrapping and raises the energetic barrier for endocytosis, effectively delaying internalization. This asymmetrical design has been shown to keep similar Janus nanoparticles localized at the cell surface for at least 24 hours in fibroblast cultures, in contrast to isotropically coated particles, which are internalized much more rapidly.[4]

A second strategy to extend membrane retention involves molecular tethering, in which nanocrystals are anchored to specific targets on the cell surface through defined chemical or physical interactions. This approach allows for precise spatial control, positioning the nanoparticle in proximity to membrane components of functional interest – such as ion channels, receptors, or specific lipid domains. Tethering can be achieved by exploiting high-affinity ligands or binding partners. For example, neurotoxins that selectively bind voltage-gated ion channels have been used to direct gold nanoparticles (AuNPs) to excitable membrane domains. One demonstrated method employed AuNP-streptavidin conjugates assembled with biotinylated Ts1 neurotoxin to target sodium channels. Alternatively, nanocrystals may be directly functionalized with neurotoxins or with antibodies directed against native membrane proteins. Other examples of molecular tethering include cholesterol-modified nanoparticles that insert into the membrane bilayer or gold nanoparticles functionalized with antimicrobial peptides that bind specific lipid structures.[5] A particularly promising tethering strategy is based on bioorthogonal chemistry, which involves selective reactions between mutually reactive groups that form covalent bonds under physiological conditions. This approach provides control over nanoparticle attachment, enabling stable and site-specific tethering. The importance of this chemistry in biological systems was highlighted by the 2022 Nobel Prize in Chemistry, awarded for foundational work in click and bioorthogonal chemistry.[6,7]

A third approach relies on biomimetic surface functionalization, in which nanoparticles are coated with components that mimic natural cellular membranes. This can include synthetic lipid bilayers, natural membrane extracts, or polymeric shells that emulate the physicochemical properties of the cell surface. For instance, gold nanocrystals functionalized with zwitterionic phosphatidylcholine-based lipid bilayers display improved biocompatibility and reduced nonspecific interactions. More advanced systems incorporate cell-derived membranes, such as red blood cell (RBC) membranes, which present immunomodulatory proteins like CD47 that signal "self" to phagocytic cells, thereby inhibiting phagocytosis and prolonging circulation time. Similarly, inverse-phosphorylcholine coatings, previously discussed in the context of quantum

dot surface chemistry, may serve both as a biomimetic interface and as a functional targeting layer. These camouflaging strategies reduce recognition by the immune system and delay internalization by endocytic pathways, supporting longer residence times at or near the membrane. When combined with directional anchoring or molecular tethering, biomimetic coatings may further enhance surface stability, minimize off-target effects, and improve the precision of nanoparticle-based neuromodulation.[8]

3. Closing Remarks and Field Outlook

The interface between nanotechnology and neurobiology offers great potential for developing minimally invasive tools to monitor and manipulate neural activity. However, realizing this vision in practice presents a range of scientific and technical challenges. Throughout this PhD project, I aimed to address several of these challenges by developing nanocrystal-based platforms for voltage sensing and photothermal stimulation, while refining the biological models and experimental setups required for their evaluation. Each step moved the field forward: improving delivery strategies, identifying key limitations in sensitivity and targeting, and outlining concrete pathways toward more reliable, and functional nanoscale neural interfaces.

This work was carried out as part of the Basque Nanoneuro Network (B3N), a collaborative initiative that brings together eight research centers across the Basque Country. Launched in 2020 under the IKUR programme of the Basque Government, the network aims to leverage regional strengths in nanoscience and neuroscience to build next-generation neurotechnologies. This thesis represents one of the early contributions to that effort, demonstrating how tools from materials science, surface chemistry, and cellular neurobiology can be integrated into a common framework. Many of the approaches explored in this dissertation include the use of quantum dots as optical sensors, genetically modified HEK cells, targeting of thermosensitive ion channels, and the prospective application of two-photon imaging.

Looking forward, the methodological refinements proposed in this dissertation – such as improved brightness of quantum dots, higher-speed imaging, and enhanced nanoparticle targeting – form a roadmap for the next phase of research. With continued progress, these strategies could transform experimental prototypes into powerful tools for both fundamental neuroscience and therapeutic intervention. While much remains to be done, the work presented here helps lay the foundation. It reflects not only the scientific curiosity that drives this field, but also the long-term vision: that one day, nanotechnology may help us better understand how the brain works – and perhaps even offer new ways to treat the diseases that affect it.

4. References for Chapter 5

(1) Tanaka, M.; Sawaguchi, T.; Hirata, Y.; Niwa, O.; et al. Properties of Modified Surface for Biosensing Interface. *J. Colloid Interface Sci.* **2017**, *497*, 309–316. https://doi.org/10.1016/j.jcis.2017.02.070.

(2) Yu, X.; Liu, Z.; Janzen, J.; Chafeeva, I.; et al. Polyvalent Choline Phosphate as a Universal Biomembrane Adhesive. *Nat. Mater.* **2012**, *11* (5), 468–476. https://doi.org/10.1038/nmat3272.

(3) McLaurin, E. J.; Vlaskin, V. A.; Gamelin, D. R. Water-Soluble Dual-Emitting Nanocrystals for Ratiometric Optical Thermometry. *J. Am. Chem. Soc.* **2011**, *133* (38), 14978–14980. https://doi.org/10.1021/ja206956t.

(4) Kadam, R.; Ghawali, J.; Waespy, M.; Maas, M.; et al. Janus Nanoparticles Designed for Extended Cell Surface Attachment. *Nanoscale* **2020**, *12* (36), 18938–18949. https://doi.org/10.1039/D0NR04061D.

(5) Carvalho-De-Souza, J. L.; Nag, O. K.; Oh, E.; Huston, A. L.; et al. Cholesterol Functionalization of Gold Nanoparticles Enhances Photoactivation of Neural Activity. *ACS Chem. Neurosci.* **2019**, *10* (3), 1478–1487. https://doi.org/10.1021/acschemneuro.8b00486.

(6) Idiago-López, J.; Moreno-Antolín, E.; Eceiza, M.; Aizpurua, J. M.; et al. From Bench to Cell: A Roadmap for Assessing the Bioorthogonal "Click" Reactivity of Magnetic Nanoparticles for Cell Surface Engineering. *Bioconjug. Chem.* **2022**, *33* (9), 1620–1633. https://doi.org/10.1021/acs.bioconjchem.2c00230.

(7) Ojima, K.; Shiraiwa, K.; Soga, K.; Doura, T.; et al. Ligand-Directed Two-Step Labeling to Quantify Neuronal Glutamate Receptor Trafficking. *Nat. Commun.* **2021**, *12* (1), 831. https://doi.org/10.1038/s41467-021-21082-x.

(8) Caselli, L.; Paolini, L.; Fong, W.-K.; Montis, C.; et al. The Gold Nanoparticle–Lipid Membrane Synergy for Nanomedical Applications. *Nanoscale Horiz.* **2025**, 10.1039.D5NH00292C. https://doi.org/10.1039/D5NH00292C.

APPENDIX

1. List of Abbreviations

AA, ascorbic acid

ALS, asymmetric least-squares (baseline correction)

AuNPs, gold nanoparticles

AuNRs, gold nanorods

BBB, blood-brain barrier

BDAC, benzyldimethylhexadecylammonium chloride

BPs, gold bipyramids

CFP, cyan fluorescent protein

CMOS, complementary metal-oxide-semiconductor

CP, choline-phosphate (headgroup)

CTAB, cetyltrimethylammonium bromide

CTAC, cetyltrimethylammonium chloride (trimethyloctylammonium chloride)

CTX, cortical (primary cortical neurons)

DAPI, 4',6-diamidino-2-phenylindole

DCM, dichloromethane

DLS, dynamic light scattering

DMEM, Dulbecco's Modified Eagle Medium

DMPC, 1,2-dimyristoyl-sn-glycero-3-phosphocholine

DOTAP, 1,2-dioleoyl-3-trimethylammonium-propane

DPPE-PEG2000, 1,2-dipalmitoyl-sn-glycero-3-phosphoethanolamine-N-[methoxy(polyethylene glycol)-2000]

DSPE, 1,2-distearoyl-sn-glycero-3-phosphoethanolamine

EDL, electrical double layer

EMCCD, electron-multiplying charge-coupled device

EPSP, excitatory postsynaptic potential

FBS, fetal bovine serum

FITC, fluorescein isothiocyanate

FOV, field of view

FRET, Förster resonance energy transfer

GECI, genetically encoded calcium indicator

GEVI, genetically encoded voltage indicator

GFP, green fluorescent protein

HEK, human embryonic kidney

IPSP, inhibitory postsynaptic potential

LBL, layer-by-layer (assembly)

LSPR, localized surface plasmon resonance

MRI, magnetic resonance imaging

NA, numerical aperture

NeuAv, NeutrAvidin

NIR, near-infrared

NP, nanoparticle

OCG, n-octyl-β-D-glucoside

PBS, phosphate-buffered saline

PEG, polyethylene glycol

PL, photoluminescence

PLQY, photoluminescence quantum yield

PSD, power spectral density

QD, quantum dot

QCSE, quantum-confined Stark effect

qCMOS, quantitative CMOS

RBC, red blood cell

ROI, region of interest

RMS, root-mean-square

SERS, surface-enhanced Raman scattering

SH-C8-CP-PEG, thiol-octyl-choline-phosphate-polyethylene glycol ligand

SH-SY5Y, human neuroblastoma cell line

sCMOS, scientific CMOS

SPR, surface plasmon resonance

SQW, spherical quantum well

TEM, transmission electron microscopy

TOPO, tri-n-octylphosphine oxide

TRP, transient receptor potential (ion channel family)

TTX, tetrodotoxin

UV-Vis-NIR, ultraviolet-visible-near-infrared spectroscopy

XPS, X-ray photoelectron spectroscopy

2. Supplementary Material for Chapter #2

2.1. Materials

Self-spiking HEK293 cells were obtained from the A. Cohen laboratory. All cell culture reagents were purchased from commercial sources and used according to the manufacturers' instructions. The following reagents were used: Dulbecco's Modified Eagle Medium (DMEM, high glucose, 4.5 g/L D-glucose, without L-glutamine and sodium pyruvate; Thermo Fisher Scientific, Cat. No. 11965-092), heat-inactivated fetal bovine serum (HI FBS; Thermo Fisher Scientific, Cat. No. 10082147), penicillin-streptomycin (10,000 U/mL; Thermo Fisher Scientific, Cat. No. 15140-122), L-glutamine (200 mM; Thermo Fisher Scientific, Cat. No. 25030-081), puromycin (Sigma-Aldrich, Cat. No. P8833), geneticin (50 mg/m; Thermo Fisher Scientific, Cat. No. 10131-035), trypsin-EDTA (Thermo Fisher Scientific, Cat. No. 25300-054), dimethyl sulfoxide (DMSO; Sigma-Aldrich, Cat. No. D2650), Pluronic Acid (vendor and catalog number to be specified), Recovery™ Cell Culture Freezing Medium (Thermo Fisher Scientific, Cat. No. 12648-010), and trypan blue (Thermo Fisher Scientific, Cat. No. 15250-061). Buffer solutions were prepared using sodium chloride (NaCl; Sigma-Aldrich, Cat. No. S9888), potassium chloride (KCl; Sigma-Aldrich, Cat. No. P5405), calcium chloride ($CaCl_2$; Sigma-Aldrich, Cat. No. xxx), magnesium chloride hexahydrate ($MgCl_2$; Sigma-Aldrich, Cat. No. xxx), HEPES (Sigma-Aldrich, Cat. No. H3375), and D-glucose (Sigma-Aldrich, Cat. No. G7021). Calcium Imaging was performed using Calcium Green-1 AM (Invitrogen by Thermo Fisher Scientific, Cat. No. C3011MP), Pluronic F-127 (Invitrogen Thermo Fisher Scientific, Cat. No. P3000MP), tetrodotoxin citrate (Tocris Bioscience, Cat. No. 1078).

2.1.1. Reagent Preparation - Recipes

Complete Growth Medium for HEK293 Cell Culture

The complete growth medium was prepared by combining 450 mL of high-glucose DMEM (4.5 g/L D-glucose, without L-glutamine and sodium pyruvate), 50 mL of heat-inactivated fetal bovine serum (HI FBS), 5 mL of penicillin-streptomycin solution (10,000 U/mL), and 5 mL of 200 mM L-glutamine. All components were thawed and combined under sterile conditions in a vacuum filtration unit, and sterile-filtered through a 0.22 µm membrane. The pH of the final medium was verified to be within the range of 7.0-7.6 and adjusted, if necessary, using sterile 1M HCl or 1M NaOH. Osmolality was measured prior to aliquoting (320-370 mOsm/kg). The prepared medium was distributed into 50 mL conical tubes, sealed with parafilm, labeled with preparation date and contents, and stored at 4°C protected from light.

Selective Growth Medium for Self-Spiking HEK293 Cells

The selective medium for genetically modified self-spiking HEK293 cells was prepared by supplementing complete DMEM containing 10% fetal bovine serum (DMEM10) with 2 µg/mL puromycin and 500 µg/mL geneticin. To achieve this, 40 µL of puromycin stock solution (1 mg/mL) and 200 µL of geneticin stock solution (50 mg/mL) were added to every 20 mL of DMEM10 immediately prior to use. A visible color change upon addition of antibiotics was noted, consistent with phenol red's pH sensitivity.

Tyrode's Solution - Recording media

The 6 mM K^+ extracellular buffer was prepared in double-deionized water with the following final concentrations: 125 mM sodium chloride (NaCl, 731.25 mg), 6 mM potassium chloride (KCl, 44.7 mg), 3 mM calcium chloride ($CaCl_2$, 33.3 mg), 1 mM magnesium chloride (MgC_2, 9.5 mg), 10 mM HEPES (238.0 mg), and 30 mM D-glucose (540 mg) per 100 mL of solution. The pH was adjusted to 7.3 using 1M NaOH, and the osmolality was confirmed to be within the range of 300-310 mOsm/kg before sterile filtration.

2.2. Methods

2.2.1. Cell Culture Protocols

Thawing of Cryopreserved HEK293 Cells

Cryopreserved HEK293 cells were rapidly thawed in a 37°C water bath for no longer than 1 minute, avoiding immersion of the vial cap to minimize contamination. The vial was immediately disinfected with 70% ethanol and transferred to a sterile laminar flow hood. Cells were gently transferred to a 15 mL centrifuge tube, and 9 mL of pre-warmed complete growth medium was added dropwise to minimize osmotic shock. The suspension was mixed carefully by gentle pipetting and centrifuged at 130 × g for 7 minutes at room temperature. The supernatant was aspirated without disturbing the cell pellet. Cells were then resuspended in 15 mL of complete medium and seeded into a T75 culture flask. Flasks were labeled accordingly and incubated at 37°C in a humidified atmosphere with 5% CO_2. Cell attachment and recovery were monitored, and cultures were passaged upon reaching ~80-90% confluency.

Passaging of HEK293 Cells

For routine subculturing, cells were maintained under sterile conditions. Growth medium and trypsin-EDTA were pre-warmed to 37°C prior to use. Trypsin-EDTA (4 mL per T75 flask) was thawed and transferred to the biosafety cabinet following surface decontamination with 70% ethanol. T75 culture flasks were removed from the incubator, and the old medium was aspirated. Trypsin was added to one corner of the flask and distributed evenly without agitation to prevent clumping. After 1-2 minutes of enzymatic detachment at room temperature, 8 mL of pre-warmed complete growth medium was added to inactivate trypsin, and the cell monolayer was dissociated by gentle pipetting.

The resulting cell suspension was transferred to a 15 mL conical tube and centrifuged at 150 × g for 8 minutes. The supernatant was aspirated, and the cell pellet was resuspended in fresh complete medium (typically 12 mL). Cell concentration and viability were determined via trypan blue exclusion assay. For this, 10 µL of cell suspension was mixed with 10 µL of 0.4% trypan blue and loaded onto a hemocytometer. Cells in the four corner squares were counted, and the average number of viable cells was calculated as:

$$C_{\text{cells}} = \left(\frac{N_1 + N_2 + N_3 + N_4}{4}\right) \times 2 \times 10^4 \text{ cells/mL}$$

Cells were then seeded at a density of 2×10^6 cells per T75 flask in 15 mL of complete medium. Culture flasks were labeled with cell type, passage number, and date, and returned to the

incubator at 37°C in a humidified 5% CO_2 atmosphere. Cell growth was monitored daily and passaging was typically performed every 48-72 hours depending on confluency.

Cryopreservation of HEK293 Cells

HEK293 cells were cryopreserved using either freshly prepared freezing medium (90% DMEM10 without antibiotics and 10% DMSO or commercial Recovery™ Cell Culture Freezing Medium. Prior to freezing, cells were harvested at ~90% confluency using 4 mL of 0.05% trypsin-EDTA followed by neutralization with 8 mL of complete growth medium, as described for routine passaging. Cells were counted using a hemocytometer and diluted to a final concentration of at least 3×10^6 viable cells/mL in cold freezing medium. The suspension was mixed thoroughly to maintain homogeneity and aliquoted (1.5-2 mL) into labeled cryogenic vials, indicating cell line, passage number, and date.

Cryovials were frozen using a passive freezing container placed at -80°C to achieve a gradual cooling rate of ~1°C/min. After overnight freezing, vials were transferred to the vapor phase of a liquid nitrogen storage system for long-term preservation.

2.2.2. Calcium Imaging

HEK293 cells were seeded onto poly-D-lysine-coated glass coverslips and cultured to 90-100% confluency. For calcium imaging, cells were loaded with 5 µM Calcium Green-1 AM in Tyrode's buffer supplemented with 0.02% (v/v) Pluronic F-127 to facilitate dye uptake. The dye stock was prepared by dissolving 5 µL of Calcium Green-1 AM in anhydrous DMSO and dividing the solution into 4 × 1 µL aliquots. Prior to use, each 1 µL aliquot was mixed with 9 µL of a 10% (w/v) Pluronic F-127 solution in DMSO to yield a 10 µL working premix. This premix was then diluted into 1 mL of Tyrode's buffer and divided into two equal portions. For staining, 0.5 mL of the dye-loading solution was added directly to the culture medium in each dish and incubated for 30 minutes at 37°C in a humidified atmosphere with 5% CO_2. Following incubation, cells were gently washed with Tyrode's buffer to remove excess dye while preserving an intact and continuous monolayer. Imaging was performed in 1 mL of Tyrode's buffer to support spontaneous activity and reproducible spiking behavior. All recordings were conducted at room temperature under ambient atmospheric conditions, without a perfusion system.

2.2.3. Fluorescence Microscope Setup

Unless indicated otherwise, all imaging of HEK cells was performed on an upright, fixed-stage epi-fluorescence microscope (Olympus BX51WI) equipped with a motorised Luigs & Neumann SM-5 X-Y stage. Excitation light was provided by a 100 W mercury arc lamp

(Olympus U-LH100HG) gated by a Uniblitz VCM-D1 shutter, while transmitted-light images were acquired using a 12 V/100 W halogen lamp powered by an Olympus TH3 transformer. Fluorophore channel selection was achieved using a Thorlabs FITC filter cube (475/85 nm excitation, 500 nm long-pass dichroic, 535/50 nm emission) matched to the spectral properties of Calcium Green-1. To reduce photobleaching and phototoxicity, neutral-density (ND) filters were inserted into the excitation path to attenuate light intensity as needed; depending on the chosen ND filter configuration, the radiant flux measured at the specimen plane was 0.5-2 mW. Samples were imaged using either a water-immersion 10×/0.30 W (UMPLFLN 10× W) or 40×/0.80 W (LUMPLFLN 40× W) objective, and emitted fluorescence was collected through the same objective and directed to a Hamamatsu ORCA-Flash 4.0 sCMOS camera (C11440-42U40) via the trinocular port. Image sequences (30-200 ms exposures, 1 × 1 or 2 × 2 binning, up to 30 fps) were acquired using HCImage Live software and subsequently processed in ImageJ/Fiji.

2.3. Additional Figures

To complement the fluorescence traces presented in Chapter 2 (Figure 2.5), here we include the corresponding frequency-domain representation of the signals. Spontaneous spiking activity of HEK cell monolayers was analyzed using Welch's method to estimate the power spectral density (PSD). This approach provides a quantitative assessment of the dominant spiking frequency and highlights variability across different samples.

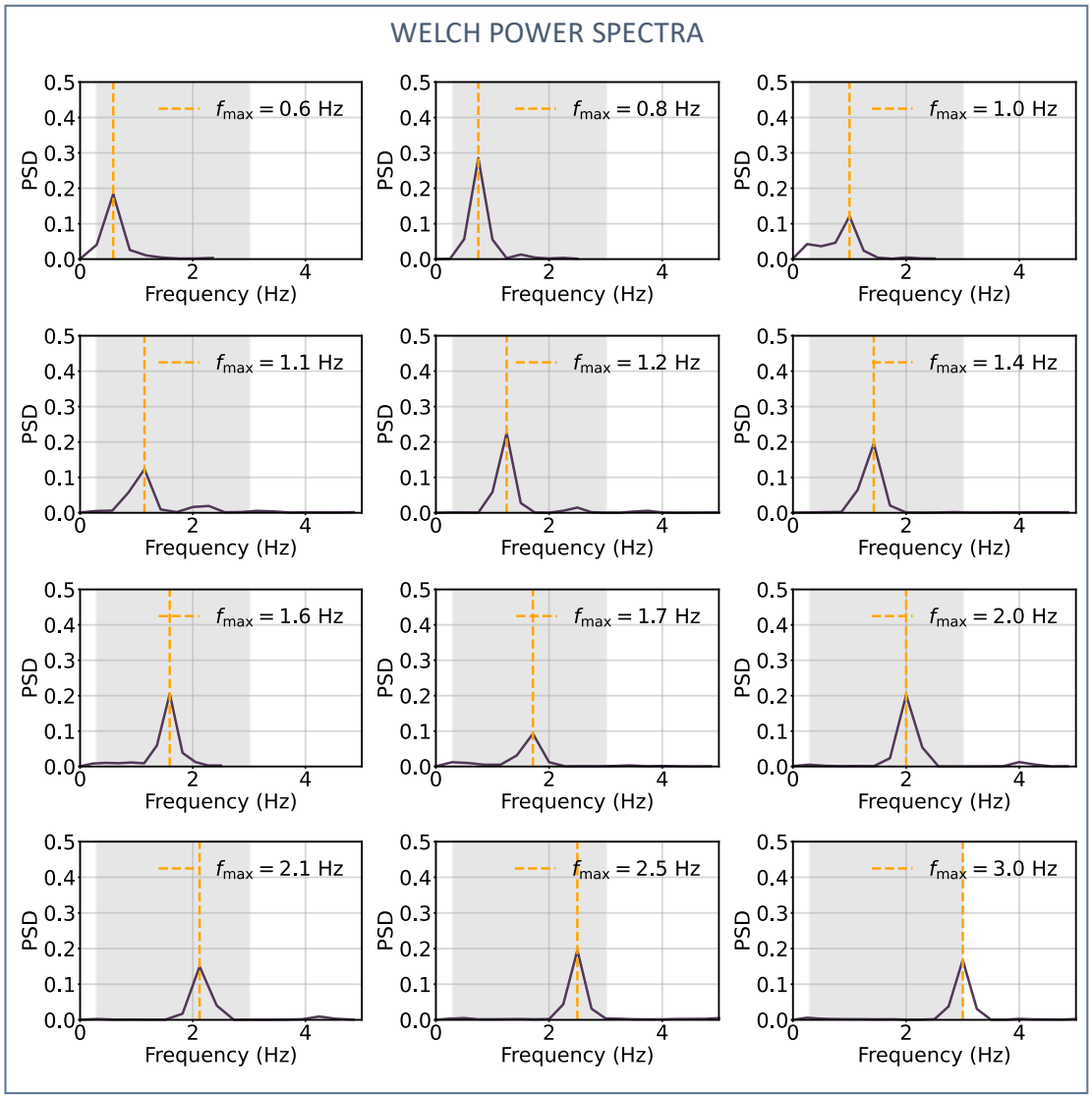

Figure A.100 Power spectral density plots of spontaneous spiking activity in HEK cell monolayers, obtained by Welch analysis of the fluorescence traces shown in Figure 2.5 (Chapter 2). Each spectrum illustrates the distribution of signal power across frequencies, with peaks corresponding to the dominant spiking rate in the respective recording.

Pharmacological validation with tetrodotoxin (TTX)

As described in Chapter 2, Section 2.2, pharmacological inhibition was used to confirm the origin of spontaneous spiking activity. Tetrodotoxin was applied as a selective blocker of voltage-gated sodium channels. An initial 120 s baseline recording was performed to confirm the presence of spontaneous activity (Figure A.101 A). TTX was then added directly to the imaging dish containing 1 mL of culture medium by introducing 1 µL of a 10 mM TTX stock solution in PBS, yielding a final concentration of 10 µM. No perfusion system was used. Recording was initiated immediately following TTX addition and continued for 300 s (Figure A.101 B). Spiking activity gradually diminished and was fully suppressed within approximately 60 s. To remove TTX, the medium was replaced through three sequential wash steps using fresh medium. A post-wash recording was then acquired for 120 s (Figure A.101 C).

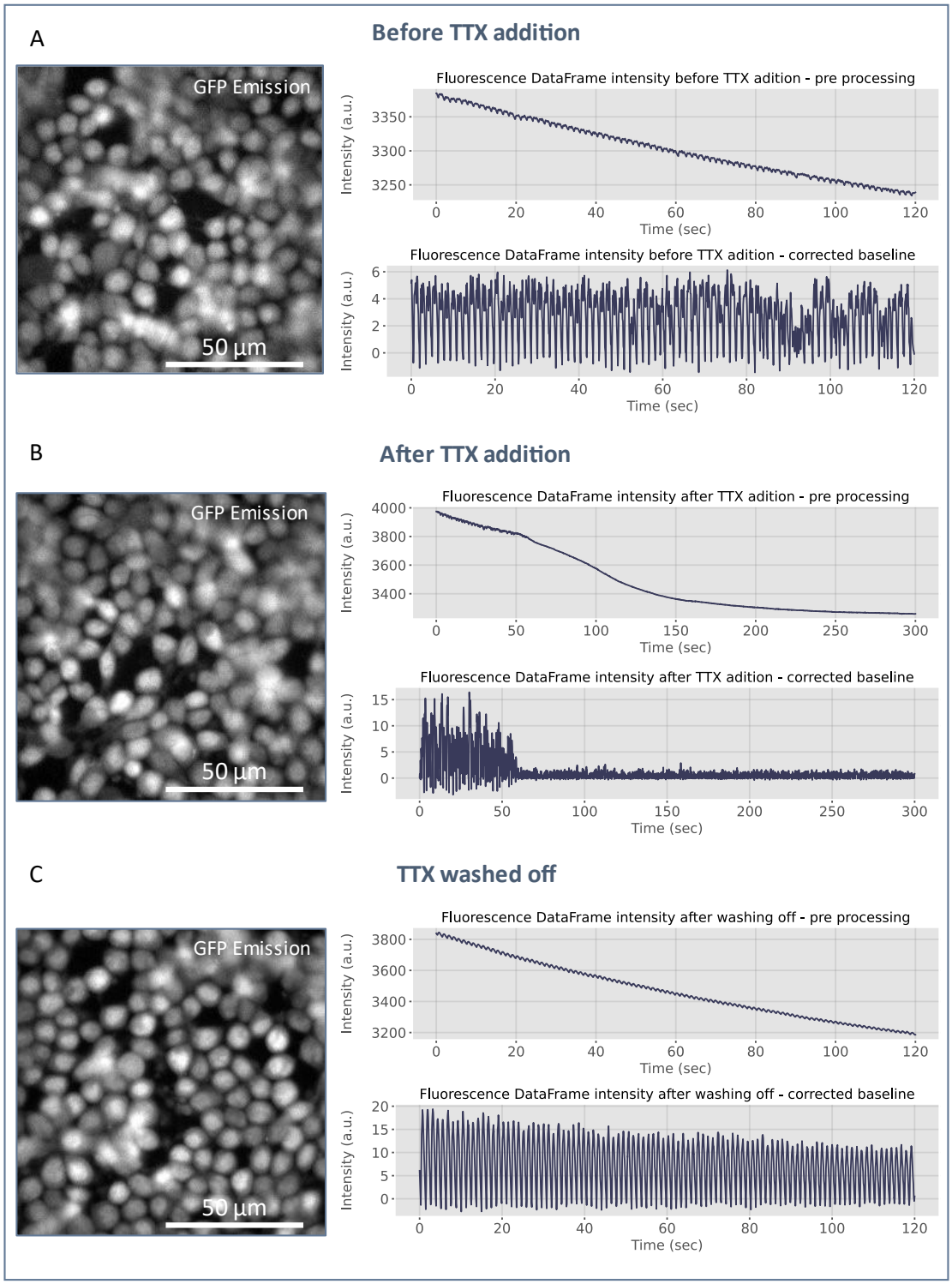

Figure A.101 Representative fluorescence images and corresponding traces recorded before (A), after (B), and following washout (C) of tetrodotoxin (TTX). Left panels show maximum intensity projections of GFP emission. Right panels display raw fluorescence intensity traces (top) and the same data following baseline correction (bottom), illustrating the effect of TTX on spontaneous spiking activity and its reversibility upon washout.

3. Supplementary Material for Chapter #3

3.1. Materials

Toluene (99.5%), hexane (98.5%), methanol (99.8%), methyl acetate (99%), acetone (99.5%), cadmium nitrate tetrahydrate (98%), oleic acid (99%), sodium hydroxide (97%), 1-octadecene (90%), diphenyl ether (99%), tetraethylene glycol dimethyl ether (tetraglyme, 99%), tetramethylthiourea (98%), hexyl isothiocyanate (95%), n dodecylamine (98%), chemicals were purchased from Sigma Aldrich and used as received.

β-D-Octyl glucoside, anhydrous, ≥99.8% dichloromethane (DCM) and toluene were purchased in Sigma Aldrich and used without further purification. Water purified using a Millipore Milli-Q water system was utilized in all experiments.

Phospholipids: 1,2-dimyristoyl-sn-glycero-3-phosphocholine (DMPC), 1,2-distearoyl-sn-glycero-3-phosphoethanolamine-N-[methoxy(polyethylene glycol)-2000] (ammonium salt) (DSPE-PEG2000), 1,2-Dioleoyl-3-trimethylammonium propane (DOTAP), along with mini extruder and polycarbonate membranes, were purchased from Avanti Polar Lipids. Chloroform, PBS buffer and reagents for cell culture were obtained from Sigma Aldrich. Commercially available CdSe/ZnS core/shell quantum dots with an emission maximum of 530 ± 5 nm and a CdSe core diameter of 2.5 nm were sourced from PlasmaChem.

3.1.1. Reagent Preparation - Recipes

Synthesis of N-hexyl-N′-dodecyl thiourea

N-hexyl-N′-dodecyl thiourea was obtained by following the procedure reported by Hendricks et al. 19 in which a toluene solution (8 mL) containing dodecylamine (1.796 g, 9.7 mmol) was mixed with a toluene solution (8 mL) containing hexylisothiocyanate (1.388 g, 9.7 mmol). The addition of amine solution triggered a quantitative and exothermic reaction. After the reaction was complete, excess toluene was removed under vacuum. This method allows for straightforward scale-up.

Synthesis of N,N′-diethyl imidazolidine selone

N,N′-diethyl imidazolidine selone was synthesized by charging a PTFE-sealable Schlenk flask equipped with a distillation apparatus with selenium (7.70 g, 97.5 mmol), triethyl orthoformate (34.36 g, 38.56 mL, 195 mmol), and N,N′-diethyl ethylenediamine (11.33 g, 13.57 mL, 97.5 mmol). The reaction mixture was degassed via three freeze-pump-thaw cycles, placed under an argon atmosphere, and stirred at 130 °C for 8 hours, during which the selenium fully

dissolved and a small volume of condensate collected in the receiving flask. After cooling to room temperature, excess triethyl orthoformate was removed by distillation under reduced pressure. The resulting residue was exposed to air, dissolved in dichloromethane, filtered through Celite, and recrystallized once outside the glovebox.

Synthesis of cadmium oleate

Cadmium oleate was prepared by stirring cadmium oxide (9.51 g, 74 mmol) in acetonitrile (95 mL) at room temperature. Trifluoroacetic acid (2.38 g, 20.9 mmol) and trifluoroacetic anhydride (16.59 g, 79 mmol) were added slowly, and the mixture was stirred for 1 hour to generate a clear cadmium trifluoroacetate solution. In a separate flask, oleic acid (41.82 g, 46.74 mL, 148 mmol), dichloromethane (740 mL), and triethylamine (19.08 g, 26.29 mL, 188.7 mmol) were combined under stirring. The cadmium trifluoroacetate solution was added dropwise to the oleic acid solution, resulting in the gradual formation of a white suspension. Acetonitrile (600 mL) was then added, and the mixture was heated to 60 °C to fully dissolve the precipitate. The solution was allowed to cool slowly to room temperature and then stored at -20 °C overnight. The resulting white solid was collected by vacuum filtration, washed thoroughly with cold acetonitrile, and dried under reduced pressure to afford cadmium oleate as a white powder.

Synthesis N-hexyl, N',N'-dibutyl thiourea

N-hexyl-N'-dodecyl thiourea was obtained analogically to the N-hexyl-N'-dodecyl thioureaby, by slowly mixing 8.0 mL of a toluene solution of dibutylamine (1.254 g, 9.7 mmol) with 8.0 mL of a toluene solution of hexyl isothiocyanate (1.388 g, 9.7 mmol). Upon completion of the reaction, residual toluene was removed under vacuum. This approach can be easily extended to larger scales.

3.2. Methods

3.2.1. Instrumentation

Dark-field (HAADF) scanning TEM imaging of SQWs, was conducted using a Talos F200X high-resolution transmission electron microscope. Bright-field TEM of SQWs was performed using a FEI Tecnai G2 20 TWIN microscope operated at 200 kV. Absorbance spectra (UV-Vis-NIR) were acquired with a Cary 3500 spectrophotometer, and fluorescence emission spectra were recorded with a Cary Eclipse fluorescence spectrophotometer (Agilent Technologies). PLQY measurements were carried out using a Horiba PTI QuantaMaster spectrofluorometer equipped with a 75 W xenon arc lamp, a 920C photomultiplier tube (PMT) detector, and a Quanta-P integrating sphere coated with Spectralon. Data acquisition and analysis were performed using FluorEssence software (version 3.8.0.60). Fluorescence lifetime measurements were conducted on a time-resolved confocal fluorescence microscope (MicroTime 200, PicoQuant) using pulsed laser excitation at 405 nm. Data acquisition and analysis, including multiexponential decay fitting, were performed with SymPhoTime 64 fluorescence lifetime imaging and correlation software (PicoQuant).

3.2.2. CryoTEM

CryoTEM analysis was performed on a 4 µL aliquot of the sample applied to Quantifoil R 2/2 copper grids (300 mesh) that had been freshly glow-discharged for 45 s using an ELMO glow discharge unit (Corduan Tech.). The grids were blotted and plunge-frozen in liquid ethane using a Leica EM GP2 automated plunge freezer (Leica Microsystems GmbH, Wetzlar, Germany). Imaging was carried out with a Krios G4 transmission electron microscope (Thermo Fisher Scientific, Waltham, MA, USA) equipped with a Gatan BioContinuum Image Filter and a K3 direct electron detector. Images were acquired at a nominal magnification of 165,000× with defocus settings from -1.5 to -2.0 µm.

3.2.3. Confocal Microscope

Confocal fluorescence imaging was performed using a Leica TCS SP5 laser scanning confocal microscope equipped with a HCX PL APO lambda blue 63×/1.20 NA water immersion objective (refractive index = 1.33). Optical sectioning was achieved with the pinhole aperture set to 1.00 Airy unit, corresponding to a physical pinhole diameter of approximately 111.5 µm, ensuring axial resolution appropriate for diffraction-limited imaging. Excitation was carried out using a 458 nm laser line, with an acousto-optic tunable filter (AOTF) transmission set to 51%, and total laser power delivered to the sample calibrated at ~29.4% of the maximum source output.

Emission was detected in a single channel via PMT 2, configured at 750 V gain, with 8-bit digitization and a linear LUT (gamma = 1.0). The image acquisition was performed at a zoom factor of 2.00, resulting in a final sampling resolution of 0.1217 µm per pixel in the lateral (X-Y) plane across a 512 × 512 pixel raster, yielding a total field of view of 62.29 µm × 62.29 µm. The acquisition was limited to a single optical plane, with Z-step size set to zero and the axial scanner deactivated. These parameters ensured Nyquist-sufficient lateral sampling and reliable optical sectioning for subsequent intensity-based image quantification.

3.2.4. Fluorescence Microscope

The fluorescence microscope setup used in this study was identical to the configuration described in the supplementary materials for Chapter 2. All imaging parameters, optical components, and acquisition settings remained consistent unless otherwise noted in the main text.

3.3. Additional Figures

Stability Study - Fluorescence Lifetime Traces

Shown below are the original fluorescence decay curves recorded for vesicles extruded through 100 nm, 400 nm, and 800 nm membranes on days 1, 2, and 5 (Figure A.102). These traces were used for triple exponential fitting, with averaged lifetime values presented in the main text (Figure 3.22, Chapter 3, Section 2.2).

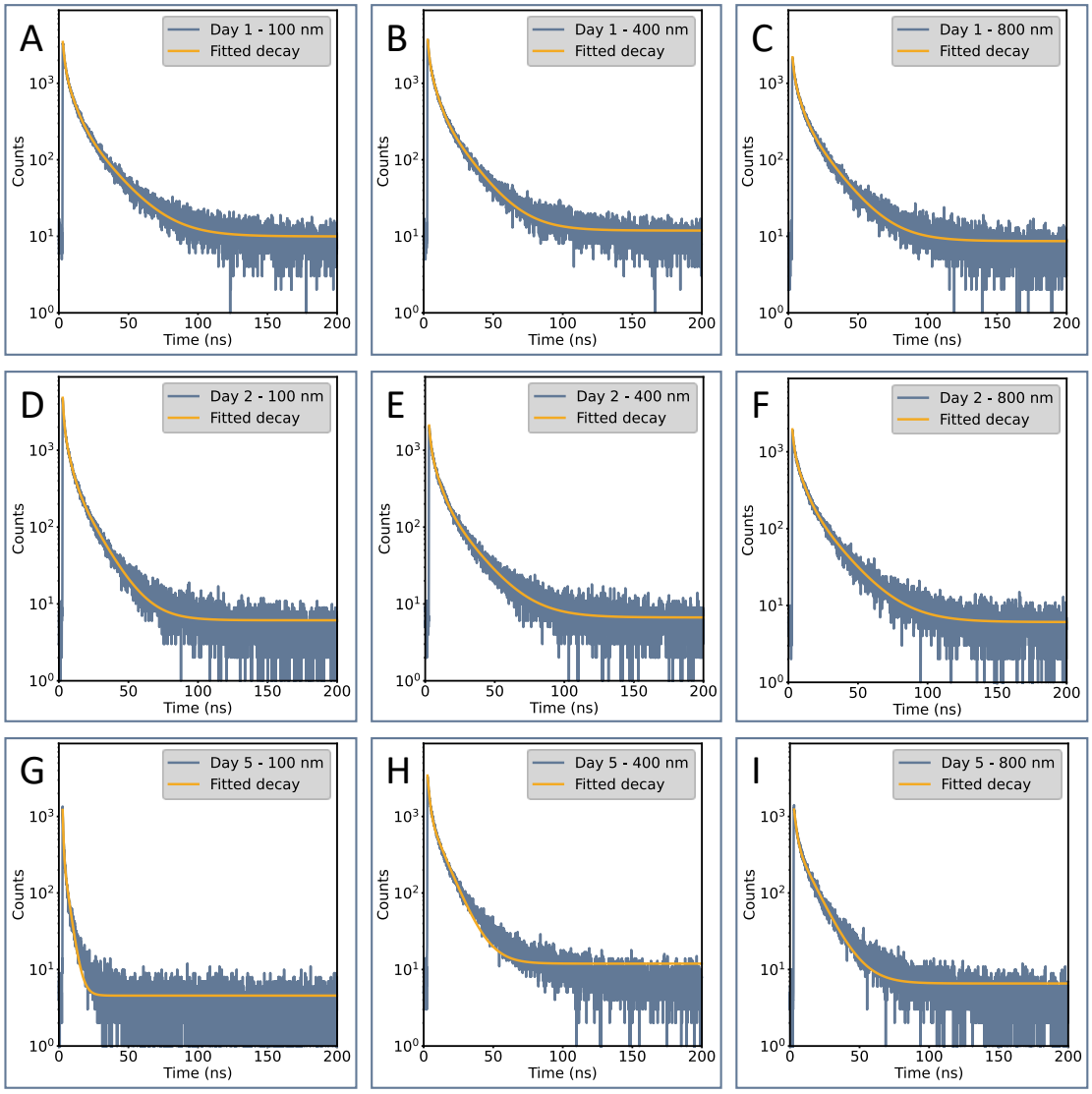

Figure A.102 Raw fluorescence lifetime decay curves for vesicles of different sizes—100 nm (A, D, G), 400 nm (B, E, H), and 800 nm (C, F, I) - measured on Day 1 (A-C), Day 2 (D-F), and Day 5 (G-I). The overlaid yellow lines represent the fitted triple exponential decays.

Optical characterization of SQWs systems used for lipid encapsulation

As discussed in Chapter 3, Section 2.2, photoluminescence quantum yield (PLQY) measurements were performed for selected quantum well systems in the presence of lipid vesicles. Shown below are the corresponding absorption and emission spectra for all synthesized systems.

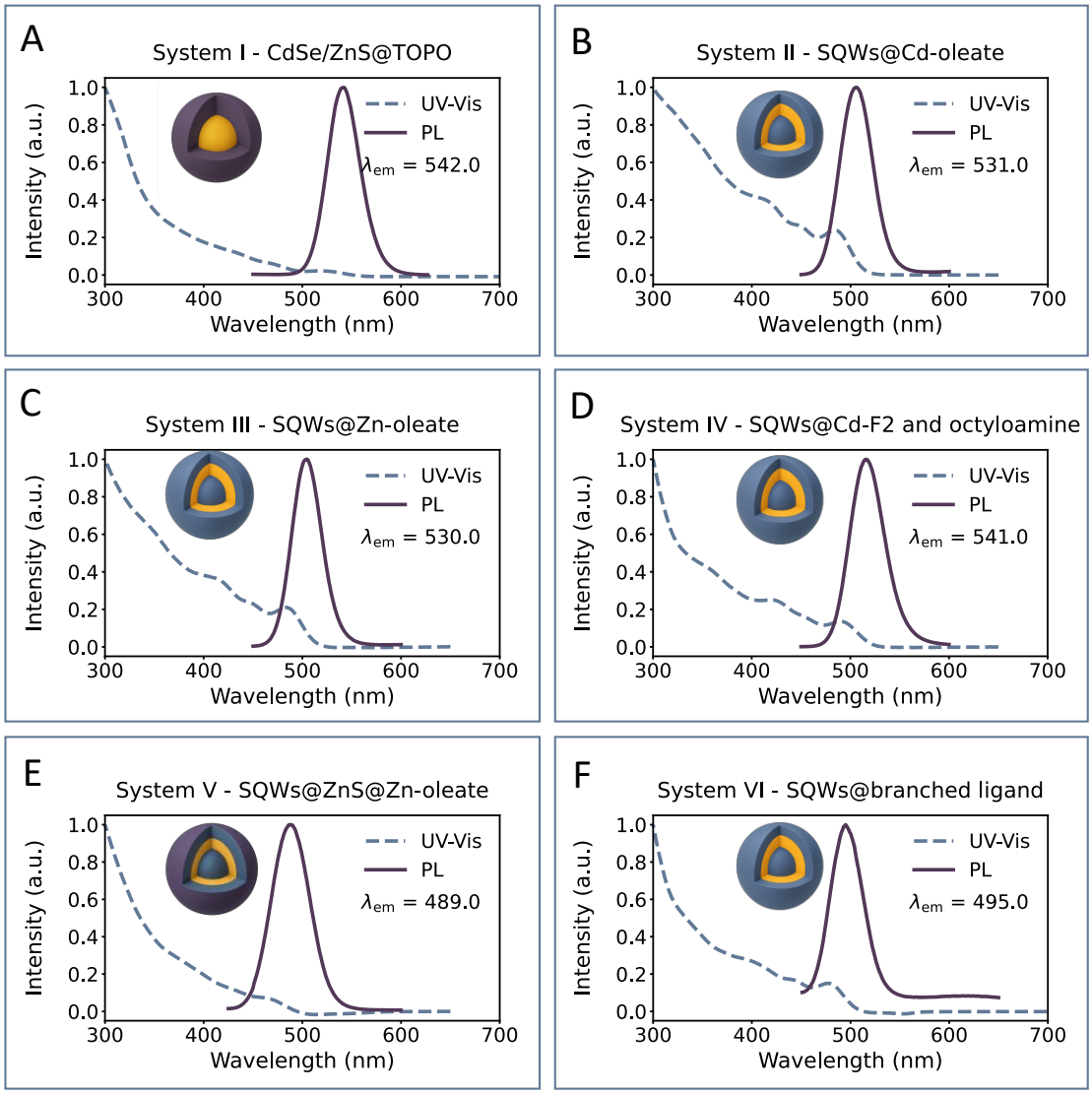

Figure A.103 Normalized absorption (dashed blue lines) and photoluminescence (solid purple lines) spectra of the investigated systems: (A) System I – CdSe/ZnS@TOPO, (B) System II – SQWs@Cd-oleate, (C) System III – SQWs@Zn-oleate, (D) System IV – SQWs@Cd-F2 and octylamine, (E) System V – SQWs@ZnS@Zn-oleate, and (F) System VI – SQWs@branched ligand. Emission maxima (λ_{em}) are indicated in each panel.

Membrane staining experiments – control sample

The image below shows the non-stained HEK293 cell sample used as a baseline reference in membrane staining experiments discussed in Chapter 3, Section 3.2. This control was imaged under identical conditions as stained samples and served as a background reference for the intensity profiles shown in Figures 3.36-3.41.

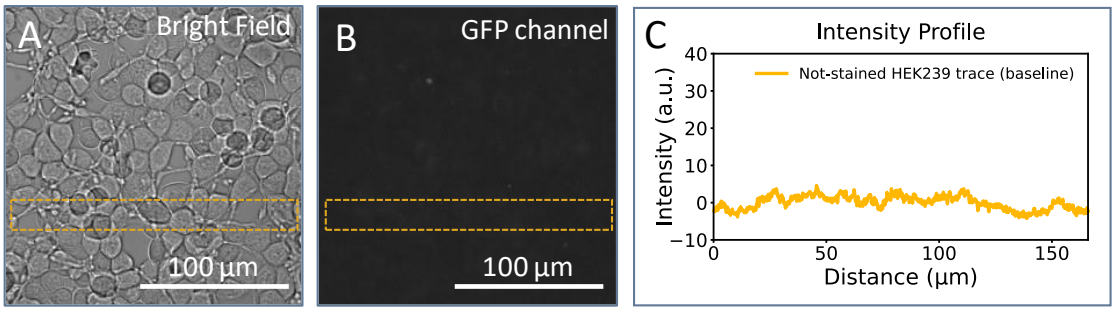

Figure A.104 Bright-field (A) and GFP channel (B) images of non-stained HEK293 cells used as a control. Panel (C) shows the fluorescence intensity profile extracted along the indicated region in the GFP channel image. The trace represents baseline autofluorescence in the absence of any membrane dye or SQW staining.

Spiking HEK Cells Recordings – Traces Comparison

To additionally support the results presented in Chapter 3, Section 3.2, representative fluorescence traces are shown for HEK cells stained with SQWs (System VI), for cells treated with TTX, and for a non-stained control (baseline). These traces serve as the basis for evaluating signal dynamics. Raw baseline-corrected and filtered traces are presented both in offset view (Figure A.105) and overlaid for direct comparison (Figure A.106).

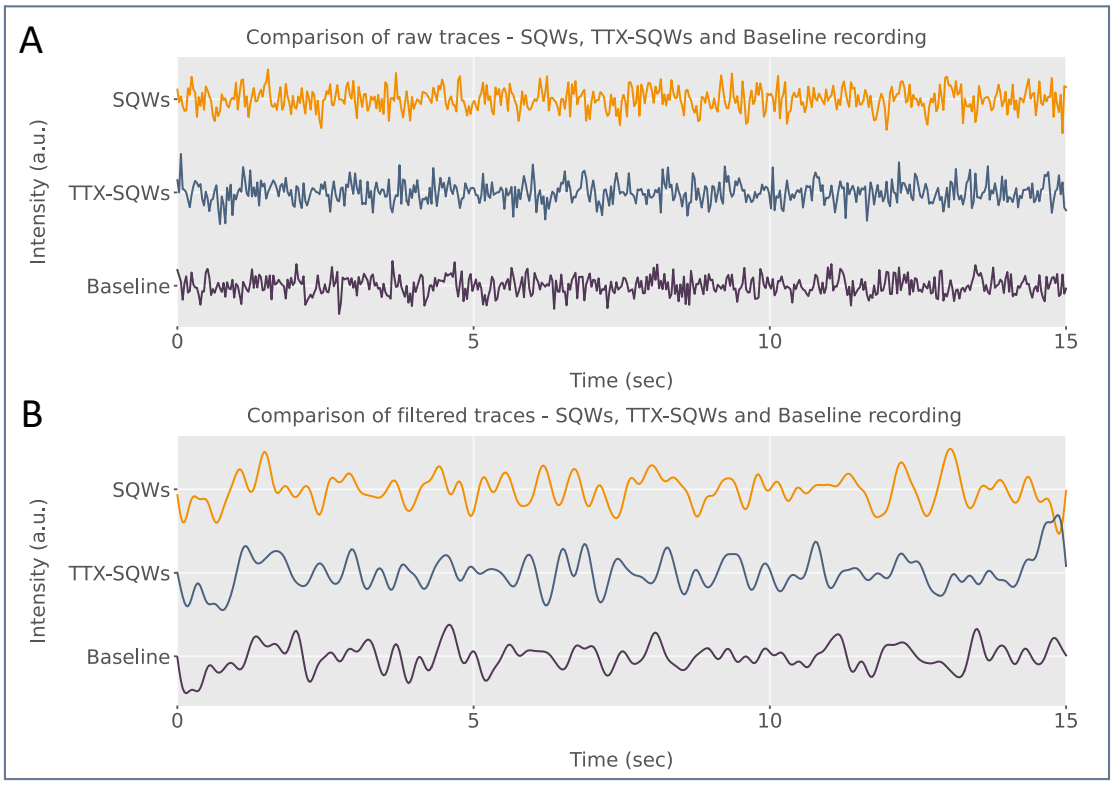

Figure A.105 Representative fluorescence traces for SQW-labeled HEK cells, TTX-treated cells, and non-stained control. (A) Baseline-corrected raw traces.(B) Filtered traces (bandpass), shown with vertical offset.

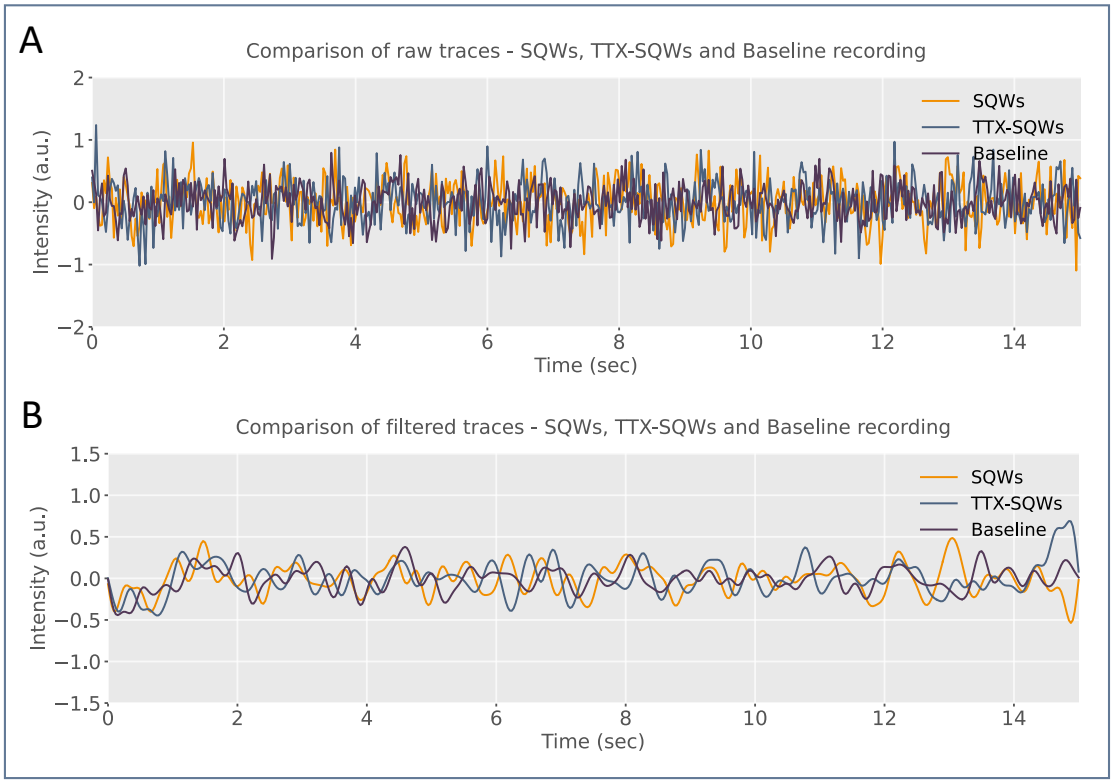

Figure A.106 Same traces as above overlaid for direct comparison. (A) Baseline-corrected raw traces. (B) Bandpass-filtered traces, highlighting differences between spiking, TTX-treated, and control conditions.

Trace averaging analysis

To assess the presence of periodic activity in the recorded fluorescence signals, a trial-averaging approach was applied. Based on the dominant frequency detected in the calcium signal, each trace was divided into equal-length segments corresponding to the expected spike period. In the absence of an external synchronization trigger, the segmentation start point was varied using a series of offsets. For each offset value, the trace was divided accordingly, and the resulting segments were averaged. This sliding-window approach allowed identification of the most favorable alignment for periodic features. Consistent, well-aligned transients were observed in calcium recordings. In contrast, traces from SQW-labeled and non-stained control cells lacked periodic structure, and their averaged signals appeared random and indistinguishable. The analysis was performed on both raw (Figure A.107) and filtered traces (Figure A.108).

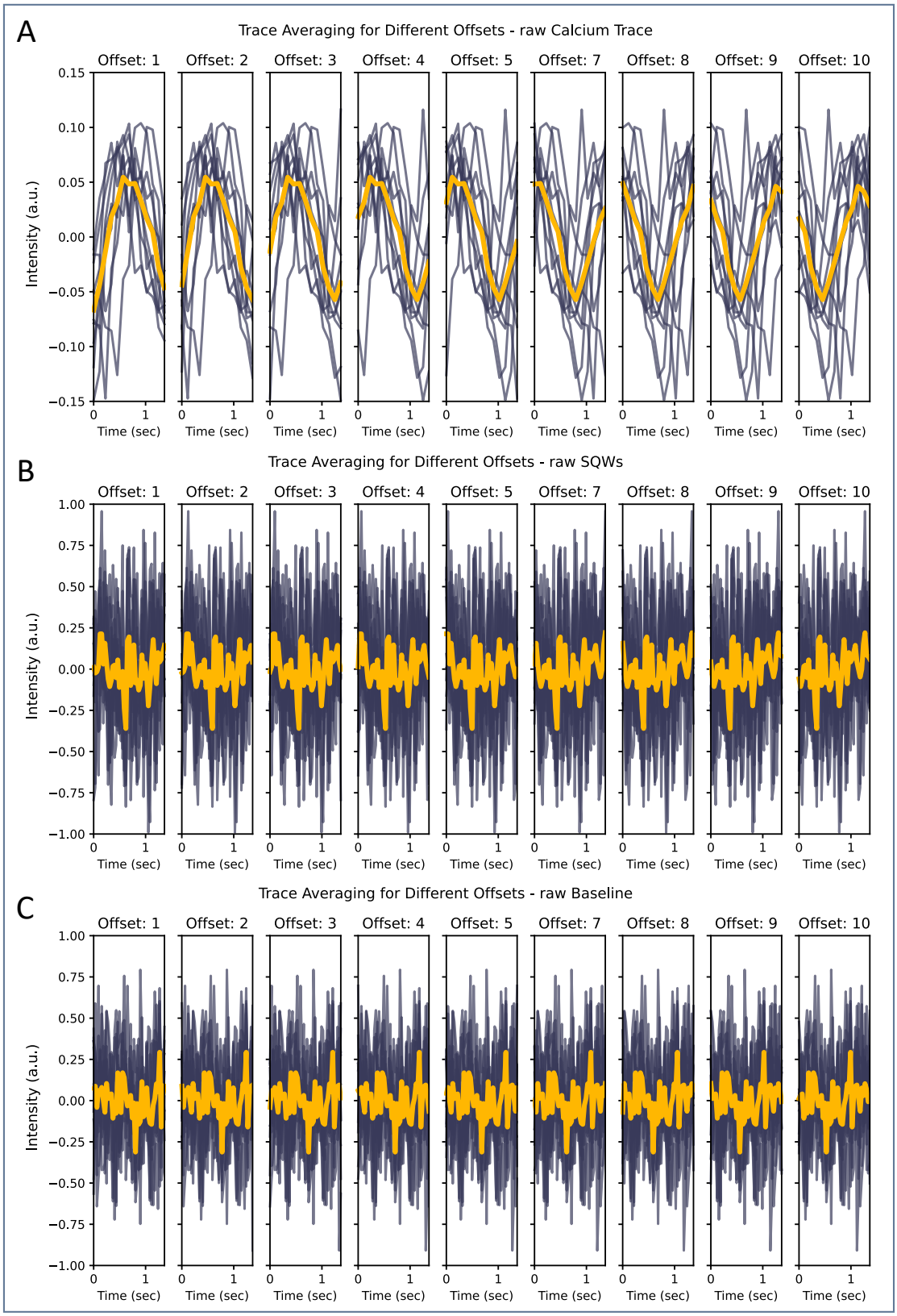

Figure A.107 Trace averaging for different offsets applied to raw (baseline-corrected, unfiltered) recordings. (A) Calcium trace shows consistent spike-aligned transients across offsets. (B) SQW-labeled signal appears noisy and non-periodic. (C) Non-stained control resembles SQW trace, indicating lack of structured signal. Yellow lines indicate averaged response; grey lines represent individual segments.

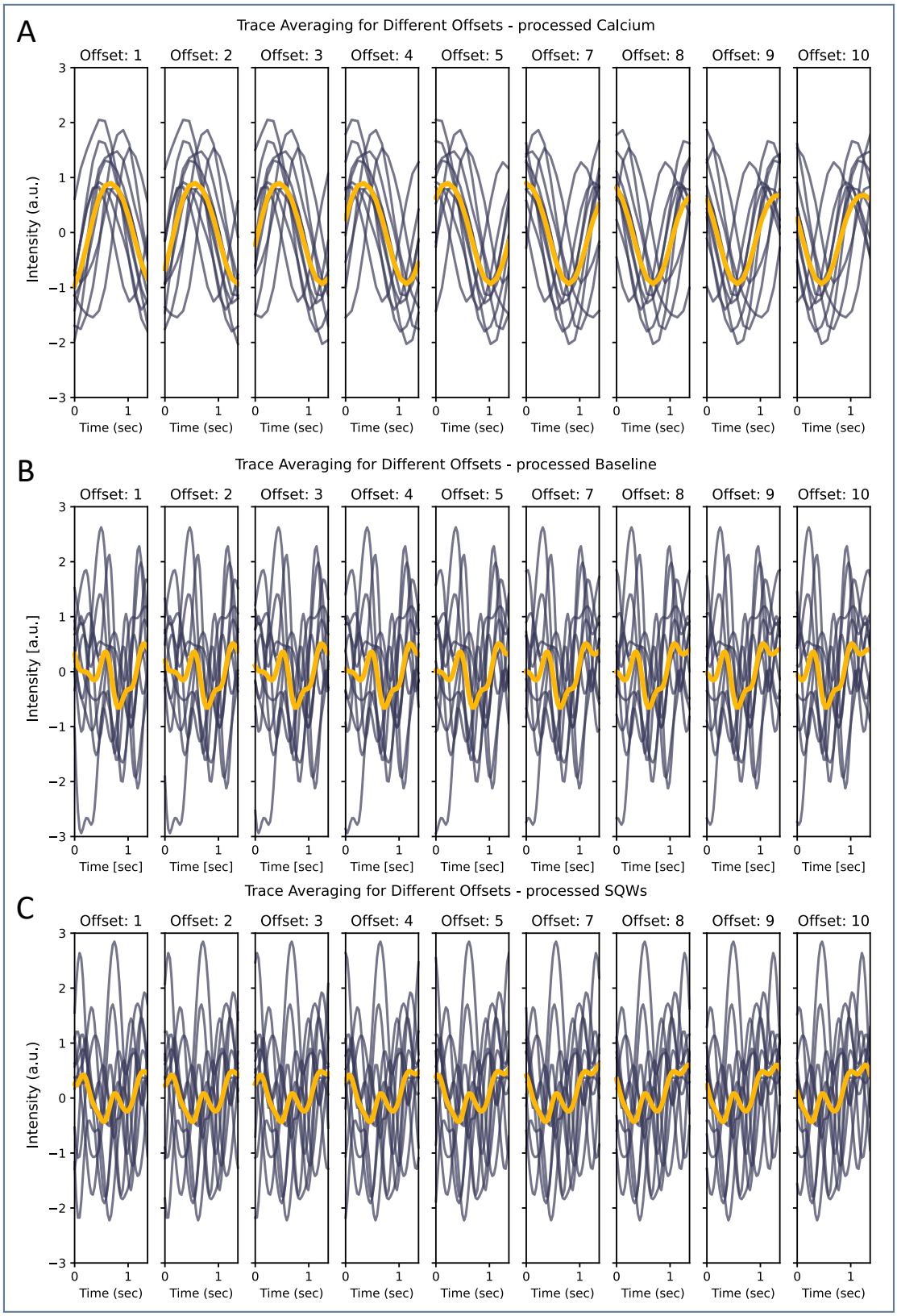

Figure A.108 Trace averaging for different offsets applied to processed (baseline-corrected and filtered) recordings. (A) Calcium trace shows robust, well-aligned periodic signal across offsets. (B) Non-stained control and (C) SQW-labeled traces remain inconsistent, with averaged signals lacking clear periodic features. Yellow lines indicate averaged response; grey lines represent individual segments.

4. Supplementary Material for Chapter #4

4.1. Materials

Gold (III) chloride trihydrate ($HAuCl_4 \cdot 3H_2O$), trisodium citrate dihydrate ($C_6H_5Na_3O_7 \cdot 2H_2O$) were purchased from Sigma Aldrich. Hexadecyltrimethylammonium bromide (CTAB) and hexadecyltrimethylammonium chloride (CTAC, 25 wt% solution), sodium hypochlorite solution (NaClO), sodium borohydride ($NaBH_4$), sodium hydroxide (NaOH), silver nitrate ($AgNO_3$) citric acid, ascorbic acid, hydrochloric acid solution (HCl) were purchased form Sigma Aldrich and use d without further purification. Avidin, NeutrAvidin, NeutrAvidin-FITC conjugate and NeutrAvidin-DyLight™ 633 conjugate along with EZ-Link™ NHS-PEG12-Biotin (No-Weigh™ Format) were purchased from ThermoFisher Scientific (Molecular Probes™).

Cell culture reagents, including DMEM/F-12, Neurobasal Plus, B-27 Plus supplements, GlutaMAX, B-27, Penicillin-Streptomycin (10,000 U/mL), poly-D-lysine, and Geltrex™ were purchased from Gibco. Texas Red™-phalloidin (by Invitrogen) and DAPI used for staining were purchased from Thermo Fisher Scientific.

4.2. Methods

4.2.1. Protocols

Turkevich Synthesis of small Au NPs@citrate

Glassware was freshly cleaned with aqua regia (3:1 v/v HCl : HNO_3), rinsed with ultrapure water (18.2 MΩ cm) and dried at 120°C. An aqueous solution of chloroauric acid ($HAuCl_4 \cdot 3H_2O$, 500 mL, 0.50 mM Au) was transferred to a 1 L flask equipped with a magnetic stirring bar. The suspension was heated to the boiling point of the solution (≈100 °C) while stirring at 700 rpm.

In parallel, a 1% w/v trisodium citrate dihydrate solution (25 mL, 38.8 mM) was pre-heated to ~ 95°C. Once the gold solution reached boiling point, the hot citrate solution was introduced in one quick shot. Heating was maintained for 15 min; during this period the colour evolved from colourless to dim bright blue/purple shade to wine-red.

After 15 min the heating plate was turned off and the flask was allowed to cool to room temperature under continued stirring. The final dispersion volume was 525 mL, giving an Au^0 concentration of 0.48 mM and a citrate: Au molar ratio of 5:1. Samples were stored in vials at 4°C.

Tailored size 30 nm spherical Au NPs@CTAB

Gold nanospheres (30 nm) were synthesized via a three-step seed-mediated growth method. In step one, 4.7 mL of 0.1 M CTAB was preheated at 35°C for 5 min, followed by addition of 25 µL of 0.05 M $HAuCl_4$. After another 5 min incubation at 35°C, 0.3 mL of freshly prepared 0.01 M ice-cold $NaBH_4$ was injected in one shot under vigorous magnetic stirring. Stirring continued for 2 min, followed by incubation for 30 min at 27°C. The seed solution (Au^0 ≈ 0.25 mM) should have an absorbance of 0.6 at 400 nm. Immediately, 72 mL of 0.1 M CTAC was mixed with 360 µL of 0.05 M $HAuCl_4$ and stirred mildly at room temperature for 10 min. Then, 27 mL of 0.1 M ascorbic acid was rapidly added, followed by immediate injection of 0.6 mL seed solution. The reaction proceeded for 60 min under mild stirring at room temperature, yielding 12 nm Au NPs (Au^0 ≈ 0.225 mM, A_{400} ≈ 0.54). The product was centrifuged at 8500 rpm for 10 min and redispersed in 5 mL water. The gold concentration was adjusted to 2.8 mM. For the final growth, 0.518 mL of the 12 nm seed solution was added to 100 mL of 15 mM BDAC pre-incubated at 35°C for 10 min. Then 0.5 mL of 0.1 M ascorbic acid was injected, followed by 0.5 mL of 0.05 M $HAuCl_4$. The solution was stirred for 30 min at 35°C. The resulting 30 nm Au NPs had Au^0 ≈ 0.26 mM and A_{400} ≈ 0.624. Oxidative shape correction was performed by adding 360 µL of 1% v/v NaClO dropwise and stirring 10 min at 35 °C. Then, 100 µL of 0.05 M $HAuCl_4$ was added dropwise, followed by a 30 min incubation at 35°C. The nanoparticles were centrifuged twice at 14 500 rpm for 10 min each and redispersed in 10 mM CTAB to reach a final gold concentration of 0.4 mM.

Seed-Mediated Synthesis of Gold Bipyramids

Gold seeds were prepared by mixing 10.0 mL of 50 mM CTAC, 0.05 mL of 50 mM $HAuCl_4$ and 0.05 mL of 1 M citric acid in a 20 mL glass vial and stirring at 20°C. Freshly prepared 0.25 mL of 25 mM $NaBH_4$ was then injected under vigorous stirring, resulting in an immediate color change from yellow to brownish; the absorbance at 400 nm was recorded (A_{400} ≈ 0.6 for a 0.25 mM gold concentration) to ensure complete reduction. The vial was sealed and the seed solution aged by heating at 80 °C with gentle stirring for 90 min, during which the color evolved from brown to red.

For bipyramid growth, 100 mL of 100 mM CTAB was heated to 30°C and sequentially mixed with 5.0 mL of 10 mM HAuCl4, 1.0 mL of 10 mM $AgNO_3$, 2.0 mL of 1 M HCl and 0.8 mL of 100 mM ascorbic acid. Under vigorous stirring at 30°C, 1.1 mL of the aged seed solution was rapidly injected and the mixture was left undisturbed at 30 °C for 2 h. The resulting gold bipyramids

were collected by two centrifugation cycles at 8 000 rpm for 30 min each and redispersed in 0.1M CTAB solution in Milli-Q water.

Detailed Biofunctionalization Protocols

Gold Nanoparticles@Citrate: Prior to functionalization, 1 mg of NeutrAvidin and NeutrAvidin-FITC powders were each dissolved in 1 mL of 10 mM PBS (pH 7.4) to yield 1 mg/mL stock solutions. In a typical reaction, 20 µL of protein stock (1 mg/mL) was added to 500 µL of citrate-stabilized AuNPs (7.2 nM) previously adjusted to pH 11 with 1 M NaOH. The mixture was vigorously stirred for 10 s and transferred to an ice bath maintained below 10 °C for 1 h to promote uniform adsorption. Unbound protein was removed by centrifugation at 5500 rpm for 60 min at 25 °C; the supernatant was carefully decanted, and the pellet was redispersed in 200 µL of Milli-Q water preadjusted to pH 11.

Gold Nanoparticles@CTAB (30 nm): A 500 µL aliquot of 30 nm CTAB-capped AuNPs (0.6 nM in 15 mM CTAB) was subjected to two successive washes: centrifuge at 7000 rpm for 20 min at 30 °C, discard supernatant, and resuspend in 200 µL Milli-Q water. The purified NPs were adjusted to pH 11, and 20 µL of 1 mg/mL NeutrAvidin (or FITC conjugate) solution was added under vigorous stirring. The reaction mixture was incubated in an ice bath (<10 °C) for 1 h. To remove excess protein, samples were centrifuged at 5500 rpm for 60 min at 25 °C, the supernatant removed, and the pellet resuspended in 200 µL water at pH 11.

Gold Bipyramids@CTAB: 500 µL aliquot of CTAB-stabilized gold bipyramids (0.5 mM Au^0 equivalent in 15 mM CTAB) was washed twice by centrifugation (7000 rpm, 20 min, 30 °C) and resuspended in 200 µL Milli-Q water. A 1:1 mixture of NeutrAvidin and NeutrAvidin-FITC stock solutions (each 1 mg/mL) was prepared, and 25 µL of this mixture was added to the bipyramid suspension adjusted to pH 11. After brief vortexing, the suspension was placed in an ice bath (<10 °C) for 1 h. Excess protein was pelleted by centrifugation at 500 rpm for 5 h at 25 °C, the supernatant decanted, and the pellet resuspended in 200 µL of pH 11 water.

SH-SY5Y Cell Culture

SH-SY5Y neuroblastoma cells were cultured in DMEM/F-12 medium supplemented with 10% fetal bovine serum (FBS) and 1% penicillin-streptomycin. Cells were maintained at 37 °C in a humidified atmosphere with 5% CO_2. Medium was replaced every 2-3 days, and cells were passaged every 3-4 days to maintain healthy growth and confluency for experimental use.

4.2.2. Instumentation

TEM of gold nanocrystals was conducted using a FEI Tecnai G2 20 TWIN microscope operated at an acceleration voltage of 200 kV. Absorbance spectra (UV-Vis-NIR) were acquired with a Cary 3500 spectrophotometer. Fluorescence emission spectra were recorded using a Cary Eclipse Fluorescence Spectrophotometer (Agilent Technologies).

4.2.3. Confocal Imaging of Fixed Cells

Confocal imaging experiments were performed to evaluate the internalization of FITC-labeled bipyramidal gold nanoparticles (BPs) by SH-SY5Y neuroblastoma cells and primary cortical (CTX) neurons, as presented in Chapter 4.3.

For SH-SY5Y cells, 7×10^4 cells per well were seeded into 8-well Ibidi chamber slides and cultured for two days in DMEM/F-12 medium supplemented with 10% FBS and 1% penicillin/streptomycin. Cells were then incubated with 0.002 nM FITC-labeled BPs for 30 minutes, 1 hour, 3 hours, or 24 hours. Two conditions were tested: direct application of BPs and pre-incubation with 5 µM NHS-PEG-biotin linker (EZ-Link™) for 15 minutes prior to nanoparticle exposure. After incubation, cells were gently washed with DPBS and prepared for fixation.

Primary cortical neurons were isolated from embryonic day 16 (E16) Wistar rat embryos (Charles River Laboratories). Brain tissue was dissected in Leibovitz's L-15 medium, followed by cortical isolation and gentle mechanical dissociation in Neurobasal Plus medium using a flame-polished pipette. The resulting suspension was centrifuged at 500 × g for 5 minutes, and the pellet was resuspended in Neurobasal Plus medium supplemented with 1× GlutaMAX, 2× B-27 Plus, and 1% penicillin/streptomycin.

CTX neurons were seeded at a density of 1×10^5 cells per well in 8-well Ibidi chamber slides, previously coated following a three-step procedure: (1) incubation with 0.1% polyethylenimine (PEI, M_w ~25,000, Sigma) in borate buffer for 1 hour, followed by three sterile water washes; (2) incubation with 1 mg/mL poly-D-lysine in DPBS for 1 hour, followed by washing and air drying; (3) incubation with 1× Geltrex in culture medium for 24 hours, followed by removal prior to cell seeding. Cells were maintained in a humidified incubator at 37 °C with 5% CO_2. Partial medium changes were performed every 4-5 days. Neurons were used for imaging experiments after 15 days in vitro (DIV), once they reached functional maturity.

Following incubation with BPs, both SH-SY5Y and CTX cells were fixed with 4% paraformaldehyde for 20 minutes at room temperature and washed three times with DPBS. Cytoskeletal actin

filaments were stained with 160 nM Texas Red-phalloidin for 20 minutes, and nuclei were stained with 300 nM DAPI (Thermo Scientific) for 5 minutes. Each staining step was followed by three 5-minute DPBS washes at room temperature.

Confocal imaging was performed on a Zeiss LSM 900 microscope using a 63× oil immersion objective. For each condition, eight representative images were acquired.

4.2.4. Transmission Electron Microscopy (TEM) of Fixed Cells

Cortical neurons (1×10^5 cells per well) were seeded into 8-well chamber slides (Thermo Scientific Nunc Lab-Tek). After 20 days in vitro (DIV), cells were incubated with functionalized bipyramids (BPs) at a final concentration of 0.02 nM for either 1 hour or 24 hours, without prior treatment with a biotin linker. Following incubation, cells were thoroughly washed with PBS to remove unbound particles. Fixation was carried out using 3% glutaraldehyde in 0.1 M phosphate-buffered saline (PBS) for 10 minutes at 37 °C, followed by an additional 1-hour fixation with fresh 3% glutaraldehyde at room temperature. Fixed samples were sent to the Centro de Investigación Príncipe Felipe (CIPF) for embedding and TEM preparation. Samples were embedded in Epoxy resin (Agar Scientific), and ultrathin sections (50 nm) were prepared using a Leica ultramicrotome. TEM imaging was performed on a TECNAI G2 20 TWIN transmission electron microscope.

4.3. Additional Figures

Stability in biological media

Uv-Vis measurements for stability assessment were performed in Multicell Spectrophotometer Cary 3500 UV-Vis-NIR with air-cooled Peltier temperature control.

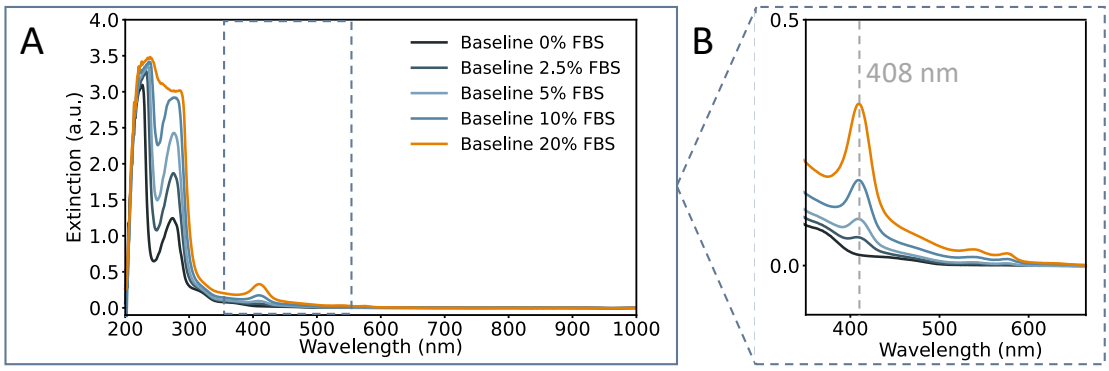

Figure A.109 UV-Vis spectra of Neurobasal medium supplemented with varying concentrations of FBS, measured using water as the baseline. These spectra were used as reference baselines for the nanoparticle measurements presented in Figure 4.9.

Dynamic light scattering was used to assess the colloidal stability of nanoparticle suspensions in biological media by monitoring changes in hydrodynamic size over time. Measurements were performed on a 3D-LS spectrometer (LS Instruments AG) equipped with a 660 nm DPSS laser (100 mW; coherence length > 10 m; noise < 0.1 % rms). The detector was positioned at scattering angles θ = 40°-140° in 10° increments; at each angle three 30 s intensity traces were acquired and averaged. From the measured intensity of scattered light, the normalized intensity autocorrelation function

$$g_2(\tau) - 1 = \frac{\langle I(t) \cdot I(t+\tau) \rangle}{\langle I \rangle^2} - 1$$

was computed and converted to the field autocorrelation via the Siegert relation,

$$g_2(\tau) = 1 + \beta \cdot |g_1(\tau)|^2$$

where β is the coherence factor. Assuming monodisperse behavior, each $g_1(\tau)$ was fitted to a single-exponential decay,

$$g_1(\tau) = exp(-\Gamma \cdot \tau)$$

yielding the decay rate Γ. The scattering vector was calculated as

$$q = \left(\frac{4 \cdot \pi \cdot n}{\lambda}\right) \sin\left(\frac{\theta}{2}\right)$$

and resulting values q^2 were plotted with Γ. Linear fitting of this dependence

$$\Gamma = D \cdot q^2$$

provided the translational diffusion coefficient D , which was then converted to the hydrodynamic radius via the Stokes-Einstein equation,

$$R_\mathrm{h} = \frac{k_B \cdot T}{(6\,\pi \cdot \eta \cdot D)}$$

where k_B is Boltzmann's constant, T the absolute temperature, and η the solvent viscosity. Values for η for water and Neurobasal with 10% FBS were taken as 0.6913 mPa and 0.958 mPa respectively (Poon, 2020).

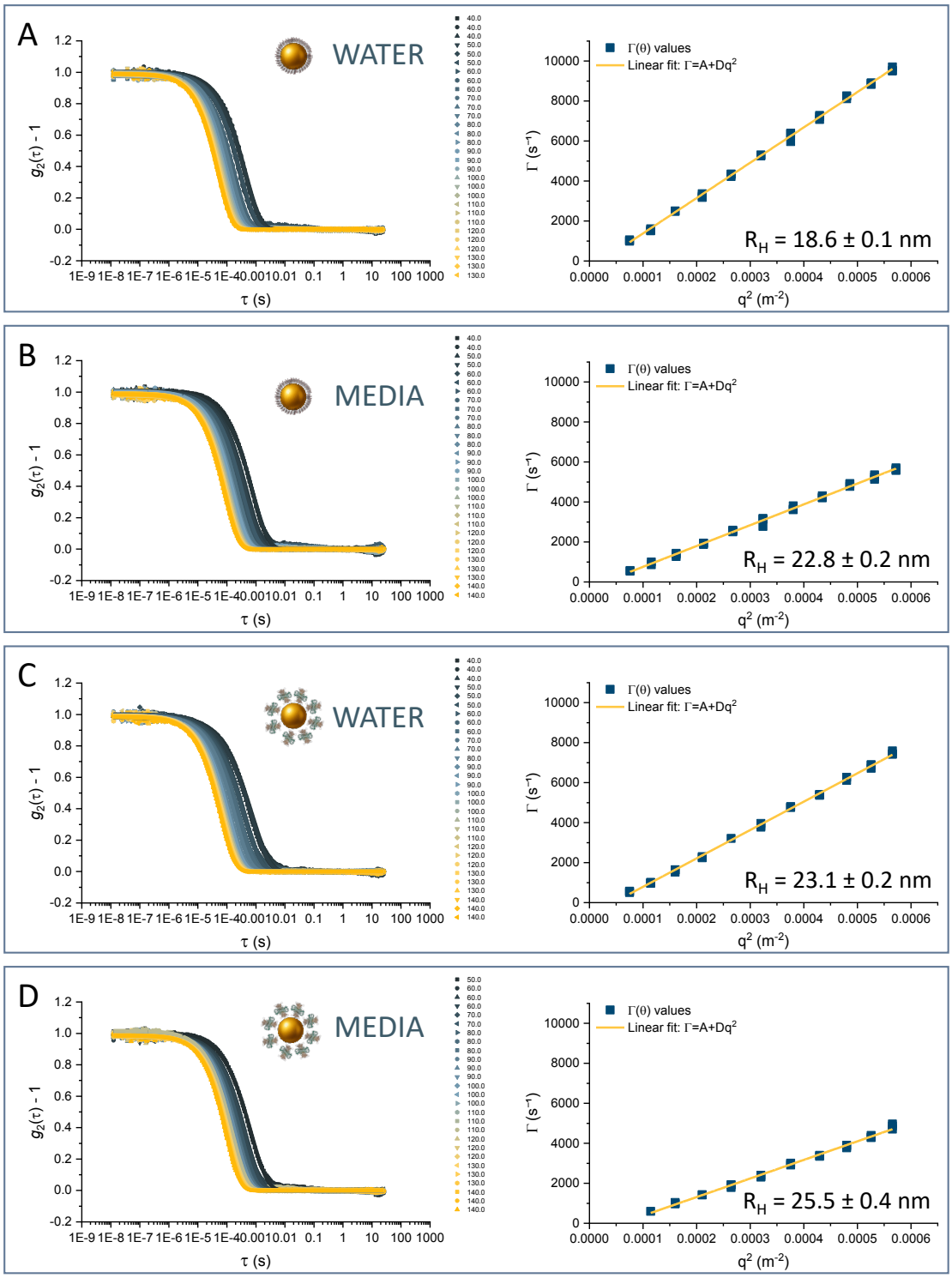

Figure A.110 Dynamic light scattering (DLS) measurements showing the autocorrelation functions (left) and corresponding diffusion coefficient plots (right) for gold nanoparticles in different conditions. (A) Uncoated gold nanoparticles dispersed in water. (B) Uncoated gold nanoparticles dispersed in Neurobasal/B27 medium. (C) NeutrAvidin-coated gold nanoparticles in water. (D) NeutrAvidin-coated gold nanoparticles in Neurobasal/B27 medium. The linear fit of the diffusion coefficient as a function of scattering vector squared (q^2) was used to calculate the hydrodynamic radius (R_H) for each condition.

In Vitro – Internalization Study

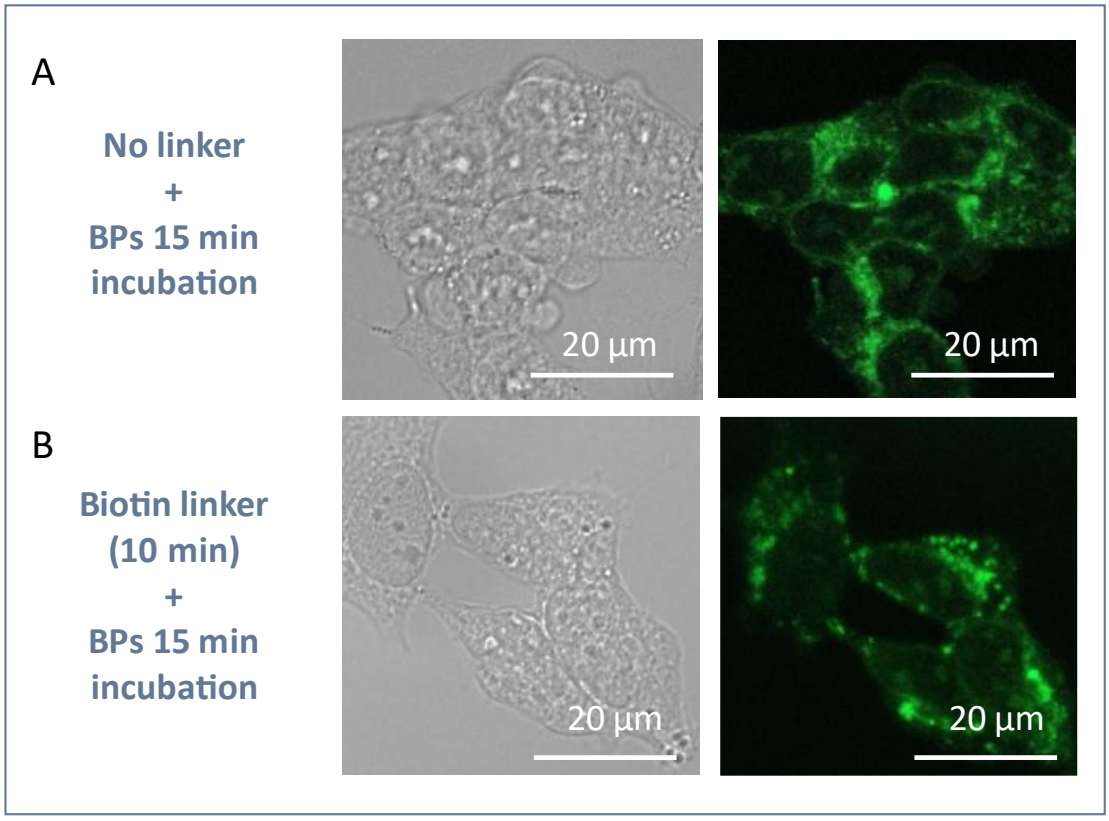

*Figure A.111 Confocal imaging of SH-SY5Y cells incubated with FITC-labeled gold bipyramids functionalized with NeutrAvidin (BPs@NeutrAv*FITC). Bright-field images (left) are shown alongside their corresponding green fluorescence channel (right), revealing nanoparticle localization. (A) Cells were incubated directly with 0.002 nM BPs for 15 minutes. (B) Cells were pre-incubated with 5 µM NHS-PEG-biotin linker for 10 minutes prior to 15-minute exposure to BPs. The green fluorescence originates from the FITC dye conjugated to the nanoparticles, allowing for visualization without additional DAPI or phalloidin staining.*

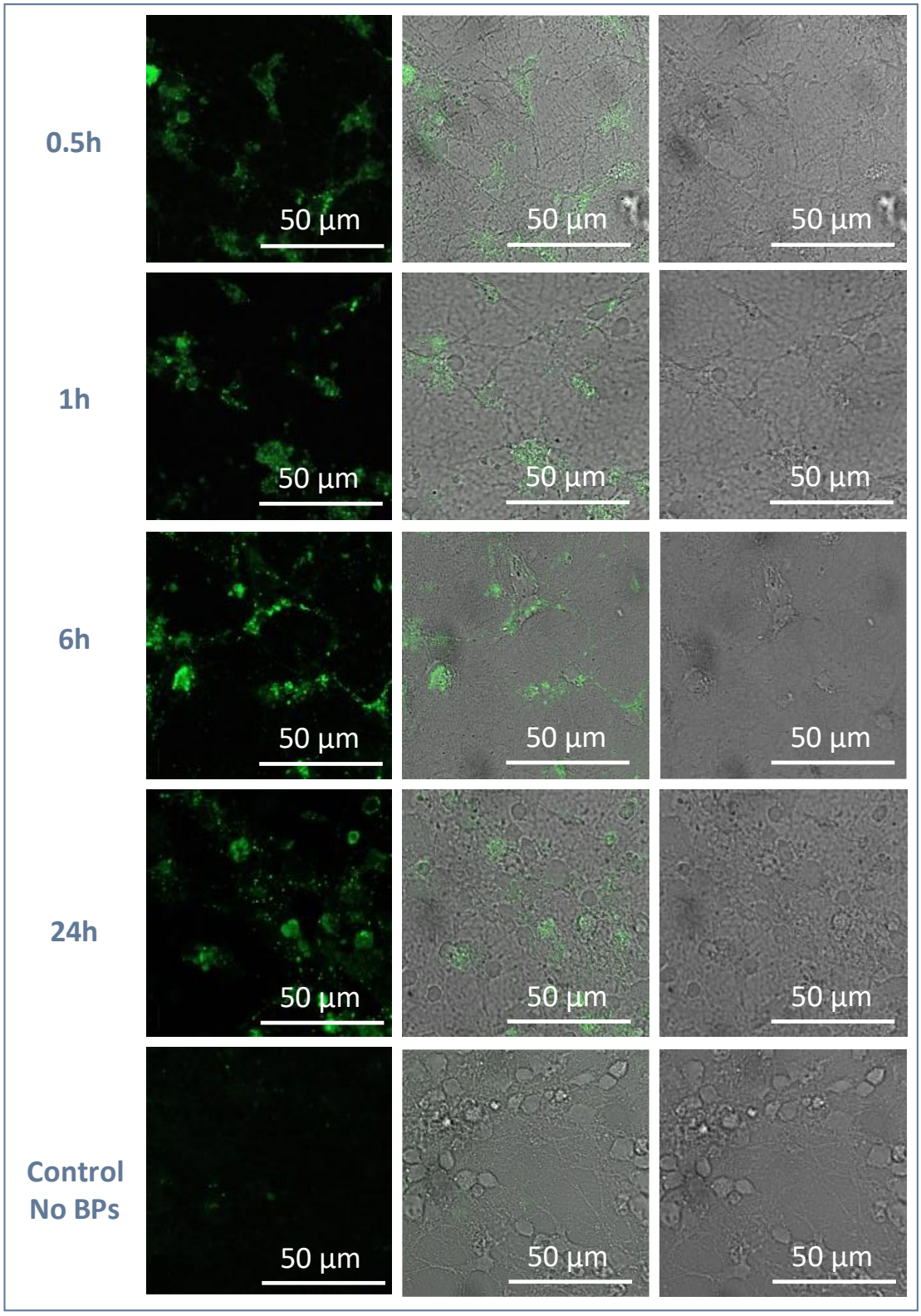

*Figure A.112 Confocal imaging of primary cortical (CTX) neurons incubated with FITC-labeled gold bipyramids (BPs@NeutrAv*FITC) at various time points to monitor nanoparticle internalization. Each row corresponds to a different incubation time: 0.5 h, 1 h, 6 h, and 24 h, with a control sample (no BPs) at the bottom. Columns show: (left) green fluorescence channel (FITC), (middle) merged fluorescence and bright-field, and (right) bright-field alone. o additional nuclear or cytoskeletal stains were applied for these observations.*

5. Data and Code Repository

All datasets, analysis scripts, and supplementary files associated with this thesis are available in an online repository at https://saco.csic.es/s/WoC52KNgGsWw6WC. The repository contains raw and processed experimental data, code used for statistical analyses and figure generation, and additional documentation that supports the results presented in the main text. The structure of the repository is organized by chapters, enabling direct access to the underlying data and analysis pipeline.

QR code to the repository:

6. Documentation of Digital Tools

6.1. Data Analysis

Data analysis and visualization were carried out using Python code executed in JupyterLab, OriginLab software, and ImageJ/Fiji for microscopy image processing. Custom scripts are included in the accompanying online repository to ensure reproducibility of the results.

6.2. Figure Preparation

Unless otherwise indicated, all figures and graphical elements included in this thesis were prepared by the author. Figure assembly was performed using Microsoft PowerPoint. Individual elements were created or processed using the following software tools (in alphabetical order): BioRender, ChemDraw, ChatGPT (OpenAI), GIMP, Inkscape, Jmol, and Pexels.

6.3. Assisted Editing and Literature Search

Software provided by OpenAI (ChatGPT models) was used to support phrasing, language corrections, and general writing assistance. Perplexity and NotebookLM were used as search engines to identify and organize relevant sources. Zotero was used for managing references and citation formatting. All scientific content, data interpretation, and conclusions were developed by the author.

Acknowledgments

I would like to acknowledge the opportunities and resources provided by my supervisors, **Marek Grzelczak** and **Rafael Yuste**, which made this research possible. I am also grateful to **Jonathan Owen** and **Mónica Carril** for welcoming me into their laboratories and for their involvement in the project. Access to these research environments shaped both the progress of this work and my scientific growth.

These four years have been a demanding journey, but I have always considered myself very lucky. Wherever I go, I find extraordinary people who accompany me on my path.

The starting point for my PhD was Donostia. A big shout-out to my AAA support group – **Adam**, **Anish**, and **Alba**. Your encouragement, guidance, and understanding meant a great deal to me. Your insights and advice helped shape the research, and even from a distance, you remained actively involved during the writing phase, helping me navigate moments of uncertainty. Thank you for everything. That gratitude extends to the fourth A – **Ane Escobar**. Your positive energy was a real support. Thank you for your biological insights, for recognizing the effort I was putting in, and for your encouraging and motivating feedback.

Adam! Dziunia – Twoja obecność i wsparcie wybiega dużo dalej niż mury CFM. Dziękuję za każdą porcję gnocchi po trudnym dniu, wspólne wieczory filmowe, pływanie, górskie wycieczki, wspólne zajawki i memy – dużo memów. You "Make Life ~~Harder~~ Easier".

Alba – you are my Ecuadorian twin, and I am so glad we met. Thank you for all the help navigating both scientific and administrative challenges. Thank you for being my translator and my Spanish voice whenever needed. For listening, for understanding, and for bringing color – not only to my hair.

Kateryna, **Adam**, **Mattia**, **Paschalis** – thank you for making our apartment to feel like HOME. The fact is that we always could find there exactly what we needed. Our house was many things (a hotel, a cinema, a restaurant, a bakery, an arena to fight insects) – but most importantly, it was a place I always felt comfortable coming back.

Jorge – for your great, universal advice ("SHUMP, Zuzanna, SHUPM!") and swimming adventures. **August** – for making "Bilbao for Vote and More" truly "More". **Lorenzo** – for carbonara lesson and short, yet meaningful, presence. **Jozef** – for the good throws and your calm attitude. **Đorđe** – for crosswords and your Eastern-European sarcasm.

The thesis writing process was closely observed by my new office mates – **Quimey**, **Asier**, **Victor**, **Rubén**, **Martin**, and **Juli**. Thank you for the pastries, the venting chats, uplifting stories and for reminding me what day of the week it was. A big thank-you to **Raúl**, **Anto**, **Sabine**, **Nathaniel**, **Caro**, **Phuong**, **Idoia**, and everyone else who made Donosti a good place to be.

Another important part of this journey took place in New York. **Noah** – thank you million for being the best adventure seeker. Thanks to you I started seeing NY in a different light and appreciated its perks. For all the escapades, quests, hidden gems, quizzes, laughs, late nights in the lab but also scientific guidance, discussions and sharing your scientific curiosity – thank you.

Teresa – only you can truly understand how traveling back and forth could be the hardest, yet most meaningful part of this PhD experience. Thank you for being a great companion through it all. You are the person connecting both worlds – all happy moments or difficulties shared with you always felt well understood.

Hakim – for your friendship. I value all your expertise, help with the setup and scientific input but also all the discussions that happened along. Thank you for the museums, the concerts, ballet performances, and for making the lab a better place. **Justin** – for all the fun you were introducing every day. For being positive even during tough times, finding joy regardless, for being "a mountain of a man". **Jojo** – for being a moral compass, and reminding me what is truly important. For swimming, hiking, all the chats, rooftop hangouts and reality checks. For making me a part of your very colorful world. **Boris** – Thank you for being such a great scientific support, for all the suggestions and tips. Thank you for celebrating all my wins with me, and for patiently helping me understand the reasons behind the setbacks. Thank you for all the coffees, lunch breaks and late cinema evenings as a fellow A-lister. You brought fresh energy when the lab began to change. Thank you, **Tzitzi** and **Victor H.**, for your patient guidance, especially at the beginning of my biological research. You both helped a lot when nothing seemed to make sense.

Darik and Ellie – thank you for being great friends. Together with **Catherin and Beans**, you made me feel like part of the local life and community. To fully understand Washington Heights, you have to live it! We survived the Dumpster Fire, and it looks like we're still standing. It was a pleasure being a silent witness to your practical jokes on Noah.

Łukasz, Alona i Miszon dzięki za wspaniałe towarzystwo na finiszu w Nowym Jorku. Dzięki Wam odkryłam nowe aspekty tego miasta i nowe pasje – bird watching w Central Parku to ostatnia rzecz jakiej się po sobie spodziewałam. Zadbaliście o to żebym nie zaginęła w odmętach laboratorium i dawaliście poczucie normalności, przypominając co jest ważne. Wspaniale było mieć Was za sąsiadów. Dziękuję!

A big thank-you to **Bereket**, **Dan** and **Galder** for your help with chemistry aspects, and to all members of the **Owen Lab** for welcoming me into your space and making me feel a part of it. To **Bella**, **Samu**, **Alex**, **Wataru**, **Jesus**, **Tabata**, **Doug**, **Mei** with the gang (**Bill**, **Bobby and Mattie**), and everyone else who made New York much more than "just a research stay" – thank you.

Dziękuję całemu mojemu rozbudowanemu systemowi wsparcia, który pozostaje w mocy mimo upływu lat i dzielących nas kilometrów: **Santorkowi**, **Marcie**, **Gregorowi z Drużyną**, **Zofce**, **Anecie**, **Krzyśkowi i Piotrowi**, **Multipolkom** i **Brudasom+** (**Adamowi**, **Zetasowi**, **Andrzejowi**, **Puchatowi** i **Koziarowi** – wraz ze wszystkimi „plusami").

And last but not least, I want to thank my amazing family, for whom I am always enough. To my wonderful and supportive parents **Katarzyna and Leszek**, my siblings **Agata and Wiktor**. And to **Paschalis**, for being my greatest support on day-to-day basis. Without you, writing this thesis would be so much harder. You helped me to keep my focus while ensuring proper rest. Thank you for grounding me, for all your care, and your loving support.

DZIĘKUJĘ!

The author acknowledges support from the IKUR Strategy (NanoNeuro Initiative), provided through a collaboration agreement between the Ikerbasque Foundation and the Materials Physics Center, on behalf of the Department of Education of the Basque Government.